Gas-liquid hydrodynamics and mass transfer around Taylor bubbles : local investigations using a colorimetric method during the flowing stage in an in-plane spiral-shaped milli-reactor and during the bubble formation process at a cross-junction geometr

Mei Mei

Université Fédérale
Toulouse Midi-Pyrénées

THÈSE

En vue de l'obtention du

DOCTORAT DE L'UNIVERSITÉ DE TOULOUSE

Délivré par l'Institut National des Sciences Appliquées de Toulouse

Présentée et soutenue par

Mei MEI

Le 14 avril 2021

Hydrodynamique et transfert de matière gaz-liquide autour des bulles de Taylor: études locales utilisant une technique colorimétrique pendant la phase d'écoulement dans un milli-réacteur plan en forme de spirale et pendant le processus de formation de bulles dans une géométrie en croix

Ecole doctorale : **MEGEP - Mécanique, Energétique, Génie civil, Procédés**

Spécialité : **Génie des Procédés et de l'Environnement**

Unité de recherche :
TBI - Toulouse Biotechnology Institute, Bio & Chemical Engineering

Thèse dirigée par
Gilles HEBRARD, Nicolas DIETRICH et Karine LOUBIERE

Jury

M. Rufat ABIEV, Rapporteur
M. Norbert KOCKMANN, Rapporteur
M. Régis PHILIPPE, Examinateur
M. Eric OLMOS, Examinateur
Mme Anne-Marie BILLET, Examinatrice
M. Gilles HEBRARD, Directeur de thèse
Mme Karine LOUBIERE, Co-directrice de thèse
M. Nicolas DIETRICH, Co-directeur de thèse

En vue de l'obtention du
DOCTORAT DE L'UNIVERSITÉ DE TOULOUSE
Délivré par l'Institut National des Sciences Appliquées de Toulouse

Présentée et soutenue par

Mei MEI

Le 14 Avril 2021

Titre: ***Hydrodynamique et transfert de matière gaz-liquide autour des bulles de Taylor: études locales utilisant une technique colorimétrique pendant la phase d'écoulement dans un milliréacteur plan en forme de spirale et pendant le processus de formation de bulles dans une géométrie en croix***

École doctorale : **MEGEP-Mécanique, Energétique, Génie civil, Procédés**

Spécialité : **Génie des Procédés et de l'Environnement**

Unités de recherche

TBI - Toulouse Biotechnology Institute (UMR INSA/CNRS 5504 - UMR INSA/INRA 792)

LGC - Laboratoire de Génie Chimique (UMR CNRS/INPT/UPS 5503)

Directrice(s) ou Directeur(s) de Thèse

Nicolas Dietrich, Gilles Hébrard et Karine Loubière

Jury

M. Rufat ABIEV	Professeur à St. Petersburg State Institute of Technology	Rapporteur
M. Norbert KOCKMANN	Professeur à Technische Universität Dortmund	Rapporteur
M. Régis PHILIPPE	Chargé de recherche CNRS, au LGPC, Lyon	Examinateur
M. Eric OLMOS	Professeur à Université de Lorraine, LRGP, Nancy	Examinateur
Mme Anne-Marie BILLET	Professeure à l'INPT-ENSIACET, LGC, Toulouse	Président
M. Nicolas DIETRICH	Maitre de conférences/HDR à l'INSA Toulouse et à TBI	Co-directeur de thèse
M. Gilles HEBRARD	Professeur à l'INSA Toulouse et à TBI	Directeur de thèse
Mme Karine LOUBIERE	Directrice de recherche au CNRS, LGC	Co-directrice de thèse
M. Benjamin LALANE	Professeur à l'INPT-ENSIACET, LGC, Toulouse	Membre Invité

Acknowledegment

I would like to take this opportunity to express my sincere gratitude to all the people who supported me during my PhD. study. It was such a wonderful and memorable journey for me.

Firstly, I would like to thank Anne-Marie Billet, the president of thesis committee, and also the reviewers of my dissertation, Rufat Abiev and Norbert Kockmann, for your insightful comments to improve and optimize the dissertation. In addition, many thanks to other committee members, Régis Philippe, Eric Olmos, and Benjamin Lalanne, for your kind suggestions and advices.

Most importantly, I would like to give my sincere thank and deepest gratitude to my supervisors: Gilles Hébrard, Nicolas Dietrich, and Karine Loubière. You brought me into this brand new but so interesting research field. All of my work could not be achieved without your guidances and supports. You've trained me how to think independently and tackle the encounting problems step-by-step with patience. Your expertise and enthusiasm always encourage me. I will carry on what you've taught me in the future work.

Also, I would like to thank Claude Le Men, José Moreau, Alain Line, Emmanuel Cid, and Abdlali Khalfaoui for their mechanical design and optical system on the experimental setups. And thanks for Bernard Galy for transporting the cameras between TBI and LGC labs. I am so impressed by the expertise on image processing from Claude. It is always a great pleasure to discuss with you.

I would like to thank Francisco Felis, who taught me a lot. You firstly showed me how to apply the colorimetric method. Your expertise on image processing really inspires me and facilates my work. And thanks to Abderrahmane Kherbeche, it is so great to have the opportunity to collaborate with you. Also, thanks to Robbie Radjagobalou for your smart method of solution preparation and arrangement of apparatus utilization. And thanks to Kritchart Wongwailikhit who

also helped me on the colorimetric method. Thanks to Feishi Xu, you helped me a lot on the TP work.

Besides, I would like to thank Alain Liné and Alexandre Boucher, for the dissusion on the theoretical analysis of gas-liquid hydrodynamics parameters. Your insightful comments help me better understand the gas-liquid hydrodynamics.

Moreover, Gaëlle Lebrun, Kaliyani Kentheswaran, Axel Canado, Zibin Nan, Ploypailin Romphophak, Carlos Mayorga Espinoza, Vincent Ngu, Ming Cheng, Irem Demir, Ibrahima Drame, Zhou Shen and Tianyi Zhang, you made my time at lab much colorful.

Also, I would like to thank my friends: Xin Yi, Xue Han and Jin Wang, for sharing happiness together and making my life at Toulouse much fun. Particularly, I would like to thank Zhihua Chen, my dearest friend, for your love and support.

Finally, I would like to thank my family, especially my parents and my brother, who always support and trust me.

Abstract

Continuous-flow technologies, especially microstructured reactors, are now recognized as relevant alternatives for batch processing, and thus for process intensification. The understanding of gas-liquid mass transfer in such microreactors is still an active research topic regarding the strong coupling between local hydrodynamics, mass transfer, and chemical reaction kinetics.

This thesis aims at studying gas-liquid hydrodynamics and mass transfer around Taylor bubbles in two configurations. The first one concerns bubbles flowing in an in-plane spiral-shaped milli-reactor, initially designed for organic photochemistry applications, and the second one involving bubbles generated at a cross-junction in a straight milli-channel. A colorimetric technique based on the resazurin dye was implemented and improved to monitor the oxygen mass transfer occurring between the air bubble and the aqueous phase.

The investigations in the in-plane spiral-shaped milli-reactor (~3 m reactor length) were first reported. Two configurations, characterized by various tube curvature ratio ranges, were compared. In terms of hydrodynamics, a linear increase of bubble length and velocity with the axial position was observed. Very long stable Taylor bubbles and liquid slugs (up to 40 and 20 times the tube inner diameter resp.) were generated. At identical Reynolds numbers, higher centrifugal force led to lower Taylor bubble lengths while slightly affecting the liquid slug lengths. Concerning the mass transfer, the variation of the equivalent oxygen concentration inside the liquid slugs was measured all along the tube. Overall volumetric mass transfer coefficients were quantified from the knowledge of the full coloration positions: they could be linearly related to the recirculation frequencies in the liquid slug and the intensification factor between the two configurations was found to be proportional to the increase in average Dean

numbers. Considering the changes in pressure drop, bubble length, and velocity, the axial variation of cumulated mass flux density was measured and an original scaling law for Sherwood number was established by introducing a normalized time and other dimensionless numbers.

A special focus was then made on the gas-liquid mass transfer around Taylor bubbles generated at a cross-junction in a straight milli-channel. The objective was to get a deeper understanding of the mass transfer mechanism during the bubble formation process. Thanks to an improved optical imaging device (monochromatic light, magnification), higher quality of images could be achieved. Among all the results obtained, one could point out, for a low two-phase superficial Reynolds number, a jet-like central oxygen concentration 'finger' occurred between the newly formed bubble and the gas finger at the bubble pinch-off point. It was also observed how the dissolved oxygen was transported first by the liquid entering from two side inlets, and later by the recirculation loop developing inside the liquid slug. For higher Reynolds numbers, a different mechanism was highlighted: two highly concentrated oxygen concentration spots were formed near the just-formed bubble rear and the channel wall region, and a much more complex flow structure in the liquid slug appeared. From the variation of averaged oxygen concentration at different positions after the cross-junction, overall mass transfer coefficients were deduced and compared with the ones obtained in the spiral-shaped milli-reactor. A unified correlation associating them to the recirculation frequencies could then be proposed, accounting for the effect of curvature ratio.

At last, this work made it possible to gain knowledge on gas-liquid hydrodynamics and mass transfer characteristics around Taylor bubbles, especially on the effect of centrifugal force, during and just after the bubble formation stage. These findings could be used to provide guidelines to implement multiphase reactions in continuous flow microstructured reactors.

Keywords: gas-liquid mass transfer, Taylor bubbles, in-plane spiral-shaped milli-reactor, bubble formation, colorimetric technique, image processing.

Résumé

Les nouvelles technologies continues, en particulier les réacteurs microstructurés, sont désormais reconnues comme des alternatives pertinentes aux procédés batch dans une démarche d'intensifier des procédés. La compréhension du transfert de matière gaz-liquide dans ces microréacteurs reste une thématique de recherche active car de nombreuses questions scientifiques demeurent, concernant notamment le fort couplage entre l'hydrodynamique, le transfert de matière et la cinétique des réactions chimiques.

Cette thèse vise à étudier l'hydrodynamique et le transfert de matière gaz-liquide autour de bulles de Taylor, spécifiquement dans deux géométries: (1) un milli-réacteur plan en forme de spirale, initialement conçu pour des applications en photochimie organique, and (2) une géométrie en croix. La technique colorimétrique utilisant la résazurine a été mise en œuvre et améliorée pour quantifier précisément le transfert de matière d'oxygène intervenant entre la bulle d'air et la phase aqueuse.

Des mesures dans le milli-réacteur plan en forme de spirale (~ 3 m de longueur) ont d'abord été effectuées. Deux configurations, caractérisées par diverses plages de rapport de courbure des tubes, ont été comparées. Une augmentation linéaire de la longueur et de la vitesse des bulles avec la position axiale a été observée. Des bulles de Taylor et des bouchons liquides très longs ont pu être générés. A même nombre de Reynolds, une force centrifuge plus élevée induit des longueurs de bulles de Taylor plus courtes et n'affecte que légèrement les longueurs des bouchons liquides. Les coefficients volumétriques de transfert de masse ont été quantifiés à partir de la connaissance des positions pour lesquelles une coloration maximale est atteinte. Ces coefficients ont été corrélés linéairement aux fréquences de recirculation dans les bouchons liquide et le

facteur d'intensification entre les deux configurations géométriques s’est avéré proportionnel à l'augmentation du nombre de Dean moyen. La variation axiale du flux massique cumulé d’oxygène transféré a été mesurée et une loi d'échelle du nombre de Sherwood a été établie.

Ensuite, un accent particulier a été porté sur des bulles de Taylor générées dans un micro-canal rectiligne, à partir d’une géométrie en croix, afin de mieux comprendre le mécanisme de transfert de matière pendant le processus de formation des bulles. Une meilleure qualité des images a été obtenue grâce à un dispositif d'imagerie optique amélioré. Pour un faible nombre de Reynolds, l’existence d’un filamentde forte concentration en oxygène central en forme de jet a été mis en évidence entre la bulle nouvellement formée et le film de gaz au niveau du point du pincement de la bulle. Il a également été observé comment l'oxygène dissous est transporté d'abord par le liquide entrant dans la géométrie en croix, et ensuite par les boucles de recirculation en cours de formation à l'intérieur du bouchon de liquide. Pour des nombres de Reynolds supérieurs, un mécanisme différent a été mis en évidence: d’une part on retrouve deux zones hautement concentrées en oxygène près de l'arrière de la bulle juste formée et en proche paroi du canal, et d’autre part une structure d'écoulement beaucoup plus complexe formée dans le bouchon liquide. A partir de la variation axiale de la concentration moyenne d'oxygène, les coefficients volumétriques de transfert de masse ont été mesurés et comparés à ceux obtenus dans le milli-réacteur en forme de spirale. Une corrélation reliant ces coefficients aux fréquences de recirculation a été proposée, prenant en compte l’effet du rapport de courbure.

Au final, ces travaux ont permis d'acquérir des connaissances sur l'hydrodynamique et le transfert de matière gaz-liquide autour de bulles de Taylor, et notamment sur l'effet de la force centrifuge et durant et après l’étape de formation de bulles. Ces résultats pourront servir pour établir des lois d’échelle en vue de la mise en œuvre de réactions polyphasiques dans des réacteurs microstructurés continus.

Mots clés : transfert de matière gaz-liquide, bulles de Taylor, milli-réacteur plan en forme de spirale, formation de bulles, méthode colorimétrique, traitement d'image.

List of Publications

Journal Publications

1. **Mei, M.**, Felis, F., Hébrard, G., Dietrich, N., & Loubière, K. (2020). Hydrodynamics of Gas–Liquid Slug Flows in a Long In-Plane Spiral Shaped Milli-Reactor. *Theoretical Foundations of Chemical Engineering*, *54*, 25-47.
   DOI: 10.1134/S0040579520010169
2. **Mei, M.**, Hébrard, G., Dietrich, N., & Loubière, K. (2020). Gas-liquid mass transfer around Taylor bubbles flowing in a long, in-plane, spiral-shaped milli-reactor. *Chemical Engineering Science*, 115717.
   DOI: 10.1016/j.ces.2020.115717
3. Kherbeche, A., **Mei, M.**, Thoraval, M. J., Hébrard, G., & Dietrich, N. (2019). Hydrodynamics and gas-liquid mass transfer around a confined sliding bubble. *Chemical Engineering Journal*, 121461.
   DOI: 10.1016/j.cej.2019.04.041
4. Dietrich, N., Wongwailikhit, K., **Mei, M.**, Xu, F., Felis, F., Kherbeche, A., Hébrard, G., & Loubière, K. (2019). Using the "Red Bottle" Experiment for the Visualization and the Fast Characterization of Gas–Liquid Mass Transfer. *Journal of Chemical Education*, *96*(5), 979-984.
   DOI: 10.1021/acs.jchemed.8b00898

Conference contributions

1. **Mei, M.**, Felis, F., Hébrard, G., Dietrich, N., & Loubière, K. Investigations of gas-liquid mass transfer around Taylor bubbles flowing in a long in-plane spiral-shaped milli-reactor. Oral presentation. The second

international progress intensification conference (IPIC2). May 2019, Leuven, Belgium.

2. Kherbeche, A. **Mei, M.**, Felis, F., Hébrard, G., Dietrich, N., & Loubière, K. Local visualization and investigation on gas-liquid mass transfer around Taylor bubbles flowing in an in-plane spiral-shaped millireactor. Oral presentation. 14th International Conference on Gas-Liquid and Gas-Liquid-Solid Reactor Engineering (GLS-14). May 2019, Guilin, China.

Content

Content

List of figures

Chapter 1

Fig. 1-8 In-plane velocity at 0.1*h* (*h* represents the height of the channel) from the top wall, before and after the start of the rapid collapse. (a) The thread has lifted from the wall, and liquid flows through the gap between the thread and the wall. Flow in the gutters runs towards the tip. (b) The thread has started to collapse, and liquid flow runs from the tip to the neck through all four gutters. Adapted from van Steijn et al. (2009).

Fig. 1-9 Comparison of velocity fields during droplet formation in oil−water+40% glycerol system for (a) $Q_c/Q_d = 2$, and (b) $Q_c/Q_d = 4$ at $Q_c = 400$ μL/min (Q_c and Q_d represent continuous and dispersed volumetric flow rates). Adapted from Sontti and Atta (2019).

Fig. 1-10 Dewetting patterns around a flowing bubble due to local thinning of film depending on the surface condition of the PDMS microchannels at similar bubble velocities (Ca ~ 10^{-3}). (a) Less wettable surfaces (receding contact angle > 25°). (b) More wettable surfaces (receding contact angle ~ 0°). Adapted from Khodaparast et al. (2017).

Fig. 1-11 Schematic diagram of mass transfer occurred in Taylor flows: green and red arrows represent the transferred gas from the bubble lateral bodies into the liquid film and the transferred gas from the bubble caps into the liquid slug.

Fig. 1-12 Summary of previously proposed mass transfer model for Taylor flow (green and blue zones in liquid represents different concentrations considered). Adapted from Nirmal et al. (2019).

Fig. 1-13 Scheme of three-layer model for two-phase Taylor flow: (a) bubbles and liquid slug in one unit cell (b) representation of each element (c) mass transfer fluxes. Meaning of each element: B1: tail of the leading bubble, B2: cap of the trailing bubble, B3: lateral surface of the bubbles, S1: the outer annular layer, S2: the inner layer; F1: the film around the leading bubble, F2: the transit film around the slug, F3: the film around the driven bubble. Representation of segments (in red squares): 1: diffusion between the hemispherical nose of the

Chapter 2

Chapter 3

calculated arc length between the two points. Illustrations of the axial position that were calculated in the configuration (b) ET and (c) MT.

Fig. 3-3 Cartography of gas-liquid Taylor flows (air and RGN colorimetric solution) obtained in the in-plane spiral-shaped milli-reactor (ET configuration) for three liquid superficial velocities and various gas superficial velocities and a local amplified observation of bubble shape (flat nose and tail).

Fig. 3-4 In-plane spiral-shaped milli-reactor: flow map for air/RGN colorimetric solution in the ET configuration. Green, blue and orange dotted lines represent the transition boundaries between the Taylor flow to the churn flow, Taylor-annular flow, and bubby flow predicted using the approach from Haase et al. (2020a), respectively.

Fig. 3-5 In-plane spiral-shaped milli-reactor (a) dimensionless bubble length versus axial position X at j_L = 1.8 cm s^{-1} for the ET configuration: (1) j_G = 1.4 cm s^{-1}; (2) j_G = 2.8 cm s^{-1}; (3) j_G = 5.1 cm s^{-1}; (4) j_G = 6.9 cm s^{-1}; dash-dotted line: the ± 5 % confidence interval. (b) Dimensionless liquid slug length versus axial position X at different conditions: (1) j_L=7.2 cm s^{-1}, j_G=0.9 cm s^{-1}, ET; (2) j_L = 7.2 cm s^{-1}, j_G = 3.3 cm s^{-1}, MT; (3) j_L = 3.6 cm s^{-1}, j_G = 1.1 cm s^{-1}, ET; (4) j_L = 3.6 cm s^{-1}, j_G = 0.9 cm s^{-1}, MT; (5) j_L = 1.8 cm s^{-1}, j_G = 16.6 cm s^{-1}, ET; (6) j_L = 1.8 cm s^{-1}, j_G = 3.2 cm s^{-1}, MT.

Fig. 3-6 In-plane spiral-shaped milli-reactor: bubble velocity versus axial position X at different conditions (1) j_L = 1.8 cm s^{-1}, j_G = 1.4 cm s^{-1}, ET; (2) j_L = 1.8 cm s^{-1}, j_G = 3.2 cm s^{-1}, MT; (3) j_L = 3.6 cm s^{-1}, j_G = 3.0 cm s^{-1}, ET, dash-dotted line: the ±5% confidence interval.

Fig. 3-7 In-plane spiral-shaped milli-reactor: (a) Linear regression coefficient F_1 versus gas-liquid superficial velocity ratio η_0 for different configurations and superficial velocities: (1) ET, (2) MT. (b) Constant F_2 versus gas-liquid flow ratio for configuration ET: (1) j_L = 1.8 cm s^{-1}; (2) j_L = 3.6 cm s^{-1}; (3) j_L = 7.2 cm s^{-1}; configuration MT: (4) j_L = 1.8 cm s^{-1}; (5) j_L = 3.6 cm s^{-1}; (6) j_L = 7.2 cm s^{-1}.

Fig. 3-8 In-plane spiral-shaped milli-reactor: (a) average dimensionless bubble length versus gas-liquid superficial velocity ratio η_0 and (b) average dimensionless liquid slug length versus the inverse of η_0; for the ET configuration: (1) j_L = 1.8 cm s^{-1}; (2) j_L = 3.6 cm s^{-1}; (3) j_L = 7.2 cm s^{-1}; and for the MT configuration: (4) j_L = 1.8 cm s^{-1}; (5) j_L = 3.6 cm s^{-1}; (6) j_L = 7.2 cm s^{-1}; (7) the least square regression law for ET, (8) the least square regression law for MT.

Fig. 3-9 In-plane spiral-shaped milli-reactor: Average bubble velocity versus two-phase superficial velocity for the ET configuration: (1) j_L = 1.8 cm s^{-1}; (2) j_L = 3.6 cm s^{-1}; (3) j_L = 7.2 cm s^{-1}; for the MT configuration: (4) j_L = 1.8 cm s^{-1}; (5) j_L = 3.6 cm s^{-1}; (6) j_L = 7.2 cm s^{-1}; solid line: (*7*) $U_B = j_{TP}$; dash-dotted line: (*8*) $U_B = 1.3\times j_{TP}$.

Fig. 3-10 In-plane spiral-shaped milli-reactor: (a) Average unit cell length $\langle L_{UC} \rangle$ versus gas-liquid superficial velocity ratio η_0: (1) ET; (2) MT; dash-dotted line: η_0 = 0.8; (b) Average relative length of the bubble $\langle \psi \rangle$ versus η_0 for the ET configuration: (1) j_L = 1.8 cm s^{-1}; (2) j_L = 3.6 cm s^{-1}; (3) j_L = 7.2 cm s^{-1}; the MT configuration:(4) j_L = 1.8 cm s^{-1}; (5) j_L = 3.6 cm s^{-1}; (6) j_L = 7.2 cm s^{-1}.

Fig. 3-11 In-plane spiral-shaped milli-reactor: comparison of pressure drop per unit of length versus gas-liquid two-phase Reynolds number at j_L = 7.2 cm s^{-1} for ET: (1) measured experimental data; (2) Lee et al (2010); (3) Bretherton et al (1961); (4) Kreutzer et al (2005); (5) Vashisth et al (2007).

Fig. 3-12 In-plane spiral-shaped milli-reactor: variation of pressure drops per unit of length versus gas-liquid superficial velocity ratio η_0 for configuration (a) ET; and (b) MT: (1) Experimental data; (2) Lee et al (2010) (3) IGL; (4) trend line for experimental data; (5) trend line for IGL; dash-dotted line: η_0 = 0.8.

Fig. 3-13 In-plane spiral-shaped milli-reactor: variation of unit cell number n_{UC} versus gas-liquid superficial velocity ratio η_0 for different configurations (1) ET and (2) MT; dash-dotted line: η_0 = 0.8.

Chapter 4

Fig. 4-1 Schematic representation of the spiral-shaped milli-reactor viewed from the top, showing the tubing configuration (ET: External Tubing; MT: Medium Tubing) and radial profile of the pixel gray value along one tube cross-sectional direction. Γ_X and Γ_Y are two orthogonal lines.

Fig. 4-2 Gas-liquid mass transfer in the in-plane spiral-shaped milli-reactor: (a) examples of individual linear calibration curves between gray value differences and equivalent O_2 concentration for two representative pixels on the image. (b) Partial raw image of gas-liquid flows. (c) Partial equivalent O_2 concentration field (normalized by the maximum concentration). Operating conditions: Re_L = 16.2, Re_G = 0.6, Re_{TP} = 24, η_0 = 0.45, $\langle De \rangle$ = 2.0, ET.

Fig. 4-3 Gas-liquid mass transfer in the in-plane spiral-shaped milli-reactor: (a) equivalent O_2 concentration fields in the liquid slugs: the time indicated in the figure corresponds to the time required for the liquid slug (in the black box), to travel to that position from the T-junction (operating conditions: Re_L = 64.9, Re_G = 1.0, Re_{TP} = 78, η_0 = 0.2, and $\langle De \rangle$ = 6.5, ET, flow direction is indicated using arrows). (b), (c), (d) Local raw visualization of the reactive RF color distribution in the liquid slugs at X = 0.1 m, operating conditions: (b) Re_L = 16.2, Re_G = 0.7, Re_{TP} = 26, η_0 = 0.6 and $\langle De \rangle$ = 2.2; (c) Re_L = 64.9, Re_G = 4.2, Re_{TP} = 121, η_0 = 0.86 and $\langle De \rangle$ = 10.0; (d) Re_L = 64.9, Re_G = 12.0, Re_{TP} = 224, η_0 = 2.45 and $\langle De \rangle$ = 18.6; ET.

Fig. 4-4 Gas-liquid mass transfer in the in-plane spiral-shaped milli-reactor: comparison of the axial evolution of normalized average equivalent O_2 concentration in the liquid slug along the tube for different operating conditions

(ET1 and MT1: Re_L = 16.2, Re_G = 0.7, Re_{TP} = 26, η_0 = 0.6, ET2 and MT2: Re_L = 32.4, Re_G = 6.3, Re_{TP} = 116, η_0 = 2.58). Here the points and lines represent experimental data and calculated data according to the exponential function $1 - \exp(-\gamma X)$, respectively. The second abscissa axis (at the top) gives the spiral radius for each configuration, corresponding to the axial position (reported on the principal abscissa axis, at the bottom).

Fig. 4-5 Gas-liquid mass transfer in the in-plane spiral-shaped milli-reactor: variation of the axial position $X_{coloration}$ for which C_{max} was achieved with the gas-liquid superficial velocity ratio η_0, solid and empty symbols represent ET and MT, Re_L = 16.2 (black color), 32.4 (red color), and 64.9 (blue color).

Fig. 4-6 Gas-liquid mass transfer in the in-plane spiral-shaped milli-reactor: relations between the average overall volumetric liquid side mass transfer coefficient, $\langle k_L \cdot a \rangle$, and the frequency of loop recirculation f_c.

Fig. 4-7 Gas-liquid mass transfer in the in-plane spiral-shaped milli-reactor: ratio between experimental $(k_L \cdot a)_{exp}$ and predicted $(k_L \cdot a)_{pre}$ versus the gas-liquid superficial velocity ratio η_0.

Fig. 4-8 Gas-liquid mass transfer in the in-plane spiral-shaped milli-reactor: Axial variation of the cumulated mass flux density $\langle \varphi_{O_2}(X) \rangle$ (case S2, without considering LF) for the tubing configurations ET and MT: (a) Re_L = 16.2; (b) Re_L = 64.9.

Fig. 4-9 Comparison between the predicted Sh_{Pre} and experimental Sh_{Exp} in case S2 (without LF) for ET configuration.

Chapter 5

Fig. 5-1 Representative bubble formation process (air and RGN colorimetric solution) at the cross-junction, operating conditions: j_L = 17.9 and j_G = 10.7 cm s^{-1}. The time interval between image sequences is 2.5 ms.

Fig. 5-9 Straight milli-channel with a cross-junction: flow map for air/RF colorimetric solution using the approach from Haase et al. (2020). Green, blue and orange dotted lines represent the transition boundaries between the Taylor flow to the churn flow, Taylor-annular flow, and bubby flow, respectively.

Fig. 5-10 Hydrodynamics of bubble formation at the cross-junction milli-channel: (a) normalized bubble length versus the gas-liquid ratio η_0. (b) Normalized liquid slug length versus the inverse of η_0. Four observing ROI positions ($X_1 / w_{hl} = 0$, $X_6 / w_{hl} = 52$, $X_8 / w_{hl} = 88$, $X_{12} / w_{hl} = 223$) and four groups of two-phase superficial velocities (j_{TP} = 28.6, 35.7, 42.9, 53.6 cm s^{-1}) were considered.

Fig. 5-11 Hydrodynamics of bubble formation at the cross-junction milli-channel: (a) Normalized unit cell length versus η_0, and (b) Relative length of bubble compared to the unit cell length ψ versus η. Four observing ROI positions ($X_1 / w_{hl} = 0$, $X_6 / w_{hl} = 52$, $X_8 / w_{hl} = 88$, $X_{12} / w_{hl} = 223$) and four groups of two-phase superficial velocities (j_{TP} = 28.6, 35.7, 42.9, 53.6 cm s^{-1}) were considered.

Fig. 5-12 Bubble velocities versus two-phase superficial velocities for four observing positions ($X_1 / w_{hl} = 0$, $X_6 / w_{hl} = 52$, $X_8 / w_{hl} = 88$, $X_{12} / w_{hl} = 223$).

Fig. 5-13 Representation of the cross-sectional shape of Taylor bubble, in a square channel: (a) circular; (b) squared with curved corners.

Fig. 5-14 Bubble formation at the cross-junction: evolution of the specific interfacial area a versus the dynamic gas hold-up β_0 under four groups of two-phase superficial velocities (j_{TP} = 28.6, 35.7, 42.9, 53.6 cm s^{-1}) at four observing positions: $X_1 / w_{hl} = 0$, $X_6 / w_{hl} = 52$, $X_8 / w_{hl} = 88$, $X_{12} / w_{hl} = 223$.

Fig. 5-15 Bubble formation at the cross-junction milli-channel: illustration of wetting (development of liquid film) phenomena at cross-junction (X = 0) for (a) air/deionized water, j_L = 21.4 cm s^{-1} and j_G = 10.7 cm s^{-1}; and (b) air/RGN colorimetric solution j_L = 17.9 cm s^{-1} and j_G = 10.7 cm s^{-1}.

Fig. 5-16 Bubble formation at the cross-junction milli-channel: illustration of dewetting phenomena (disappearance of liquid film) at X = 17 mm for air/RGN

colorimetric solution (a) j_L = 7.2 cm s^{-1} and j_G = 14.3 cm s^{-1}; and (b) j_L = 7.2 cm s^{-1} and j_G = 7.2 cm s^{-1}.

Chapter 6

Fig. 6-1 Raw images containing various [RZ] in milli-channel used for the calibration procedure.

Fig. 6-2 Calibration relations for mass transfer in the milli-channel with a cross-junction: (a) Calibration relationships between [RF] (considering 93% purity) and the absorbance of resorufin at different ROI positions. (b) Calibration relationships between equivalent O_2 concentration and the absorbance of resorufin at different ROI positions.

Fig. 6-3 Image processing implemented to study the gas-liquid mass transfer during the bubble formation stage: (a) raw image of gas-liquid flow. (b) Image with remaining liquid of RF signal. (c) Image with remaining liquid of GL and NaOH. (d) Equivalent O_2 concentration. Operating condition: j_L = 17.9 cm s^{-1}, j_G = 10.7 cm s^{-1} at the cross-junction.

Fig. 6-4 Time-variation of the equivalent O_2 concentration fields during the bubble pinch-off process at X_1 = 0 mm, operating condition: j_L = 0.2 cm s^{-1}, j_G = 0.2 cm s^{-1} and Re_{TP} = 8.

Fig. 6-5 Time-variation of the equivalent O_2 concentration fields during the bubble pinch-off process for various operating conditions at X_1 = 0 mm: (a) j_L = 10.7 cm s^{-1}, j_G = 10.7 cm s^{-1} and Re_{TP} = 416, (b) j_L = 14.3 cm s^{-1}, j_G = 14.3 cm s^{-1} and Re_{TP} = 555, (c) j_L = 21.4 cm s^{-1}, j_G = 21.4 cm s^{-1} and Re_{TP} = 832.

Fig. 6-6 Equivalent O_2 concentration fields during the bubble flowing process at j_{TP} = 28.6 cm s^{-1} under different gas-liquid superficial velocity ratio: (a) η_0 = 3, b) η_0 = 1, (c) η_0 = 0.6. The time indicated in the figure corresponds to the time required for the liquid slug to travel to the X position. Black arrows indicate the flow direction.

Chapter 7

List of tables

Chapter 1

Chapter 2

Chapter 3

Chapter 4

Nomenclature

Latin letters

Symbol	*Description*	*SI Units*
a	Interfacial area per unit cell	[m^{-1}]
A	Absorbance, Eq. (6-1)	[-]
$C^*_{O_{2_L}}$	Oxygen concentration at saturation in the liquid phase	[$kg \cdot m^{-3}$]
$C_{O_{2_L}}$	Equivalent oxygen concentration in the liquid phase	[$kg \cdot m^{-3}$]
$\overline{C_{O_{2_L}}}$	Average equivalent oxygen concentration in the liquid slug	[$kg \cdot m^{-3}$]
$C_{O_{2_G}}$	Oxygen concentration in the gas phase	[$kg \cdot m^{-3}$]
$C_{\max}$	Maximum oxygen concentration, Eq. (2-4)	[$kg \cdot m^{-3}$]
c	Molar concentration	[$mol \cdot m^{-3}$]
C_1	Constant related to the Archimedean spiral equation, Eq.(2-1))	[m]
C_2	Constant related to the Archimedean spiral equation, Eq. (2-1)	[$m.rad^{-1}$]
$C_{3\text{-}6}$	Constants related to the dimensionless length, Eq. (3-10), (3-11)	[-]
C_7	Constant related to the bubble velocity, Eq. (3-12)	[-]
C_8	Constant related to the bubble velocity, Eq. (3-12)	[$m\ s^{-1}$]
$C_{9\text{-}10}$	Empirical values adopted in Lee et al. (2010), Eq. (3-18)	[-]
D_{SR}	Diameter for Archimedean spiral, Table 2-3	[m]
$D_{SR,\,0}$	Initial diameter for Archimedean spiral	[m]
D_{O2}	Diffusion coefficient of oxygen in the liquid phase	[$m^2\ s^{-1}$]
d_{it}	Inner diameter of the spiral tube	[m]
d_B	Equivalent diameter with identical surface area of Taylor bubble	[m]
E	Chemical enhancement factor, Eq. (4-12)	[-]
E_i	Limit enhancement factor, Eq. (4-13)	[-]
E_{De}	Intensification factor between two configurations, Eq. (4-8)	[-]
F_1	Constant related to the variation of bubble length with axial position, Eq. (3-8)	[-]
F_2	Constant related to the variation of bubble velocity with axial position, Eq. (3-9)	[s^{-1}]

F_3	Constant related to the variation of bubble pressure with axial position, Eq. (A 7-8)	[Pa m^{-1}]
f_c	Frequency of recirculation in the liquid slug, Eq. (4-6)	[s^{-1}]
f_{BF}	Bubble formation frequency	[s^{-1}]
$f_{filling}$	Frequency of gas filling during bubble formation	[s^{-1}]
$f_{squeezing}$	Frequency of liquid squeezing during bubble formation	[s^{-1}]
g	Gravitational acceleration	[m s^{-1}]
H	Henry constant	[m^3 Pa mol^{-1}]
I	Intensity, i.e., gray values	[-]
k_2	Reaction rate constant	[L mol^{-1} s^{-1}]
k_L	Liquid side mass transfer coefficient	[m·s^{-1}]
$k_L \cdot a$	Volumetric liquid side mass transfer coefficient	[s^{-1}]
j_G	Superficial velocity of the gas phase ($j_G = Q_G/\Omega$)	[m·s^{-1}]
j_L	Superficial velocity of the liquid phase ($j_L = Q_L/\Omega$)	[m·s^{-1}]
j_{TP}	Total superficial velocity for two phase flow ($j_{TP}=j_G+j_L$)	[m·s^{-1}]
L_{arc}	Arc length between two points of the spiral shape	[m]
L_{SR}	Sectional distance for Archimedean spiral	[m]
L_R	Spiral tube length of the spiral-shaped reactor	[m]
L_B	Bubble length	[m]
L_{B0}	Initial bubble length right after bubble formation, Eq. (3-8)	[m]
L_S	Liquid slug length	[m]
$\langle L_B \rangle$	Bubble length averaged over the whole length of the tube	[m]
$\langle L_S \rangle$	Liquid slug averaged length over the whole length of the tube	[m]
l	Optical path length	[m]
l_{GF}	Gas finger length right after bubble pinch-off	[m]
M_{O2}	Molar mass of oxygen	[kg mol^{-1}]
m	Mass	[kg]
N	Number of the recirculation loops	[-]
n	Number	[-]
p_B	Pressure inside the bubble	[Pa]
p_{B0}	Initial pressure inside the bubble, i.e., right after bubble formation	[Pa]

p_r	Pressure recorded in the gas feed line	[Pa]
P_{SR}	Pitch distance in the spiral-shaped milli-reactor	[m]
Q	Volumetric flow rate	[m^3 s^{-1}]
R	Ideal gas constant (8.314)	[kg m^2 K^{-1} mol^{-1} s^{-2}]
r	Radial coordinate of the spiral circle	[m]
sc	Slope coefficient, Eq. (6-2)	[-]
S_B	Bubble surface area	[m^2]
S	Area	[m^2]
T	Temperature	[K]
t	Time	[s]
t^*	Normalized time by coloration time	[-]
$t_{coloration}$	Coloration time reaching the maximum oxygen concentration	[s]
$t_{filling}$	Gas filling time during bubble formation	[s]
$t_{squeezing}$	Liquid squeezing time during bubble formation	[s]
t_{BF}	Bubble formation time	[s]
U_{B0}	Initial bubble velocity, i.e., right after bubble formation, Eq. (3-9)	[m s^{-1}]
U_B	Bubble velocity	[m s^{-1}]
$\langle U_B \rangle$	Bubble velocity averaged over the whole length of the tube	[m s^{-1}]
V	Volume	[m^3]
W	Dimensionless constant, Eq. (4-21) and (4-22)	[-]
w_h	Channel horizontal width	[m]
w_{hl}	Channel hydraulic diameter	[m]
w_{neck}	Minimum width of gas finger during bubble formation	[m]
w_{side}	Horizontal width of the liquid inlet side channel	[m]
w_v	Channel depth	[m]
X	Axial position along the spiral tube from the bubble formation point	[m]
x	x axis in Cartesian coordinates	[\]
y	y axis in Cartesian coordinates	[\]
z	z axis in Cartesian coordinates	[\]
Z	Pressure drop ratio	[\]

Greek symbols

α_{O2}	Mole fraction of oxygen in the gas phase	[-]
β	Dynamic gas hold-up defined as $\beta = \frac{j_G}{j_G + j_L}$	[-]
δ	Film thickness	[m]
ε	Molar attenuation coefficient	[L mol^{-1} cm^{-1}]
ζ	Coefficient, Eq. (6-2)	[kg m^{-4}]
η	Ratio of the superficial velocities of the gas and the liquid phases	[-]
θ	Angular angle	[rad]
Θ	Contact angle	[°]
ι	Specific power consumtion	[W m^{-3}]
Λ	Chisholm parameter, Eq. (1-11)	[-]
λ	curvature ratio, defined as $\lambda = 2r/d_{it}$	[-]
μ	Dynamic viscosity of the phase	[Pa s]
ρ	Density of the phase	[kg m^{-3}]
Υ	Coefficient defined in Eq. (A 3-3)	[L mol^{-1}]
σ_L	Surface tension of the liquid phase	[N m^{-1}]
ς	Variable of sample data	[\]
Ω	Cross-sectional area of the tube or channel	[m^2]
φ_{O_2}	Mass flux of oxygen	[kg·m^{-2}·s^{-1}]
ψ	Relative length of the bubble defined as $\psi = \frac{L_B}{L_{UC}}$	[-]
ω	Linear dimensionless coefficient, Eq. (4-7)	[-]

Dimensionless numbers

Bond number	$\mathrm{Bo} = \frac{(\rho_L - \rho_G) {d_{it}}^2 g}{\sigma_L}$

Two-phase Capillary number	$\mathrm{Ca}_{TP} = \frac{\mu_\mathrm{L} j_\mathrm{TP}}{\sigma_\mathrm{L}}$
Liquid Capillary number	$\mathrm{Ca}_L = \frac{\mu_L j_L}{\sigma_L}$
Dean number	$\mathrm{De} = \mathrm{Re}\sqrt{\frac{1}{\lambda}}$
Hatta number	$Ha = \frac{\sqrt{k_2 \, C_{DH,0} \, D_{O2}}}{k_L}$
Péclet number	$Pe_B = Sc \, \mathrm{Re}_B = \frac{U_\mathrm{B} D}{D_{O2}}$, D=d_it or w_{hl}
Two-phase Reynolds number	$\mathrm{Re}_{TP} = \frac{\rho_\mathrm{L} j_\mathrm{TP} D}{\mu_\mathrm{L}}$, D=d_it or w_{hl}
Bubble Reynolds number	$\mathrm{Re}_B = \frac{\rho_\mathrm{L} U_\mathrm{B} d_B}{\mu_\mathrm{L}}$
Liquid Reynolds number	$\mathrm{Re}_L = \frac{\rho_\mathrm{L} j_\mathrm{L} D}{\mu_\mathrm{L}}$, D=d_it or w_{hl}
Gas Reynolds number	$\mathrm{Re}_G = \frac{\rho_\mathrm{G} j_\mathrm{G} D}{\mu_\mathrm{G}}$, D=d_it or w_{hl}
Schmidt number	$\mathrm{Sc} = \frac{\mu_\mathrm{L}}{\rho_L D_{O2}}$
Sherwood number	$\mathrm{Sh} = \frac{\langle \varphi_{O_2} \rangle \, d_B}{E \, D_{O2} \, C^*_{O_2 L}}$
Two-phase Weber number	$\mathrm{We}_{TP} = \mathrm{Ca} \times \mathrm{Re} = \frac{\rho_\mathrm{L} \, {j_\mathrm{TP}}^2 \, D}{\sigma_\mathrm{L}}$, D=d_it or w_{hl}
Gas Weber number	$\mathrm{We}_G = \frac{\rho_L {j_G}^2 D}{\sigma_L}$, D=d_it or w_{hl}

Abbreviations

CFD	Computational fluid dynamics
CLSVOF	Coupled Level Set and Volume of Fluids method
DH	Dihydroresorufin
ET	Exterior tubing configuration
FEP	Fluorinated Ethylene Propylene
fps	Frames per second
GL	Glucose
LED	Light-emitting diode
LF	Liquid film

MAD	Mean absolute deviation
MAPE	Mean absolute percentage error
MAPER	Mean absolute percentage error of regression
MT	Medium tubing configuration
PDMS	Polydimethylsiloxane
PIV	Particle imaging velocimetry
PMMA	Poly-Methyl-Methacrylate
RF	Resorufin
RGN	Resazurin, Glucose, NaOH colorimetric solution
ROI	Region-of-interest
RZ	Resazurin
SD	Standard deviation error
STD	Standard deviation
VOF	Volume of fluid
$\langle\,\rangle$	Mean value
[]	Concentration
Δ	Difference/change

Subscripts and Superscripts

ACA	Advancing contact angle
Air/RZ	Air and resazurin solution
atm	Atmospheric pressure
B	Bubble
B_cap	Bubble caps
B_film	Lateral bubble contacting liquid film
BF	Bubble formation
CAH	Contact angle hysteresis
circulation	Recirculation loop
cirmax	Maximal circle
corner	Alongside corner
eq	Equivalent

exp	Experimental data
filling	Filling stage during bubble formation
fric	Friction
G	Gas phase
h	Horizontal direction
IGL	Ideal gas law
it	Inner diameter of the tube
inlet	Inlet
i	Integer number
j	Integer number
L	Liquid phase
max	Maximum
out	Outlet
overall	Overall process
pre	Predicted data
RCA	Receding contact angle
rl	Real
r	Record value
S	Liquid slug
SR	Spiral-shaped milli-reactor
squeezing	Squeezing stage during bubble formation
TP	Two-phase flow
tot	Total
UC	Unit cell
v	Vertical direction
wall	Alongside wall
0	Initial
2D	Two dimensional

Chapter 1. Introduction

1.1 Context for the presented work

Gas-liquid mass transfer is a key phenomenon controlling the performances of multiphase reactors, which are widely encountered in chemical and environmental processes, such as organic photochemistry (Radjagobalou et al., 2018; Radjagobalou et al., 2020), hydrogenation reactions (Haase and Bauer, 2011; Martínez et al., 2016; Yue, 2017; Paul et al., 2018), oxidation reactions (Pollington et al., 2009; Gemoets et al., 2016; Guo et al., 2017; Paul et al., 2018) or gas fermentation (Garcia-Ochoa et al., 2010; Benizri et al., 2019; Van Hecke et al., 2019). When the characteristic times of gas-liquid mass transfer are not short enough compared to those of the chemical reaction kinetics, low production yields, and poor chemical selectivity may be induced.

With respect to safety, compactness, quality and eco-impact issues, some cutting-edge technologies for process intensification (Jensen, 2001; Gourdon et al., 2015; Stankiewicz et al., 2019), such as continuous-flow micro-structured technologies (heat-exchanger-reactor, monolith reactor, micro-reactor, etc.) have emerged as alternatives to conventional equipments (e.g., batch reactors). They usually involve miniaturized and confined spaces on the scale of micro/millimeter and operate in continuous mode. The advantages of such miniaturization are to offer enhanced heat and mass transfer, efficient mixing, and high exchange surface areas (Haase et al., 2016; Yao et al., 2021), and in return higher yields and selectivity. The combination of continuous-flow micro-structured technology with multiphase flows has been considered as an efficient method for multiphase

process intensification, leading to the emergence of the very active field of the multiphase microfluidics (Geng et al., 2020).

Among all the two-phase flow patterns in micro/milli-channels, Taylor flow is one of the most widely investigated regimes as it provides stable, regular, and easily controllable conditions with enhanced heat and mass transfer efficiencies due to the recirculation loops appearing in the liquid slug (in the moving coordinate reference in terms of the bubble) and to the liquid lubrication films at the walls (Sobieszuk et al., 2012).

The following chapter will focus on gas-liquid two-phase systems, and give a brief overview of the gas-liquid hydrodynamics and mass transfer characteristics in Taylor flow, thus highlighting the remaining research gaps and issues.

1.2 Brief state-of-art

In this section, the gas-liquid hydrodynamics and mass transfer will be described in sections 1.2.1 and 1.2.2., respectively. In terms of gas-liquid hydrodynamics, sub-section 1.2.1.1 will first introduce the flow regimes encountered in micro/milli-channel and the characteristics of Taylor flow. Then, bubble formation regime, liquid lubrication film and pressure drop are discussed in sub-sections 1.2.1.2., 1.2.1.3., and 1.2.1.4, respectively. For the mass transfer, sub-section 1.2.2.1 will first introduce the mass transfer mechanisms and modeling for Taylor flow. Then, experimental measurements methods are classified in sub-section 1.2.2.2. The effect of the channel's geometry will be discussed in section 1.2.3.

1.2.1 Gas-liquid hydrodynamics

The understanding of Taylor flow hydrodynamics in micro/milli-channels is a fundamental prerequisite for studying mass transfer and heat transfer. This includes precise knowledge of the flow regime, bubble formation, bubble lengths, liquid slug lengths, and bubble velocities. There are already some exhaustive and relevant reviews about hydrodynamics for Taylor flows in straight channels. More detailed descriptions can be found in Haase et al. (2016), Abiev et al. (2017), Verma and Ghosh (2019), and Yao et al. (2021) . The following sections aim at extracting the main results.

1.2.1.1 Flow regimes

Over the past three decades, numerous studies have been performed to investigate the adiabatic gas-liquid two-phase flow in straight micro/milli-channels (horizontal or vertical with up/downstream). The gas-liquid flow regimes describe specific spatial distributions of both phases and were usually the first step for engineers to identify, as they greatly affect the pressure drop, heat transfer, and mass transfer, etc., thus influencing the performances of the apparatus. Many researchers classified the flow regimes through photographic image (taken by cameras) analysis. Five main flow regimes in micro/milli-channels were reported by most of the researchers: annular flow, bubbly flow, churn flow, Taylor flow, and Taylor-annular flow. The main characteristics of each flow regime were summarized and described as below.

- Bubbly flow usually occurred at extremely low gas superficial velocities and high liquid superficial velocities, characterized by distorted, distinct, and small bubbles, of which diameters were lower than the channel hydraulic diameters.
- Taylor flow (or slug flow) was widely encountered under a large range of gas and liquid superficial velocities (moderate), characterized by

regular, segmented, and long bubbles (named Taylor bubble) with nearly hemispherical caps, of which diameters were higher than the channel hydraulic diameters. The Taylor bubble body occupied most of the channel and its cross-sectional shape changed with channel cross-sectional shapes.

- Taylor-annular flow and annular flow had similar characteristics: gas phase occupied in the center of the channel, and liquid phase appeared between the gas and channels.
- Churn flow was formed at both high gas and liquid superficial velocities. Unlike Taylor flow, churn flow was irregular and with tiny bubbles dispersed in the liquid slug.

An example of flow regimes is presented in Fig. 1-1.

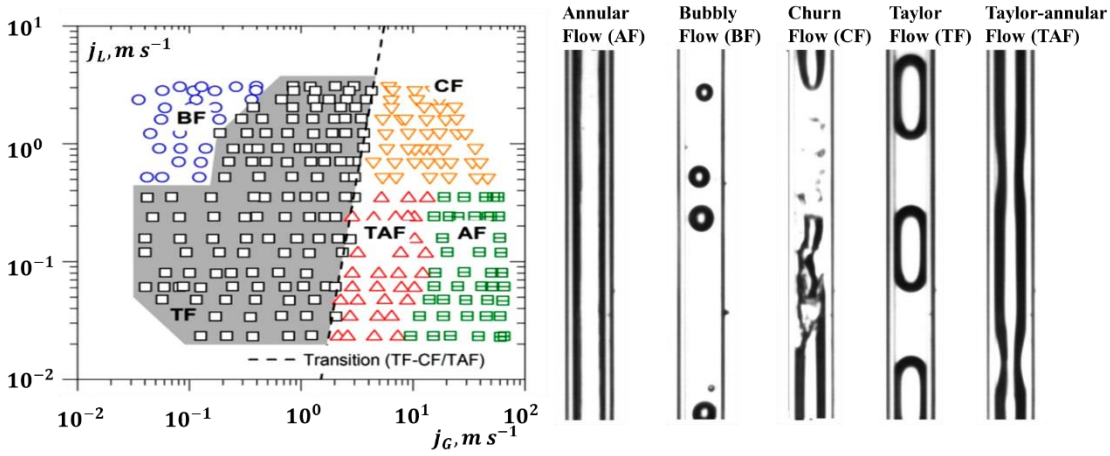

Fig. 1-1 Example of flow map for air-water in a horizontal circular milli-channel (d_{it}: 1.45 mm). Adapted from Haase et al. (2020).

The flow regimes were affected by various parameters, such as the gas and liquid flow rates, the fluid properties (e.g., surface tension, viscosity, wettability, etc.), the channel geometries (size and cross section), inlet geometry (e.g., T and Y junctions, cross-junctions, and co-flowing inlet) and inclination. However, at

present, no single universal map (i.e., considering all the parameters affecting flow regime) has successfully been derived for predicting gas-liquid flow regimes. In general, the flow maps proposed by researchers were only valid for some specific geometries or fluid pairs. One can thus commonly observe that the transition boundaries on flow maps varied significantly among different studies, even for similar channel dimensions and operating domain, as shown in Fig. 1-2. Recently, Haase et al. (2020a) summarized the flow maps available in the literature and proposed a generalized approach to describe the flow transitions among different regimes in milli-channels by using decision trees (determining inlet geometries).

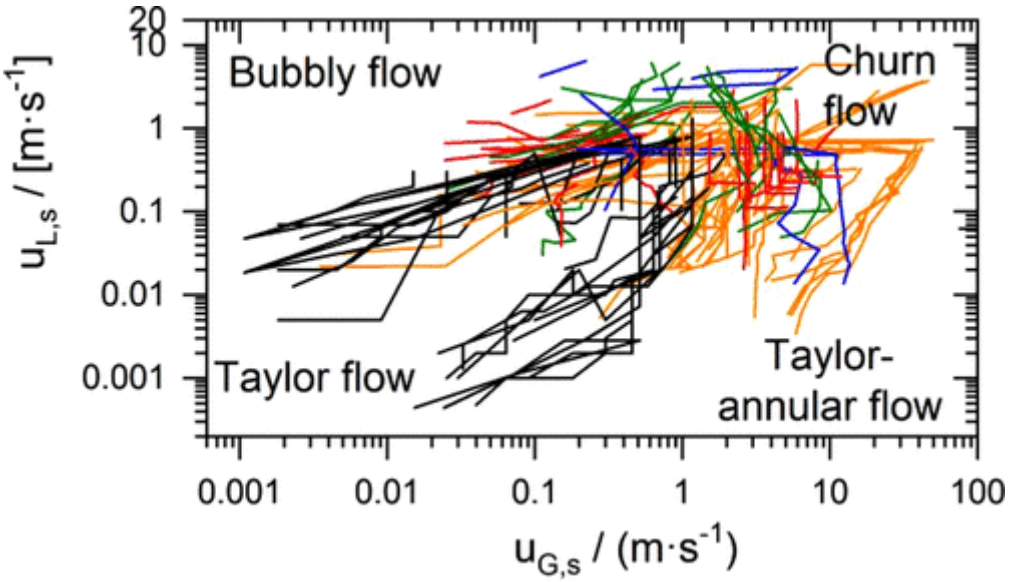

Fig. 1-2 Superimposed flow transitions for selected flow maps in milli-channels ($u_{G,s}$ and $u_{L,s}$ are gas and liquid superficial velocities). The different colored lines refer to different inlet designs. Adapted from Haase et al. (2020).

These authors also proposed mathematical relationships based on seven dimensionless numbers to describe the transitions between Taylor flow and other flow regimes, namely, bubbly flow, Taylor-annular and churn flow. These dimensionless numbers were described as below:

- Gas-liquid superficial velocity ratio: $\eta = \frac{j_G}{j_L}$ (1-1)

where j_G and j_L were the gas and liquid superficial velocities, respectively.

- Gas to liquid viscosity ratio: $\frac{\mu_G}{\mu_L}$ (1-2)

where μ_G and μ_L were the gas and liquid dynamic viscosities, respectively.

- Gas to liquid density ratio: $\frac{\rho_G}{\rho_L}$ (1-3)

where ρ_G and ρ_L were the gas and liquid densities, respectively.

- Liquid Reynolds number: $Re_L = \frac{\rho_L d j_L}{\mu_L}$ (1-4)

where d was the channel hydraulic diameter.

- Liquid Weber number: $We_L = \frac{\rho_L d {j_L}^2}{\sigma_L}$ (1-5)

where σ_L was the liquid phase surface tension.

- Dimensionless contact angle: $\Theta^* = \frac{\pi \Theta}{180^\circ}$ (1-6)

where Θ was the contact angle of the channel wall.

- Channel form factor: $R_A = \frac{A_{cirmax}}{\Omega}$ (1-7)

which represented the area ratio between the maximal area of a circular fitted into the channel cross section A_{cirmax} and the cross-sectional area of the channel Ω.

Therefore, considering these defined dimensionless numbers, the transition boundaries between the Taylor flow and other flow regimes were listed in Table 1-1. Haase et al. (2020a) showed how it was convenient to predict the flow regimes for specific operating conditions, fluid properties, channel

parameters, and inlet geometries, etc. However, the proposed transition boundaries are limited by the precision of the used experimental data collected from literature. Thus, it is still necessary to develop some smart-designed configurations involving non-subjective judgement methods for flow regimes and enriching some inadequate data.

Table 1-1 Summary of transition boundaries between the Taylor flow and other flow regimes for different inlet geometries. Adapted from Haase et al. (2020a).

Flow regimes	Inlet geometries	Transition boundaries
Churn flow	T and Y-junctions	$\frac{j_G}{j_L} = 11.94 {We_L}^{-0.58} e^{-0.30\Theta^*} {R_A}^{0.41}$
	Cross-junctions	$\frac{j_G}{j_L} = 2.15 \cdot 10^6 {We_L}^{-0.72} (\frac{\rho_G}{\rho_L})^{1.79} {R_A}^{0.94}$
Taylor-annular flow	T-junctions	$\frac{j_G}{j_L} = 9.72 \cdot 10^{-11} {We_L}^{-0.40} (\frac{\rho_G}{\rho_L})^{-3.91}$
	Cross-junctions	$\frac{j_G}{j_L} = 17.5 {We_L}^{-0.33}$
	Static mixers	$\frac{j_G}{j_L} = 43.7 {We_L}^{-0.45}$
Bubbly flow	T-junctions	$\frac{j_G}{j_L} = 4.9 \cdot 10^{-8} {We_L}^{0.62} (\frac{\mu_G}{\mu_L})^{-3.94}$
	Y-junctions	$\frac{j_G}{{j_L}^{-0.89}} = 1.03 \cdot 10^{-3} {We_L}^{1.15} (\frac{\mu_G}{\mu_L})^{-0.77}$
	Cross-junctions	$\frac{j_G}{j_L} = 1.49 \cdot 10^3 {Re_L}^{-1.40} {We_L}^{0.48} {R_A}^{0.88}$

Taylor flow

Among all the distinguished flow regimes, Taylor flow draws the most scientific interest due to its segmented and regular flow structure, and it can be

operated under a large gas and liquid flow rate domain. As shown in Fig. 1-3, the liquid phase separated by Taylor bubbles are called liquid slugs. Due to the periodic appearance of Taylor bubbles and liquid slugs, the unit cell containing one Taylor bubble and one liquid slug is defined to facilitate the formalization. The length of bubble and liquid slug are also indicated in Fig. 1-3. The bubble velocity is generally calculated according to the displacement of the bubble centroid.

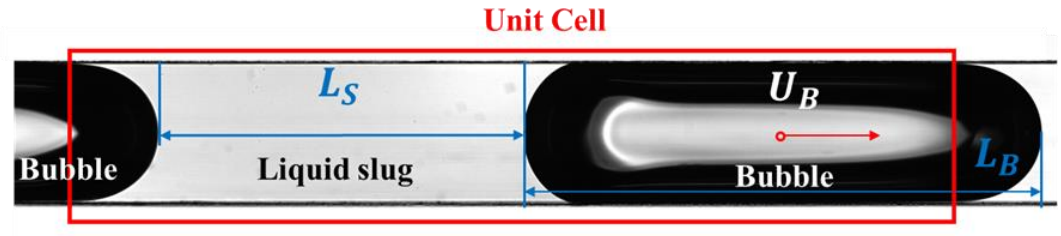

Fig. 1-3 Illustration of bubbles, liquid slugs, and unit cell for Taylor flow, and schematic representation of bubble length (L_B), liquid slug length (L_S) and bubble velocity (U_B) in a milli-channel.

For wetted channel (hydrophilic for aqueous media), there was generally a thin liquid film between the Taylor bubble and channel walls. The evaluation of the liquid film thickness was first theoretically formalized by Bretherton (1961). More details will be given in the subsequent chapters.

The study of Taylor flow motion dated back to 1960s by Taylor (1961) in a circular channel, who first postulated the recirculation loop and proposed three types of flow recirculation loop by stagnation points. The recirculation loop flow pattern in liquid slugs was later confirmed experimentally using PIV (Thulasidas et al., 1997) and related to capillary number ($Ca_{TP} = \frac{\mu_L j_{TP}}{\sigma_L}$). Fig. 1-4 illustrates the flow streamlines and recirculation loops in the liquid slug. The velocity of the bubbles was lower than the fluid speed at the centerline of the liquid slug. As a result of mass conservation, and confinement by bubble caps and channel walls,

the liquid inside liquid slug formed the recirculation loop. Apart from two symmetrical vortices, there were secondary vortices at the bubble nose and rear region. More detailed information of recirculation loop were reported in the reviews of Yao et al. (2018) and Yao et al. (2021). In addition, the recirculation effect was at a maximum when there was no film since all liquid phase inside of the liquid slug could completely confined between the bubble caps.

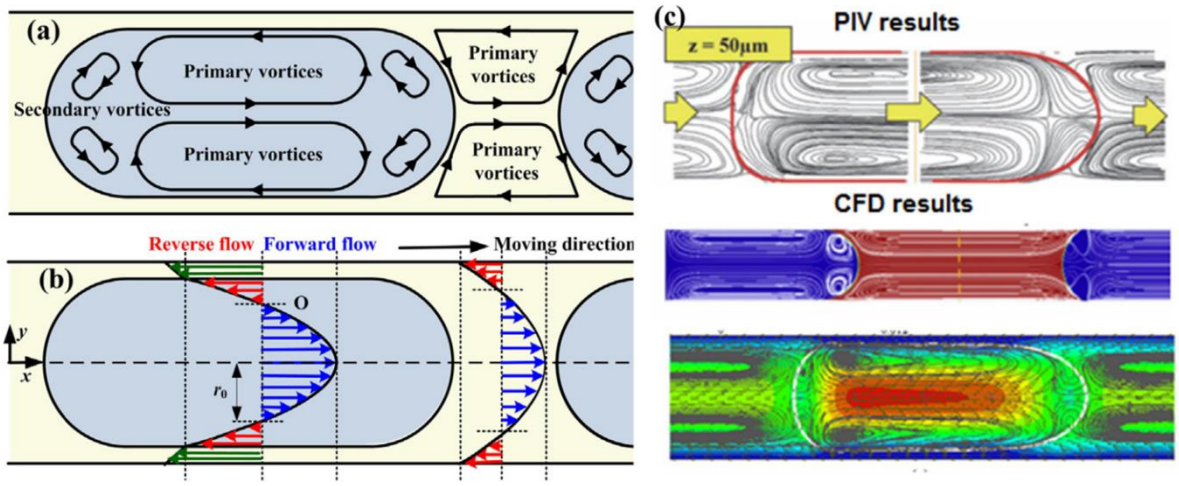

Fig. 1-4 Illustration of recirculation loops: (a) the recirculation flows in droplets and liquid slugs (b) model illustrating the absolute velocity profile as well as forward and reverse flow in the reference of droplet. O is the stagnant point and r_0 is its radial location. (c) PIV and CFD results of recirculation loops in both phases. Adapted from Yao et al. (2021).

1.2.1.2 Bubble formation

The microtechnology devices allow to produce highly regular, repeatable, and mono-dispersed bubbles and liquid slugs, which is a very interesting feature for carrying out multiphase reactions, especially when competitive and/or consecutive reactions take place. For that, special attention should be paid to the bubble formation process, which has been investigated through experimental and simulation methods (Fu and Ma, 2015), because the question of "when and how bubble pinch-off happens" directly determines the bubble size, frequency and

flow regimes (Dang et al., 2013). The main factors influencing bubble pinch-off in microfluidic devices were found as follows: the channel geometry (Garstecki et al., 2006; Dietrich et al., 2008), the gas-liquid superficial velocity ratio (Garstecki et al., 2006), the viscosity of the liquid phase (Lu et al., 2014b; Zhang et al., 2017), interfacial tension (Lu et al., 2014a) between two phases, rheological property (Fu et al., 2011a, c; Fu et al., 2012) of the liquid phase and surfactants (Li et al., 2020a). In particular, the channel geometry could be further characterized by the inlet geometry (e.g., T-junction, flow-focusing/cross-junction and co-flowing geometries), wettability of channel, and cross-sectional shapes (Garstecki et al., 2006).

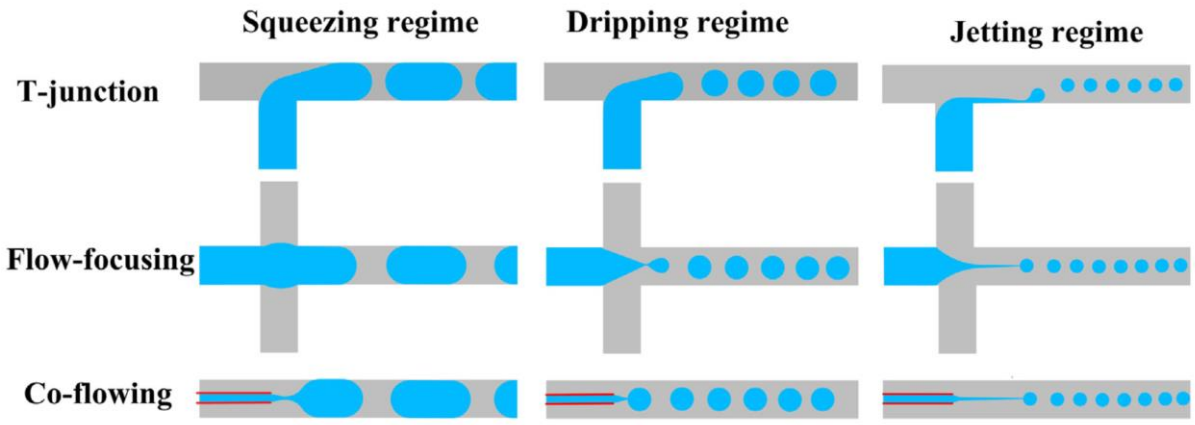

Fig. 1-5 Schematic representations of bubble formations regimes depending on the inlet geometries. Adapted from Yao et al. (2021).

The bubble formation mechanisms in microfluidic devices were widely classified into three patterns (Fu and Ma, 2015), i.e., squeezing, dripping (shearing), and jetting regimes (Xu et al., 2008), as illustrated in Fig. 1-5, which were analyzed through image analysis or numerical simulations. The bubble breakup patterns were influenced by the balance between exerted forces on the gas finger (or gas thread), namely interfacial force, viscous shear force, and inertia force (Dollet et al., 2008).

Among them, the jetting regime (De Menech et al., 2008; Fu et al., 2009; Castro-Hernández et al., 2011; Xu et al., 2014) was usually encountered under high capillary numbers, and the bubbles were pinched-off by the surrounding liquid downstream the inlet (e.g., cross-junction, or gas micro-capillary). The pinch-off was usually triggered by the balance between viscous shear force and interfacial force. In the jetting regime, the generated bubble sizes were far smaller compared to the channel size.

In the squeezing regime (Garstecki et al., 2006), the dispersed phase penetrated into the main channel, propagated towards the wall and downstream, resulting in a blockage of continuous phase flow. Due to this blockage, the increased pressure force induced at the upstream of the gas thread finally triggered the breakup. The interfacial force dominated the viscous force (i.e., low Capillary numbers). Under the squeezing schemes of bubble formation, this process could be described by three stages: filling (or expansion), squeezing (or collapse), and fast pinch-off (or nonlinear breakup).

The dripping (shearing) regime was a transition regime between the squeezing and jetting regime, which was also encountered under high Capillary number. The gas phase entered the main channel without blocking it, leading to that the liquid phase could still freely bypass the gas thread. The viscous shear force also took a major role in rupturing bubbles, which were detached near the cross junction or gas micro-capillary.

Concerning the transitions between these formation regimes, Garstecki et al. (2006) found that the transition between the squeezing and dripping regimes occurred for a critical Capillary number equal to 10^{-2}. Later Xu et al. (2008) and Fu et al. (2010b) further specified the Capillary number domains for different formation regimes. The Capillary number ranges for squeezing and shearing regimes were identified at (10^{-4}, 0.0058) and (0.013, 0.1), respectively. In addition, at a medium range of Ca $\in$(0.0058, 0.013) between these two regimes, both

squeezing pressure and the shearing force affected the collapse. This transition regime was defined as ‘squeezing to dripping’ regime (Xu et al., 2008; Fu et al., 2011b).

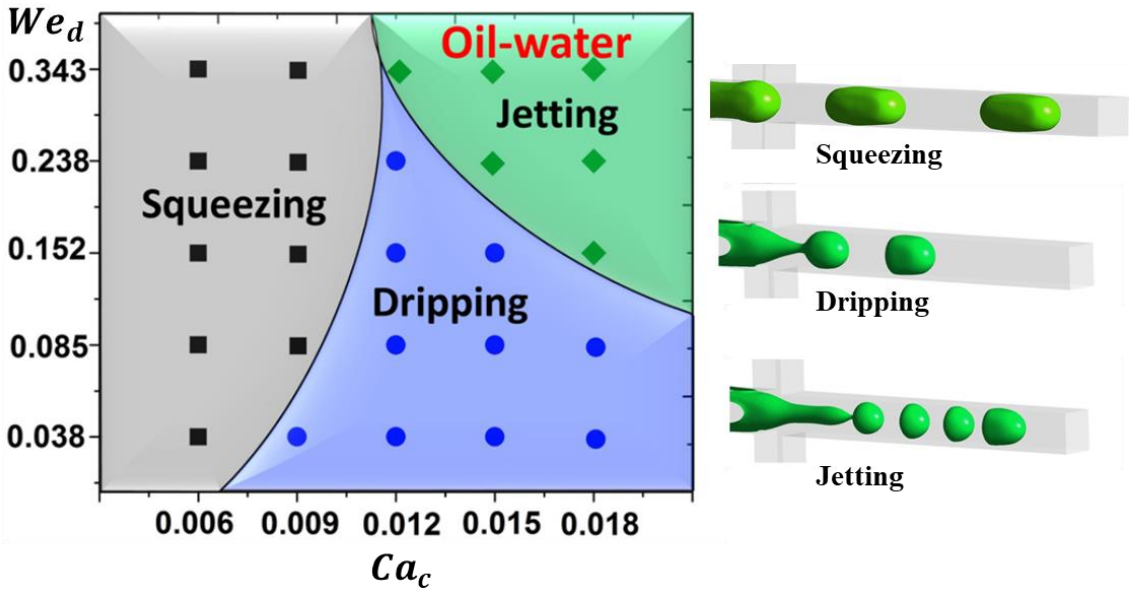

Fig. 1-6 Flow pattern maps of droplet formation in a cross-junction microchannel (600×600 μm) containing for oil−water (Ca_c and We_d represent the continuous Capillary number and dispersed Weber number). Adapted from Sontti and Atta (2019).

Recently, Sontti and Atta (2019) identified the droplet formation maps depending on the continuous phase (water) Capillary number and dispersed phase (oil) Weber number, as shown in Fig. 1-6, which clearly demonstrated the transition boundaries between different regimes. In addition, this work highlighted the critical role of dispersed Weber numbers. Furthermore, Madana and Ali (2020) simulated the droplet formation using VOF method in a T-junction and classified the droplet formation regimes to five types, as shown in the Fig. 1-7. This flow regime map indicated that the droplet formation regimes and their transitions were governed by Capillary numbers and gas-liquid flow ratio. However, the transition judgements between different formation regimes were rough and fuzzy, and not quantitatively characterized in these studies (Liu and

Zhang, 2011; Li et al., 2019a). Therefore, future studies of the axial position of gas finger right after the bubble pinch-off (or the axial position of minimum gas thread neck right before breakup) should be implemented to give more accurate quantitative descriptions between different formation regimes. Li et al., (2020a) found that the pinch-off positions may change slightly at different breakup loops.

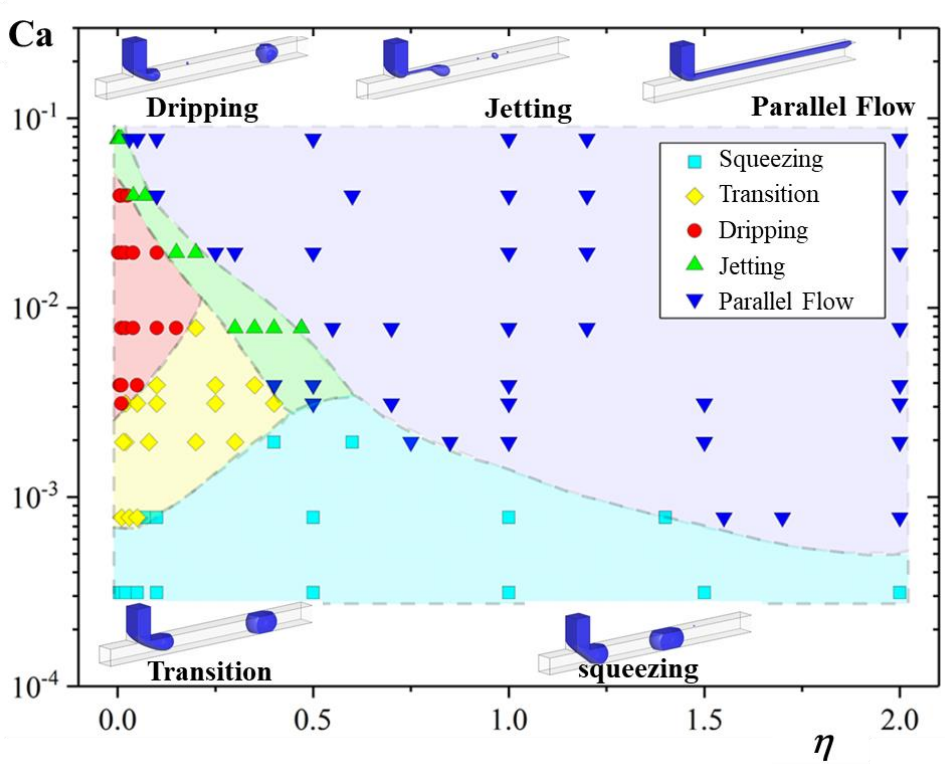

Fig. 1-7 Flow regimes of droplet formation as a function of Capillary number Ca_{TP} and gas-liquid superficial velocity ratio η in a T-junction (100×100 μm) with contact angle at 135°. Adapted by Li et al. (2019a)

Garstecki et al. (2005) were the pioneers to explore the bubble formation mechanisms in confined channels. They found that the linear collapse was determined by the confinement of the channel. They further assumed that the nonlinear breakup was triggered by the Rayleigh-Plateau instability. Later on, van Steijn et al. (2007) and van Steijn et al. (2009) observed through μPIV experiments that the reverse flow around the gas thread determined when the

pinch-off occurred and highlighted the crucial role of gutter flow in neck collapse, as shown in Fig. 1-8. It is shown from the in-plane velocity vectors that there was a reverse liquid flow through gutters (marked by the red box in Fig. 1-8), which determined the rapid collapse of bubbles.

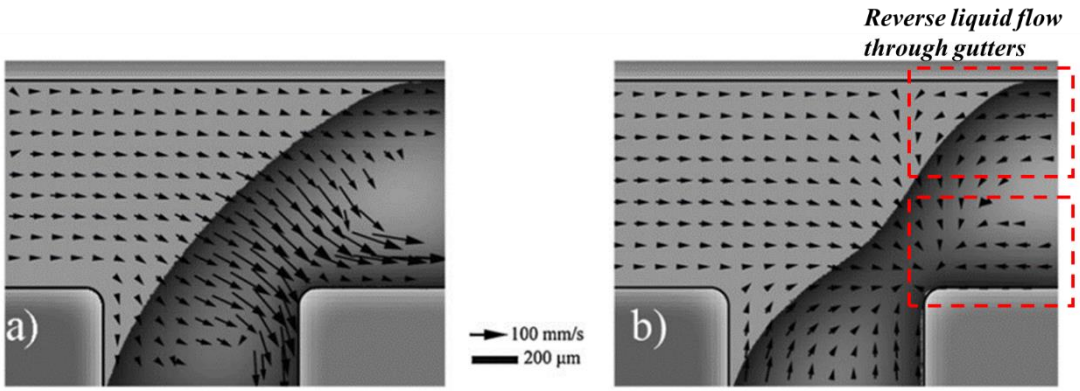

Fig. 1-8 In-plane velocity at 0.1*h* (*h* represents the height of the channel) from the top wall, before and after the start of the rapid collapse. (a) The thread has lifted from the wall, and liquid flows through the gap between the thread and the wall. Flow in the gutters runs towards the tip. (b) The thread has started to collapse, and liquid flow runs from the tip to the neck through all four gutters. Adapted from van Steijn et al. (2009).

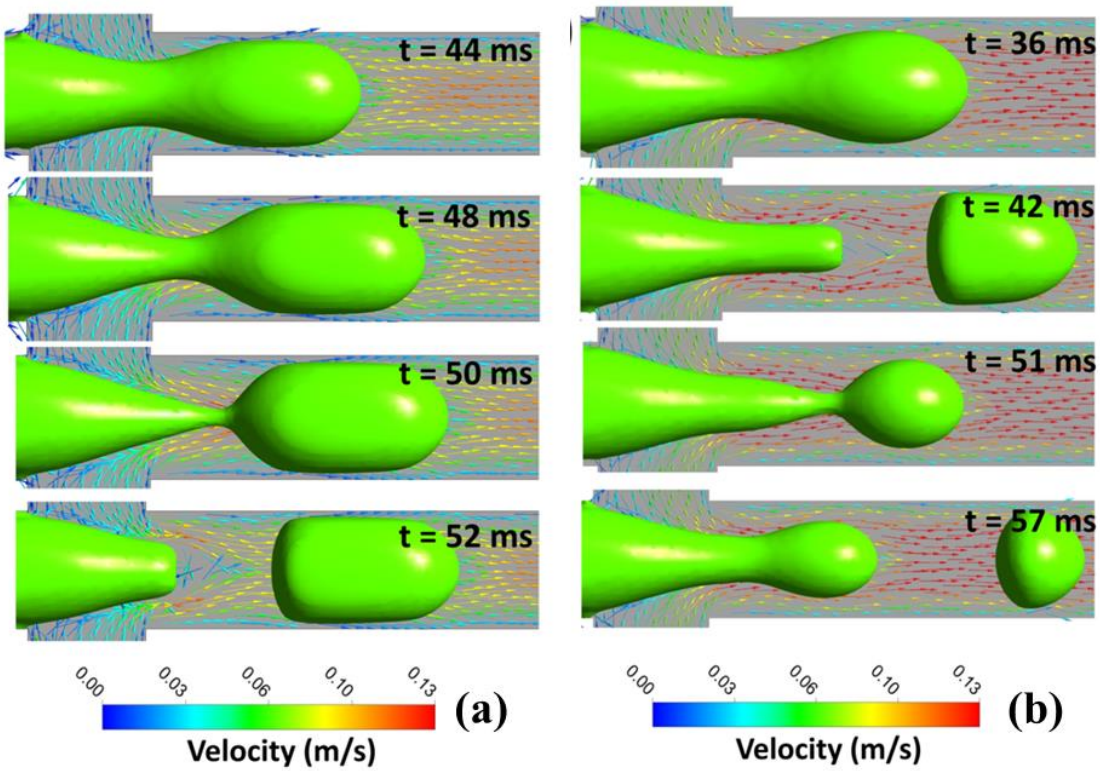

Fig. 1-9 Comparison of velocity fields during droplet formation in oil−water+40% glycerol system for (a) $Q_c/Q_d = 2$, and (b) $Q_c/Q_d = 4$ at $Q_c = 400$ μL/min (Q_c and Q_d represent continuous and dispersed volumetric flow rates). Adapted from Sontti and Atta (2019).

In addition, Fig. 1-9 illustrates the velocity fields during droplet formation in a cross-junction. With an increase of the volumetric flow rates between the continuous and dispersed phases, the droplet tended to be ruptured downstream the cross-junction. When the continuous phase from side channels entered into the cross-junction, the velocity magnitudes around the neck (minimum width) of droplet were higher.

Many researchers (Garstecki et al., 2006; Dollet et al., 2008; Fu et al., 2010a; Lu et al., 2014a) also investigated the minimum width of the gas finger w_{neck} and found a power law relationship between it and the remaining time t_{remain} until pinch-off, as below:

$$w_{neck} = {t_{remain}}^{\vartheta} \tag{1-8}$$

where ϑ was the power law exponent, which was found at 1/3 (Dollet et al., 2008; Fu et al., 2010a) or 2/5 (Van Hoeve et al., 2011) or 1/2 (Lu et al., 2014a) or 1/6 for non-Newtonian liquid (Fu et al., 2012). Fu et al. (2010a) and Lu et al. (2014a) observed two stages of collapse processes, the liquid squeezing collapse and the free pinch-off stage. They showed that an exponent of 0.33 corresponded to the liquid squeezing stage and was affected by the liquid confinement but independent with liquid flow rates and viscosity. However, during the free pinch-off stage, an exponent of 0.5 was identified, independent with the liquid flow rates as well.

Table 1-2 summarizes the main studies about the bubble or droplet formation in microfluidic devices. One should note that, at present, the dynamics of bubble breakup are still not fully understood, requiring further investigations on the flow fields within and around bubbles (Duxenneuner et al., 2014).

Table 1-2 Works related to bubble or droplet formation in microfluidic devices.

Reference	Channel geometries: Cross-sectional shape	Channel geometries: Dimension	Channel geometries: Aspect ratio (a/b)	Inlet geometry	Key factors	Formation mechanism	Formation stages	Method	Main contents
Garstecki et al. (2006)	Rectangular	$w_{inwater}/w_{inoil}(w_{main})$: 1-4 h=33, 79μm w_{main}=50, 100, 200μm	1.3-6.1	T-junction	Viscosity, surfactant, geometries,	Squeezing, shearing	4	Experiments camera	transition from squeezing to shearing at Ca around 10^{-2}
Dietrich et al. (2008)	Square PMMA	500×500μm, 1000 ×1000μm	1	Flow-focusing	Angle of the flow-focusing junction: 60°,90°,180°,	Pressure difference in two phases	\	Experiments micro-PIV	Relations of bubble length
van Steijn et al. (2009)	Rectangular PDMS glass	w_{in}= 133, 800μm h=56,800μm w_{main}=100,800μm	1.8	T-junction	Air-ethanol	Squeezing	Filling and squeezing stage	Experiments micro-PIV 10 kfps	Reverse flow in gutters determines non-linear breakup
Fu et al. (2012)	Square PMMA	600×600μm 400×400μm	1	Flow-focusing	Non-Newtonian	Squeezing, shearing	Expansion Collapse Rupture	Experiments micro-PIV	Exponent ϑ at 1/6
Dietrich et al. (2013b)	Square PMMA	500×500μm, 1000 ×1000μm	1	Flow-focusing	Dimensions of the channel	\	\	Experiments micro-PIV	Relations of the bubble volume
Lu et al. (2014a) and Lu et al. (2014b)	Square PMMA	600×600μm	1	Flow-focusing	Viscosity, surface tension	Squeezing, shearing	I: Liquid squeezing collapse; II: free pinch-off stage	Experiments, high speed camera	Exponent ϑ at 0.33 and 0.5 for I and II stage

To be continued

Reference	Channel geometries			Inlet geometry	Key factors	Formation mechanism	Formation stages	Method	Main contents
	Cross-sectional shape	Dimension	Aspect ratio (a/b)						
Sontti and Atta (2019)	Square	600×600μm	1	Flow-focusing	Oil and water/water-glycerol	Squeezing, shearing and jetting	\	Numerical simulation, CLSVOF	Viscosity and surface tension and flow rate ratios
Li et al. (2019a)	Square	100×100μm	1	T-junction	Modified ribs after T-junctions	Squeezing, transition, dripping, jetting, and parallel regimes	\	Numerical simulation, VOF	Better monodispersed droplet by rectangular rib
Li et al. (2020b) and Li et al. (2020a)	Square glass	600×600μm	1	Flow-focusing	Gas: Helium and Nitrogen; Liquid viscosity and surfactants	\	Squeezing and free pinch-off stages	Experiments High speed camera	Viscosity and surface tension effects on bubble formation and pinch-off period

Table 1-3 Correlations of liquid film thickness in microfluidic devices (Capillary number $\boldsymbol{Ca_{TP}} = \frac{\mu_L j_{TP}}{\sigma_L}$, Reynold number $\mathbf{Re}_{\boldsymbol{TP}} = \frac{\rho_L j_{TP} D_c}{\mu_L}$, and Weber number $We_{TP}=Ca_{TP}\cdot\times Re_{TP}$).

Reference	Cross-sectional shape	Range of Ca	Correlations	Method
Bretherton (1961)	Circular	Ca<0.003	$\delta/D_c = 0.67Ca^{2/3}$	Theoretical
Irandoust and Andersson (1989)	Circular, glass, 1-2mm	Ca<2	$\delta/D_c = 0.18[1-\exp(-3.1Ca^{0.54})]$	Optical and theoretical
Aussillous and Quéré (2000)	Circular, 0.84-2.92mm	Ca<1.4	$\delta/D_c = 1.34Ca^{2/3}/(1+1.34\times 2.5Ca^{2/3})$	Optical
Han and Shikazono (2009)	Circular, glass, 0.3-1.3mm	Ca<0.25	$\frac{\delta}{D_c} = \frac{0.67Ca^{2/3}}{1+3.13Ca^{2/3}+0.504Ca^{0.672}Re^{0.589}-0.352We^{0.629}}$ (Re<2000)	Laser focus displacement meter
Kolb and Cerro (1991), Thulasidas et al. (1995), Hazel and Heil (2002)	Square, 2mm	Ca<0.1	$\delta_{side}/D_c = 0.05$ or 0.01 $\frac{\delta_{corner}}{D_c} = 0.5(1-\exp(-2.25Ca^{0.445}))$, fitted by Kreutzer et al. (2005a)	Optical Numerical
Fries et al. (2008)	Rectangular, 200μm	Ca<10^{-3}	$\delta_{side}/D_c = 0.02$ $\delta_{corner}/D_c = 0.1$	Confocal laser scanning microscopy
Yao et al. (2019)	Rectangular	(6.5×10^{-3}, 5.25×10^{-2})	$\frac{\delta_{corner}}{w} = 0.217-0.154\exp(-8.428Ca^{0.628})$	Optical

1.2.1.3 Liquid lubrication film

The liquid lubrication film located at the channel's walls is a key parameter in Taylor flow as closely controlling the efficiency of mass and heat transfer in micro/milli-channels (Patel et al., 2017; Atasi et al., 2018; Ye et al., 2020).

Various experimental methods have been applied to measure the liquid film thickness, as summarized by Tibiriçá et al. (2010). Considering the underlying physical principles, they could be divided into acoustic (Al-Aufi et al., 2019), electrical (Huang et al., 2017), optical (Chen et al., 2015; Li et al., 2019b) and tomographic (Boden et al., 2014) methods.

The liquid film thickness was impacted by the cross-sectional shape of the channel, Capillary, Weber and Reynolds numbers (Giavedoni and Saita, 1999; Heil, 2001). The main theoretical or empirical relationships enabling to predict the liquid film thickness, noted δ, are reported in Table 1-3.

It is important to keep in mind that, in perfectly wetted circular channels, the liquid film thickness was uniform in the cross-sectional direction whereas in perfectly wetted square or rectangular channels, the liquid film was thicker in the corners and thinner near the channel side walls. Using the double light path method, Yao et al. (2015) experimentally confirmed that the liquid bypassed the gas bubbles through channel corners, leading to leakage flow and that gas bubbles behaved like leaky pistons. They also observed that the maximum particle (polystyrene particles to trace flow characteristics) velocities of leakage flow could be 10 times higher compared to the bubble velocity during the bubble formation and 2 times higher during bubble flowing process. Howard and Walsh (2013) also demonstrated the coupling relations between the liquid film thickness and the bubble velocities in a circular capillary, which were mutually impacted.

The spatial distribution of the film (thickness, homogeneity along the channel's length) strongly depended on the properties of the wall's surface, and in particular the roughness and wettability; the occurrence of strong heterogeneities can induce significant disturbances of the gas-liquid flow patterns (Cubaud et al., 2006). Thus, one could observe some dewetting phenomena (Khodaparast et al., 2017) or rupture of liquid film (Kreutzer et al., 2018) during the bubble flowing, especially when the wettability of channel surface was poor (partially wetting). As illustrated in Fig. 1-10, the complex variation of the liquid film made the measurement more difficult. Even for the same bubble, at different cross-sectional positions from the bubble nose to bubble rear, the developed liquid film patterns were different. To avoid such phenomena, specific surface treatments on the channel's wall were generally implemented.

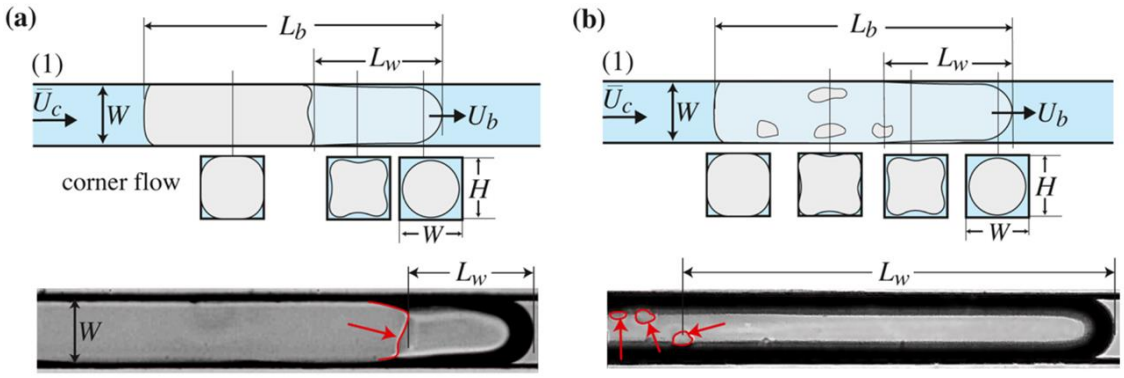

Fig. 1-10 Dewetting patterns around a flowing bubble due to local thinning of film depending on the surface condition of the PDMS microchannels at similar bubble velocities (Ca ~ 10^{-3}). (a) Less wettable surfaces (receding contact angle>25°). (b) More wettable surfaces (receding contact angle~0°). Adapted from Khodaparast et al. (2017).

Although the important role of liquid film has been widely recognized, its contribution to the gas-liquid mass transfer remained difficult to measure experimentally. Most studies focused mainly on the mass transfer within liquid

slugs, but it is a challenge to directly visualize how strong the mass transfer occurs in the liquid film.

1.2.1.4 Pressure drop

The understanding and accurate prediction of the pressure drop is of great importance for designing micro/milli-reactor.

It is well-known that the pressure drop of a single phase for circular cross section under fully developed Hagen-Poiseuille flow could be calculated as below (Kreutzer et al., 2005b):

$$\frac{\Delta p}{L} = f_{Re} \frac{\rho U^2}{2} \frac{4}{d} \tag{1-9}$$

where the friction coefficient f_{Re} was equal to 16/Re.

For two-phase flows, in particular for Taylor flows, various approaches were proposed to predict the related two-phase pressure drop (Eain et al., 2015), consisting in homogeneous and separated flow models. The homogeneous model considered the two phases as a pseudo fluid which was characterized by the average properties (i.e., homogeneous density and viscosity by void fraction) and calculated the pressure drop using single phase model. On the contrary, the separated flow model took account the contributions of each phase and their interactions.

Generally, the total pressure drop depended on several contributions: friction, acceleration, gravity, shape and sizes of the bubbles, and losses (entrance/exit effects) (Fries et al., 2008; Lewis and Wang, 2018; Lewis and Wang, 2019).

In steady flows and in micro/milli devices, the frictional effect remained the main contribution, as commonly calculated according to the Lockhart-Martinelli (noted L-M) model (Lockhart and Martinelli, 1949):

$$(\frac{\Delta p}{L})_{TP} = (\frac{\Delta p}{L})_L {\phi_L}^2 \quad (1\text{-}10)$$

$${\phi_L}^2 = 1 + \frac{\Lambda}{Z} + \frac{1}{Z^2} \quad (1\text{-}11)$$

$$Z^2 = (\frac{\Delta p}{L})_L / (\frac{\Delta p}{L})_G \quad (1\text{-}12)$$

where $(\frac{\Delta p}{L})_L$ and $(\frac{\Delta p}{L})_G$ were liquid and gas single-phase pressure drops. Here Λ represented the Chisholm factor (Chisholm, 1967) and it was an empirical parameter correlated to experimental conditions.

This L-M correlation was originally proposed from the horizontal straight channel, and thus needed to take other parameters into account, namely, the spiral, coiled or meandering geometry of the channel. Vashisth and Nigam (2007) compared the frictional pressure drop in a coiled flow inverter and the one in a straight helix and straight tube, and they observed an increase of pressure drop with a factor between 2.5 and 3. Kurt et al. (2017) also found that the pressure drop in curved channels with small curvature ratios were higher than the one in straight channels.

Concerning the Taylor flow regime, Abiev (2011) proposed a mathematical model for the pressure drop which considers the contribution of the rearrangement of velocity profile in liquid slug, and of the formation or renewal of interface area during the bubble flowing. They pointed out the importance of bubble numbers on the pressure losses.

Furthermore, several studies also have shown the important role of surface wettability in the overall pressure drop in gas-liquid Taylor flows, either through experiments (Lee and Lee, 2010; Choi et al., 2011), modelling (Qu et al., 2014; Mei et al., 2020a) or numerical simulations (Kumar et al., 2007). Apart from the frictional pressure drop, they observed that the capillary pressure drop induced by

the contact angle hysteresis (CAH) for the poorly wetting cases (contact angle > 90°) was higher than the frictional pressure drop. The wettability could also change the bubbles and liquid slug shape (Ide et al., 2008), and induce longer bubble and liquid slug lengths (Abdelwahed et al., 2012). In addition, Cubaud et al. (2006) investigated the liquid film of the gas-liquid flow in various hydrophilic and hydrophobic channels. They found that unlike in hydrophilic flows, bubbles were not lubricated under hydrophobic flows and three phase contacting triple lines (gas/liquid/solid, i.e., the bubble caps and liquid slugs and channel walls) were thus created. The moving triple contact line resulted in higher energy dissipation than inertia and viscous forces did (Lee and Lee, 2008).

1.2.2 Gas-liquid mass transfer in Taylor flows

1.2.2.1 Mass transfer mechanism and modeling

Many questions remain to be addressed with respect to the strong coupling between local hydrodynamics, gas-liquid mass transfer, and even with chemical reaction kinetics. For example, the size and velocity of a bubble may vary along the channel because of the mass transfer phenomena, and the pressure drop (Eskin and Mostowfi, 2012; Zhang et al., 2018; Nirmal et al., 2019). For gases with high solubility, this variation of bubble size and velocity were strongly pronounced, and even more when the transported gas was quickly consumed by the reaction in the liquid phase.

Some theoretical models, as reviewed by Abiev (2020), have proposed interesting insights revealing the mass transfer mechanisms for Taylor flows, which included the gas transported: (1) from the bubble caps to the adjacent liquid slug as indicated by red arrows, and (2) from the bubble body to the liquid film adjacent to the channel wall, as depicted by green arrows in Fig. 1-11. These two

parts were affected by the recirculation motion in the liquid slug and by the possible saturation of the liquid film, respectively.

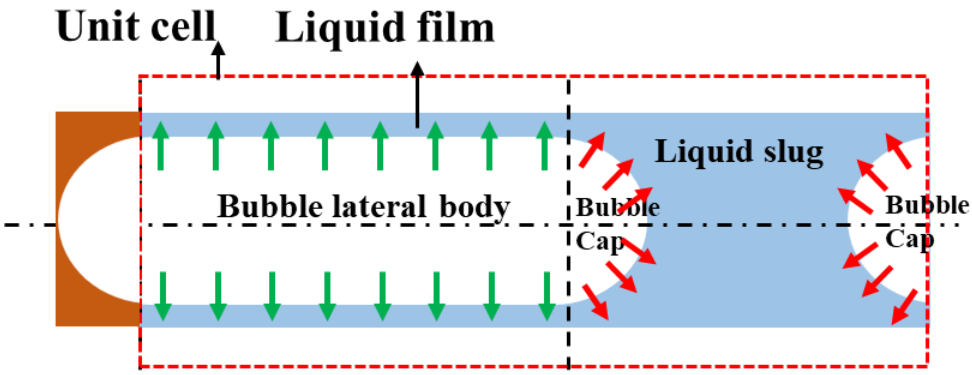

Fig. 1-11 Schematic diagram of mass transfer occurred in Taylor flows: green and red arrows represent the transferred gas from the bubble lateral bodies into the liquid film and the transferred gas from the bubble caps into the liquid slug.

The overall mass transfer ($k_L \cdot a$) in gas liquid Taylor flows in micro or milli devices has been studied through different kinds of approaches, most of which were global methods and a few were local approaches. Various empirical and semi-empirical correlations have thus been put forward, as reported by Haase et al. (2016) and Sattari-Najafabadi et al. (2018). These correlations (Bercic and Pintar, 1997; Van Baten and Krishna, 2004; Vandu et al., 2005; Yue et al., 2007; Yao et al., 2014; Yao et al., 2020) have pointed out the key factors that contributed to the mass transfer coefficients: the diffusion coefficient, unit cell length, bubble velocity, gas hold-up, and liquid phase properties, etc. Nevertheless, these correlations, often dimensional, fail to capture the effect of the channel geometry and the different physical mechanisms (diffusive and convective) controlling mass transfer rates.

At last, depending on the methods and operating conditions, some representative correlations are listed in Table 1-4, which will be used later for comparisons in Chapter 4.

Table 1-4 Selected correlations/models for calculating mass transfer coefficients for Taylor flow in milli-channels.

Reference	Correlations	Methods and conditions
Bercic and Pintar (1997)	$k_{\mathrm{L}}\, a = \frac{0.111 {j_{TP}}^{1.19}}{[\frac{1}{\eta+1}(L_B+L_S)]^{0.57}}$	Global offline, straight capillary (d_{it} 1.5 to 3.1 mm)
Vandu et al. (2005)	$k_{\mathrm{L}}\, a = 4.5\sqrt{\frac{DU_B}{L_{UC}}}\frac{1}{d_{it}}$	Global offline, straight capillary (d_{it} 1 to 3 mm)
Yue et al. (2007)	$Sh\, a = \frac{1}{d_{it}}(0.084 Re_G^{0.213} Re_L^{0.937} Sc_L^{0.5})$	Global offline, square straight channel (0.2 and 0.4 mm)
Van Baten and Krishna (2004)	$(k_{\mathrm{L}}a)_{cap} = \frac{2\sqrt{2}}{\pi}\sqrt{\frac{DU_B}{d_{it}}}\frac{4}{L_{UC}}$ $(k_{\mathrm{L}}a)_{film} = 2\sqrt{\frac{U_B D}{\pi L_F}}(\frac{\ln(1/\Delta)}{1-\Delta})\frac{4L_F}{d_{it}L_{UC}}$ $\Delta = f(Fo)$	CFD simulations, circular tube (1.5, 2 and 3 mm)
Dietrich et al. (2013a)	$(k_{\mathrm{L}})_{cap} = \frac{2\sqrt{2}}{\pi}\sqrt{\frac{DU_B}{d_{it}}}$; $(a)_{cap} = \frac{4}{L_{UC}}$ $(k_{\mathrm{L}})_{film} = \frac{2}{\sqrt{\pi}}\sqrt{\frac{DU_B}{L_B-d_{it}}}$; $(a)_{film} = \frac{4(L_B-d_{it})}{L_{UC}d_{it}}$	Colorimetric local method, square channel (2 mm)
Butler et al. (2016)	$(k_{\mathrm{L}}a)_{cap} = \frac{2\sqrt{2}}{\pi}\sqrt{\frac{DU_B}{d_{it}}}\frac{4}{L_{UC}}$, L_S<2d_{it} $(k_{\mathrm{L}}a)_{cap} = \frac{2\sqrt{2}}{1.8\,\pi}\sqrt{\frac{DU_B}{d_{it}}}\frac{4}{L_{UC}}$, L_S>2d_{it}	PLIF-I local method, vertical tube (3 mm)

For Taylor flows in micro/milli-channels, Nirmal et al. (2019) classified the mass transfer models into three types, as illustrated in Fig. 1-12.

For the first type of models (Bercic and Pintar, 1997; Vandu et al., 2005; Lefortier et al., 2012; Yao et al., 2014), it is assumed that (1) the liquid film around bubbles, liquid film around liquid slugs and liquid slugs had the equal dissolved species concentrations at any given time; (2) bubble velocity was constant during dissolution; (3) the average mass transfer coefficient inside one unit cell was used.

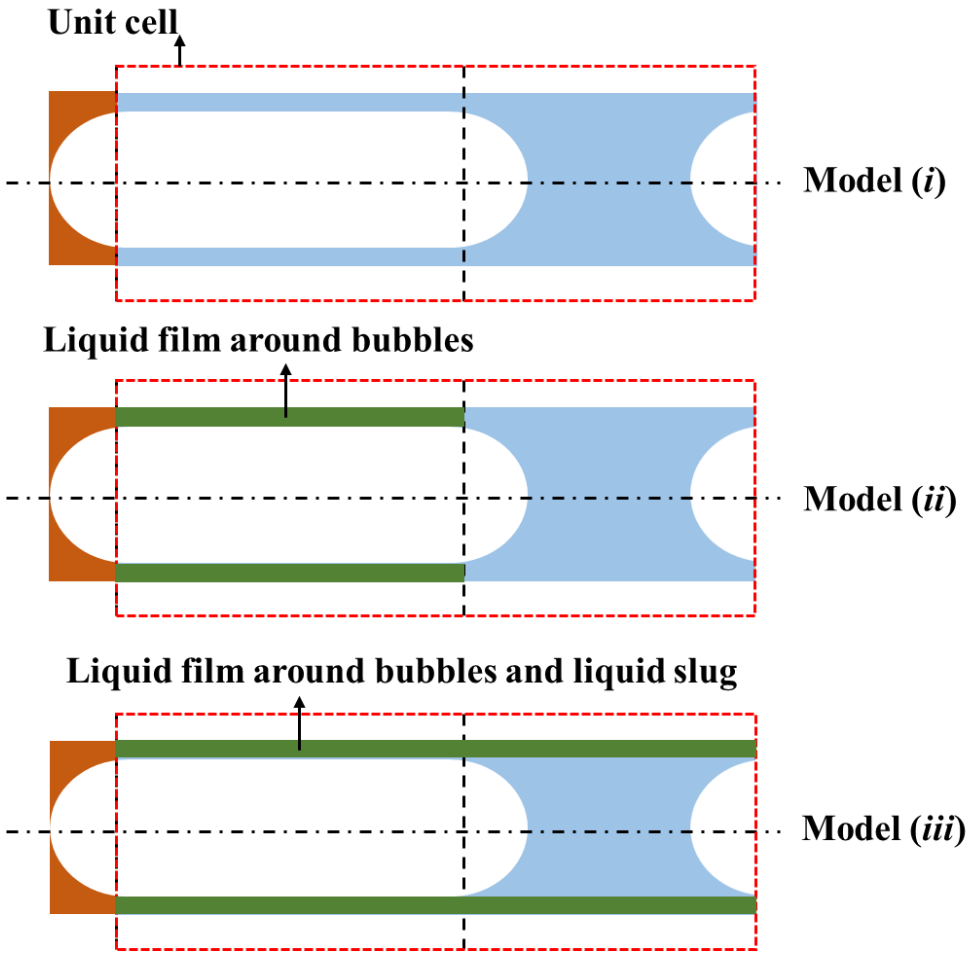

Fig. 1-12 Summary of previously proposed mass transfer model for Taylor flow (green and blue zones in liquid represents different concentrations considered). Adapted from Nirmal et al. (2019).

For the second type of models (Abolhasani et al., 2012; Eskin and Mostowfi, 2012), the liquid slugs and the liquid film around liquid slugs were assumed with identical dissolved species concentration and the liquid film around bubbles was described as plug flow. This model could deal with variant bubble velocity along the channel.

Finally, for the third type of models, Butler et al. (2016) treated the liquid film around bubbles and liquid slugs as one liquid film with uniform dissolved species concentrations. Bubble velocity was assumed constant during dissolution as well.

As pointed by Nirmal et al. (2019), the main limitations of such models were that the bubble velocity and size were assumed constant throughout the channel and that the variation of the mass transfer coefficient during the dissolution process was not taken into account. Therefore, there is a need to identify the time or axial variation of the transport rates for modeling purposes. A first attempt was presented by Pan et al. (2014) using experimental studies and CFD simulations. Later, the complete evolution of the spatial and temporal concentration field within the liquid slugs and the dynamic $k_L \cdot a$ coefficients were presented by Yang et al. (2017b) who solved the coupled transport and reaction equations numerically. Other researchers (Yin et al., 2018; Zhang et al., 2018) have carried out experiments to measure these temporal evolutions of k_L (or variations of mass transfer with axial position in the channel). They also observed a decrease of $k_L \cdot a$ and k_L with increasing travel time in the channel (or axial position in the channel). Few studies (Eskin and Mostowfi, 2012) have studied the combined action of pressure drop and dissolution, although this case was commonly encountered in practice (the continuous-flow, micro-structured equipment involving long channels or tubes to achieve high residence times). Due to the widely used curved channel in practice, the combined action on mass transfer of the pressure drop and centrifugal effects needs to be explored further.

Further specifically, Abiev (2013); Abiev (2020) proposed a three-layer model to fully consider the diffusive and convection mass transfer for Taylor flow, as shown in Fig. 1-13.

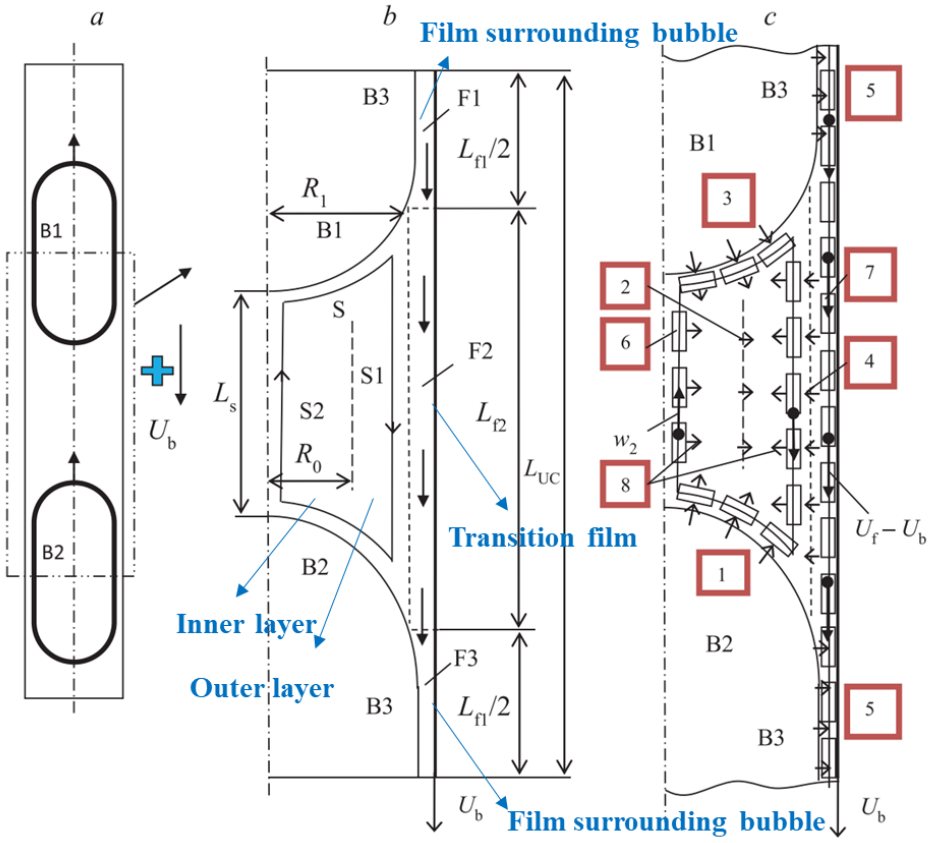

Fig. 1-13 Scheme of three-layer model for two-phase Taylor flow: (a) bubbles and liquid slug in one unit cell (b) representation of each element (c) mass transfer fluxes. Meaning of each element: B1: tail of the leading bubble, B2: cap of the trailing bubble, B3: lateral surface of the bubbles, S1: the outer annular layer, S2: the inner layer; F1: the film around the leading bubble, F2: the transit film around the slug, F3: the film around the driven bubble. Representation of segments (in red squares): 1: diffusion between the hemispherical nose of the driven bubble B2 and the slug S, 2: diffusion between two layers of the slug (S1, S2), 3: diffusion between the hemispherical tail of the leading bubble B1 and the slug S, 4: diffusion between transit film F2 and the annular layer S1 of the slug, 5: diffusion between bubbles lateral side B3 and the films F1, F3, 6: convective transfer in the slug elements S1, S2 by means of Taylor vortex, 7: convective transfer in the films F1, F2, F3, 8: radial diffusion within two layers of the slug (S1, S2). Adapted from Abiev (2020).

They considered the diffusive transfer between the bubble caps and the liquid slug inner and outer layers, and between the transition liquid films and the outer layers of liquid slug, and between the bubble lateral bodies to the liquid films surrounding the bubble. The considered convective transfer were the convection induced by Taylor vortex in the inner and outer layers of liquid slug and the convection in liquid films. The proposed three-layer model has presented better coincidence, with the experimental data from Bercic and Pintar (1997), Butler et al. (2016), and Haase et al. (2020b), and it confirmed the huge contributions from convection items in modeling the overall gas-liquid mass transfer. They also highlighted the proportional correlations between the overall gas-liquid mass transfer coefficients and recirculation frequencies inside liquid slugs.

1.2.2.2 Experimental measurements for mass transfer

For several decades, the development of experimental methods for investigating gas-liquid mass transfer has been an active topic. Some very interesting reviews could be found in Paul et al. (2018) and Sattari-Najafabadi et al. (2018).

Generally, they could be classified into global and local methods. For global methods, samples containing both phases were collected (absorption method) at the outlet of the micro/milli-reactor or directly measured online (e.g., using probes or sensors) at the inlet and the outlet, in order to analyze the desired phase and then calculate the overall volumetric mass transfer coefficients (Roudet et al., 2011). Therefore, only a global description of the mass transfer could be given and there is no detailed information of what happened exactly and how it varied inside of the channel. To obtain local information (particularly dissolved species concentration fields), researchers developed different approaches, such as fluorescence techniques, bubble volume change tracking, colorimetric techniques, and Raman spectroscopy (Deleau et al., 2020). They are detailed in the following sections.

I. Fluorescence technique

Fluorescence techniques could be classified as traditional fluorescence technique (Planar Laser Induced Fluorescence, PLIF) and the inhibited fluorescence technique (Planar Laser Induced Fluorescence with Inhibition, PLIF-I).

PLIF is a powerful method used for studying heat and mass transfer by visualizing spatial and temporal fields of a passive or reactive scalar. The fluorescence dye was chosen according to the following properties: a high quenching constant, be readily soluble, and no significant surface activity. The

principle of PLIF was referred as follows. A thin laser sheet illuminated a flow region to excite the fluorescence dye molecules initially seeded in the fluid. The absorption peak of the dye was close to the laser excitation wavelength, leading to the re-emission of a portion of the absorbed energy at a longer wavelength, as fluorescence. Fluorescein and rhodamine were the most typically organic fluorescent dyes in PLIF methods (Rüttinger et al., 2018). Finally, the re-emission fluorescent intensity can be associated with the local dye concentrations.

For the PLIF-I, the occurrence of some quenchers in the liquid phase (e.g., dissolved molecules of CO_2 and O_2) could inhibit the induced fluorescence intensity. By measuring the fluorescence intensity, one becomes possible to deduce the value of the dissolved species concentration (i.e., the concentrations of the quencher molecules that inhibit the fluorescence signal), considering that the dye was homogeneously pre-mixed in the fluid at fixed concentration. For example, carbon dioxide dissolved in aqueous solution tended to inhibit the fluorescence of fluorescein, while the fluorescence emitted from ruthenium (Kastens et al., 2017a) and pyrene butyric acid (PBA) were sensitive by the presence of oxygen.

Applying PLIF technique to Taylor flows presented some challenges. First, the re-emitted fluorescence signal may be reflected by the channel wall and/or by gas-liquid interfaces, leading to non-negligible uncertainties and data calibration difficulties. Quantifying mass transfer in the vicinity of a bubble was particularly tricky. For example, as illustrated in Fig. 1-14, a white ring can be observed around the bubble as well as a bubble shadow. An intensity contrast appeared between the solution at the left side and at the right side of the bubble. Therefore, obtaining accurate concentrations near the gas interface remained challenging.

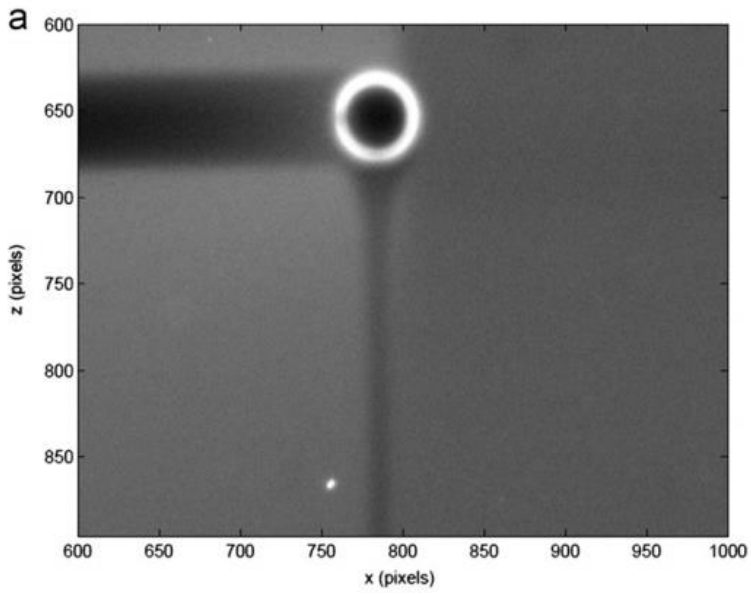

Fig. 1-14 PLIF image of a rising air bubble. Extracted from Dani et al. (2007).

Butler et al. (2016) first investigated mass transfer of a Taylor oxygen bubble by means of PLIF-I technique and deduced the oxygen concentration using the ruthenium fluorescence intensities. Butler et al. (2018) solved the scattered light problem (near the bubble interface) by using the images of nitrogen (i.e., without quenching signal) as the reference background and subtracting them from the images of oxygen (i.e., with quenching signal). In a vertical millimetric channel (3 mm d_{it}), by implementing a specific image processing, Butler et al. (2018) could analyze the separate contributions of the bubble caps and the lubrication films to the overall $k_L \cdot a$. They pointed out that the model proposed by Van Baten and Krishna (2004) was not suitable to predict the $k_L \cdot a$ values for cases of slug length shorter than twice the channel diameter. These authors also showed that the overall $k_L \cdot a$ was proportional to the recirculation frequency inside liquid slug.

II. Volume change tracking by image analysis

When the solubility of species that transferred from the gas phase into liquid phase was sufficiently high, the volume of Taylor bubble may significantly decrease along the channel, as shown in Fig. 1-15, and can thus be considered as an indicator of the mass transfer process.

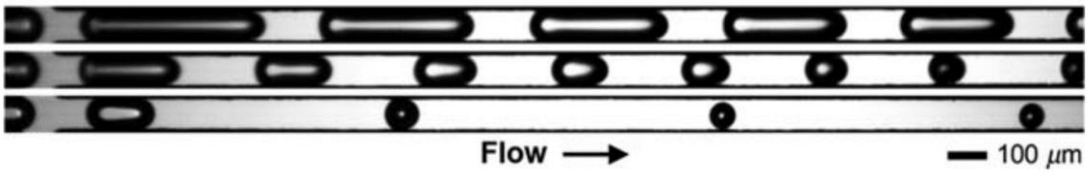

Fig. 1-15 Examples of bubble volume decrease for strongly diffusive CO_2 bubbles in methanol. Adapted from Sun and Cubaud (2011).

Tan et al. (2012b) first proposed this method to investigate instantaneous mass transfer of gas-liquid segmented flow and the contribution of bubble formation stage. A direct mass transfer model based on the change in bubble volume was proposed, as follows:

$$\frac{1}{HRT}\left(V_{g0} - V_g + V_{ge}\ln\frac{V_{g0}-V_{ge}}{V_g-V_{ge}}\right) = K_L a \cdot t \tag{1-13}$$

where V_{g0} and V_{ge} represented the initial and final bubble volume. H, R and T Henry constant, gas constant and temperature, respectively. By plotting the time-variation of the left of equation (1-13), the liquid side overall mass transfer coefficient ($K_L a$) could be directly obtained.

Yao et al. (2014) developed the mass transfer model through the change of the bubble lengths assuming that the bubble shape in cross sectional area did

not change. The following equation was given from the mass balance of gas phase in one unit cell:

$$L_B = L_{B0} + \frac{C^* - C_0}{U_B A_B} V_L \frac{RT}{P} j_L (e^{\frac{k_L a}{j_L} x} - 1) \quad (1\text{-}14)$$

where L_{B0} and L_B represented the initial and instantaneous bubble length, U_B and A_B the bubble velocity and cross-sectional area of bubble, V_L the liquid volume. Therefore, the bubble length could be fitted by an exponential function and volumetric liquid side mass transfer coefficient ($k_L a$) could be deduced from the fitted exponents.

In addition, Hosoda et al. (2014) got the stereoscopic images of bubble by two synchronized cameras (front and side) and thus established a three-dimensional description of bubble volume change. The calculation of the volumetric liquid side mass transfer coefficient $k_L a$ was deduced from the mass balance of gas phase in the liquid phase.

Although the overall mass transfer coefficient could be deduced by this type of method, the direct dissolved species concentration field could not be obtained. In the meantime, this method is quite limited by the accuracy of bubble volume change, and thus requires to use gas species with high solubility.

III. Colorimetric techniques

The colorimetric techniques were based on the measures of a change in color intensity in the liquid medium that can be correlated to the concentration of the species transferred from the bubbles. Various inorganic or organic chemical compounds were available for this purpose, which were classified to redox reactions (Dietrich et al., 2013a; Dietrich et al., 2019; Krieger et al., 2020), pH-

based reactions (Burns and Ramshaw, 2001; Dessimoz et al., 2008), and reactions based on metal-complex molecules (Tice et al., 2003; Kastens et al., 2017b).

The choice of different dyes in colorimetric methods mainly depends on the following factors:

- the toxic and economic factors,
- the kinetics of the colorimetric reaction,
- the intensity of the color generated,
- the liquid phase properties,
- the gas phase properties.

i. Redox reactions

According to the literature, methylene blue (Piccione et al., 2017), resazurin (Dietrich et al., 2013a) and leuco-indigo carmine (Krieger et al., 2017) were the mainly used dyes.

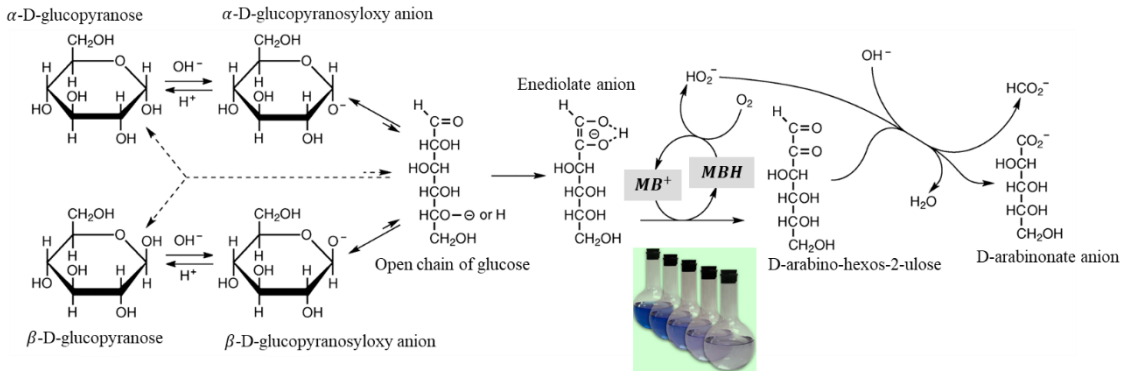

Fig. 1-16 Reactions occurring in the ‘blue bottle’ experiment. Adapted from Anderson et al. (2012).

Methylene blue is well-known from ‘blue bottle’ experiment (Cook et al., 1994), which is dated back to the 1920s (Henry Lane, 1924). In the ‘blue bottle’ experiment, the reaction occurred in the presence of glucose in alkaline solution.

Blue dye (MB^+) was reduced to colorless hyaline leucomethylene blue (MBH), and MBH was transformed into blue MB^+ by reacting with dissolved oxygen, as shown in Fig. 1-16. Piccione et al. (2017) used the Methylene blue to visually demonstrate the mass transfer rates and scale-up effects in agitation reactors with different sizes (1L and 10L).

Dietrich et al. (2013a) first proposed the colorimetric technique to investigate mass-transfer in Taylor flows. This technique is based on an oxygen sensitive dye, resazurin. Further details will be given in Chapter 2. As Fig. 1-17 shows, the change of color resulted from reversible oxidation (fast) and reduction (slow) reactions between resorufin (pink) and dihydroresorufin (colorless).

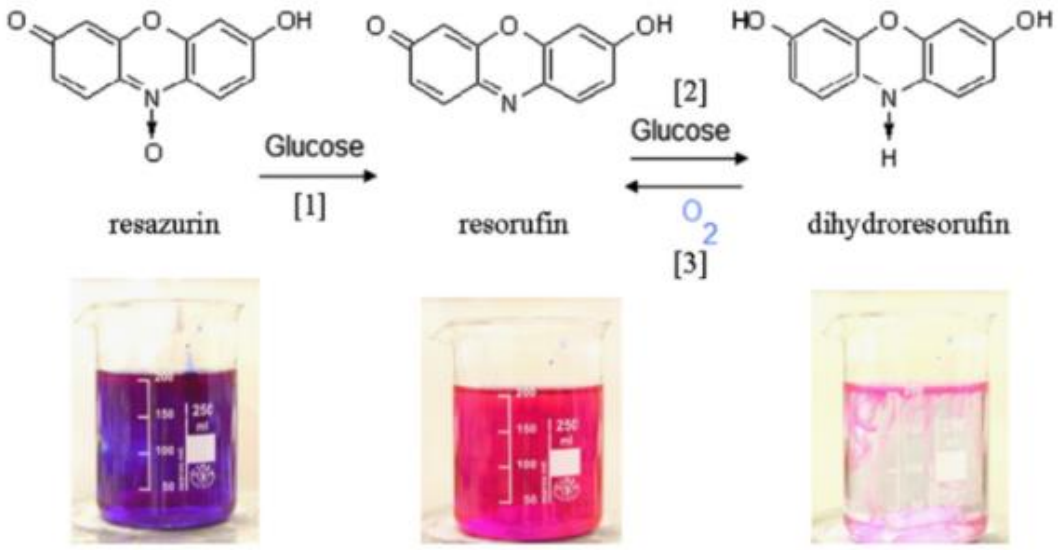

Fig. 1-17 Principles of the colorimetric method base on the use of resazurin. Extracted from Dietrich et al. (2013a)

These authors showed that the equivalent dissolved oxygen concentration fields could be obtained from color intensity level maps, and from them, the mass transfer coefficients could be deduced. Most importantly, a local description of equivalent dissolved oxygen concentration fields could be obtained and gave better understanding on gas-liquid mass transfer mechanisms. In addition, Yang

et al. (2016a) investigated the eventual enhancement of gas-liquid mass transfer by this oxygen colorimetric reaction. By determining kinetics constant and diffusion coefficients, the Hatta number and enhancement factor were deduced. Under their specific operating conditions, they demonstrated that there was no enhancement of the gas-liquid mass transfer, even if the reaction was extremely fast (few milliseconds). By using the same technique, Yang et al. (2016b) and Yang et al. (2017a) further investigated the contribution of the bubble formation stage to overall mass transfer process and the mass transfer intensification due to the presence of bends in square channels.

Krieger et al. (2017) utilized another redox dye, leuco-indigo carmine, to visualize local mass transfer and concentration distributions. Because of the anionic radical intermediate state, chemical selectivity was also investigated. As shown in Fig. 1-18, in presence of glucose in alkaline solution, keto-indigo carmine (blue) was reduced to anionic radical intermediate (red), which was further reduced to leuco-indigo carmine (yellow). The reaction rates of reductions and oxidations were slow (several minutes) and fast (a few milliseconds) respectively. In addition, as there was an overlap between three different indigo carmine colors, a specific calibration procedure was achieved by imaging processing technique, combined with UV/Vis spectrometer methods to allow the isolation of each indigo carmine contribution. The degradation of keto-indigo carmine during the reduction step was also considered.

Fig. 1-18 Reversible redox reactions of leuco-indigo carmine to keto-indigo carmine with glucose as reducing agent and oxygen as oxidizing agent. Color change (yellow-red-blue) is illustrated in flask experiments. Extracted from Krieger et al. (2017).

The main limitation of such colorimetric technique (resazurin or leuco-indigo carmine) is that the observed color signals are averaged along the channel depth, which makes them better suitable for symmetrical flows or flows without strong three-dimensional effects.

Recently, Xu et al. (2020) compared three visualization methods for gas-liquid mass transfer (i.e., PLIF, PLIF-I and colorimetric (resazurin) methods) and proposed several guidelines to choose the most suitable visualization methods under different conditions for a free rising bubble. The main advantages and disadvantages of these methods identified by these authors are shown in Fig. 1-19. In addition, it is also noted that lasers are not used in colorimetric methods, facilitating the implementation.

	Advantage ☑ or limitation ☒
PLIF-I	☑ Tracks mass transfer in the wake far from the surface ☑ Accurate quantification of flow flux ☑ Characterizes the diffusion ☒ Reflection at the bubble surface ☒ Significant background noise ☒ Shadow of the bubble
PLIF	☑ Tracks mass transfer in the wake far from the surface ☑ Less background noises ☒ Cannot characterize the diffusion of oxygen ☒ Reflection at the bubble surface ☒ Extra chemicals
Colorimetric technique	☑ Tracks mass transfer even near the bubble ☑ No reflection near the bubble ☒ Cannot characterize the diffusion of oxygen ☒ Complex composition of the recorded image ☒ Extra chemicals

Fig. 1-19 Comparison of advantages and limitations of three techniques (PLIF, PLIF-I and colorimetric methods), adapted from Xu et al. (2020).

ii. pH indicators

Neutralization reactions have also been applied to visualize mass transfer in liquid-liquid systems. Burns and Ramshaw (2001) carried out such reactions to monitor the extraction of acetic acid (CH_3COOH) from kerosene to aqueous solution within NaOH or KOH. As shown in Fig. 1-20, the phenol red pH indicator added to the NaOH solution allowed to monitor the color change from pink to yellow along the length of microchannel. From the titration time and the amount of transferred acetic acid, the mass transfer coefficients could be deduced. This technique was further used to study mass transfer timescales in capillary microchannels (Kashid, 2007). Another pH indicator, bromothymol blue was then

utilized to change color at pH=7 (blue-yellow) by neutralization of the strong acid (trichloroacetic acid) extracted from toluene or hexane to the alkaline aqueous solution containing NaOH (Dessimoz et al., 2008). Fluid properties and flow patterns (parallel and slug flow) were investigated, showing different dominated parameters in mass transfer. Recently, Méhault et al. (2021) applied the phenolphthalein indicator into more complex of liquid-(gas-liquid)-liquid flow system by alternated Taylor flow to prevent the droplets coalescence, and demonstrated the mass transfer from one aqueous droplet into another aqueous droplet. This offered applications to perform cascades reactions in a single continuous flow reactor.

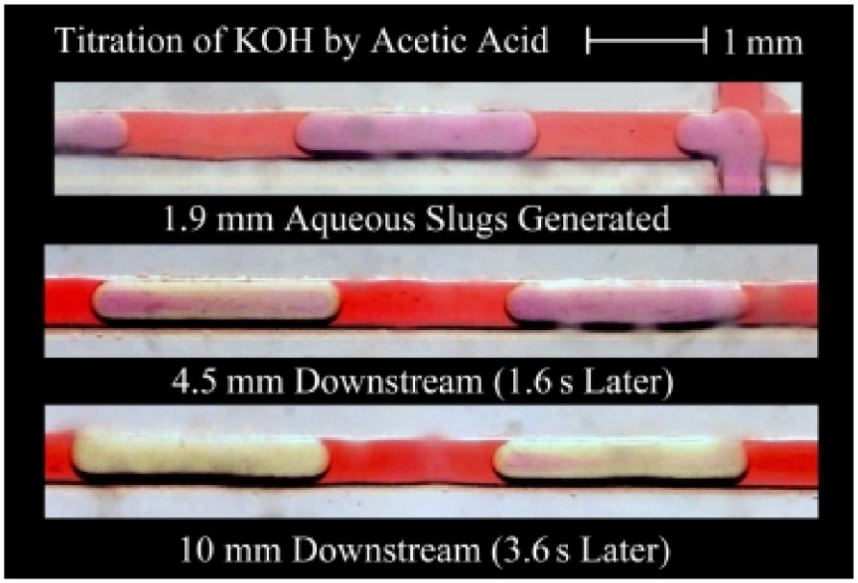

Fig. 1-20 Pattern of acetic acid transfer process from kerosene to aqueous phase containing KOH and phenol red indicator. Adapted from Burns and Ramshaw (2001).

iii. Metal-complex molecules

The use of reactions involving metal-complex molecules to study oxygen transfer appeared during last five years (Kastens et al., 2017b; Paul et al., 2018;

Felis et al., 2019). The change of color depended on the oxidation state of the metal center, as shown in the following equation from Kastens et al. (2017b):

$$\left[Cu(\mathrm{I})\left((NH_3)\right)_4\right]^+ (\text{colorless}) \overset{O_2}{\rightarrow} \left[Cu(\mathrm{II})\left((NH_3)\right)_4\right]^{2+} (\text{deep blue}) \quad (1\text{-}15)$$

The oxidation state Cu (II) (deep blue) was more stable than the non-oxidated state Cu (I) (colorless) and the oxidation reaction was very fast. Fig. 1-21 presents the changed deep blue color at the wake of a single Taylor bubble, obtained with PIV-LIF images. They revealed the occurrence of coherent structures at the bubble wake and enabled to identify three different wake structures, while quantitative characterization of local oxygen concentration and oxygen transfer flux were not derived in this study.

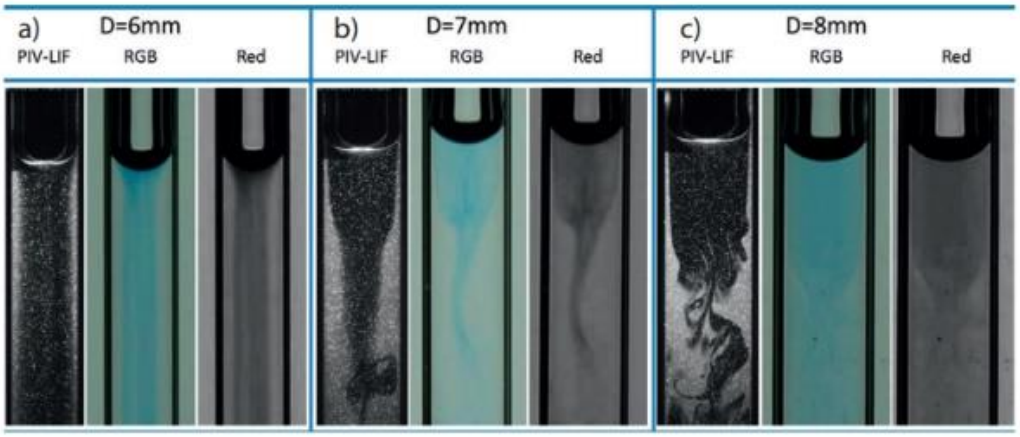

Fig. 1-21 Wake structure and oxygen transfer image in various channels. Adapted from Kastens et al. (2017b).

When implementing metal-complex molecules, the liquid phase to use may become no more aqueous, but rather consisted of organic solvents (e.g., acetonitrile), which induced the variation of fluid properties (e.g., Schmidt number, Capillary number).

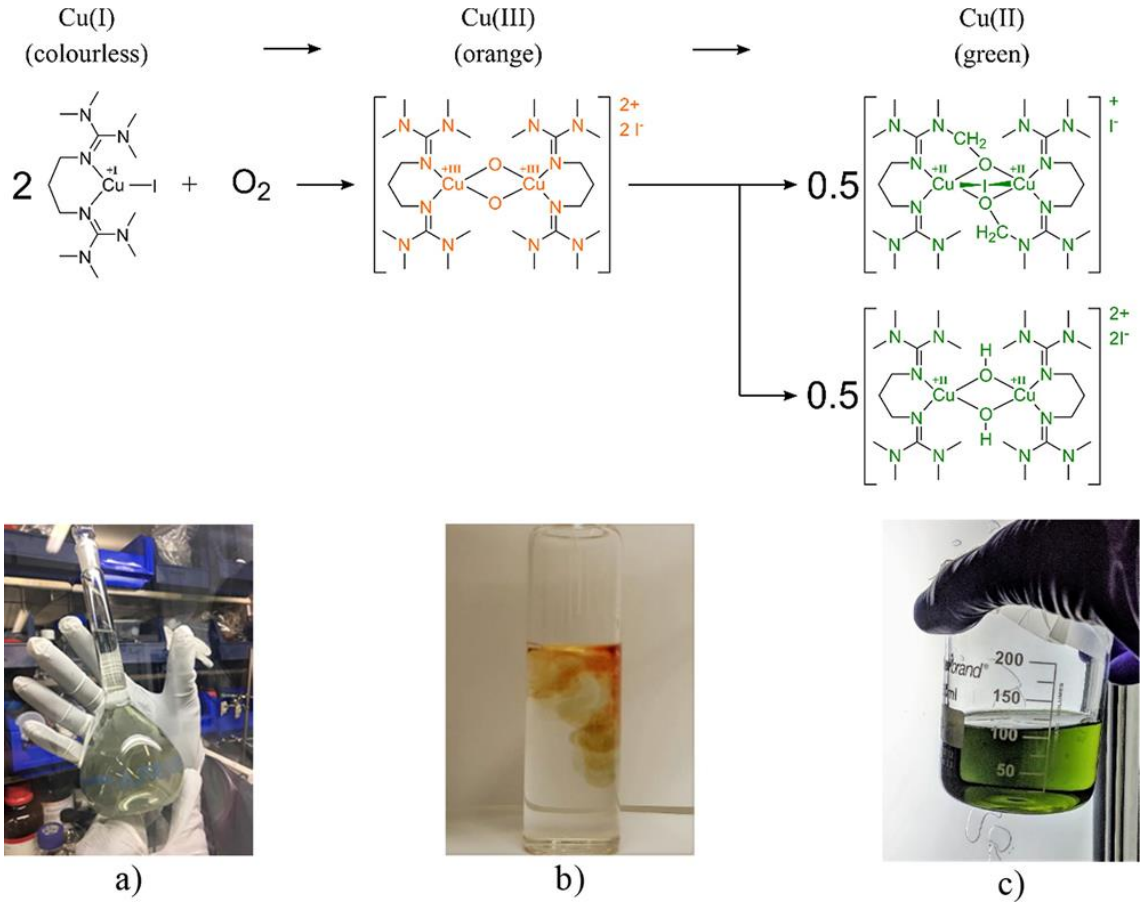

Fig. 1-22 Reactions of Cu(btmgp)I copper complex system. (a) Colorless Cu(I) prepared in an oxygen-free argon glove-box. (b) Open bottle visualization of the orange Cu(III) reaction with air. (c) Final product of the reaction, green Cu(II). Extracted from Felis et al. (2019)

Felis et al. (2019) used another bio-inspired copper complex (Herres-Pawlis et al., 2005), Cu(btmgp)I (colorless), which could be oxidized into $[Cu_2O_2(btmgp)_2]I_2$ (orange). This orange Cu(III) complex was unstable and decayed into two Cu(II) complexes, presenting permanent pale-green color at last, as shown in Fig. 1-22. By establishing an ad hoc calibration relation, the equivalent oxygen concentration fields in the wake of a single bubble flowing in a thin-gap cell was measured. In addition, by varying the bubble size, different regimes in terms of hydrodynamics, and thus of mass transfer, could be achieved, leading to a scaling law relating dimensionless Sherwood number with Peclet number. The enhancement factor caused by the chemical reaction was also

discussed, and found between 1.12 and 1.15, meaning that the measured Sherwood numbers were slightly over-estimated.

1.2.3 Effect of the channel's geometry on gas-liquid hydrodynamics and mass transfer

Curved geometries, such as meandering channels (Yang et al., 2017a), helically coiled tubes (Kurt et al., 2017), spiral-shaped tubes (Aillet et al., 2014) or tubes with bends (Hipolito et al., 2010) have been widely used for designing of miniaturized multiphase reactors (Vashisth et al., 2008), because they could provide: (i) efficient cross-sectional mixing; (ii) intensified mass transfer and heat transfer and (iii) increased compactness and narrow residence time distribution (even if an increase of pressure drop also exists). Due to the bends or to the tube curvatures, a so-called Dean flow may be generated, characterized by the occurrence of secondary vortices (Fries and von Rohr, 2009). Many different types of curved channel geometries (Gao et al., 2020) have been investigated, such as coil-in-coil, toroidal helical, coiled flow inverter, alternating-axis helical, and in-plane spiral-shaped milli-reactors, as shown in Fig. 1-23.

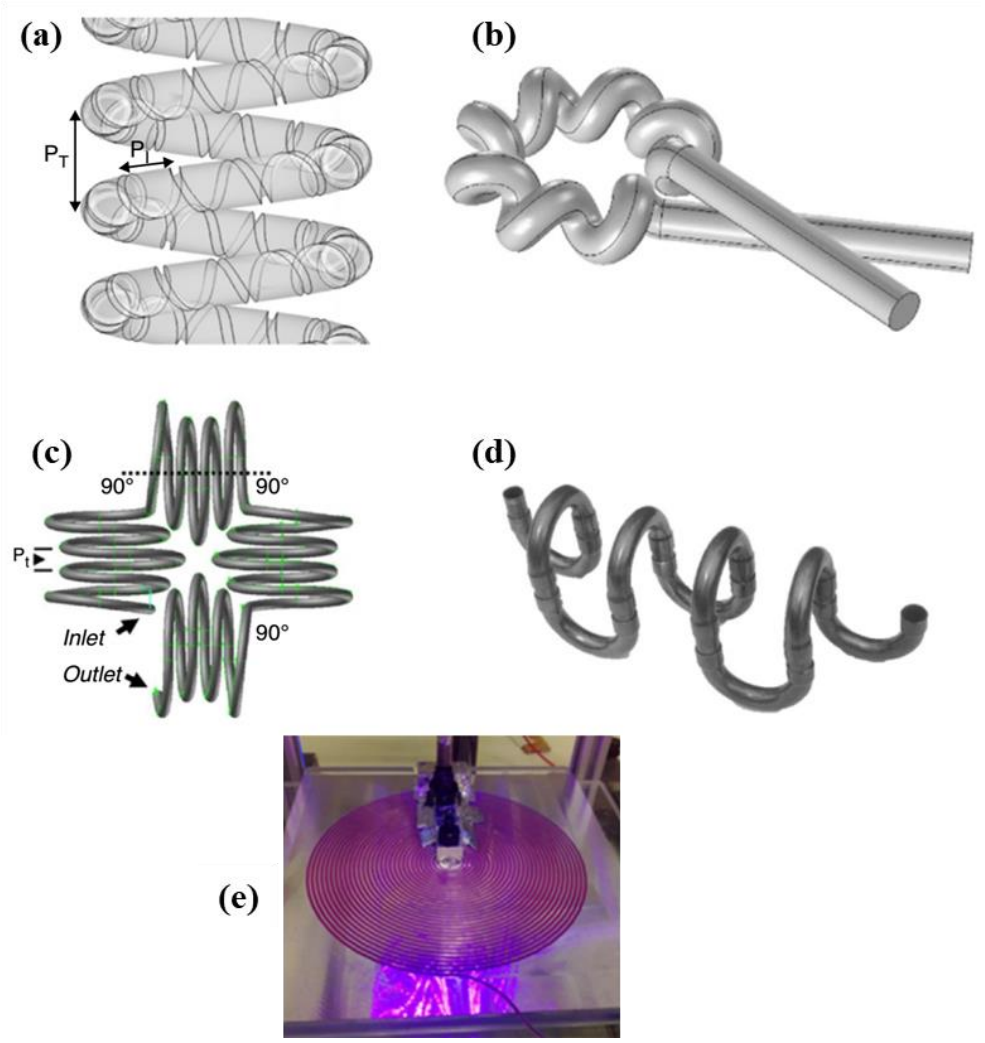

Fig. 1-23 Illustration of different types of curved channel geometries: (a) 3D printed coil-in-coil reactor, (b) toroidal helical pipe, (c) wavering coiled flow inverter reactor, (d) alternating-axis helical reactor (adapted from Gao et al. (2020)), and (e) in plane spiral-shaped reactor (extracted from Loubière et al. (2016)).

The in-plane spiral-shaped reactor, recently developed for carrying out organic photochemical reactions and acquiring kinetic data (Aillet et al., 2014; Aillet et al., 2016; Loubière et al., 2016), provided an alternative design: the curvature changes continuously along the channel length while remaining in the same plane.

Many previous works related to curved geometries have focused on single phase flows (Fellouah et al., 2006; Kováts et al., 2020), separating particles

(Jimenez et al., 2017) and mixing (Fries and von Rohr, 2009; Kurt et al., 2017). Concering the gas-liquid flow in curved geometries, Fries and von Rohr (2009) and Zaloha et al. (2012) have investigated the influence of bends in millimetric channels on the gas-liquid hydrodynamics (i.e., flow regime, mixing efficiency, and interfacial area). Muradoglu and Stone (2007) made a numerical study of the motion of gas bubbles in curved channels and found that the liquid lubrication film at the outer wall was thicker than the one at the inner wall. The lubrication theory predicted that the slip velocity of the bubble relative to the liquid would always be higher in a curved channel than the one in a straight channel and would increase monotonically with the decrease of the channel curvature ratio (the curved channel diameter divided by the cross-sectional diameter of the channel).

The gas-liquid Taylor flow in curved channels with various curvature ratios (5-30) was also simulated numerically by Kumar et al. (2007), using the volume of fluid (VOF) method for interface tracking. They pointed out that, in contrast to the case in a straight channel, the bubble and liquid slug lengths were not only controlled by inlet geometries and by the total two-phase superficial velocities, but were also dependent on the curvature ratio. Shorter slug lengths were achieved at lower curvature ratios because of the stronger centrifugal force. The surface tension and wall surface adhesion were also found to affect the slug lengths.

Kawahara et al. (2011) investigated the gas-liquid flow characteristics in a micro-channel with return bends and, interestingly, observed that there was an increase of bubble length (i.e., a gas volume expansion caused by pressure drop) in the long micro-channel as the bubble flowed downstream. This study also highlighted the important effects of pressure drop (estimated at about 22-68 kPa for four bend experiments and 13-55 kPa for single bend experiments) on the gas-liquid hydrodynamic characteristics. Therefore, the pressure drop in in-plane

spiral-shaped reactors and under hydrophobic conditions should be carefully analyzed and correctly predicted to further guide the microreactors design.

Concerning gas-liquid mass transfer in curved geometries, Roudet et al. (2011) investigated how curvatures affected the overall gas-liquid mass transfer coefficients using a global experimental approach (oxygen probes). Kuhn and Jensen (2012) applied a pH-sensitive laser-induced fluorescence technique to locally quantify the mass transfer rates of carbon dioxide and compared the overall gas-liquid mass transfer coefficients in spiral and meandering microreactors, and found increased value in the spiral design. Most works considered Taylor bubbles flowing in a straight micro/milli channel or tube, as thoroughly reviewed by several authors (Abiev et al., 2017; Paul et al., 2018; Sattari-Najafabadi et al., 2018), even if curved channels or pipes were well-known for improving performances in terms of mixing and transfer phenomena (Ghobadi and Muzychka, 2013; Kováts et al., 2018). Visualizing and measuring the transferred component concentration at local scale (Krieger et al., 2017; Krieger et al., 2020) remained rare in curved channels. In the case of Taylor flows, the recirculation loops in the liquid slug became no longer symmetrical about the centerline of the channel as in straight channels but present a complex three-dimensional structure (Zaloha et al., 2012; Krieger et al., 2019) as shown in Fig. 1-24. In addition, the shape and intensity of recirculation loop depended on the channel width and turning radius (see Fig. 1-24 (b)).

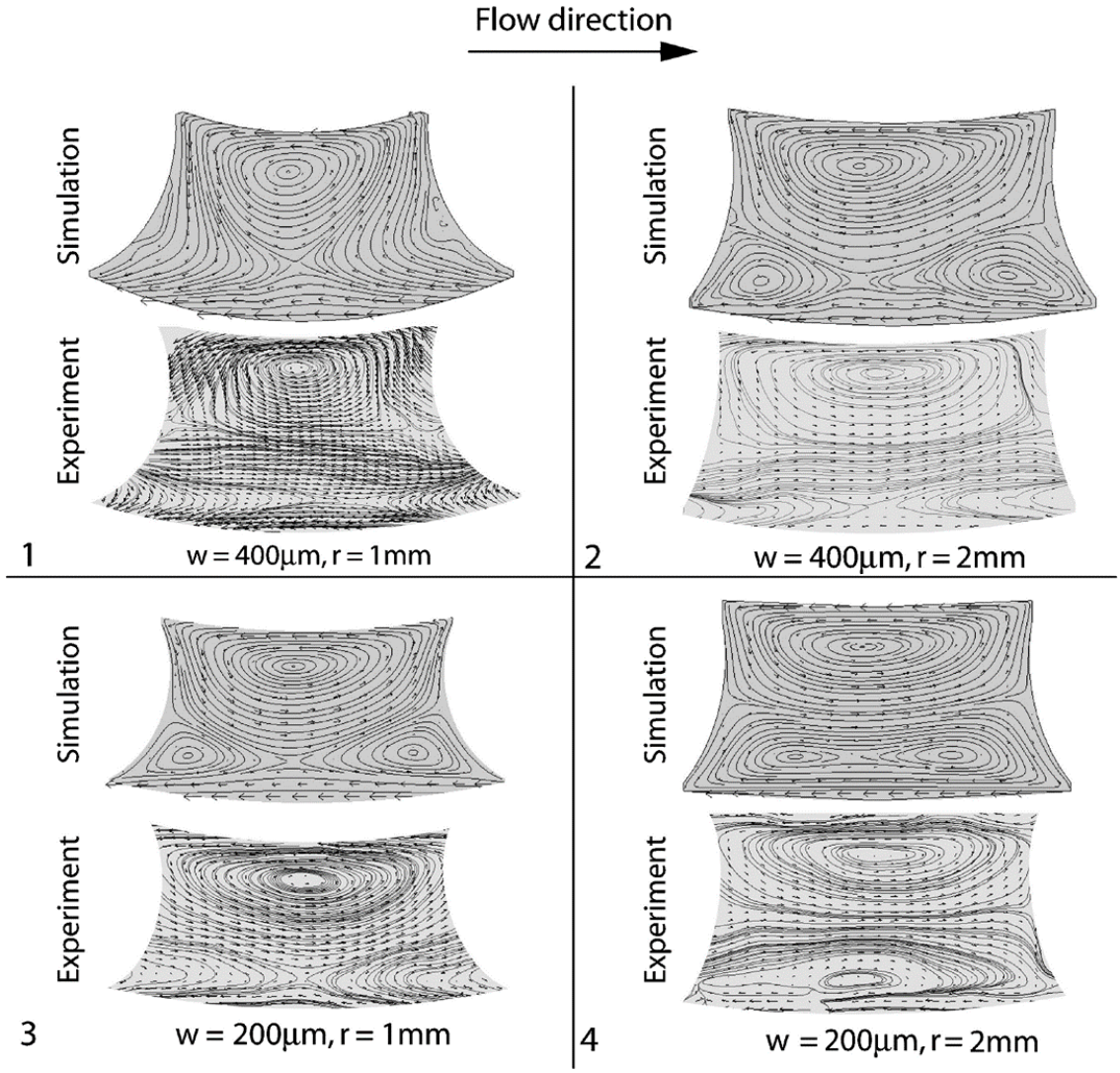

Fig. 1-24 Recirculation loops within liquid slug in the bend: comparison of simulation and µ-PIV experiments under different geometry conditions (*w* and *r* represent channel width and turning radius), j_{TP} = 0.16 m s^{-1}. Adapted from Fries and von Rohr (2009).

Due to the shifted position of the recirculation loops and the occurrence of secondary flow patterns, the gas-liquid mass transfer mechanisms in curved channels are more complex than the ones in straight channels. Recent studies have focused on hydrodynamics, heat transfer (Vashisth et al., 2008) and mixing (Zhang et al., 2016) for two-phase flows. Kurt et al. (2017) investigated the pressure drop and conversion of sodium sulfite in a coiled flow inverter (1 mm d_{it}), finding a 14% higher conversion. Krieger et al. (2017), Krieger et al. (2019),

Krieger et al. (2020), Kováts et al. (2018) and Yang et al. (2017a) have applied colorimetric techniques (i.e., using indigo carmine, methylene blue or resazurin) to visualize the oxygen concentration in helically coiled curved devices or meandering channels, and also observed intensified mass transfer due to the centrifugal force.

1.3 Research aim and thesis outline

Regarding this context, the thesis aims at contributing to this scientific field by studying gas-liquid hydrodynamics and mass transfer around Taylor bubbles. A specific attention will be paid on two configurations: air bubbles flowing in an in-plane spiral-shaped milli-reactor, initially designed for organic photochemistry applications, and air bubbles generated at a cross-junction in a straight milli-channel. For this purpose, a colorimetric technique based on the resazurin dye was implemented and improved to monitor the oxygen mass transfer occurring between air bubble and aqueous phase. By developing specific image acquisition and processing, it became possible to measure the dissolved oxygen concentration fields in the liquid phase, revealing them as a function of the axial position and operating conditions.

The thesis is structured as follows. After introducing the context and a brief state-of-art in the Chapter 1, Chapter 2 will be devoted to the description of the basic methods and techniques, namely (i) the principle of the colorimetric method and the related implementation guidelines, (ii) the experimental setup, image acquisition systems and related image processing methods. The specific algorithms developed to extract the gas-liquid hydrodynamics characteristics and the equivalent oxygen concentration fields for each setup will be detailed in subsequent chapters. Chapter 3 and 4 deals with investigations of Taylor flows in

an in-plane spiral-shaped milli-reactors, in terms of gas-liquid hydrodynamic and mass transfer, respectively. The investigations carried out during and after the bubble formation stage at a cross-junction in a straight milli-channel will be presented in two chapters: Chapter 5 for hydrodynamics and Chapter 6 for mass transfer. Finally, Chapter 7 will summarize all the main results and give out some perspectives for future studies.

Chapter 2. Experimental methods and techniques

Introduction

This chapter will introduce the colorimetric method based on the resazurin dye which was used throughout this thesis. Section 2.1 gives the basic principles of colorimetric reaction and the procedures for preparing the aqueous solution of resazurin. The absorption spectra of resazurin and resorufin were also measured and discussed. In section 2.2, two experimental setups are described: the in-plane spiral-shaped milli-reactor and the straight milli-channel with a cross-junction. Finally, the related image acquisition system and image processing processes will be presented in section 2.3.

2.1 Colorimetric method based on the resazurin dye

2.1.1 Principles

Some basic principles on the colorimetric methods have been introduced in Chapter 1. This section will give some further views. The colorimetric technique proposed by Dietrich et al. (2013a) is based on an oxygen-sensitive dye, resazurin (molecular mass: 229.19 g mol^{-1}, Sigma Aldrich, CAS 199303, purity 93%, noted RZ,), of which the complete chemical IUPAC name is 7-hydroxy-3H-phenoxazin-3-one-10-oxide. The overall scheme of the redox reactions is shown in Fig. 2-1. Resazurin (blue and not fluorescent) is first irreversibly reduced to resorufin (noted RF, pink and highly fluorescent, molecular mass of 213.19 g mol^{-1}), which is reversibly reduced to dihydroresorufin (noted DH, colorless and not fluorescent). These reactions take place in presence of glucose and sodium

hydroxide. When there is dissolved oxygen, two moles of DH are oxidized with one mole of O_2, generating two moles of RF.

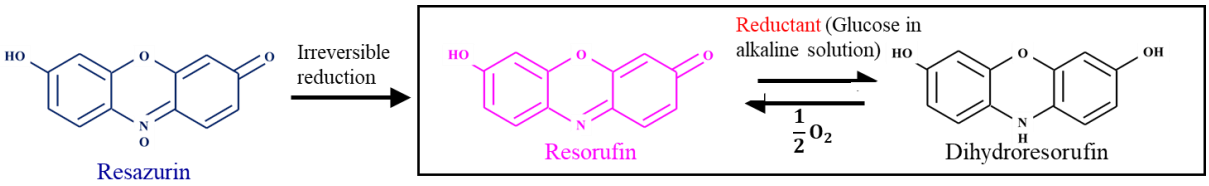

Fig. 2-1 Overall redox reaction mechanism of the resazurin-based colorimetric method.

At present, the mechanism is not fully understood in detail, particularly regarding the oxidation products of glucose. Analogously, many researchers have previously investigated the methylene-blue with glucose in alkaline environments, known as the 'blue bottle' experiment. Pons et al. (2000) and Pons et al. (2002) thought the gluconate (gluconic acid) is the main products of glucose oxidation, but this is not a consensus view. Anderson et al. (2012) proposed a two-stage process including the enolization of the glucose and the oxidation of enolized glucose by methylene-blue and thought the D-arabinonate was the final oxidation product of glucose. Therefore, this complex oxidation products of glucose needs to be further studied.

2.1.2 Procedure for preparing the resazurin solution

The initial concentration of resazurin is a fundamental parameter and should be thus carefully chosen. It depends on the experimental devices and conditions (particularly on the observation depth), but also on the image acquisition system (i.e., the sensitivity and resolution of the camera). Even if the experience can guide this choice, preliminary tests are always required to verify if the level of gray values and the related variations are in acceptable ranges.

Anyway, one should keep in mind that the maximal value is fixed by the solubility of the resazurin, estimated around 1 g L^{-1} in the aqueous solution.

In Table 2-1, the previous works using the RZ colorimetric technique are listed, as well as the related experimental devices and conditions.

Table 2-1 List of the works applying in the resazurin-based colorimetric methods, and details on the conditions in which they were implemented (* represents the case without considering purity).

References	[RZ], $g\ L^{-1}$	[NaOH], $g\ L^{-1}$	[GL], $g\ L^{-1}$	Experimental device	Camera parameters
Dietrich et al. (2013a)	0.10^{*}	20	20	Square PMMA milli-channel (2×2mm)	APX Photron, 10 bits, 2000 fps, 20 μm per pixel
Kherbeche et al. (2013)	0.10^{*}	20	20	Hele-Shaw PMMA cell with 2mm depth	Photron SA3, 2000fps
Yang et al. (2016b)	1^{*}	30	30	Square PMMA milli-channel (0.5×0.5mm)	Photron SA3, 8 bits, 4000fps, 10 μm per pixel
Yang et al. (2017a)	0.10^{*}	20	20	Meandering square PMMA milli-channel (2×2mm)	Photron SA3, 8 bits, 2000fps, 20 μm per pixel
Kováts et al. (2018)	$(4.35 \times 10^{-2})^{*}$	9.6	17.4	Helical glass pipe (D_{inner}=6mm)	High speed camera imager Pro HS 4M, 12 bits, 100fps, 2016×2016 pixels (11×11 μm)

Dietrich and Hebrard (2018)	0.10*	20	20	Bubble column (100×100×300 mm)	CCD color camera (Guppy Pro, 8 bits, 1024×1024 pixels, 23 μm per pixel)
Felis et al. (2018)	0.10*	20	20	Thin-gap cell (1×200×400mm)	sCMOS PCO Edge, 16 bits, 2560×2160 pixels,
Dietrich et al. (2019)	0.1167*	20	20	Glass bubble column (0.045 m in diameter, 0.40 m high, 0.23 m height of liquid)	high-speed monochromatic camera (Miro-M110)
Kherbeche et al. (2019)	0.10 (0.08 considering purity)	20	20	Hele-Shaw PMMA cell of 3mm depth with inclined wall inside	Color image (Basler acA1920-15Ouc, 8 bits, 1344×1024 pixels, 77 μm per pixel)
Mei et al. (2020a) and Mei et al. (2020b)	0.125 (0.105 considering purity)	20	20	In-plane spiral-shaped FEP milli-tube (d_{it}=1mm)	sCMOS PCO Edge camera (16 bits, 2560×2160 pixels, 54 μm per pixel)
Liu et al. (2020)	0.30*	20	20	Rectangular glass meandering microchannel (600×300 μm)	High speed CMOS camera (phantom M310, 17.6 μm per pixel, 12 bits)
Yang et al. (2020)	0.10*	20	20	PMMA square milli-channel (2×2 mm)	High speed CMOS camera (phantom M310,200fps, 10.5μm per pixel)

It can be seen from Table 2-1 that, depending on the observation depths and the bits numbers of the camera, the chosen RZ concentration varies. Generally, when the observing depth is at 1-3 mm, the RZ concentration could be at about 0.1 $g\ L^{-1}$, whereas when the depth of the observing channel is tiny (i.e., at several hundreds of micro-meters), such as the cases in Yang et al. (2016b) and Liu et al. (2020), increasing the RZ concentration is recommended to achieve a high signal quality. Furthermore, the bits number of the camera controls the dynamic ranges of the gray level scales (e.g., n bits → 2^n levels, leading to 8 bits → 256 levels; 12 bits → 4096 levels; 16 bits → 65536 levels). It is important to keep in mind that, if the RZ concentration is too high (leading to highly pink images), the corresponding gray level value will be very low, and even close to the ones related to the black-out images (without backlight, gray level value approaches to 0). In this case, the noises and uncertainties caused by camera itself will be relatively high, which should be avoided.

In this thesis, the tube or channel depth ranges between 1 and 2 mm. Therefore, the initial RZ concentration could be chosen at 0.1 $g\ L^{-1}$ and will be adjusted according to the camera properties and the imaging system. By default, the concentrations of D-glucose anhydrous (Sigma Aldrich, CAS 50-99-7) and sodium hydroxide (Sigma Aldrich, CAS 1310-73-2) were fixed equal to 20 $g\ L^{-1}$. All the products were purchased and directly used without any further purification. Note that the purity of the RZ dye should be considered later when calculating the mass transfer characteristics, as further indicated in subsequent sections.

The procedure for preparing aqueous colorimetric solution (noted RGN, i.e., Resazurin, Glucose and NaOH) is reported in Fig. 2-2. The first step (1) consists of preparing a highly concentrated mother solution of RZ. To make sure that the resazurin powder is perfectly dissolved in the deionized water, the RZ solution is mixed using a magnetic stirrer for one hour. If the RZ is still not perfectly dissolved, an ultrasonic bath can be used in addition. Note that this

mother solution should be prepared freshly and used on the same day. Then (step 2), the NaOH pellets are weighted, added to the deionized water, and fully mixed using a magnetic stirrer for 10 minutes. After (step 3), the glucose powder is weighted, added to the deionized water, and mixed for 10 minutes. Finally (step 4), an ad hoc volume of the mother solution of RZ is added to the prepared aqueous solution of glucose and NaOH solution, this volume being chosen to achieve the desired RZ concentration. After mixing, RZ is irreversibly converted to RF and further reversibly to DH.

One can then observe near the surface of the RGN colorimetric solution, the appearance of the pink color which results from the oxidation reaction that happens between DH and O_2. While at the bottom of the solution bulk, the solution remains almost colorless due to the lack of oxygen (the diffusion of the oxygen from the surface being a very low process). Therefore, two color states of the prepared colorimetric solution can exist:

- If the solution is vigorously shaken or continuously injected with O_2, then the solution will remain pink (RF) color.
- If the solution is sealed with a water-tight stopper and keep stagnant, then the solution will appear colorless (DH).

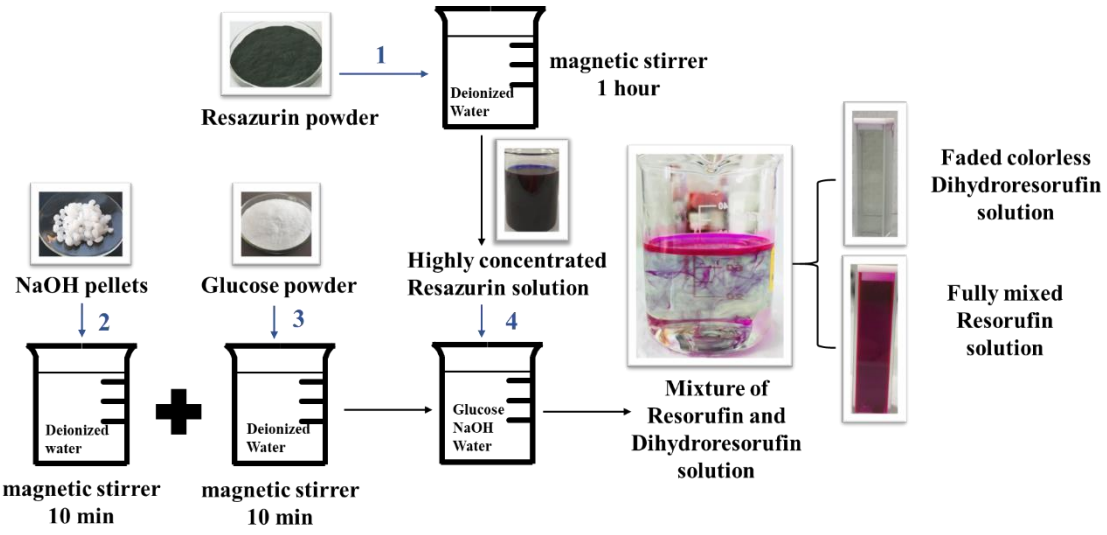

Fig. 2-2 Procedure for preparing the RGN colorimetric solution.

However, some unwanted side reactions can arise once the dye solution was prepared. After about one to two hours, a yellow color (instead of colorless) can appear, as shown in Fig. 2-3 (a). It is probably due to the deprotonation of the glucose (Badreddine et al., 2015) or subsequent oxidation of glucose or auto-oxidation of the glucose (Pons et al., 2002; Pons et al., 2004). Glucose in alkaline solutions may undergo several reactions, which depended on the pH, the temperature and the fraction of glucose in the form of alkali salt (Shaffer and Friedemann, 1930; Plunkett and Evans, 1938). The complex possibilities of producing acids (e.g., saccharinic acid and lactic acid) and autoxidation followed by condensation, which led to colored species. To prevent unwanted side reactions, it is absolutely required to freshly prepare the solutions and use them before the appearance of yellow color.

Fig. 2-3 Illustration of the yellow color in RGN colorimetric solution that can appear several hours after the solution preparation.

2.1.3 Absorption spectra of resazurin and resorufin

In this section, the absorption spectra of the RZ and RF are presented, as well as the variation of the absorbance with time occurring during the oxidation reaction. The aqueous solutions of RF were prepared according to the procedure from Fig. 2-2. Note that, for the aqueous solutions of RZ, neither glucose nor NaOH was added.

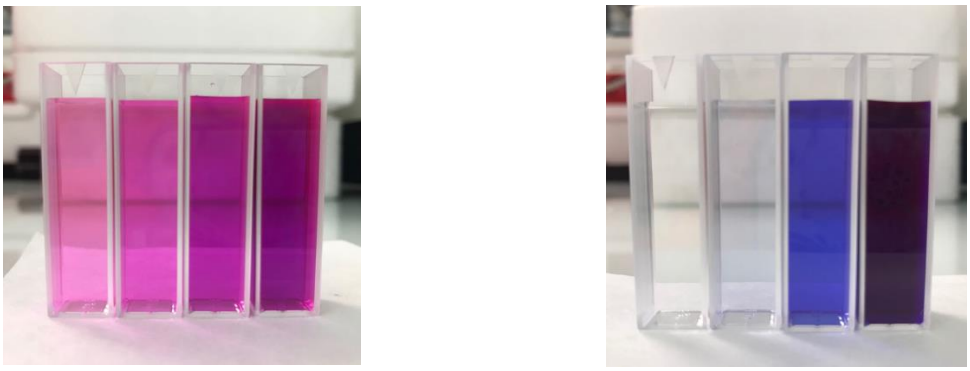

(a) (b)

Fig. 2-4 Aqueous solutions of (a) RF and (b) RZ in the cuvette at different concentrations.

The absorption spectra of RZ and RF were measured by a Jasco V-630 spectrophotometer. Various concentrations of RF (see Fig. 2-4 (a)) and RZ (see Fig. 2-4 (b)) were prepared.

Fig. 2-5 presents the measured absorption spectra for RF with 0.10×10^{-4}, 0.20×10^{-4} and 0.41×10^{-4} $mol\ L^{-1}$ and RZ with 4.36×10^{-7} and 4.36×10^{-6} $mol\ L^{-1}$. It can be observed that the maximal absorption peaks of RF and RZ solutions were in the visible domain, around 570 nm and 600 nm respectively, which was consistent with the values reported in the literature (Perrot et al., 2003; Zrimšek et al., 2004; Doneux et al., 2016). When the absorbance values A of RZ and RF were below 2, the values of A logically increased with the increase of the RZ and RF concentrations according to the same multiple rates of their concentrations.

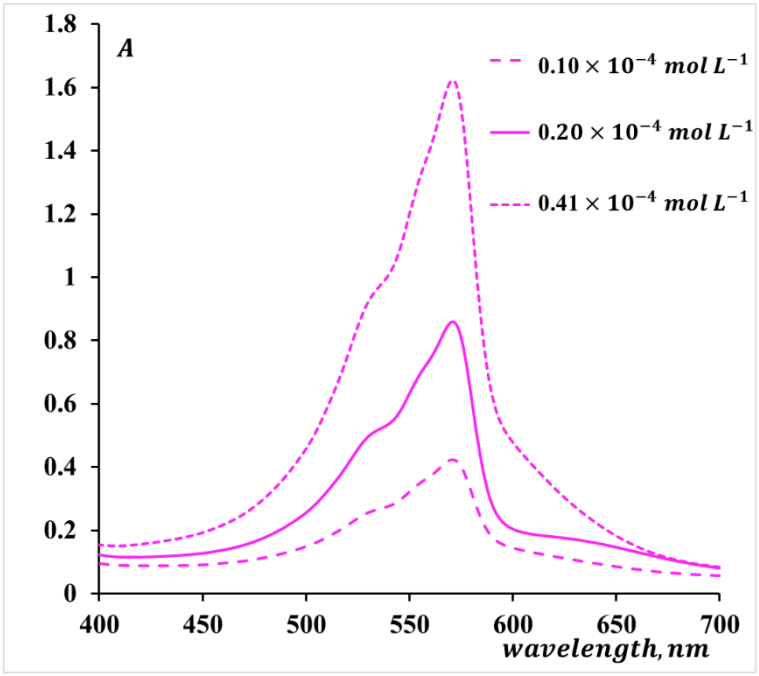

(a)

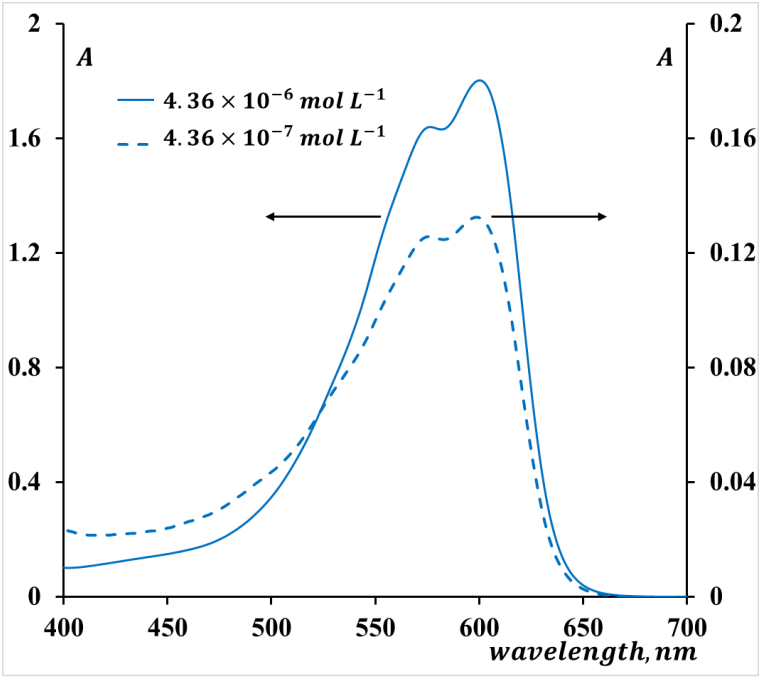

(b)

Fig. 2-5 Absorbance spectra of different (a) RF and (b) RZ solutions.

The reduction reaction of RF into DH (i.e., the back reaction from pink to colorless) was further investigated. The objective is to quantify the characteristic time required to fully convert RF into DH. This can be accurately done by spectroscopic measurements, which enabled to monitor the variation of

absorbance with time at the peak wavelength of RF absorbance (i.e., 570 nm). Once the RZ solution was prepared, a continuous injection of air gas was made to turn the initial solution of DH into RF solution. Then, the oxygen-saturated solution of RF was immediately poured into a spectrophotometric cuvette, and a PTFE cover was put on the cuvette to prevent further oxidation with ambient air at the free surface. For these experiments, the concentration of RZ was fixed at 0.1 g L^{-1} (0.093 g L^{-1} considering purity), and the concentrations of NaOH and GL were varied to study their effects on the reduction reaction from RF to DH, as shown in Table 2-2.

Table 2-2 Study of the back reaction from RZ into DH: various entries corresponding to different concentrations of NaOH and GL ([RZ] = 0.1 g L^{-1} for all entries).

Entry	[NaOH], $g\ L^{-1}$	[GL], $g\ L^{-1}$
a	20	20
b	10	20
c	2	20
d	4	4
e	20	10
f	10	25
g	10	10
h	10	5

The temporal variations of the absorbance at 570 nm are presented in Fig. 2-6 (the time interval between spectra acquisition was 10 seconds). It continuously decreased until reaching a plateau after a few hundred seconds or even longer, depending on the concentrations of GL and NaOH.

At [GL] = 20 $g\ L^{-1}$ for entries a, b, and c, one can observe that an increase of [NaOH] accelerated the reduction reaction rates, leading to the characteristic times varied from 15 000 s (about 4 hours) to 200 s.

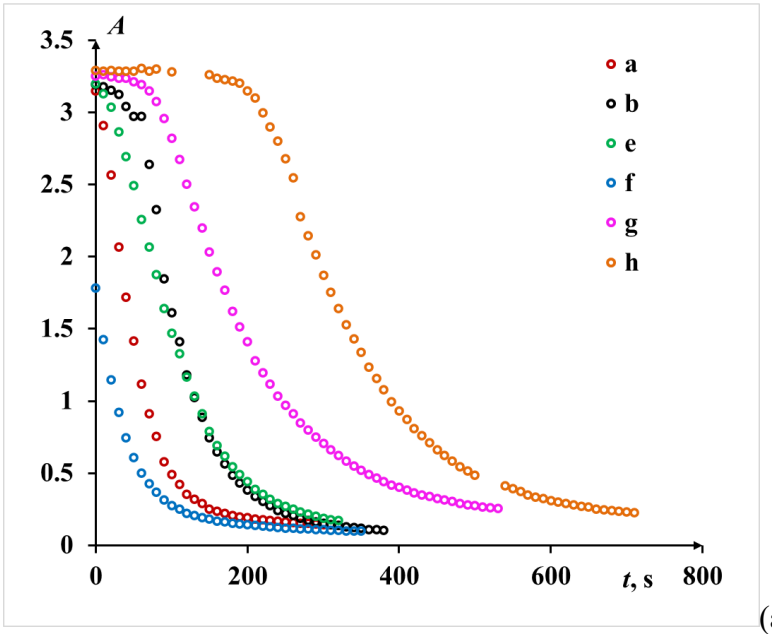

(a)

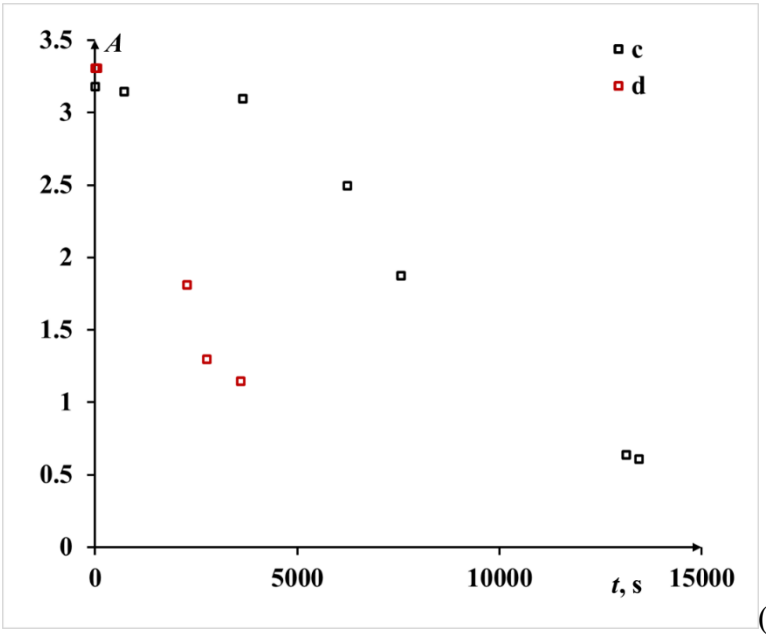

(b)

Fig. 2-6 Variation of the absorbance *A* with time for various concentrations of NaOH and GL at 570 nm wavelength: (a) entries a, b, e, f, g, and h, (b) entries c and d.

For entries g and h in Fig. 2-6, it is interesting to note that an initial plateau was present. This can be explained by the fact that, during this period, some oxygen molecules still appeared in the solution and reacted with DH to form RF, and as the oxidation reaction rates was faster than the reduction one, the absorbance *A* remained constant. After several times, when the dissolved O_2 was

exhausted, the oxidation of DH stopped, and the reduction of RF took place, resulting in a decrease of absorbance.

For entries c and d in Fig. 2-6, it is seen that small values of [NaOH] and [GL] induced extremely slow kinetic rates.

At [NaOH] =10 $g\ L^{-1}$ for entries f, g, and h, and [NaOH] = 20 $g\ L^{-1}$ for entries a and e, an increase of [GL] accelerated the reduction reaction rates and decreased the duration of the initial plateau.

One should note that, for all entries, the solutions were too concentrated in terms of the resorufin concentrations, leading to the saturation of the absorbance measured by the spectrophotometer.

Further studies need to be implemented to accurately study the kinetics of this reduction reaction. However, one can keep in mind that the characteristic time of the oxidation reaction (from DH to RF) was around 7.2 ms when [GL] and [NaOH] were at 20 g L^{-1}, as shown by Yang et al. (2016a), and was thus far smaller (28 times) than the characteristic time of the back-reduction reaction, which was around 200 s (see entry a) with identical reactant concentrations.

In the subsequent experiments, the concentrations of NaOH and glucose were fixed at 20 g L^{-1}.

2.2 Experimental setups and flow materials

In this study, two types of experimental setups were used: (1) in-plane spiral-shaped milli-reactor, and (2) straight milli-channel with a cross-junction. They are described in the following sections.

2.2.1 In-plane spiral-shaped milli-reactor

Experimental setup

The experimental setup is shown in 错误!未找到引用源。. The in-plane spiral-shaped milli-reactor consisted of a circular Fluorinated Ethylene Propylene (FEP) tube, inserted inside a square channel carved into a flat Poly-Methyl-Methacrylate (PMMA) plate (200×200×20mm^3) and wound according to an Archimedean spiral geometry. The inner and outer diameters of the FEP tube (reference: 1675L, Cluzeau Info Labo®, France) were 1 and 3 mm, respectively. This experimental setup is located at the Laboratoire de Génie Chimique (LGC, UMR 5503), in the building of the ENSIACET school.

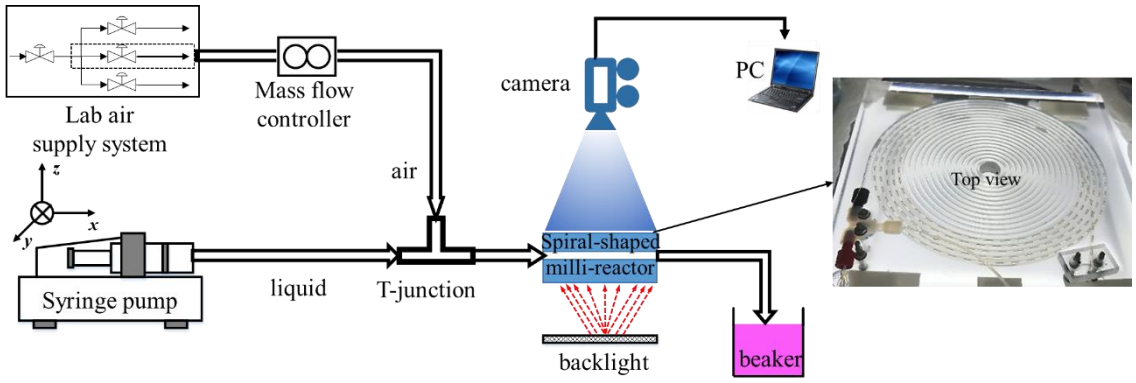

Fig. 2-7 Schematic diagram of the experimental setup for the in-plane spiral-shaped milli-reactor.

The geometrical parameters of the Archimedean spiral are illustrated in Table 2-3 and in Fig. 2-8 (a).

Table 2-3 Geometrical parameters related to the Archimedean spiral.

Spiral shape	D_{SR}, mm	n_{SR}	P_{SR}, mm	L_{SR}, mm
Milli-reactor	5	19.25	4	2.95

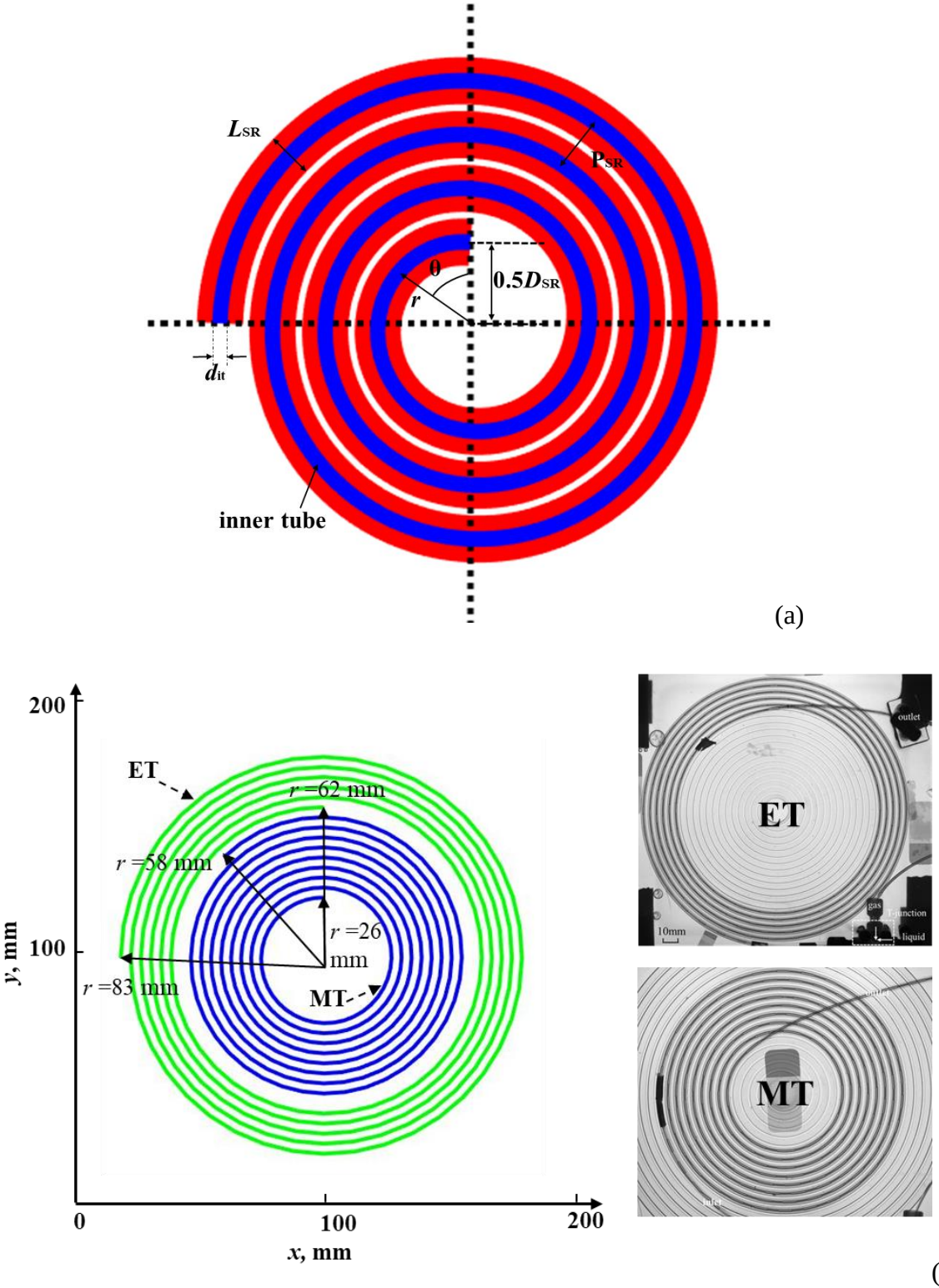

Fig. 2-8 (a) Geometrical parameters of the spiral-shaped milli-reactor, D_{SR}, L_{SR}, P_{SR} and d_{it} are initial diameter, sectional distance, pitch distance and inner diameter of the tube, respectively. (b) Representation of the two tubing configurations (ET and MT are Exterior Tubing and Medium Tubing) and images showing aqueous solution flowing in two tubing configurations.

In polar coordinates, the Archimedean spiral could be described by:

$$r = C_1 + C_2\theta \tag{2-1}$$

where r (mm) and θ (rad) were the radial coordinate and the angular coordinate, and the coefficients C_1 and C_2 were equal to 5 mm and $2/\pi$ mm rad^{-1}, respectively.

To study the effect of the centrifugal force on the gas-liquid hydrodynamics and mass transfer, two configurations of tubing with identical lengths (~3m) were investigated in this study, defined according to their wound positions on the plate. In this way, the intensity of the centrifugal forces could be changed while keeping the intensity of inertial force constant. As shown in Fig. 2-8 (b), the first configuration corresponded to a tube wound from the 1st to the 6th spiral circles (named Exterior Tube and noted ET) and the second one related to a tube wound from the 7th to 15th spiral circles (named Medium Tube and noted MT). Their exact lengths (L_R) were 2.97 m and 2.90 m, respectively.

The relative predominance of the centrifugal forces with respect to the inertial forces was expressed by the Dean number:

$$\mathrm{De} = \mathrm{Re}\sqrt{\frac{1}{\lambda}} \tag{2-2}$$

where λ referred to the curvature ratio, $\lambda = 2r / d_{it}$, which depended on the spiral radial radius, r, and on the inner diameter of the tube d_{it}. The Reynolds number, Re, was defined as:

$$\mathrm{Re} = \frac{\rho_L \times d_{it} \times j_{TP}}{\mu_L} \tag{2-3}$$

where j_{TP} was the two-phase superficial velocity ($j_{TP} = j_L + j_G$), ρ_L and μ_L the density and dynamic viscosity of liquid, respectively.

In the experiments, the curvature ratio, λ, ranged from 124 to 166 for the ET configuration and from 52 to 116 for the MT configuration, corresponding to radial coordinates, *r*, from 62 mm to 83 mm for ET and from 26 mm to 58 mm for MT. Then, the associated average curvature ratios, ⟨λ⟩, for ET and MT were 145 and 84, respectively. From ⟨λ⟩ and at various Reynolds numbers, the average Dean number, ⟨De⟩, was calculated for each operating condition, as reported in Appendix 1 (Table A 1-1 and Table A 1-2).

During the experiments, the entire milli-reactor was put into a glass tank filled with water to avoid optical distortion (the refractive index of FEP material being 1.34 (Hosoda et al., 2014), so almost equal to the value at 1.33 of water).

Flow control equipment

Air was used as the gas phase and was fed in using laboratory compressed air pipelines, the air flow rates being controlled by a Horibastec airflow controller (Model: SEC-Z512MGX or SEC-7320). The tube outlet was at atmospheric pressure (no counter-pressure valve was used). The liquid phase was pumped by a neMESYS syringe pump (Model: NEM-B100-01 A) equipped with a 100 mL Harvard Instruments syringe and the liquid flow rates were regulated by a mass flow control system (Model: NEM-B100-01 A). Liquid flow rates, Q_L, ranged from 0.85 to 3.40 mL min^{-1} and gas flow rates, Q_{G0} (Q_{G0} was calculated at the inlet conditions and calibrated by the temperatures and pressures), from 0.39 to 8.33 mL min^{-1}. The associated liquid and gas superficial velocities, noted j_L ($j_L = Q_L/\Omega$, Ω is the cross-sectional area) and j_{G0} ($j_{G0} = Q_{G0}/\Omega$), respectively, were defined from 1.8 to 7.2 cm s^{-1} and 0.8 to 17.7 cm s^{-1}. The gas-liquid superficial velocity ratio, η_0 (($\eta_0 = j_{G0} / j_L$, corresponding to the inlet conditions), varied between 0.13 and 9.52. After changing the gas and liquid flow rates, it was necessary to wait two or three times the residence time (up to 2 minutes) to

achieve stable, steady two-phase flow (the residence time was approximately equal to the ratio between the tube length L_R and the total two-phase superficial velocities j_{TP}).

Fluid properties

All the experiments were performed at atmospheric pressure (1.013×10^5 Pa) and room temperature (293.15 K). The liquid phase consisted of solutions containing D-glucose anhydrous (Fischer-Scientific, CAS 50-99-7), sodium hydroxide (VWR, CAS 1310-73-2) and resazurin (Sigma Aldrich, CAS 62758-13-8, purity 84%). The D-glucose anhydrous and sodium hydroxide were both diluted at 20 g L^{-1} in deionized water while the concentration of resazurin was equal to 0.105 g L^{-1} (considering purity, chosen after some preliminary tests). Therefore, a maximal oxygen concentration that could be characterized by the resazurin was equal to 7.3 mg L^{-1}, calculated as Eq. (2-4)).

$$C_{max} = \frac{[RZ]\cdot M_{O_2}}{2\cdot M_{RZ}} \quad (2\text{-}4)$$

where M_{O2} and M_{RZ} were the molar masses of O_2 and resazurin, respectively. [RZ] was the mass concentration of resazurin, in mg L^{-1}.

The physical-chemical properties of the solutions measured by Dietrich et al. (2013a) and Yang et al. (2017a) at a slightly lower concentration (0.117 g L^{-1}) were considered in this study at the atmosphere pressure and room temperature (293.15 K), and listed in Table 2-4. The contact angle of the prepared solution on the FEP tubing material was measured by a Drop shape analyzer-DSA100 (Krüss) at room temperature (293.15 K), as shown in Appendix 2. A value of 98.7 ± 0.4°was found, which was in agreement with the contact angle of 106° reported by (Barajas and Panton, 1993) for deionized water on FEP material. This

confirmed that the FEP tube remained hydrophobic with respect to the resazurin solutions.

Table 2-4 Physical properties of the fluid used in the in-plane spiral-shaped milli-reactor, C_{max} represents the maximum oxygen concentration which could be characterised by resazurin dye according the stoichiometry relations, calculated by Eq. (2-4).

Fluid	Concentration, (g L^{-1})	Density, (kg m^{-3})	Viscosity, (mPa s)	Surface tension, (mN m^{-1})	C_{max} (mg L^{-1})
Liquid (RZ, GL, NaOH)	RZ: 0.105 GL:20 NaOH:20	1004.5	1.118	75	7.3
Air (21% oxygen)	\	1.21	1.79×10^{-2}	\	\

2.2.2 Straight milli-channel with a cross-junction

Experimental setup

The experimental setup is illustrated in Fig. 2-9 (a). The device was fabricated in a transparent polymethylmethacrylate (PMMA) plate ($100\times600\times2mm^3$) and sandwiched by other two PMMA plates ($100\times600\times4mm^3$) with screws and sealing rings. The contacting geometry to generate bubbles is a cross-junction, in which the two fluids merged in a cross where the gas was flowing in the main channel and the liquid was supplied with two orthogonal channels, with the same width as the main channel, to squeeze the bubbles. All the channels, including the injection inlets of gas and liquid, and the main channel, were designed with the same square cross sections ($w^2 \cong 2\times2$ mm^2). The dimensions of the square channel deviated from 2 mm due to the manufacturing

precision and mounting deformation of the channel. For this reason, the exact dimensions of the channels will be calibrated firstly (see Appendix 3). The length of the gas inlet, liquid inlet, and main channels were 30 mm, 45 mm, and 550 mm, respectively.

With the help of sliding support design, the camera could be horizontally changed to different region-of-interest (ROI) positions (see Fig. 2-9 (b)), in order to investigate the mass transfer during the bubble formation stage, and during the bubble flowing stage, respectively. Some of the observing positions (from X_6 to X_{11}) were specially selected to maintain same flowing time under various operating flow rates (Q_{TP}: from 60 to 160 mL min^{-1}). Note here that the observing position X represented the beginning position of the ROI window.

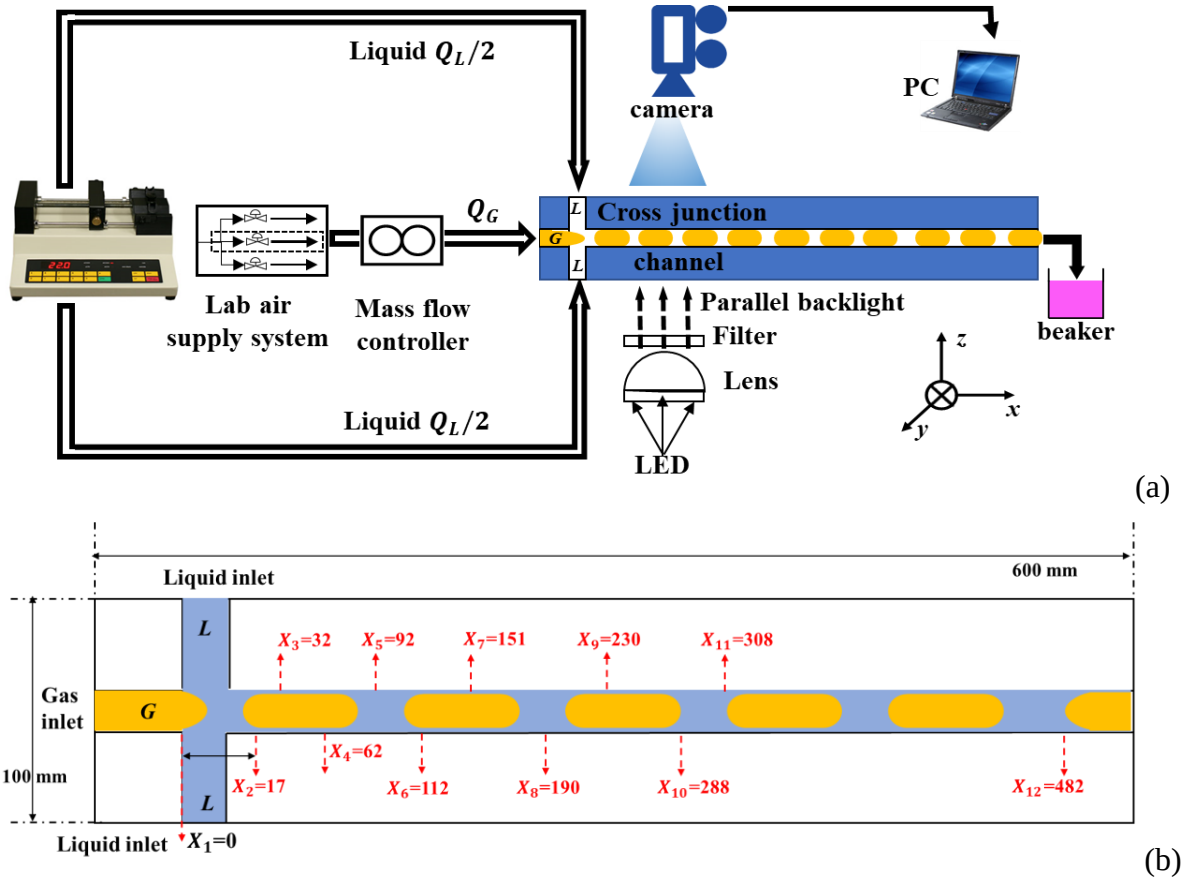

Fig. 2-9 (a) Schematic representations of the experimental setup. (b) Geometry of the straight milli-channel with a cross-junction. The 12 axial positions, X (expressed in mm), showing the region-of-interest (ROI), are marked by the red arrows. At $X = 0$, the two phases enter in contact.

This experimental setup is located at the Toulouse Biotechnology Institute (TBI UMR INSA/CNRS 5504; INSA/INRA 792), on the campus of the INSA school.

Flow control equipment

Air, as gas phase, was fed from house compressed air lines and the flow rate was controlled by a DPC17S-V0L6-BB5 airflow controller (calibrated under 101.4 kPa and 21.1 °C). Liquid solutions were both supplied from a 60 mL syringe in a syringe pump (Harvard Apparatus, PHD 22/2000, USA). The gas was introduced to the main channel and the liquid was injected from two side channels at the same flow rates ($Q_L/2$). After changing to a new flow rate condition, at least two times of residence time (up to 4 seconds) of milli-channel were assured to reach a steady gas-liquid flow, which was verified by the camera through the bubble and liquid slug length.

Table 2-5 Physical properties of the fluid used in the straight milli-channel with a cross-junction, C_{max} represents the maximum oxygen concentration which could be characterised by resazurin dye according the stoichiometry relations, calculated by Eq. (2-4).

Fluid	Concentration, ($g\ L^{-1}$)	Density, ($kg\ m^{-3}$)	Viscosity, (mPa s)	Surface tension, ($mN\ m^{-1}$)	C_{max} ($mg\ L^{-1}$)
Liquid (RZ, GL, NaOH)	RZ: 0.074 GL:20 NaOH:20	1004.5	1.118	75	5.2
Air (21% oxygen)	\	1.21	1.79×10^{-2}	\	\

Fluid properties

The liquid phase was composed of D-glucose anhydrous (Sigma Aldrich, CAS 50-99-7) at a concentration of 20 $g\ L^{-1}$, sodium hydroxide (Sigma Aldrich, CAS 1310-73-2) at a concentration of 20 $g\ L^{-1}$, and resazurin (Sigma Aldrich, CAS 199303, purity 93%) at a concentration of 0.074 $g\ L^{-1}$ (considering purity, and corresponding to a maximal concentration of oxygen that could be consumed equal to 5.2 mg L^{-1}). Table 2-5 presents the physical properties of the fluids used in the straight milli-channel at the atmosphere pressure and room temperature (293.15 K). All experiments were conducted under atmospheric pressure (no counter-pressure valve was used at the outlet of the channel) and at room temperature (around 20° C), with several conditions of Reynolds, Capillary and Weber numbers.

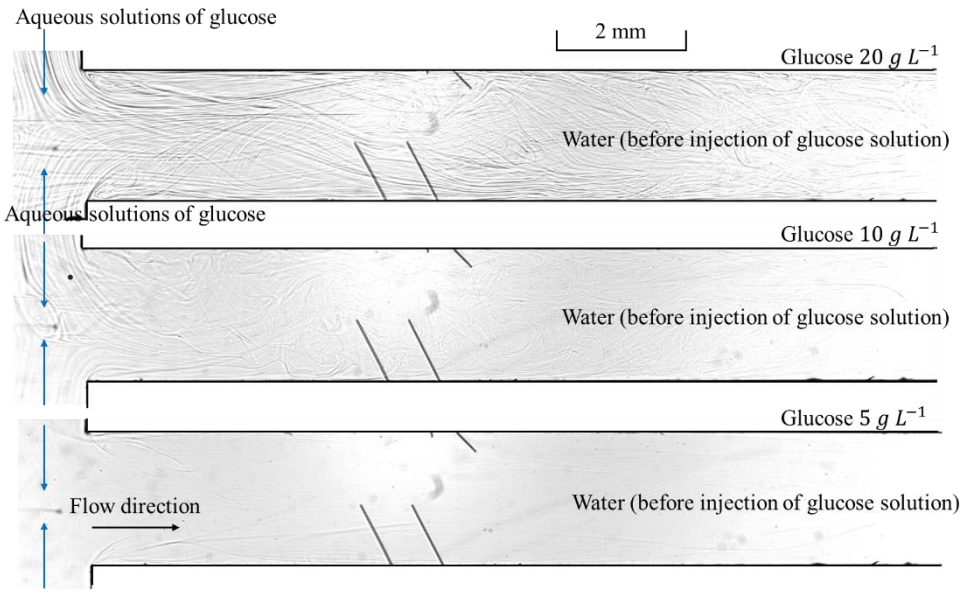

Fig. 2-10 Illustration of the mixing between aqueous solutions of glucose and dionized water at the cross-junction under different concentrations of glucose.

As illustration, Fig. 2-10 shows how the mixing between the aqueous solution of glucose and water occurred at the cross-junction, depending on the

concentrations of glucose. This phenomenon could be easily visualized because the fluid density and refraction index were different between the aqueous solution of glucose and water. However, for the mass transfer experiments (requiring to add resazurin), this distortion of the gray value was undesired and needed to be prevented. Therefore, before injecting the colorless solution of DH into the cross-junction channel, an aqueous solution of GL and NaOH solution having the same concentrations as the ones in the solution of DH (i.e., 20 g L^{-1}) was systematically injected and filled into the channel first. By this way, the optical distortion as visualized in Fig. 2-10 could be avoided.

2.3 Image acquisition and image processing

2.3.1 In-plane spiral-shaped milli-reactor

The gas-liquid hydrodynamics inside the in-plane spiral-shaped milli-reactor was investigated by using an imaging system. The tube was lit by a Phlox-LedW-BL LED (Light-emitting diode) backlight (300×220 mm^2) and the images of the bubbles flowing along the tube were recorded by a 16-bit sCMOS PCO Edge camera. The acquisition time (i.e., the time interval between two consecutive images) was fixed at 0.02 s and the exposure time was 0.5 ms. The image resolution was 2560×2160 px^2. The camera was equipped with a Nikon AF micro Nikkor f/2.8 lens (50 mm for ET and 60 mm for MT). The regions of interest were dependent on the configurations, 197.99×167.05 mm^2 (ET) and 138.53×116.75 mm^2 (MT), so 77.3 μm (ET) and 54.0 μm (MT) for one pixel respectively.

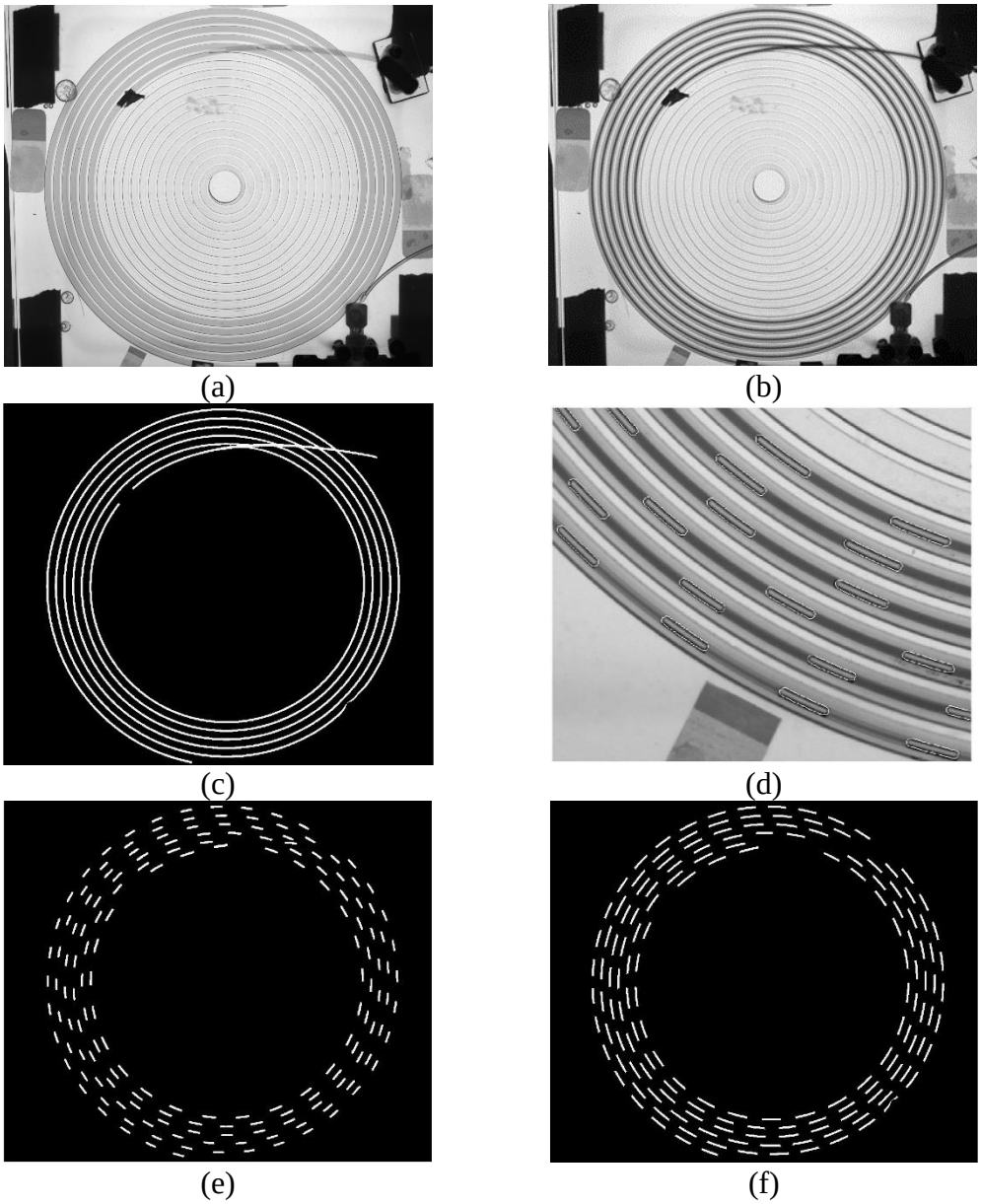

Fig. 2-11 Sequences of image processing implemented in the case of the in-plane spiral-shaped milli-reactor: (a) raw image of the tube filled with colorless solution without resazurin. (b) Raw image of the tube filled with saturated oxygen solution with resazurin (pink). (c) Inner-tube mask. (d) Comparison of extracted bubble edges overlapping the original image (white line represents extracted bubble edge). (e) Detection of bubbles. (f) Detection of liquid slugs. Operating condition: $j_G = 0.9$ cm s^{-1} and $j_L = 1.8$ cm s^{-1} in the ET configuration.

Before the T-junction (ref. P-633-01 from Info Labo®; inner diameter of 1.25 mm), the inner diameters of the gas and the liquid inlet tubing were 0.5 and 1 mm. After the T-junction where the bubbles were generated (see 错误!未找到

引用源。 (b)), the gas-liquid flow was recorded over a large range of axial locations, noted *X*, from 0.25 to 2.50 m (ET and MT). Note that $X = 0$ represented the bubble formation point (i.e., T-junction). A typical raw image of the gas-liquid flow in ET is shown in 错误!未找到引用源。 (b).

To extract the hydrodynamic parameters (bubble and liquid lengths, bubble velocity and void fraction, etc.) from the raw image, an image post-treatment algorithm was implemented in Matlab® software (R2017b). First, two groups of background images were acquired: in the first one, shown in Fig. 2-11 (a), the tube was filled with the solution without resazurin (colorless) and, in the second one, shown in Fig. 2-11 (b), with the solution with resazurin and previously saturated with oxygen (pink color). Then, the background division approach was used to extract the inner tube from the background. The tube mask image was obtained by dividing the background image when the tube was filled with saturated dye solution (Fig. 2-11 (b)), by the one filled with colorless solution (Fig. 2-11 (a)). By subtracting this inner-tube mask (Fig. 2-11 (c)) from the raw image, only gas-liquid flow inside the tube would be accurately extracted on the image and other noises outside the tube were efficiently eliminated.

Gas bubble detection was generated by combining the multilevel threshold based on Otsu's method (Otsu, 1979) and Canny edge detection. Taking advantage of the significant difference between the gray intensities in the bubble inner part (high) and in the liquid slug part (low), the multilevel threshold was first applied to obtain a bubble mask. This resulted in all the bubbles being extracted on the image, and roughly eliminated the liquid part. Then the Canny edge detection method was further used to accurately extract bubble edges.

Fig. 2-11 (d) presents an example of the extracted bubble edges (white) superimposed on the original raw image, demonstrating a good accuracy and efficiency of this method. Then, the liquid slug image (Fig. 2-11 (f)) was acquired by subtracting the bubble image from the tube mask (Fig. 2-11 (c)). This image

processing made it possible to accurately detect all the bubbles and liquid slugs inside the tube, as displayed in Fig. 2-11 (e) and (f) respectively. The general Matlab codes for the image processing in the in-plane spiral-shaped milli-reactor were described in Appendix 4.

2.3.2 Straight milli-channel with a cross-junction

The gas-liquid flows were lighted by a M530L4 LED (Light-emitting diode, bandwidth at 35 nm) and images were recorded by a Basler acA1920-155μm camera (1920×1200 pixels, 12 bits) equipped with a 50 mm 1:1.4 Nikkor lens. This 530nm wavelength of green LED was chosen in accordance with the absorption spectra of resorufin, which presented high absorbance near 530nm (see Fig. 2-5 (a)). The LED was equipped to an aspheric condenser lens (ACL5040U-A, ϕ 50 mm) to generate parallel light beam and a NE2R10A absorptive ND filter was added to increase the LED intensity stability. The camera was set to work at a recording rate of 400 fps (i.e., acquisition time at 2.5 ms) with an exposure time of 22 μs. The spatial resolution of the images was at 8.25 μm per pixel. A unique region-of-interest (ROI) window with the size of 1900×305 pixels (15.7×2.5 mm^2) was used for all observing positions along the channel.

By applying the procedures of image processing described in section 2.3.1, bubbles and liquid slugs could be detected, as shown in Fig. 2-12. The general Matlab codes for the image processing in the straight milli-channel with a cross-junction were described in Appendix 4.

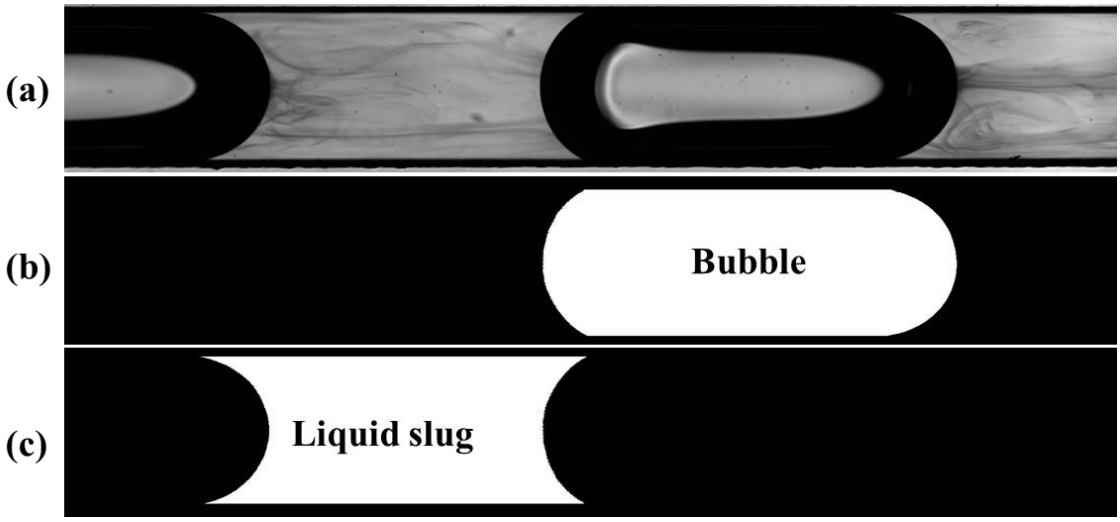

Fig. 2-12 Sequences of image processing implemented in the case of the straight milli-channel with a cross-junction: (a) raw image of Taylor flow (air and RGN colorimetric solution). (b) Detection of the bubble. (c) Detection of the liquid slug. Operating condition: j_G = 14.3 cm s^{-1} and j_L = 14.3 cm s^{-1}.

2.3.3 Comparison of the image acquisition conditions

To conclude, Table 2-6 summarizes the image acquisition system and operating conditions for the two setups implemented in this work, namely the in-plane spiral-shaped milli-reactor in section 2.3.1 and the straight milli-channel with a cross-junction in section 2.3.2.

The image acquisition system in the straight milli-channel with a cross-junction was improved in two aspects.

- First, magnification was improved in terms of the resolution, so that more details could be detected, and the LED light with a spheric condenser lens also improved the image contrast.
- Secondly, a monochromatic light (i.e., green diode) was implemented to illuminate the setup instead of the polychromatic light (i.e., Phlox-LedW-BL LED backlight).

The last improvement made possible to verify the Beer-Lambert law (see Eq. (6-1) and Eq. (A 3-1)) for the calibration between the equivalent oxygen

concentration and the absorbance of resorufin. Indeed, the Beer-Lambert law, describing the exponentional attenuation of light along the light penetration depth, can be theoretically applied only at given specific wavelength since the molar attenuation coefficient varied at different wavelengths. However, it is also worth noting that the application of the Beer-Lambert law also assumed that the concentration of the dissolved species inside the illuminated volume considered was homogeneous. In the setups investigated in this theis, this condition could not be always verified which clearly induced some limitations and/or imposed caution in the result analysis when applying the present colorimetric method.

Table 2-6 Comparison of the image acquisition system and operating conditions in the in-plane spiral-shaped milli-reactor and the straight milli-channel with a cross-junction.

Contents	In-plane spiral-shaped milli-reactor	Straight milli-channel with a cross-junction
Backlight	Phlox-LedW-BL LED panel, polychromatic light	M530L4 LED with a NE2R10A absorptive ND filter, collimated monochromatic light (530nm)
Camera	sCMOS PCO Edge camera, resolution: 77.3 μm (ET) and 54.0 μm (MT) per pixel, 16-bit	Basler acA1920-155μm camera, resolution: 8.25 μm per pixel, 12-bit
Cross-sectional dimension	Circular tube (d_{it} = 1 mm)	Square channel ($w \approx 2$ mm)
Resazurin concentration	0.105 g L^{-1}	0.074 g L^{-1}

In addition, the concentration of RZ aqueous solution implemented in the straight milli-channel with a cross-section was slightly smaller than the one used for the spiral-shaped milli-reactor. It was logical since the depth of the straight channel was almost 2 times the one of the spiral-shaped tube (i.e., higher channel

depth needed less concentrated RZ concentration). This concentration was deduced after some preliminary tests which have showed that extremely low gray values of images (lower than 50, meaning high uncertainties) were achieved when higher concentration of RZ aqueous solution (i.e., [RZ] > 0.074 g L^{-1}) were injected into the channels, which should be avoided.

Chapter 3. Hydrodynamic of gas-liquid slug flows in a long, in-plane spiral-shaped milli-reactor

Abstract

In this chapter, the investigations of gas-liquid Taylor flows in an in-plane spiral-shaped milli-reactor with various tube curvature ratios ($52 < \lambda < 166$) are reported. Thanks to the compactness of the reactor and the use of an ad hoc imaging system and processing, the axial evolution of bubble lengths and velocities could be recorded and extracted along the whole reactor length (~ 3 m). The experimental results showed a significant linear increase of bubble length and velocity with axial position. Very long, stable Taylor bubbles (L_B/d_{it} up to 40) and liquid slugs were generated, probably due to the poor wettability of the tube surface. At identical inertial force (i.e., identical Reynolds number), a higher centrifugal force (i.e., lower tube curvature ratio) likely led to shorter Taylor bubble lengths while only slightly affecting the liquid slug lengths. The axial pressure drop could be estimated from the axial increase in bubble volume and compared with the measured pressure drop and the one predicted by the correlations from the literature. By considering both the friction and capillary pressure drops, it was observed that the predicted two-phase pressure drop was slightly dependent on the centrifugal force and that the capillary pressure drop, determined from the unit cell number, Capillary number and static contact angle, was dominant.

This chapter has been published as Mei, M., Felis, F., Hébrard, G., Dietrich, N., & Loubière, K. (2020). Hydrodynamics of gas–liquid slug flows in a long in-plane spiral-shaped milli-reactor. *Theoretical Foundations of Chemical Engineering*, *54*, 25-47.

Introduction

As reported in the Chapter 1 (section 1.2.3), the hydrodynamics characteristics of gas-liquid Taylor flow were affected by the bends or curved geometries of the channel, due to the secondary flows resulted from centrifugal force. This chapter will present the results in terms of gas-liquid hydrodynamics obtained in the long, in-plane, spiral-shaped millimetric reactor. With respect to the state-of-art, the main originality of this study is that the tubing curvature ratio changes continuously all along the channel, while remaining in the same plane. This structure was initially developed for organic photochemistry applications (Aillet et al., 2016; Loubière et al., 2017). Two different geometrical configurations were considered, each presenting a different range of curvature ratios.

Section 3.1 gives out the experimental setup and corresponding image processing for calculating gas-liquid hydrodynamics. Flow regimes and bubble shape will be first identified in section 3.2.1. Then, in section 3.2.2, the variation of the hydrodynamic characteristics (bubble and liquid slug lengths, and bubble velocities) along the axial position in the tube will be obtained and analyzed under various total gas-liquid superficial velocities, gas-liquid superficial velocity ratios, and curvature ratios. Section 3.2.3 and 3.2.4 will present the average hydrodynamic characteristics (e.g., average bubble and liquid slug lengths, and average bubble velocity). Section 3.2.5 will describe the unit cell lengths and the relative lengths of bubble. Finally, in section 3.2.6, the friction and capillary pressure drops will be compared with the measured pressure drop and correlations from literature.

3.1 Materials and methods

3.1.1 Experimental setup

The experimental setup, flow control equipment and fluid properties have been described in Chapter 2 (section 2.2.1).

3.1.2 Gas-liquid hydrodynamic characteristics

After detecting the bubble and liquid slug images (see Chapter 2, section 2.3.1.), an algorithm to extract the hydrodynamic characteristics for Taylor flows was compiled in Matlab® R2017b and the Image Processing Toolbox package (see Appendix 4). The characteristics concerned were bubble lengths, bubble velocities and liquid slug lengths averaged over the whole length of the spiral-shaped tube, $\langle L_B \rangle$ (mm), $\langle U_B \rangle$ (cm s^{-1}) and $\langle L_S \rangle$ (mm), together with their variations with the axial locations in the spiral-shaped tube, $L_B(X)$ (mm), $U_B(X)$ (cm s^{-1}) and $L_S(X)$ (mm).

A Taylor bubble or liquid slug inside the spiral tube was described by a "curved" cylinder, namely by a cylinder with a curve as its main axis (in opposition to cylinders with straight line axis), in agreement with the experimental observations (see section 3.1). The bubble and liquid slug lengths were calculated based on the hypothesis that the nose and tail of the curved bubble and liquid slug were flat and that the liquid film thickness is negligible.

Under these assumptions, as shown in Fig. 3-1, the bubble area could be deduced from the difference between the outer sector OM_1M_2, S_{outer}, and the inner sector OM_3M_4, S_{inner}, such as:

$$S_{\mathrm{inner,B}} = \frac{\theta}{2}\left(R - \frac{d_{\mathrm{it}}}{2}\right)^2 \qquad (3\text{-}1)$$

$$S_{\text{outer,B}} = \frac{\theta}{2}(R + \frac{d_{\text{it}}}{2})^2 \tag{3-2}$$

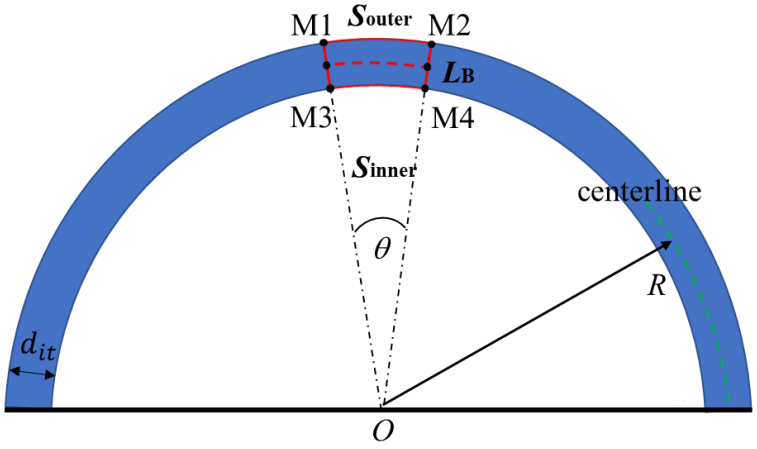

Fig. 3-1 Schematic diagram used to calculate the bubble and liquid slug lengths in the in-plane spiral-shaped milli-reactor.

Therefore, the two-dimensional bubble area on images, $S_{\text{B, 2D}}$, was given as below:

$$S_{\text{B,2D}} = A_{\text{outer,B}} - A_{\text{inner,B}} = Rd_{\text{it}}\theta \tag{3-3}$$

The bubble length, L_{B}, was defined according to:

$$L_B = R\theta \tag{3-4}$$

By combining Eqs. (3-3) and (3-4), one obtained:

$$L_{\text{B}} = \frac{S_{\text{B,2D}}}{d_{\text{it}}} \tag{3-5}$$

Similarly, the liquid slug length can also be deduced from the two-dimensional liquid slug area, $S_{\text{S, 2D}}$, and d_{it}, as:

$$L_S = \theta R = \frac{S_{\text{outer,S}} - S_{\text{inner,S}}}{d_{\text{it}}} = \frac{S_{\text{S,2D}}}{d_{\text{it}}} \quad (3\text{-}6)$$

It should, however, be noted that this calculation was valid only if the liquid film had negligible thickness. Based on the correlations proposed by Bretherton (1961), which were applied to small Capillary number (2×10^{-7} to 1×10^{-2}), the liquid film was found ranging from 3.5 and 15.8 μm thick in the present experiments, which could be considered as negligible (smaller than 2% of d_{it}). Note that, the minimum pixel resolution for images was 54 μm (5% of d_{it}), thus preventing these values being verified experimentally. This point will be further discussed in the subsequent section for pressure drop.

The average lengths of bubbles and liquid slugs, $\langle L_{\text{B}} \rangle$ and $\langle L_{\text{S}} \rangle$, were further averaged by considering the bubbles or liquid slugs detected in 50 images. The bubble velocity was calculated from the distance travelled by the bubble centroid between two consecutive images, divided by the acquisition time. To find the correct distance, the closest distance (5-250 pixels), calculated from the centroid's original position in the first frame to its moving position in the second frame, was used as the selection criterion. It was systematically verified that the new bubble centroid (in the second frame) was located at a farther axial position than the initial bubble centroid (in the first frame). The mean bubble velocity, $\langle U_{\text{B}} \rangle$, was calculated by averaging over all the Taylor bubble velocities detected along the tube length at each frame and then by considering 100 image frames.

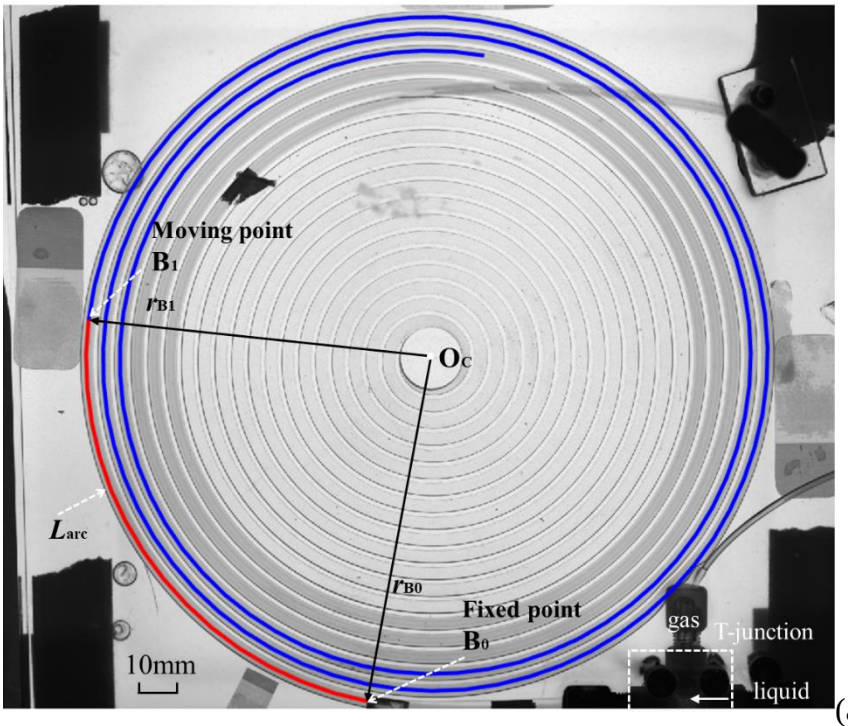
Moving point
B1
r'B1
OC
Larc
r'B0
Fixed point
B0
gas
T-junction
liquid
10mm

(a)

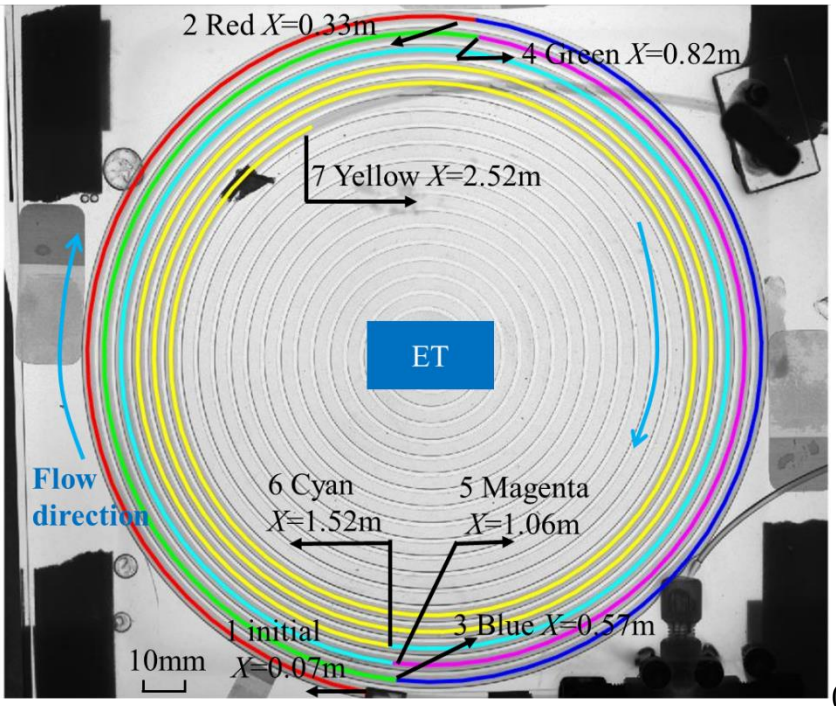
2 Red X=0.33m
4 Green X=0.82m
7 Yellow X=2.52m
ET
Flow direction
6 Cyan X=1.52m
5 Magenta X=1.06m
3 Blue X=0.57m
1 initial X=0.07m
10mm

(b)

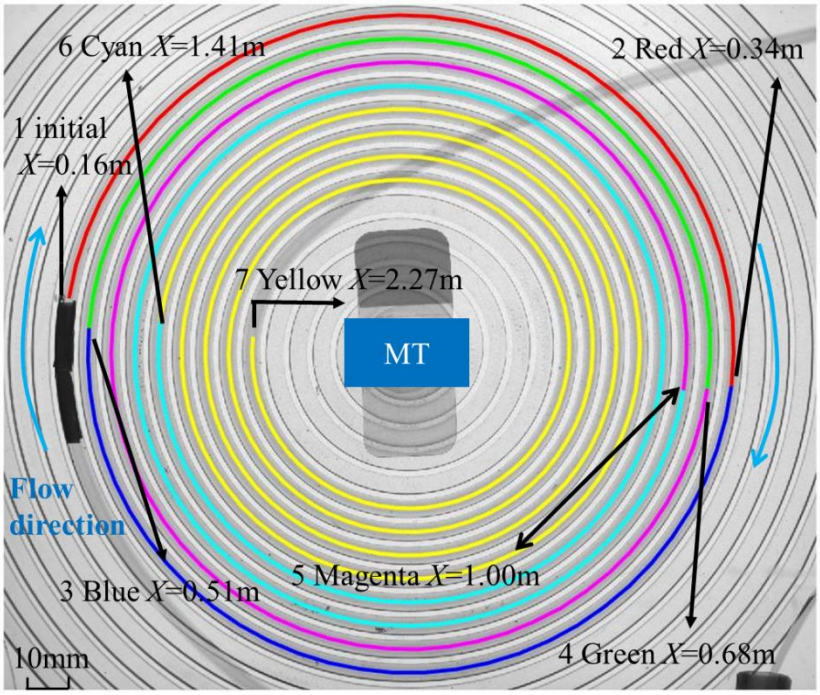

(c)

Fig. 3-2 (a) Schematic diagram used for calculating axial position; O_C refers to the spiral-shaped centroid, r_{B0} and r_{B1} represent the spiral radius of a fixed point (B_0) and a moving point of the bubble centroid in the spiral curve (B_1); L_{arc} is the calculated arc length between the two points. Illustrations of the axial position that were calculated in the configuration (b) ET and (c) MT.

For the whole set of Taylor bubbles detected on a given image, the associated bubble lengths, $L_B(X)$, and the bubble velocities, $U_B(X)$, were initially ranked according to their radial radius, r, namely, to the radial distance from their centroid to the centroid of the spiral shape (point O_c in Fig. 3-2). To convert this radius into an axial position X, the corresponding arc length from the T-junction was determined. Eq. (3-7) was used to calculate the arc length between two random points, B_0 and B_1, on the spiral curve in polar coordinates, (Fig. 3-2 (a))

$$L_{\text{arc}} = \int_{\theta_{B0}}^{\theta_{B1}} \sqrt{r^2 + (\frac{dr}{d\theta})^2}\, d\theta = \int_{\theta_{B0}}^{\theta_{B1}} \sqrt{(C_1 + C_2\theta)^2 + {C_2}^2}\, d\theta \tag{3-7}$$

where θ_{B0} and θ_{B1} represented the initial angle of a fixed point B_0 on the image and the moving angle of a random bubble (point B_1), which could be calculated

from Eq. (2-1) knowing that the radii r_{B0} and r_{B1} were derived directly from the image. This fixed point B_0 was measured and known for the distance from the bubble formation point (Fig. 3-2 (a)). After calculating the arc length of any random bubble from the fixed point B_0, the axial position *X* could be obtained for any detected bubble. Fig. 3-2 (b) and (c) illustrate the calculated axial positions all along the tube for ET and MT configurations. Finally, the evolution of bubble lengths and velocities along the axial position could be obtained.

For any given operating condition, the mean absolute percentage error (MAPE, defined in Appendix 5) of bubble lengths, liquid slug lengths and bubble velocities were smaller than 10%, 5% and 10%, respectively, of the average values.

3.2 Results and discussion

3.2.1 Flow regimes and bubble shape

As shown in Chapter 1, the gas-liquid flow regimes can be affected by several parameters such as the total gas-liquid superficial velocities j_{TP}, the gas-liquid superficial velocity ratio η_0 ($\eta_0 = j_{G0} / j_L$), flow channel geometries, physical properties of the two phases, and wall wetting properties (Haase et al., 2016). The relative influence of these parameters can be quantified by various dimensionless numbers. In this study, the Bond number, ($\mathrm{Bo} = \frac{(\rho_L - \rho_G) {d_{it}}^2 g}{\sigma_L}$), was equal to 0.13; the Capillary number, ($\mathrm{Ca}_{TP} = \frac{\mu_L j_{TP}}{\sigma_L}$), ranged from 0.4×10^{-3} to 3.7×10^{-3}; and the Reynolds number, ($\mathrm{Re}_{TP} = \frac{\rho_L d_{it} j_{TP}}{\mu_L}$), ranged from 24 to 224. The Weber number, ($\mathrm{We}_{TP} = \mathrm{Ca}_{TP} \times \mathrm{Re}_{TP}$), varied from 9.2×10^{-3} to 8.3×10^{-1}. All these dimensionless numbers indicated that the interfacial forces predominated over the

inertial forces and the frictional forces. It is worthwhile to characterize the effect of the centrifugal forces by means of the Dean number, De (see Eq. (2-2)). Whatever the conditions and configurations, the values of De ranged from 2.0 to 22.1 (see Appendix 1).

Fig. 3-3 presents typical images of stable, uniform Taylor flows observed in the ET configuration with varying superficial gas flow rates and for three liquid flow rates. It can be observed that (i) increasing gas superficial velocity or decreasing liquid superficial velocity induced greater bubble lengths; (ii) as the bubble flowed in the tube (from the outer/left to the inner/right spirals), there was a significant increase in the bubble volume along the axial position (a similar trend was also observed in MT, not shown); and (iii) for all the operating conditions, the bubbles had a nearly flat nose and tail. This observation justifies the assumption made in the image post-processing that the bubble could be described by curved cylinders.

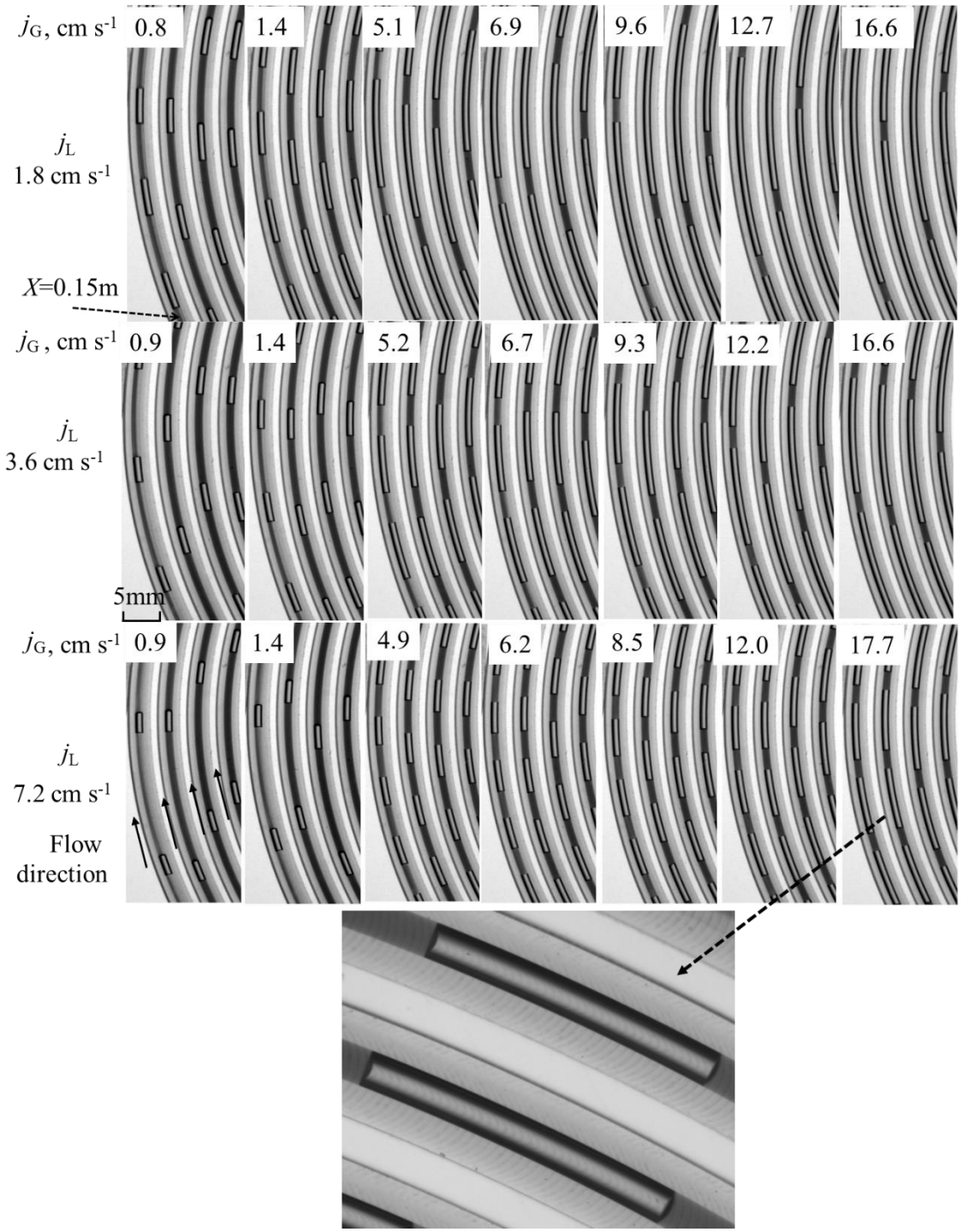

Fig. 3-3 Cartography of gas-liquid Taylor flows (air and RGN colorimetric solution) obtained in the in-plane spiral-shaped milli-reactor (ET configuration) for three liquid superficial velocities and various gas superficial velocities and a local amplified observation of bubble shape (flat nose and tail).

Most Taylor bubbles observed in the literature had a hemispherical shape for the nose and tail, but some papers have also reported such flat bubbles. For example, Ide et al. (2008) investigated the Taylor bubble shapes in circular micro-tubes (fused silica, d_{it}, 100 μm) treated to obtain various surface wettabilities. They found that the Taylor bubble and liquid slug had a flat nose and tail in the poorly wetting tubes at low liquid flow rates but became semi-hemispherical at higher liquid flow rates as in well-wetting micro-tubes. The flat shapes reported in Kurt et al. (2017) were also observed in a poorly wetting tube (FEP) with inner diameter of 1 mm. However, it should be kept in mind that these "flat" bubbles and liquid slugs in hydrophobic channels may be not exactly flat, but mildly convex in the same direction, as reported by Cubaud et al. (2006). All these findings would suggest that this uncommon curved-cylinder bubble shape (flat nose and tail) was probably due to the hydrophobic properties of the tubes (static contact angle bigger than 90°, see Appendix 2), and closely related to the occurrence of dynamic contact angles as well.

In addition, as reviewed in Chapter 1 (section 1.2.1.1), Haase et al. (2020a) proposed a generalized approach to predict the transitions between different flow regimes. Fig. 3-4 demonstrates the flow map calculated according to the proposed transition boundaries in Table 1-1 for the ET configuration. Their approach well predicted that the flow regime under the present operating conditions (considering the inlet geometry and the wettability of tube) was fully located at the Taylor regime, which was consistent with our observations from Fig. 3-3.

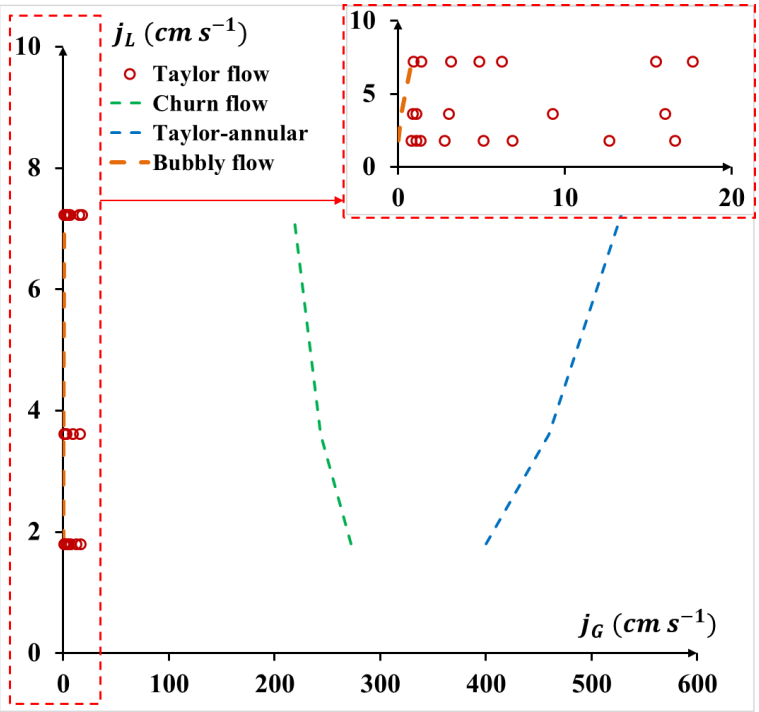

Fig. 3-4 In-plane spiral-shaped milli-reactor: flow map for air/RGN colorimetric solution in the ET configuration. Green, blue and orange dotted lines represent the transition boundaries between the Taylor flow to the churn flow, Taylor-annular flow, and bubby flow predicted using the approach from Haase et al. (2020a), respectively.

3.2.2 Axial variation of the bubble and liquid length and bubble velocity

As displayed in Fig. 3-5 (a) and (b), whatever the operating condition and tube configuration, the bubble lengths increased linearly along the axial position while the liquid slug lengths remained constant along the axial position. Fig. 3-6 shows that the bubble velocity also followed a linear axial increase. This suggests that the expansion effects of the gas phase were not negligible in the present long tubing (3 m), but there were no effects on the liquid phase since it was incompressible.

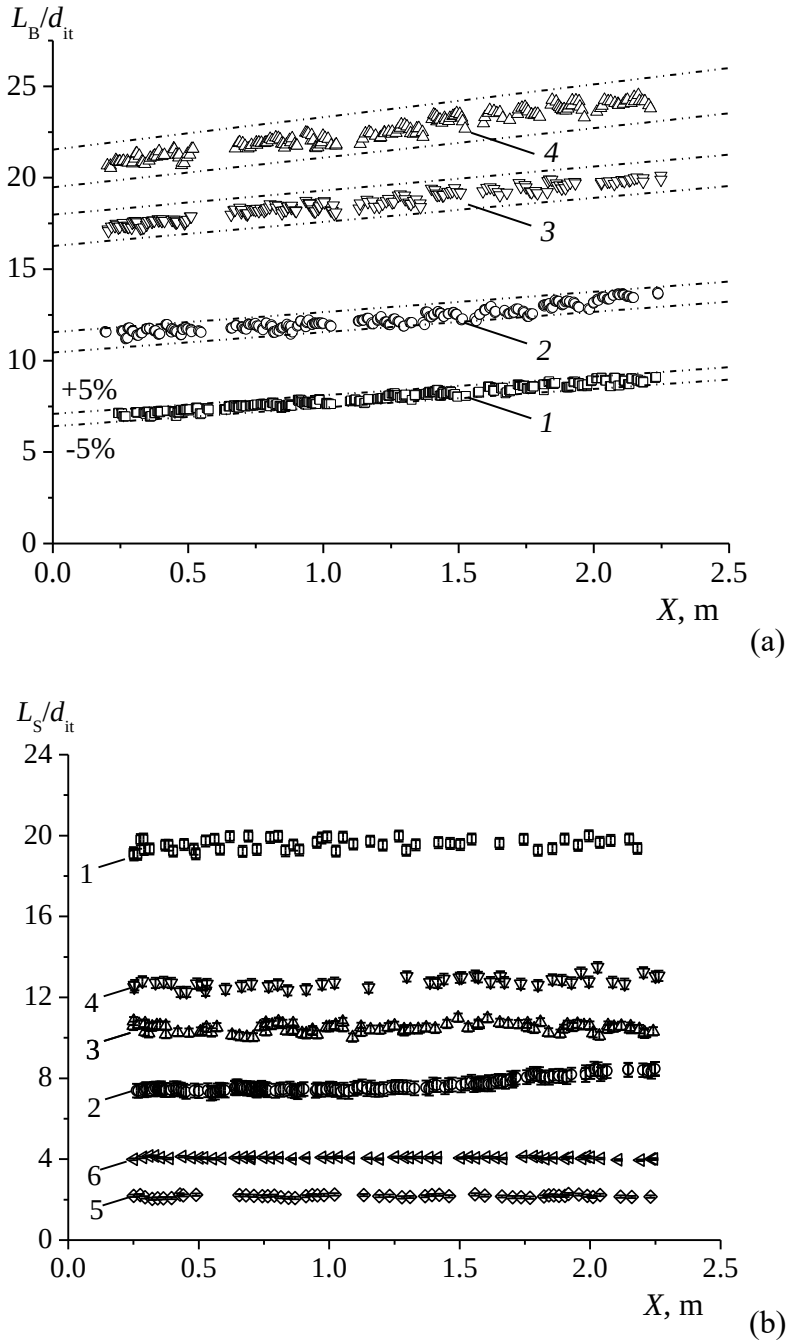

Fig. 3-5 In-plane spiral-shaped milli-reactor (a) dimensionless bubble length versus axial position X at j_L = 1.8 cm s^{-1} for the ET configuration: (1) j_G = 1.4 cm s^{-1}; (2) j_G = 2.8 cm s^{-1}; (3) j_G = 5.1 cm s^{-1}; (4) j_G = 6.9 cm s^{-1}; dash-dotted line: the ± 5 % confidence interval. (b) Dimensionless liquid slug length versus axial position X at different conditions: (1) j_L=7.2 cm s^{-1}, j_G=0.9 cm s^{-1}, ET; (2) j_L = 7.2 cm s^{-1}, j_G = 3.3 cm s^{-1}, MT; (3) j_L = 3.6 cm s^{-1}, j_G = 1.1 cm s^{-1}, ET; (4) j_L = 3.6 cm s^{-1}, j_G = 0.9 cm s^{-1}, MT; (5) j_L = 1.8 cm s^{-1}, j_G = 16.6 cm s^{-1}, ET; (6) j_L = 1.8 cm s^{-1}, j_G = 3.2 cm s^{-1}, MT.

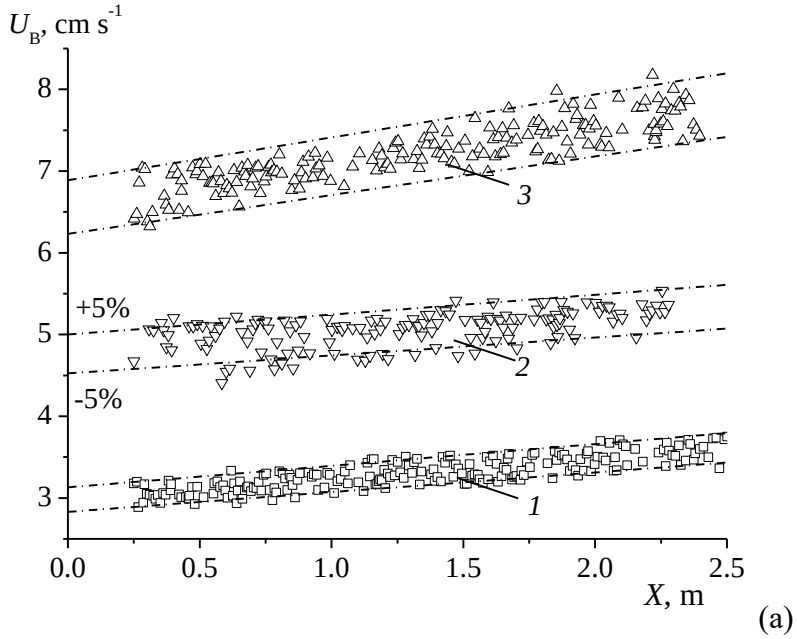

Fig. 3-6 In-plane spiral-shaped milli-reactor: bubble velocity versus axial position X at different conditions (1) j_L = 1.8 cm s^{-1}, j_G = 1.4 cm s^{-1}, ET; (2) j_L = 1.8 cm s^{-1}, j_G = 3.2 cm s^{-1}, MT; (3) j_L = 3.6 cm s^{-1}, j_G = 3.0 cm s^{-1}, ET, dash-dotted line: the ±5% confidence interval.

These findings were in good agreement with the trends found by Molla et al. (2011), who also investigated the lengths and velocities of the gas bubbles and liquid slugs along a rectangular micro-channel (0.8 m in length, 117 μm in width and 58 μm in height). The linear axial evolution of bubble length and velocity could be expressed as below:

$$L_{\mathrm{B}}(X) = F_1 X + L_{\mathrm{B0}} \tag{3-8}$$

$$U_{\mathrm{B}}(X) = F_2 X + U_{\mathrm{B0}} \tag{3-9}$$

where F_1 and F_2 referred to the slopes of the straight lines related to bubble length and velocity with axial location; L_{B0} and U_{B0} were the initial bubble length and velocity, namely the ones immediately after the bubble formation.

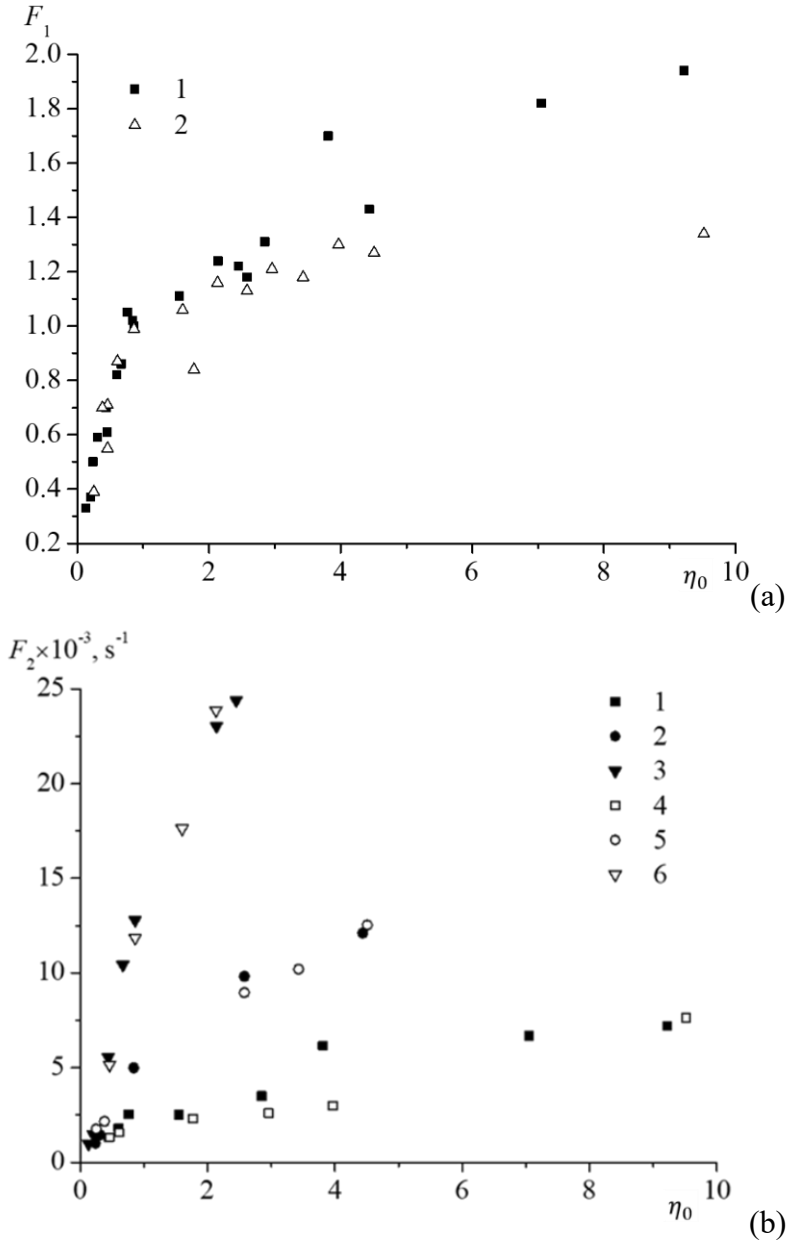

Fig. 3-7 In-plane spiral-shaped milli-reactor (a) Linear regression coefficient F_1 versus gas-liquid superficial velocity ratio η_0 for different configurations and superficial velocities: (1) ET, (2) MT. (b) Constant F_2 versus gas-liquid flow ratio for configuration ET: (1) j_L = 1.8 cm s^{-1}; (2) j_L = 3.6 cm s^{-1}; (3) j_L = 7.2 cm s^{-1}; configuration MT: (4) j_L = 1.8 cm s^{-1}; (5) j_L = 3.6 cm s^{-1}; (6) j_L = 7.2 cm s^{-1}.

By using the image processing and the least squares regression method, all the slopes and initial values at X = 0 were calculated and listed in Appendix 1

(Table A 1-1 and Table A 1-2) for each operating condition. Considering that the plotted bubble lengths and velocities were within a ± 5% confidence interval, it can be observed that the slope of the bubble length, F_1, and the slope of the bubble velocity, F_2, increased with the gas superficial flow rates at a given liquid superficial flow rate (Fig. 3-7 (a) and (b)).

The estimated coefficients F_1 are plotted against gas-liquid superficial velocity ratio, η_0, as shown in Fig. 3-7 (a) (note that η_0 was calculated at the inlet conditions in this paper). It is seen that (i) for increasing η_0, the slope F_1 increased strongly until $\eta_0 \approx 0.8$, then the growth rate slowed down, and that (ii) the difference between the ET and MT configurations remained negligible when $\eta_0 < 0.8$, but smaller values of F_1 were obtained for the MT configuration after $\eta_0 \approx 0.8$. The F_1 should be correlated with the pressure drop, which was related to the unit cell length and the unit cell number, and further discussed in section 3.2.6.

As shown in Fig. 3-7 (b), the growth rates of bubble velocities with axial position, F_2, are plotted versus gas-liquid superficial velocity ratios in two configurations. They increased linearly with η_0 at a given j_L, and vice versa. However, the effect of centrifugal force on F_2 was negligible since there was no significant difference in two configurations. Therefore, the acceleration of the bubble velocity (i.e., F_2) was mainly caused by the significant pressure drop.

3.2.3 Average bubble and liquid slug lengths

Fig. 3-8 (a) and (b) show the variation of the average dimensionless bubble length, $\langle L_B \rangle / d_{it}$, and liquid slug length, $\langle L_S \rangle / d_{it}$, as a function of η_0 for the ET and MT configurations, respectively. The angle brackets symbol "$\langle\ \rangle$" was used to represent the average value.

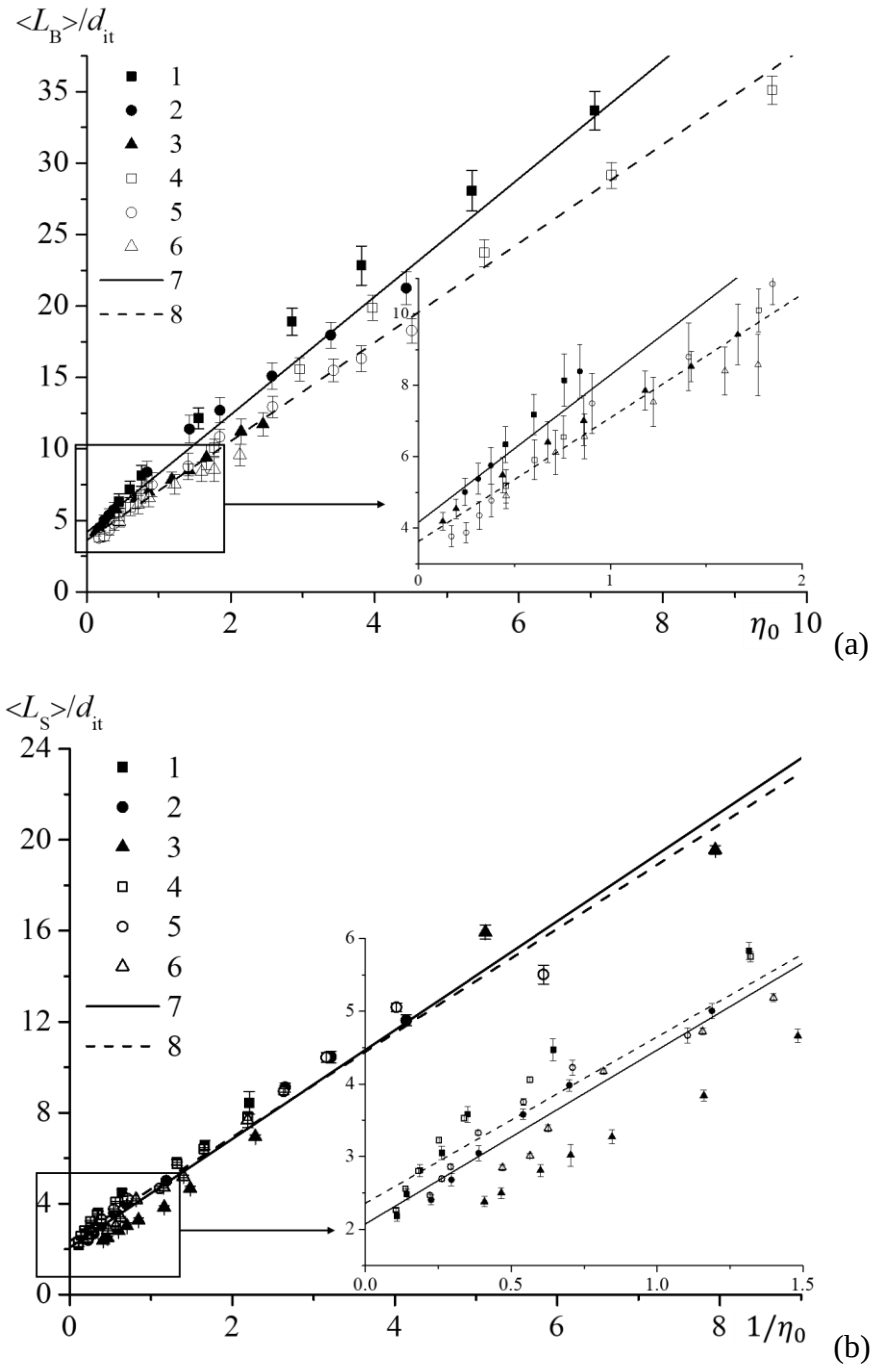

Fig. 3-8 In-plane spiral-shaped milli-reactor: (a) average dimensionless bubble length versus gas-liquid superficial velocity ratio η_0 and (b) average dimensionless liquid slug length versus the inverse of η_0; for the ET configuration: (1) j_L = 1.8 cm s^{-1}; (2) j_L = 3.6 cm s^{-1}; (3) j_L = 7.2 cm s^{-1}; and for the MT configuration: (4) j_L = 1.8 cm s^{-1}; (5) j_L = 3.6 cm s^{-1}; (6) j_L = 7.2 cm s^{-1}; (7) the least square regression law for ET, (8) the least square regression law for MT.

As expected, the average bubble and slug lengths over the tubing length increased linearly with η_0 and the inverse of η_0, respectively. Compared to many works (Haase et al., 2016), some extremely long stable bubbles could be originally generated in the spiral-shaped tube used here: the smallest and largest lengths were 3.9 and 40.4 mm for bubbles, and 2.2 and 19.6 mm for liquid slugs. The regime where the bubble length was smaller than the tube inner diameter (i.e., bubbly flow) could not be reached in this study, as it led to unsteady flows. The standard deviation (STD, see Appendix 5) bars in Fig. 3-8 (a) were relatively large (up to 10%), due to the significant increase of bubble length $L_B(X)$ along the axial distance X (discussed in section 3.2.2).

The bubble and liquid slug lengths could be predicted by the following scaling laws:

$$\frac{\langle L_B \rangle}{d_{it}} = C_3 + C_4 \frac{j_G}{j_L} = C_3 + C_4 \eta_0 \tag{3-10}$$

$$\frac{\langle L_S \rangle}{d_{it}} = C_5 + C_6 \frac{j_L}{j_G} = C_5 + C_6 \frac{1}{\eta_0} \tag{3-11}$$

where the constants C_3-C_6 were dependent on the configuration, the inlet geometry (e.g. T-junction, flow-focusing/cross-junction or co-flowing geometries), the fluid properties and the wetting properties (Abadie et al., 2012).

The estimated coefficients are listed in Table 3-1. The coefficients obtained for bubble length, C_3 and C_4, were almost equal for a given configuration: $C_3 \approx C_4 \approx 4.15$ (MAPE = 0.4%) for ET while $C_3 \approx C_4 \approx 3.55$ (MAPE = 2.4%) for MT. The coefficients obtained for liquid slug lengths, C_5 and C_6, were almost equal, $C_5 \approx C_6 \approx 2.28$ (MAPE = 3.1%) for both configurations. At a given gas-liquid superficial velocity ratio, η_0, it can be seen from Fig. 3-8 (a) that the average bubble lengths in the ET configuration were bigger than that in the MT

configuration, whatever the conditions. As the associated average curvature ratios, $\langle\lambda\rangle$, for ET and MT were 145 and 84, this implied that the bubbles were shorter under higher centrifugal forces (lower $\langle\lambda\rangle$), which was consistent with the simulation results reported by Kumar et al. (2007).

Table 3-1 In-plane spiral-shaped milli-reactor: scaling laws for bubble and liquid slug lengths, the empirical coefficients being associated with Eqs. (3-10) and (3-11). MAPER represents the Mean Absolute Percentage Error of Regression, defined in Appendix 5.

configuration	$\frac{L_B}{d_{it}} = C_3 + C_4 \frac{j_G}{j_L}$			$\frac{L_S}{d_{it}} = C_5 + C_6 \frac{j_L}{j_G}$		
	C_3	C_4	MAPER, %	C_5	C_6	MAPER, %
ET	4.13	4.16	5.2	2.39	2.07	7.2
MT	3.46	3.63	4.4	2.29	2.36	4.3

The constant C_3 was larger than the widely-adopted coefficient for a squeezing regime proposed by van Steijn et al. (2007) and Garstecki et al. (2006) , which was close to 1. This could be explained by the hydrophobic wall materials (Abdelwahed et al., 2012) and also by the increase of bubble length along the reactor. Abdelwahed et al. (2012) reported such large coefficients ($C_3 \approx C_4 \approx 3$) in the case of a train of confined bubbles inside a millimetric cylindrical T-junction device. They showed experimentally that the wetting behaviour played a significant role in the formation and motion of the bubble. In particular, they found that, in the squeezing regime, under the same flow conditions, the gas penetrated inside the stream more easily and more rapidly for a wetting liquid than for a non-wetting one, in which the slip condition on the wall was no longer prevalent.

These findings have shown that the bubble and slug lengths were governed mainly by the ratio between gas and liquid velocities, but that the wettability and centrifugal force also had noteworthy influences.

3.2.4 Average bubble velocity

Fig. 3-9 shows the average bubble velocity, $\langle U_B \rangle$, versus the total gas-liquid superficial velocity, j_{TP} (calculated at the inlet conditions), for different liquid flow rates in the ET and MT configurations.

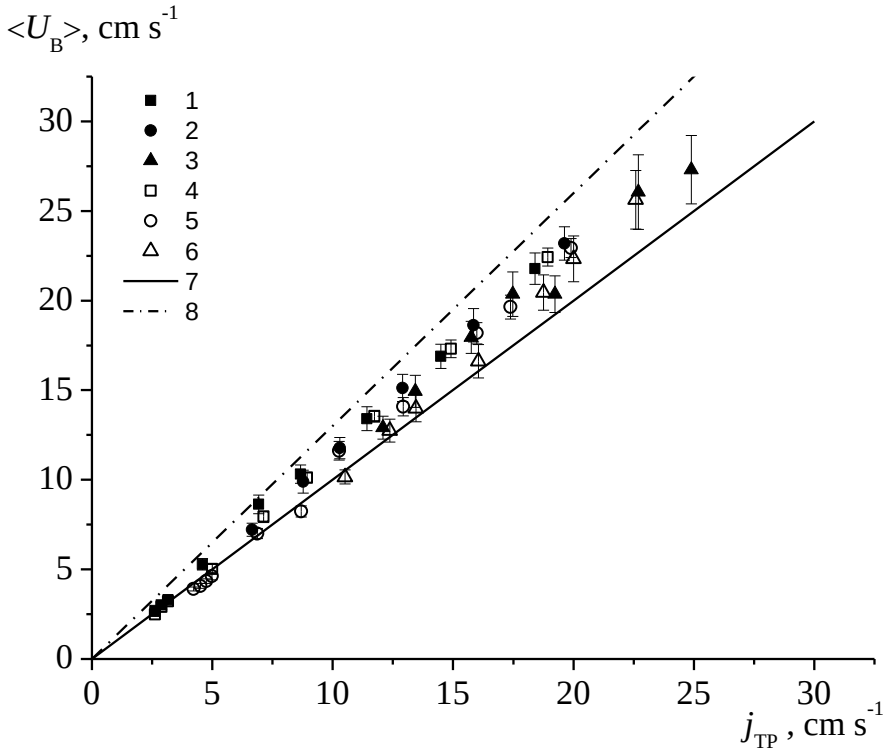

Fig. 3-9 In-plane spiral-shaped milli-reactor: Average bubble velocity versus two-phase superficial velocity for the ET configuration: (1) j_L = 1.8 cm s^{-1}; (2) j_L = 3.6 cm s^{-1}; (3) j_L = 7.2 cm s^{-1}; for the MT configuration: (4) j_L = 1.8 cm s^{-1}; (5) j_L = 3.6 cm s^{-1}; (6) j_L = 7.2 cm s^{-1}; solid line: (*7*) $U_B = j_{TP}$; dash-dotted line: (*8*) $U_B = 1.3\times j_{TP}$.

It can be seen that (i) $\langle U_B \rangle$ was higher than j_{TP} and followed a linear evolution and, (ii) the bubble velocities obtained with the ET configuration did not differ significantly from those in the MT configuration. This trend could be described using the well adapted drift flux model (Laborie et al., 1999):

$$\langle U_B \rangle = C_7 j_{TP} + C_8 \quad (3\text{-}12)$$

where C_7 and C_8 were the distribution factor and the drift velocity. For the horizontal tubes, the drift velocity was negligible, so $C_8 \approx 0$. The factor C_7 was found to be 1.17 (MAPER 7.3%), which was in accordance with the values encountered in the literature (varying between 0.85 and 1.38 (Tsoligkas et al., 2007)). It is interesting to note that, if the initial bubble velocity, U_{B0}, (i.e., the velocity just after the bubble formation) was considered instead of $\langle U_B \rangle$, then the value of C_7 was approximately 1.

3.2.5 Unit cell length and relative length of the bubble

The average unit cell length was determined by the bubble and liquid slug lengths, as follows:

$$\langle L_{UC} \rangle = \langle L_S \rangle + \langle L_B \rangle \quad (3\text{-}13)$$

The relative length of the bubble, $\langle \psi \rangle$, was calculated as:

$$\langle \psi \rangle = \frac{\langle L_B \rangle}{\langle L_{UC} \rangle} \quad (3\text{-}14)$$

The variation of the unit cell length, $\langle L_{UC} \rangle$, and the relative length of the bubble, $\langle \psi \rangle$, were plotted against η_0 in Fig. 3-10 (a) and (b).

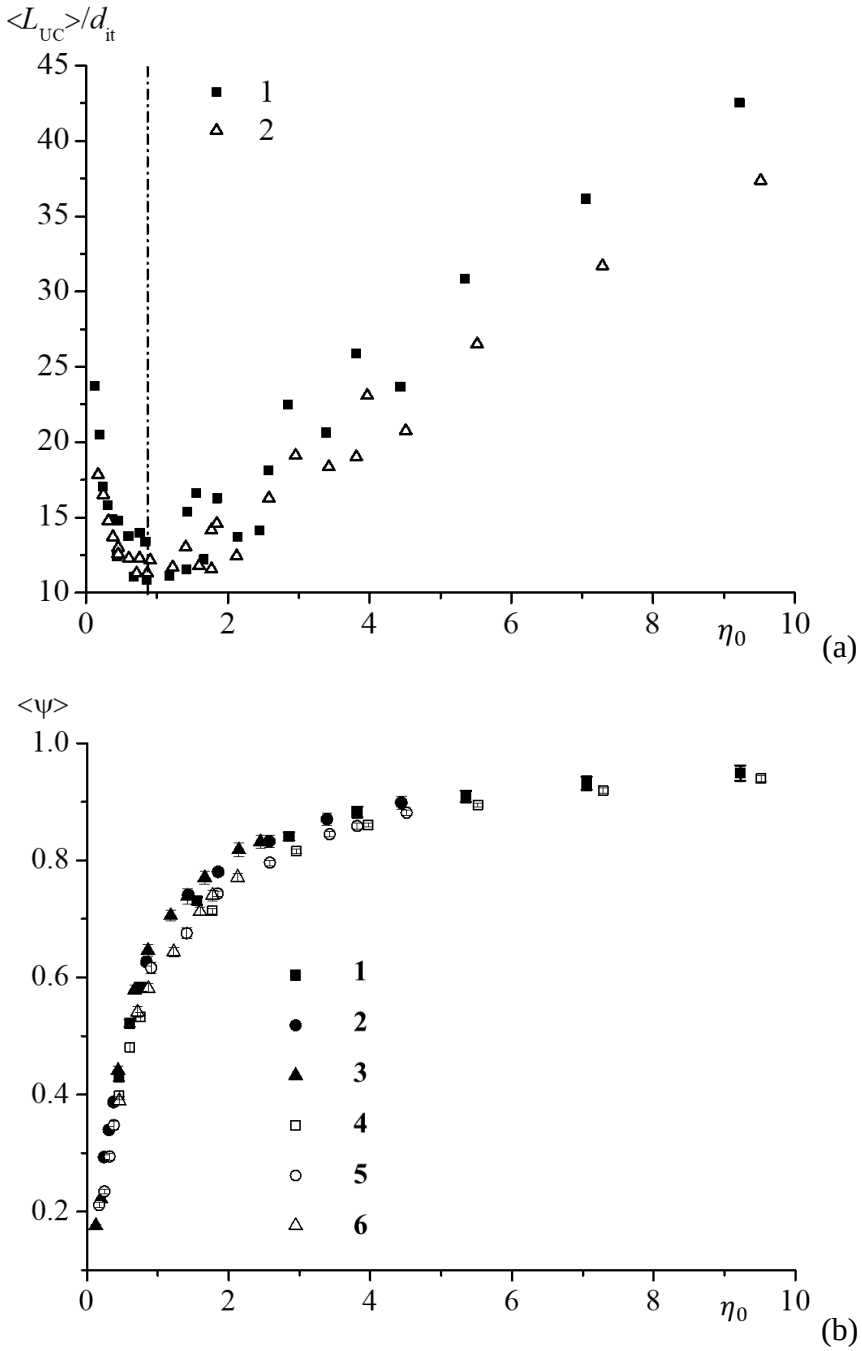

Fig. 3-10 In-plane spiral-shaped milli-reactor: (a) Average unit cell length $\langle L_{UC} \rangle$ versus gas-liquid superficial velocity ratio η_0: (1) ET; (2) MT; dash-dotted line: $\eta_0 = 0.8$; (b) Average relative length of the bubble $\langle \psi \rangle$ versus η for the ET configuration: (1) $j_L = 1.8$ cm s^{-1}; (2) $j_L = 3.6$ cm s^{-1}; (3) $j_L = 7.2$ cm s^{-1}; the MT configuration:(4) $j_L = 1.8$ cm s^{-1}; (5) $j_L = 3.6$ cm s^{-1}; (6) $j_L = 7.2$ cm s^{-1}.

At fixed j_L, as j_G increased (η_0 increasing), the length of the unit cells L_{UC} decreased to a minimum value and afterwards increased. This trend (i.e., the occurrence of a minimal value) can be explained by the fact that, when η_0 was smaller than 0.8, the liquid slug length decreased as j_G increased, while the bubble length increased.

Surprisingly, the values of $\langle\psi\rangle$ were almost identical whatever the liquid superficial velocity. They were, however, slightly higher in the ET configuration than in the MT, which was in agreement with the fact that the bubbles were longer in the ET configuration due to less pronounced effects of centrifugal forces and a slightly smaller pressure drop. It can also be observed that $\langle\psi\rangle$ first increased dramatically with the gas-liquid superficial velocity ratio, and then reached a plateau when $\eta_0 > 6$. This plateau corresponded to very high values of $\langle\psi\rangle$ (close to 0.95), indicating very long bubbles and very short liquid slugs. When compared to the literature, such a result was quite original.

3.2.6 Pressure drop

In this study, the air pressure passing through the mass flow controller at the gas feeding line was measured and noted p_r. The mass flow controller was at 4.25 m (noted L_1), far before the T-junction point, and the inner diameter of the gas supply tube, d_G, was 0.5 mm. Considering a fully developed Hagen-Poiseuille flow of a single phase in a tube (Kreutzer et al., 2005b), the pressure drop in the gas feeding line before the T-junction, Δp_1, could be calculated for each gas flow rate.

The total pressure drop from the gas inlet (right before T-junction position) to the two-phase flow outlet, Δp_{r0}, could then be deduced from Δp_1 and from the absolute pressure recorded by the mass flow controller, p_r, as:

$$\Delta p_{\mathrm{r0}} = (p_{\mathrm{r}} - p_{\mathrm{out}}) - \Delta p_1 \tag{3-15}$$

Therefore, the total pressure drop per unit of length $(\Delta p/L)_{\mathrm{r0}}$ was given by the total pressure drop, Δp_{r0}, divided by the entire reactor length L_{R}.

Let us now consider the overall pressure drop Δp_{tot}, including the pressure loss related to the micro-reactor inlet and outlet effects, and the two-phase Taylor flow pressure drop due to the frictional and capillary forces, as follows:

$$\Delta p_{\mathrm{tot}} = \Delta p_{\mathrm{inlet}} + \Delta p_{\mathrm{out}} + \Delta p_{\mathrm{TP}} \tag{3-16}$$

Some correlations have been proposed in the literature to calculate the two-phase Taylor flow pressure drop (Δp_{TP}): they are listed in Table 3-2. The associated predicted values were plotted, together with the measured pressure gradient, $(\Delta p/L)_{\mathrm{r0}}$, in Fig. 3-11.

Table 3-2 Correlations for the two-phase flow pressure drop in the literature.

Reference	Pressure drop	Frictional correlations	Frictional factors f
(Vashisth and Nigam, 2007)	$\Delta p_{\mathrm{TP}} = \Delta p_{\mathrm{fric}}$	$(\frac{\Delta p_{\mathrm{TP}}}{L_{\mathrm{R}}})_{\mathrm{fric}} = \frac{f \rho_{\mathrm{TP}} \alpha {j_{\mathrm{TP}}}^2}{2d}$	$f = \frac{16}{\mathrm{Re}_{\mathrm{TP}}} (\frac{j_{\mathrm{L}}}{j_{\mathrm{G}}})^2 [1 + 9.63 (\frac{\mathrm{Re}_{\mathrm{G}}}{\mathrm{Re}_{\mathrm{L}}})^{0.747} \mathrm{Re}_{\mathrm{TP}}^{-0.019}]$
(Kreutzer et al., 2005b)	$\Delta p_{\mathrm{TP}} = \Delta p_{\mathrm{fric}}$	$(\frac{\Delta p_{\mathrm{TP}}}{L_{\mathrm{R}}})_{\mathrm{fric}} = \frac{2f \rho_{\mathrm{L}} \beta {j_{\mathrm{TP}}}^2}{d}$	$f = \frac{16}{\mathrm{Re}_{\mathrm{TP}}} [1 + 0.17 \frac{d}{L_{\mathrm{s}}} (\frac{\mathrm{Re}}{\mathrm{Ca}})^{0.33}]$
(Bretherton, 1961)	$\Delta p_{\mathrm{TP}} = \Delta p_{\mathrm{fric}}$		$f = \frac{16}{\mathrm{Re}_{\mathrm{TP}}} [1 + 0.465 \frac{d}{L_s} (\frac{1}{\mathrm{Ca}})^{0.33}]$
(Lee and Lee, 2010)	$\Delta p_{\mathrm{TP}} = (\Delta p_G)_{fric} + (\Delta p_{\mathrm{L}})_{\mathrm{fric}} + \Delta p_{\mathrm{CAH}}$	$(\frac{\Delta p_{\mathrm{G}}}{L_{\mathrm{R}}})_{\mathrm{fric}} = \frac{2 f_{\mathrm{G}} \rho_{\mathrm{G}} \beta {j_{\mathrm{TP}}}^2}{d}$ $(\frac{\Delta p_{\mathrm{L}}}{L_{\mathrm{R}}})_{\mathrm{fric}} = \frac{2 f_{\mathrm{L}} \rho_{\mathrm{L}} (1-\beta) {j_{\mathrm{TP}}}^2}{d}$	$f_{\mathrm{G}} = \frac{16}{\mathrm{Re}_{\mathrm{G}}}$ $f_{\mathrm{L}} = \frac{16}{\mathrm{Re}_{\mathrm{L}}}$

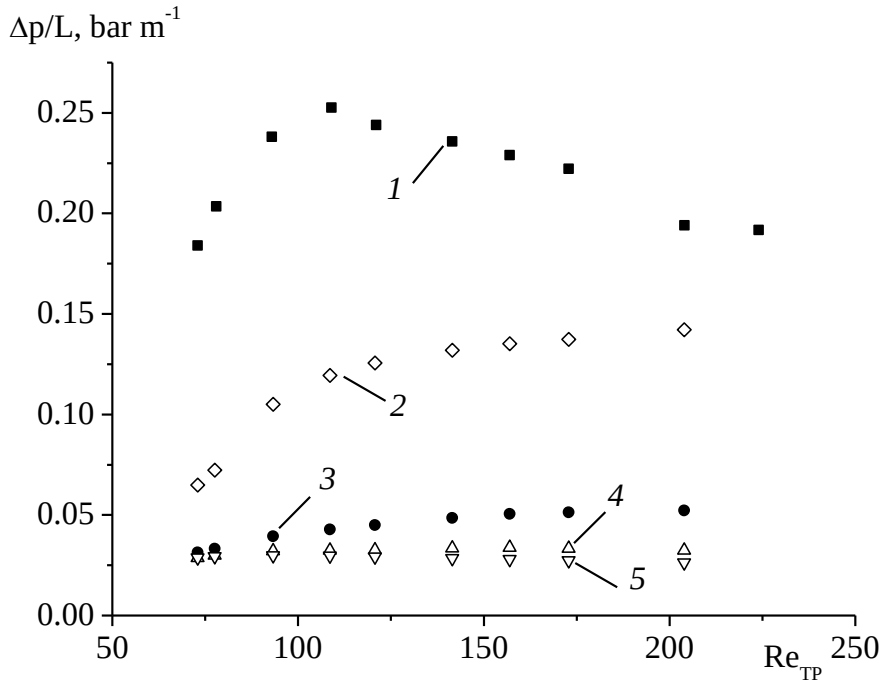

Fig. 3-11 In-plane spiral-shaped milli-reactor: comparison of pressure drop per unit of length versus gas-liquid two-phase Reynolds number at j_L = 7.2 cm s^{-1} for ET: (1) measured experimental data; (2) Lee et al (2010); (3) Bretherton et al (1961); (4) Kreutzer et al (2005); (5) Vashisth et al (2007).

Theoretically, the predicted value of $(\Delta p/L)$ should be slightly smaller than the experimental ones, $(\Delta p/L)_{r0}$, as it did not take account of the pressure losses from the inlet and outlet parts. However, the predicted pressure drops were observed to be markedly lower than the measured pressure drop when only the frictional pressure drop was considered, such as in the correlations of Bretherton (1961), Kreutzer et al. (2005b), and Vashisth and Nigam (2007). The correlation from Lee and Lee (2010) differed by the fact that it included the capillary pressure drop. The total capillary pressure drops caused by the contact angle hysteresis (noted CAH) in the milli-reactor could be calculated as below:

$$(\Delta p)_{\mathrm{CAH}} = -\frac{4\sigma}{d_{\mathrm{it}}}(\cos\Theta_{\mathrm{RCA}} - \cos\Theta_{\mathrm{ACA}})n_{\mathrm{UC}} \qquad (3\text{-}17)$$

where Θ_{RCA} and Θ_{ACA} represented receding contact angle (RCA) and the advancing contact angle (ACA), respectively, and n_{UC} was the unit cell number ($n_{UC} = L_R/L_{UC}$).

The ACA and RCA were calculated from the static contact angle, Θ_s (98.7° in this study, see Appendix 2), and from the coefficients C_9 and C_{10} adopted by Lee and Lee (2010) and equal to 0.82 and 0.118, respectively.

$$\Theta_{ACA} = \cos^{-1}[\cos\Theta_s - C_9 \mathrm{Ca}^{C_{10}}(\cos\Theta_s + 1)] \quad (3\text{-}18)$$

$$\Theta_{RCA} = 2\Theta_s - \Theta_{ACA} \quad (3\text{-}19)$$

This calculation of capillary pressure drop assumed that there was no liquid film between the Taylor bubble and the FEP material wall surface. Fig. 3-11 clearly shows that the predictions from the correlation of Lee and Lee (2010) were the closest to the measured pressure gradient. These findings would indicate that the dominant role was played by the capillary pressure drop rather than the frictional pressure drop.

Furthermore, the pressure drop could be estimated from the bubble volume change, considering the Ideal Gas Law (IGL) and assuming that the volume change caused by mass transfer of oxygen was negligible. From the previous variation of axial bubble length, the bubble volume could be derived from Eq. (3-8) as below:

$$V_B(X) = \Omega(F_1 X + L_{B0}) \quad (3\text{-}20)$$

where Ω ($\Omega = \pi d_{it}^2/4$) referred to the cross-sectional area of the inner tube. Therefore, the axial variation of pressure inside the bubble, noted $p_B(X)$, could be estimated by:

$$p_{\mathrm{B}}(X) = p_{\mathrm{B}_{\mathrm{out}}} \frac{V_{\mathrm{B}_{\mathrm{out}}}}{V_{\mathrm{B}}(X)} \quad (3\text{-}21)$$

where $p_{\mathrm{B}_{\mathrm{out}}}$ represented the pressure at the outlet of the micro-reactor, which was equal to atmospheric pressure, and $V_{\mathrm{B}_{\mathrm{out}}}$ was the bubble volume at the outlet, calculated from the linear regression F_1 and L_{B0}. As the bubble volume, $V_{\mathrm{B}}(X)$, increased linearly with X, the pressure was assumed to decrease linearly with X. The initial pressures inside bubbles, p_{B0}, calculated using $V_{\mathrm{B0}} = \Omega L_{\mathrm{B0}}$ were reported in Appendix 1 (Table A 1-1 and Table A 1-2). Finally, the pressure gradient deduced from the bubble volume change and the Ideal Gas Law was derived from:

$$(\Delta p/L)_{\mathrm{IGL}}=(p_{\mathrm{B0}}-p_{\mathrm{B}_{\mathrm{out}}})/L_{\mathrm{R}} \quad (3\text{-}22)$$

Fig. 3-12 compares the three different methods for evaluating the pressure drop as a function of the gas-liquid superficial velocity ratio η_0. It can be observed that the pressure drops estimated from IGL remained smaller than the predicted ones. Here again, this was quite logical as the pressure drop estimated from IGL did not involve the pressure drops related to the Taylor bubble formation (at the inlet) and to the two-phase flow separation at the outlet. More interestingly, the variation of $(\Delta p/\mathrm{L})_{\mathrm{IGL}}$ and $(\Delta p/\mathrm{L})_{\mathrm{r0}}$ presented identical trends: they first increased quickly for $\eta_0 < 0.8$ and, after this value, decreased. From Fig. 3-10 (a) and Fig. 3-13, one can deduce that, at this specific value $\eta_0 = 0.8$, the unit cell length L_{UC} and the unit cell number n_{UC} achieved a minimum and a maximum respectively (n_{UC} being calculated using the tube length L_{R} divided by L_{UC}). The peak in the pressure drop observed in Fig. 3-12 corresponded to the maximum value of the total number of moving contact lines, namely to the maximum number of unit cells. This was consistent with the conclusions of Choi et al. (2011): unlike the pressure drop in fully wetting plug flows, the energy dissipated by the moving

contact lines in poorly wetting plug flows played an important role compared to the frictional pressure dissipated by the liquid phase.

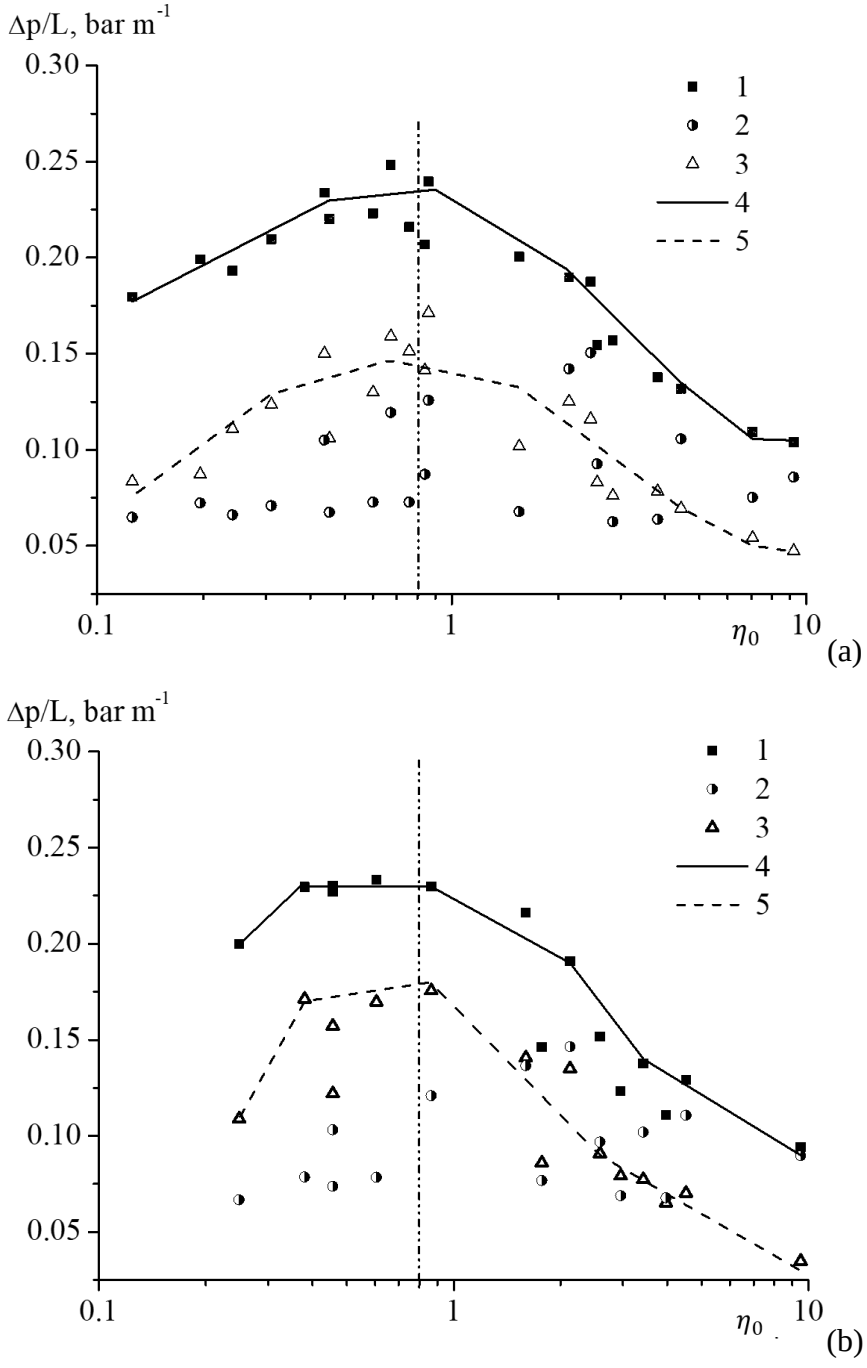

Fig. 3-12 In-plane spiral-shaped milli-reactor: variation of pressure drops per unit of length versus gas-liquid superficial velocity ratio η_0 for configuration (a) ET; and (b) MT: (1) Experimental data; (2) Lee et al (2010) (3) IGL; (4) trend line for experimental data; (5) trend line for IGL; dash-dotted line: $\eta_0 = 0.8$.

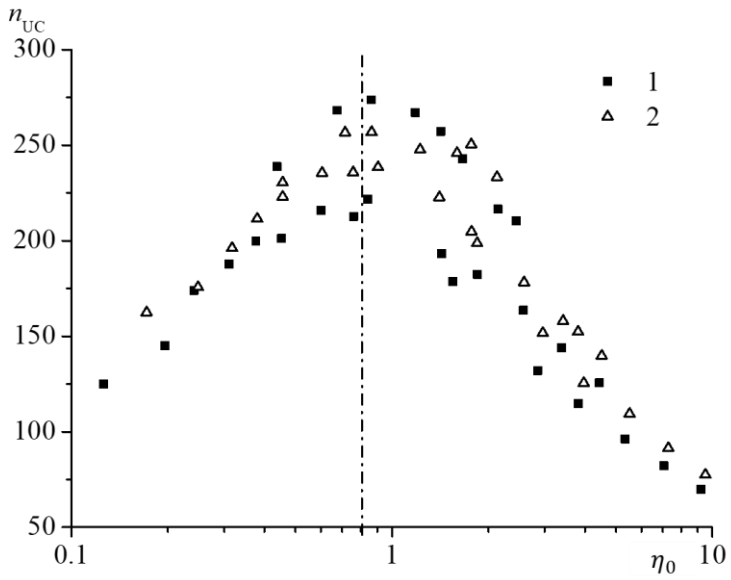

Fig. 3-13 In-plane spiral-shaped milli-reactor: variation of unit cell number n_{UC} versus gas-liquid superficial velocity ratio η_0 for different configurations (1) ET and (2) MT; dash-dotted line: $\eta_0 = 0.8$.

Fig. 3-12 (a) and (b) also show that the pressure drops in the ET and MT configurations were very close, suggesting that an increase of centrifugal forces (from ET to MT) did not have a major impact on the pressure drop. The figures revealed that the pressure drops predicted by Lee and Lee (2010) were relatively closer to the pressure drops estimated from IGL, but the trend was not clear.

In conclusion, these findings suggest that, in poorly wetting flows, further works are required to predict the pressure drop more accurately, but also that the number of unit cells n_{UC} would be the dominant factor controlling the pressure drop, being determined by the length of the bubbles and the liquid slugs.

3.3 Conclusion

Gas-liquid two-phase Taylor flows have been investigated in a long, in-plane, spiral-shaped milli-reactor for a large range of curvature ratios and Reynolds numbers.

The main findings are the following:

1) Unlike those commonly observed in the literature, the Taylor bubbles were very long and had a flat nose and tail, probably due to the poorly wetting FEP tubes.
2) The axial bubble length and velocity increased linearly with axial position, and the rates of increase were closely related to the pressure drop and centrifugal force. Along the axial position, there was no variation of the liquid slug lengths.
3) The formation of bubbles and liquid slugs followed the squeezing mechanism and their average lengths were mainly dependent on the gas-liquid superficial velocity ratio, η_0. Higher centrifugal force resulted in shorter Taylor bubbles and had no significant effect on liquid slug lengths.
4) The pressure drops per unit of length estimated by IGL and the correlation of Lee et al. were compared with the measured pressure drops. In particular, the capillary pressure drop was found to be dominant when compared to the frictional pressure drop, and correlated with the total unit cell numbers in the reactor.

All these findings give important information for understanding the characteristics of gas-liquid hydrodynamics in a long, spiral-shaped tube, which could serve as a basis for implementing gas-liquid mass transfer and reaction in continuous flow reactors.

Chapter 4. Gas-liquid mass transfer around Taylor bubbles flowing in a long, in-plane, spiral-shaped milli-reactor

Abstract

Gas–liquid mass transfer was investigated around Taylor bubbles flowing in a long, in-plane, spiral-shaped milli-reactor involving two configurations with identical lengths and different ranges of tubing curvature ratio. Using the resazurin based colorimetric technique and image post-treatment, the variation of the equivalent O_2 concentration inside the liquid slugs was measured. The coloration positions, corresponding to 99% of the maximum oxygen concentration reached in the liquid slug, changed significantly under various operating conditions. Overall volumetric liquid side mass transfer coefficients were evaluated on the basis of these coloration positions, without considering the hydrodynamics change. A proportionality relationship was established between these coefficients and the recirculation frequencies inside the liquid slugs, and the intensification factor between two configurations was found to be proportional to the increase in average Dean numbers. Considering the changes in pressure drop, bubble length and velocity, the axial variation of cumulated mass flux density could be measured. It decreased along the tube length and finally tended towards a constant value. At last, an original scaling law for the Sherwood number was proposed by introducing a normalized time, dimensionless liquid slug length, and the Péclet and Dean numbers.

This chapter has been published as Mei, M., Hébrard, G., Dietrich, N., & Loubière, K. (2020). Gas-liquid mass transfer around Taylor bubbles flowing in a long, in-plane, spiral-shaped milli-reactor. *Chemical Engineering Science*, 115717.

Introduction

In Chapter 3, the gas-liquid hydrodynamics (bubble velocity, bubble length and liquid slug length, pressure drop) was characterized in a long, in-plane, spiral-shaped milli-reactor. In the continuity, this chapter reports investigations on the gas-liquid mass transfer process around Taylor bubbles flowing in this reactor. This chapter will be organized as follows.

Section 4.1 will describe the specific image post-treatment developed for determining the mass transfer characteristics in this spiral-shaped milli-reactor, in particular the calibration process. In section 4.2, the results will be presented in detail. The equivalent oxygen concentration fields in the liquid slugs will be first reported at various operating conditions in section 4.2.1, and compared between the two geometrical configurations (ET and MT). Section 4.2.2 will describe the mass balance established in the liquid phase. The averaged overall volumetric liquid side mass transfer coefficients will be then calculated and discussed in section 4.2.3, in particular with respect to the recirculation frequencies inside liquid slug. Then, in section 4.2.4 and 4.2.5, considering the axial variations of gas-liquid hydrodynamics, the mass flux density was obtained. At last, all the experimental data will be brought together to propose a scaling law for the Sherwood number as a function of the normalized time and other dimensionless numbers.

4.1 Materials and methods

4.1.1 Experimental setup

The experimental setup, flow control equipment and fluid properties have been described in Chapter 2 (section 2.2.1).

4.1.2 Gas-liquid mass transfer characteristics

After the image acquisition, the gas-liquid mass transfer characteristics were determined by three main image processing steps (implemented in Matlab® R2017b, see Appendix 4): (i) extraction of liquid slugs and bubbles from the images (see Chapter 2, section 2.3.1); (ii) determination of the calibration curve; and (iii) conversion, pixel-by-pixel, of the gray values in the liquid slugs into equivalent oxygen concentrations. Remind that the term "equivalent" was used because, in reality, the oxygen concentration in the liquid phase was zero: oxygen was fully consumed by DH as long as there was enough DH in the liquid (see Yang et al. (2016a)).

For the calibration process, five aqueous solutions of resazurin at different concentrations were prepared: 0.021, 0.042, 0.076, 0.084 and 0.105 g L^{-1} (purity being considered). At each concentration, 200 frames of the fully saturated solution (i.e., pink RF) flowing in the milli-reactor were taken. This process was repeated three times with solutions of the same concentration to reduce experimental uncertainties. Finally, for each RZ concentration, a time-averaged gray value image was obtained by averaging the 200 images, aiming at eliminating the slight deviation between instantaneous gray values.

The objective was to monitor the variation of the concentration all along the tube length (~3m). For that, global images of the entire spiral-shaped milli-reactor were taken, thus leading to wide observing windows (ET: 197.99×167.05 mm^2, MT: 138.53×116.75 mm^2). Due to these wide observing windows, and the circular cross section of the FEP tube, significant deviations in gray values were observed for given RZ concentration, depending on the spiral tubing and on the radial positions at a given spiral turn.

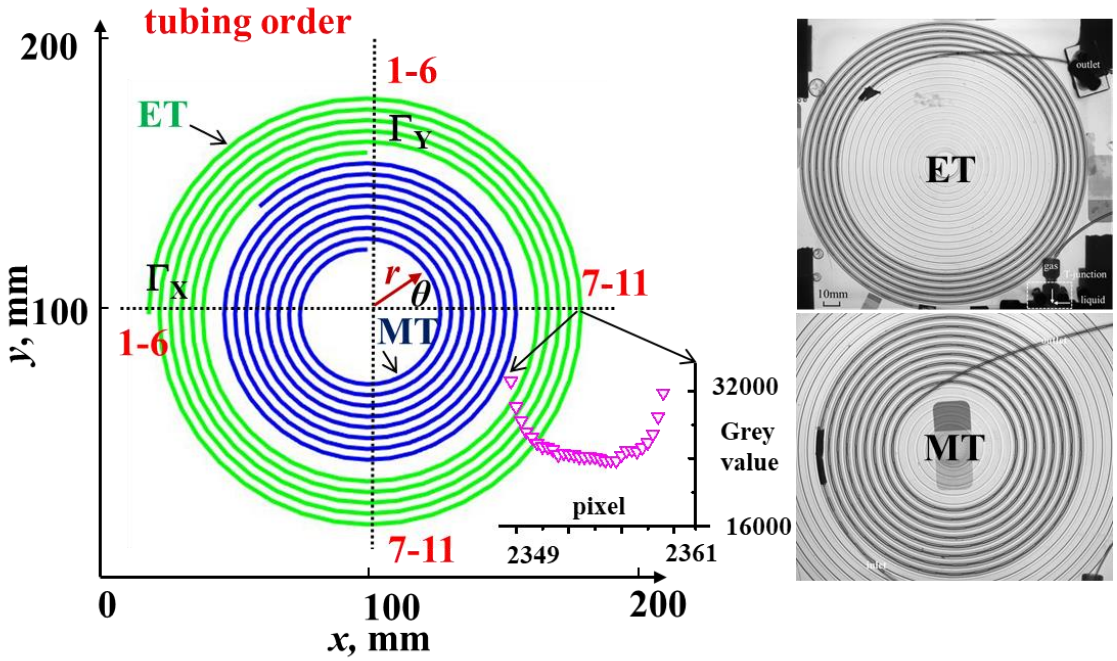

Fig. 4-1 Schematic representation of the spiral-shaped milli-reactor viewed from the top, showing the tubing configuration (ET: External Tubing; MT: Medium Tubing) and radial profile of the pixel gray value along one tube cross-sectional direction. Γ_X and Γ_Y are two orthogonal lines.

As a reminder, Fig. 4-1 shows again the geometry of the spiral-shaped milli-reactor, and the two configurations investigated (ET and MT). Taking an example of the gray value distribution along Γ_X direction for the aqueous solution of RF (corresponding to [RZ] = 0.042 g L^{-1}) flowing inside the tube, this distribution, inserted in Fig. 4-1, clearly demonstrated that the gray values were not uniform along the Γ_X direction of the tubing order number N° 11: they were lower at the centerline of the tube and higher at the edge of the tube wall (note that gray value ranged from 0 to 2^{16}-1, corresponding to black and white respectively). This parabolic shape of the gray value distribution was due to the variable liquid thicknesses along the tube circular cross section, which led to more dark color (i.e., smaller gray values) being cumulated at the centerline of the tube. To overcome this issue of non-uniform distribution, a pixel-by-pixel calibration was applied to minimize the errors, which meant that the calibration relation curve

was calculated independently, pixel by pixel. The comparisons of the global calibration and pixel-by-pixel calibration are given in Appendix 6.

Fig. 4-2 (a) shows typical relationships between the equivalent O_2 concentration and the normalized difference of gray value, ΔG:

$$\Delta G = \frac{I_0 - I}{I_{00}} \tag{4-1}$$

where I_0 and I were the gray intensities at a zero resorufin concentration and at a given concentration, respectively, and I_{00} was the maximum 16-bit intensity, at 2^{16}-1.

In Fig. 4-2 (a), two representative pixels, named Pixel 1 and Pixel 2, have been chosen from the images to show the regressed linear relations using the least squares method (MAPER varied between 10% and 17%). Pixels 1 and 2 represented the pixels with 10% and 17% MAPER and were close to the tube wall and the tube centerline, respectively. Because of the changing thickness at different radial positions, more intensities cumulated around the tube centerline, leading to larger values of ΔG for the Pixel 2. After applying the pixel-by-pixel calibration to the raw image (Fig. 4-2 (b)), the corresponding equivalent O_2 concentration field was obtained, as illustrated in Fig. 4-2 (c). All parts except for those corresponding to the liquid slugs were erased and set to zero concentration (blue color in Fig. 4-2 (c)).

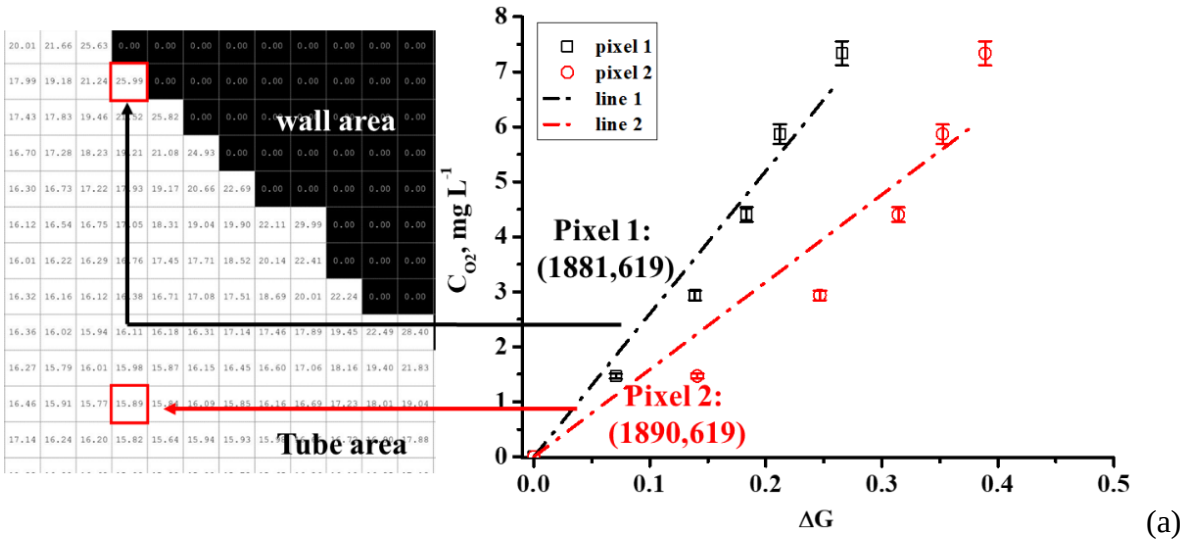

(a)

(b)

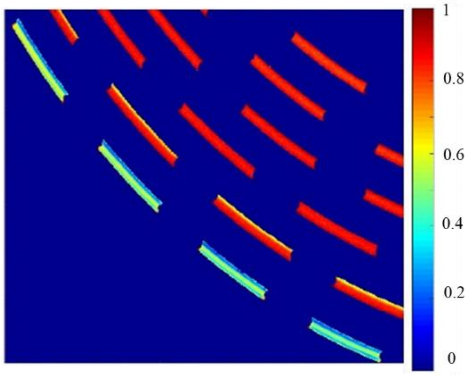

(c)

Fig. 4-2 Gas-liquid mass transfer in the in-plane spiral-shaped milli-reactor: (a) examples of individual linear calibration curves between gray value differences and equivalent O_2 concentration for two representative pixels on the image. (b) Partial raw image of gas-liquid flows. (c) Partial equivalent O_2 concentration field (normalized by the maximum concentration). Operating conditions: Re_L = 16.2, Re_G = 0.6, Re_{TP} = 24, η_0 = 0.45, ⟨De⟩ = 2.0, ET.

4.2 Results and discussion

4.2.1 Equivalent oxygen concentration fields

After applying the pixel-by-pixel calibration, the equivalent O_2 concentration in the liquid slug of one unit cell (averaged over the tube depth),

was extracted at a certain axial position X (the mass centroid position of the liquid slug) from the image processing as follows:

$$\overline{C_{O_{2_L}}}(X) = \frac{\iiint C(x,y)\,dx\,dy\,dz}{\langle L_S \rangle\,\Omega} \tag{4-2}$$

where Ω was the cross-sectional area of the tube and X represented the distance from the T-junction (i.e., X = 0 was the position of bubble formation). It is important to note that this integral was calculated by considering only the liquid slug volume, and not the liquid film around bubbles. Unfortunately, due to the limited resolution of the camera and to the tiny thickness of the liquid film assuming the latter would occur (varying from 3.5 to 15.8 μm, see section 3.1.2), the concentration in the liquid film could not be measured.

Fig. 4-3 (a) presents the equivalent O_2 concentration fields in the liquid slugs along the axial positions in the tube for the ET configuration. The time indicated in the figure corresponded to the time required for the liquid slug, in the black box, to travel to that position from the T-junction (where gas and liquid started to contact), and the liquid slug in the black box represented the considered liquid slug. It can be observed that, as the bubbles flowed along the channel, the amount of equivalent O_2 in the liquid slug increased gradually until an equilibrium steady state was reached (no more color change, i.e., no more RF increase).

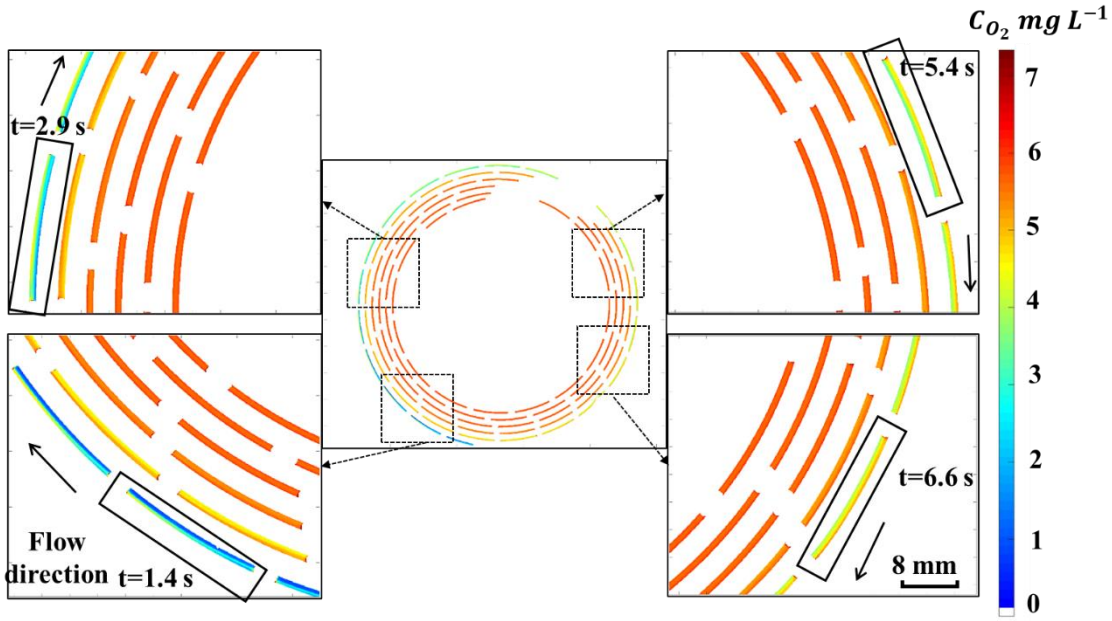

(a)

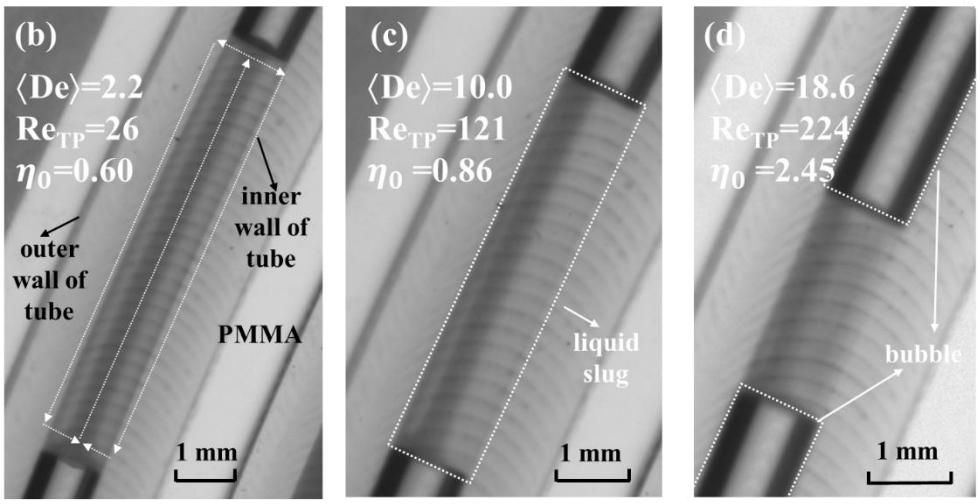

Fig. 4-3 Gas-liquid mass transfer in the in-plane spiral-shaped milli-reactor: (a) equivalent O_2 concentration fields in the liquid slugs: the time indicated in the figure corresponds to the time required for the liquid slug (in the black box), to travel to that position from the T-junction (operating conditions: Re_L = 64.9, Re_G = 1.0, Re_{TP} = 78, η_0 = 0.2, and ⟨De⟩ = 6.5, ET, flow direction is indicated using arrows). (b), (c), (d) Local raw visualization of the reactive RF color distribution in the liquid slugs at X = 0.1 m, operating conditions: (b) Re_L = 16.2, Re_G = 0.7, Re_{TP} = 26, η_0 = 0.6 and ⟨De⟩ = 2.2; (c) Re_L = 64.9, Re_G = 4.2, Re_{TP} = 121, η_0 = 0.86 and ⟨De⟩ = 10.0; (d) Re_L = 64.9, Re_G = 12.0, Re_{TP} = 224, η_0 = 2.45 and ⟨De⟩ = 18.6; ET.

From the flow patterns inside the liquid slug visualized in Fig. 4-3 (b) and (c), the symmetrical liquid recirculation loops that appeared inside the liquid slugs for straight tubes could no longer be observed when ⟨De⟩ increased. In Fig. 4-3 (d), with a further increase of Re_{TP} and ⟨De⟩, the reactive RF color had a more homogeneous distribution in the liquid slug compared to the previous two cases.

Fig. 4-4 shows the variation of the average equivalent O_2 concentration inside the liquid slug, normalized by the maximum concentration C_{max} (6.5 mg L^{-1}, see Appendix 6) in the liquid slug, along the axial position, for both tubing configurations (i.e., ET and MT), and with two identical sets of operating conditions (with same Re_{TP} and gas-liquid superficial velocity ratio $\eta_0 = j_{G0}/j_L$). First, a good fit with experimental data was obtained using the function $\frac{C_{O2}}{C_{max}} = 1 - \exp(-\gamma X)$, where γ was a regression coefficient dependent on the operating conditions. The percentage of the standard deviation (STD, see Appendix 5) between experimental and fitted data were smaller than 5% for all the operating conditions. Second, whatever the operating conditions, the equivalent O_2 concentration increased rapidly along the tube until it reached a constant value, i.e., $\frac{C_{O2}}{C_{max}} = 1$. When all the molecules of DH were consumed by the transferred oxygen, there was no more change in the equivalent O_2 concentration. For the RZ concentration used (0.105 g L^{-1}), this occurred for axial locations X larger than 1 m, whatever the operating conditions.

To uncouple the effects of centrifugal forces from the inertial forces, it was necessary to fix the value of Re_{TP}, the average Dean numbers in MT being 1.31 times higher than in ET ($\langle De \rangle_{MT} = 1.31 \langle De \rangle_{ET}$). In Fig. 4-4, under identical Re_{TP} and η_0, the equivalent O_2 concentration at the same axial position X was significantly higher in the MT than that in the ET. This indicated that there was a significant intensification of mass transfer rates caused only by the centrifugal forces (i.e., by smaller tube spiral radius), leading to a faster increase of the equivalent O_2 concentration in the MT configuration.

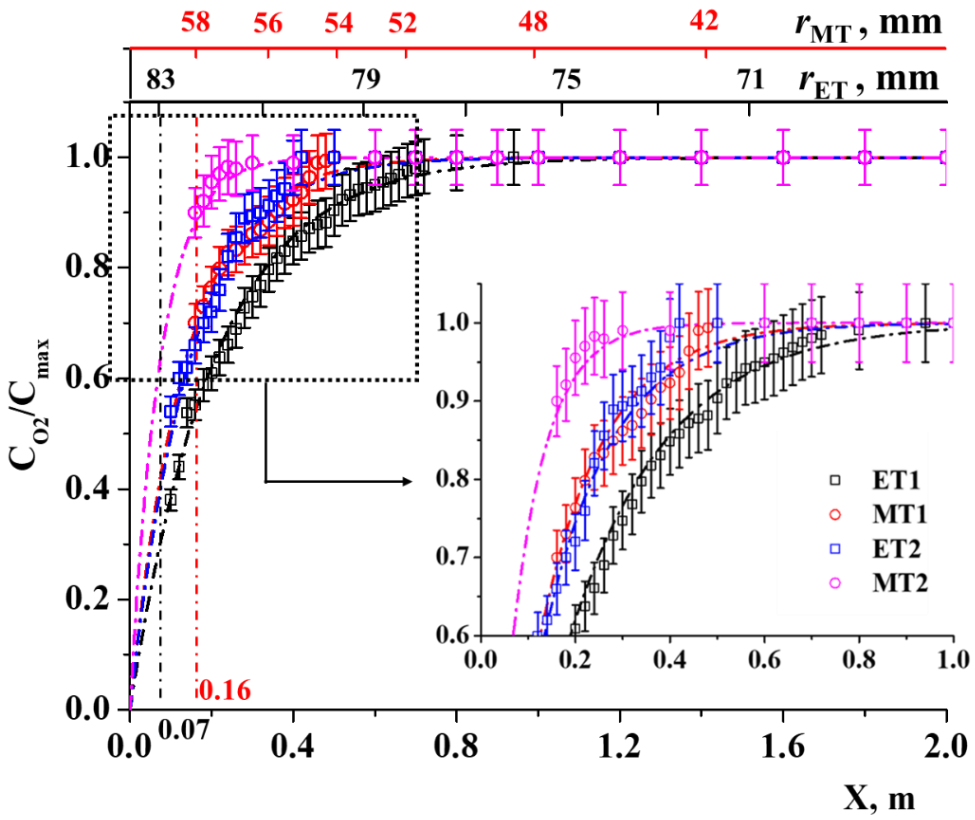

Fig. 4-4 Gas-liquid mass transfer in the in-plane spiral-shaped milli-reactor: comparison of the axial evolution of normalized average equivalent O_2 concentration in the liquid slug along the tube for different operating conditions (ET1 and MT1: Re_L = 16.2, Re_G = 0.7, Re_{TP} = 26, η_0 = 0.6, ET2 and MT2: Re_L = 32.4, Re_G = 6.3, Re_{TP} = 116, η_0 = 2.58). Here the points and lines represent experimental data and calculated data according to the exponential function $\mathbf{1 - exp\ (-\gamma X)}$, respectively. The second abscissa axis (at the top) gives the spiral radius for each configuration, corresponding to the axial position (reported on the principal abscissa axis, at the bottom).

The axial positions at which 99% of C_{max} was achieved, noted $X_{coloration}$, were plotted in Fig. 4-5 for all the operating conditions. Generally, $X_{coloration}$ was achieved after a second spiral turn for ET and MT. It can be observed that $X_{coloration}$ values in the MT were smaller than those in the ET configuration, thus confirming that the centrifugal force had an intensification effect on the mass transfer rates. In addition, $X_{coloration}$ decreased with increasing η_0 (i.e., gas Reynolds number Re_G)

at a given liquid Reynolds number Re_L, which corresponded to a faster achievement of C_{max} in shorter liquid slugs and higher Re_{TP}.

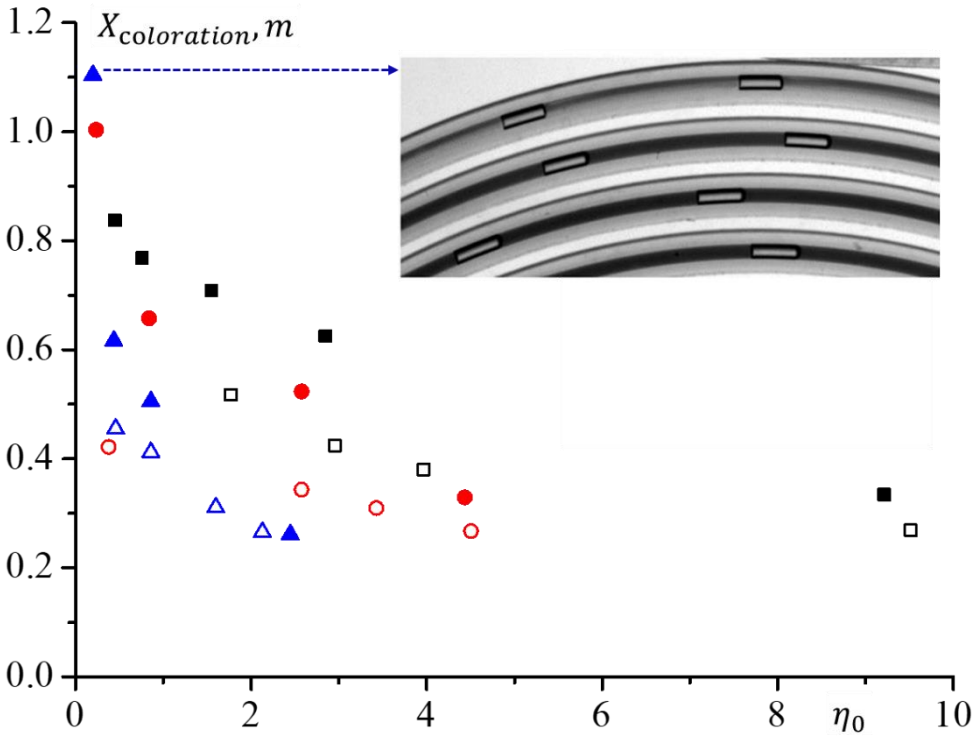

Fig. 4-5 Gas-liquid mass transfer in the in-plane spiral-shaped milli-reactor: variation of the axial position $X_{coloration}$ for which C_{max} was achieved with the gas-liquid superficial velocity ratio η_0, solid and empty symbols represent ET and MT, Re_L = 16.2 (black color), 32.4 (red color), and 64.9 (blue color).

When Re_L was much higher than Re_G, (small η_0, see the solid blue triangle point in Fig. 4-5), the ratio between the average liquid slug length and bubble length, $\langle L_S \rangle$ / $\langle L_B \rangle$, was 3.5 (meaning very long liquid slugs), and the distances required to reach C_{max} were significantly longer than other conditions.

4.2.2 Mass transfer

As the experiments were carried out in long tubes (~3m), non-negligible changes of the bubble length (noted L_B) and bubble velocity (noted U_B) along the length of the tube, and a significant pressure drop were observed in Chapter 3.

Two different mechanisms could contribute to such variations: pressure drop and mass transfer of O_2 from the gas to the liquid. They had opposite effects: mass transfer of O_2 from gas to liquid tended to decrease the bubble volume while the pressure drop resulted in gas expansion. The centrifugal effects induced by the tube curvature (Dean number) could also act on these phenomena and modify their contributions. For these reasons, in the following calculations, the variation of bubble volume and velocity, and the pressure drop along the tube should be considered.

The overall volumetric liquid side mass transfer coefficient $k_L \cdot a$ along the tube length could be deduced from the oxygen mass balance in the liquid phase, and changed during the mass transfer process (instead of assuming a constant value):

$$\frac{\mathrm{d}\overline{C_{\mathrm{O_{2L}}}(X)}}{\mathrm{d}t} = E\ k_{\mathrm{L}}(X)\ a(X)\ (C^*_{\mathrm{O_{2L}}}(\mathrm{X}) - \overline{C_{\mathrm{O_{2L}}}(X)}_{rl}) \tag{4-3}$$

where t represented here the time required for the bubble to travel to the position X from the T-junction ($t = X / \langle U_B \rangle$) and $\overline{C_{\mathrm{O_{2L}}}(X)}_{rl}$ was equal to zero because of a full consumption of O_2 by DH in the liquid slug. E was the chemical enhancement factor, which was the ratio between the average mass fluxes with the resazurin-based reaction, and with the pure physical absorption, and $C^*_{O_{2L}}$ was the O_2 concentration at saturation (calculated accounting for pressure drop, see Appendix 7). Note that all the parameters involved in Eq. (4-3) depended on the axial position.

4.2.3 Average overall volumetric mass transfer coefficient

In a first step, the average overall volumetric liquid side mass transfer coefficients, $k_L \cdot a$, were calculated simply and directly. For that, $C^*_{O_{2L}}$, and $k_L \cdot a$

were assumed constant during the whole mass transfer process, and the average gas-liquid hydrodynamics (e.g., $\langle U_B \rangle$) were considered. From the stoichiometry of dihydroresorufin and O_2, two moles of DH react with one mole of O_2, and the relationships between $\overline{C_{O_{2_L}}(X)}$ and the resazurin concentration are (Dietrich et al., 2019):

$$\frac{1}{M_{O2}} \frac{\mathrm{d}\overline{C_{O_{2L}}}}{\mathrm{d}t} = -\frac{1}{2} \frac{\mathrm{d}n_{DH}}{\mathrm{d}t} = -\frac{1}{2} \frac{1}{M_{RZ}} \frac{\mathrm{d}C_{RZ}}{\mathrm{d}t} \tag{4-4}$$

where M_{O2} and M_{RZ} were the molar masses of O_2 and resazurin, respectively. The n_{DH} and C_{RZ} were the molar amount of DH and the mass concentration of resazurin, respectively.

In addition, the overall volumetric liquid side mass transfer coefficients $k_L \cdot a$ could be deduced from Eq. (4-3). Various authors (Yang et al., 2017a; Dietrich et al., 2019) have found that the enhancement factor E was equal to 1 when the order of magnitude of k_L was about 10^{-4} m s^{-1} (typically encountered in milli-reactors). Therefore, E was considered equal to 1 here.

By combining Eqs. (4-3) and (4-4) and integrating from t=0 to the full coloration time, $t_{coloration}$, the following equation could be thus deduced to obtain the average overall volumetric liquid side mass transfer coefficients, noted $\langle k_L \cdot a \rangle$:

$$\langle k_L\, a \rangle = \frac{C_{RZ}}{\langle C^*_{O_{2L}} \rangle} \frac{M_{O2}}{2\, M_{RZ}} \frac{1}{t_{coloration}} \tag{4-5}$$

where the coloration time $t_{coloration}$ was equal to $X_{coloration} / \langle U_B \rangle$.

Similarly, the Eq. (4-5), in which C_{RZ} was included, was a general formula to conveniently link $t_{coloration}$ and $\langle k_L \cdot a \rangle$, as adopted in Dietrich et al. (2019) for bubbles rising in stagnant liquid. As long as the axial location ($X_{coloration}$) achieving the full coloration was deduced for each operating condition (shown in Fig. 4-5), $\langle k_L \cdot a \rangle$ can be directly evaluated from Eq. (4-5).

As the Taylor vortices inside the liquid slug play an important role in the mass transfer mechanism, it is interesting to consider the frequency of the recirculation loops adopted from Abiev et al. (2019) as:

$$f_c = \frac{j_{TP} - \langle U_B \rangle / 2}{2 \langle L_S \rangle} \approx \frac{\langle U_B \rangle}{4 \langle L_S \rangle} \tag{4-6}$$

which reflected the amount of elementary mass transfer per unit of time.

In Fig. 4-6, the average overall volumetric liquid side mass transfer coefficient, $\langle k_L \cdot a \rangle$, (deduced from Eq. (4-5)) is plotted against the frequency f_c. It can be seen that (i) whatever the tubing configuration, $\langle k_L \cdot a \rangle$ varied linearly with f_c, which was physically consistent, and (ii) at the same f_c, $\langle k_L \cdot a \rangle$ were rather higher in MT than in ET.

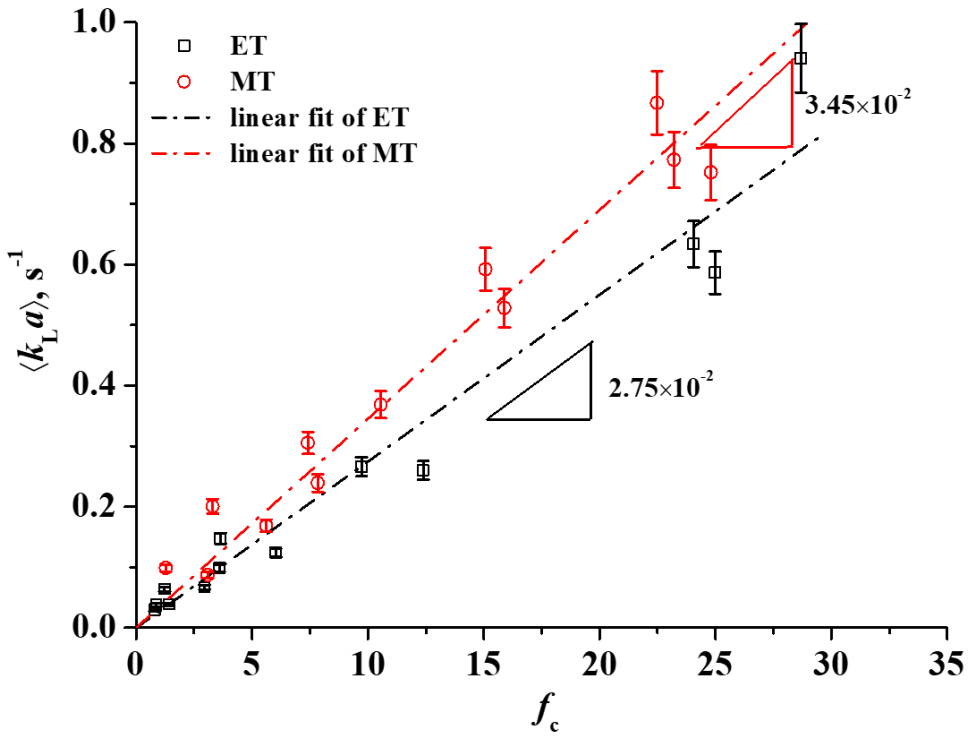

Fig. 4-6 Gas-liquid mass transfer in the in-plane spiral-shaped milli-reactor: relations between the average overall volumetric liquid side mass transfer coefficient, $\langle k_L \cdot a \rangle$, and the frequency of loop recirculation f_c.

To better quantify the latter observation, these average overall coefficients were fitted by linear relations using least squares regression, as follows,

$$\langle k_L.a\rangle = \omega\, f_c \tag{4-7}$$

where ω was a linear dimensionless coefficient that depended on the tubing configuration.

The intensification factor of centrifugal force for two configurations was introduced as follows:

$$E_{\mathrm{De}} = \frac{\omega_{MT}}{\omega_{ET}} \tag{4-8}$$

The linear dimensionless coefficients for ET and MT were found equal to 2.75×10^{-2} and 3.45×10^{-2}, respectively, thus leading to an E_{De} of 1.25. In addition, the average square root of the inverse of the average curvature ratio increased 1.31 times from ET to MT (i.e., $\sqrt{\frac{1}{<\lambda>}}_{MT} / \sqrt{\frac{1}{<\lambda>}}_{ET} = 1.31$). This finding would suggest that the intensification factor for mass transfer between the two curvature ratio configurations was almost proportional to the increase of $\sqrt{\frac{1}{<\lambda>}}$ (mean absolute deviation, MAD = 2%, see Appendix 5), such that:

$$E_{\mathrm{De}} = \frac{\langle k_L{\cdot}a\rangle_{MT}}{\langle k_L{\cdot}a\rangle_{ET}} \approx \sqrt{\frac{<\lambda>_{ET}}{<\lambda>_{MT}}} \tag{4-9}$$

This result was consistent with the linear relation found by Tan et al. (2012b), showing that the intensification of the mass transfer coefficients was closely related to the curvature ratio.

Finally, it can be observed that the present $\langle k_L{\cdot}a\rangle$ values had the same order of magnitude as those in Yang et al. (2017a) and Roudet et al. (2011). In addition, the experimental $\langle k_L{\cdot}a\rangle$ were compared to the predicted $\langle k_L{\cdot}a\rangle$ using some correlations from the literature. As shown in Fig. 4-7, the values predicted using the correlation of Van Baten and Krishna (2004) only considered the contribution of the bubble caps, $(k_L{\cdot}a)_{\mathrm{cap}}$. It can be seen that the values predicted by Bercic and Pintar (1997) and Vandu et al. (2005) were higher than the experimental data,

which was quite reasonable because the present experimental data did not include the contribution from the bubble body to the liquid film. In addition, when η_0 was smaller than 2, there was good agreement between the values predicted using Van Baten and Krishna (2004) and the experimental data, but an underestimation when η_0 was larger than 2. This can be explained by the complex flow caused by the overlap of the Taylor flow and the Dean flow for η_0 greater than 2. In this case, as liquid slug lengths were half the bubble lengths, the times for one recirculation were significantly decreased, leading to higher $\langle k_L \cdot a \rangle$ compared to predicted values.

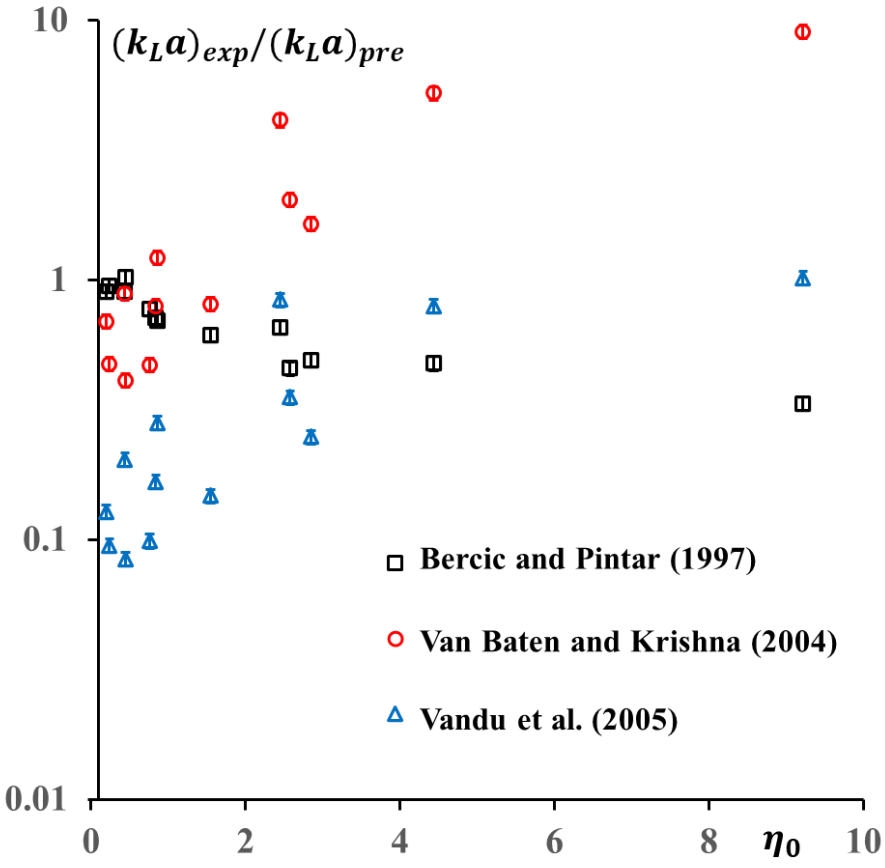

Fig. 4-7 Gas-liquid mass transfer in the in-plane spiral-shaped milli-reactor: ratio between experimental $(k_L \cdot a)_{exp}$ and predicted $(k_L \cdot a)_{pre}$ versus the gas-liquid superficial velocity ratio η_0.

4.2.4 Axial variation of the mass flux density

The available bubble surface for mass transfer, S_B, accounting for the contribution of the liquid film or not, could be estimated considering two cases:

- (case S1) the liquid film around a Taylor bubble was considered, then $S_B(X) = \pi d_{it}(\frac{d_{it}}{2} + L_B(X))$
- (case S2) the liquid film around the Taylor bubble was not considered, then $S_B = \frac{\pi d_{it}^2}{2}$

The corresponding axial mass flux density φ_{O_2}(X) was then calculated for two cases respectively. The procedure implemented to calculate the axial evolution of the mass flux density and Sherwood number is shown in Table 4-1.

Table 4-1 Gas-liquid mass transfer in the in-plane spiral-shaped milli-reactor: the axial mass flux density and Sherwood number considering LF (Liquid Film) or not.

<table>
<tr><td colspan="2">Step 1: obtain the oxygen mass $m_{O_2}(X)$ in one liquid slug, kg
$m_{O_2}(X) = \iiint C(x,y)\,\mathrm{d}x\,\mathrm{d}y\,\mathrm{d}z$</td></tr>
<tr><td colspan="2">Step 2: compute the instantaneous mass flux density in one unit cell, kg m^{-2} s^{-1}
$\varphi_{O_2}(X) = \frac{U_B(X)}{S_B(X)}\frac{\mathrm{d}m_{O_2}(X)}{dX}$</td></tr>
<tr><td>without considering LF
$S_B = \frac{\pi {d_{it}}^2}{2}$</td><td>considering LF
$S_B(X) = \pi d_{it}(\frac{d_{it}}{2} + L_B(X))$</td></tr>
<tr><td colspan="2">Step 3: calculate Sh number from accumulated mass flux density in one unit cell;
$\mathrm{Sh}(X) = \frac{\langle\varphi_{O_2}(X)\rangle \cdot d_B(X)}{E \cdot C^*_{O_{2L}}(X) \cdot D_{O2}}$ where $\langle\varphi_{O_2}(X)\rangle_j = \frac{\sum_{i=1}^{j}[\varphi_{O_2}(X)_i]}{j}$, j ≤ n,</td></tr>
<tr><td>without considering LF
$d_B = \frac{d_{it}}{\sqrt{2}}$</td><td>considering LF
$d_B = \sqrt{\frac{d_{it}}{2}(d_{it} + 2L_B(X))}$</td></tr>
</table>

To make the mass flux density dimensionless, the Sherwood number based on the cumulated mass flux density, Sh, was introduced:

$$\mathrm{Sh}(X) = \frac{\langle \varphi_{O_2}(\mathrm{X}) \rangle \, d_B(X)}{E \, D_{O2} \, C^*_{O_2 L}(X)} \tag{4-10}$$

where d_B was the equivalent diameter of a spherical bubble having a surface area identical to the one measured, which was also significantly dependent on the assumption made for the liquid film (see Table 4-1).

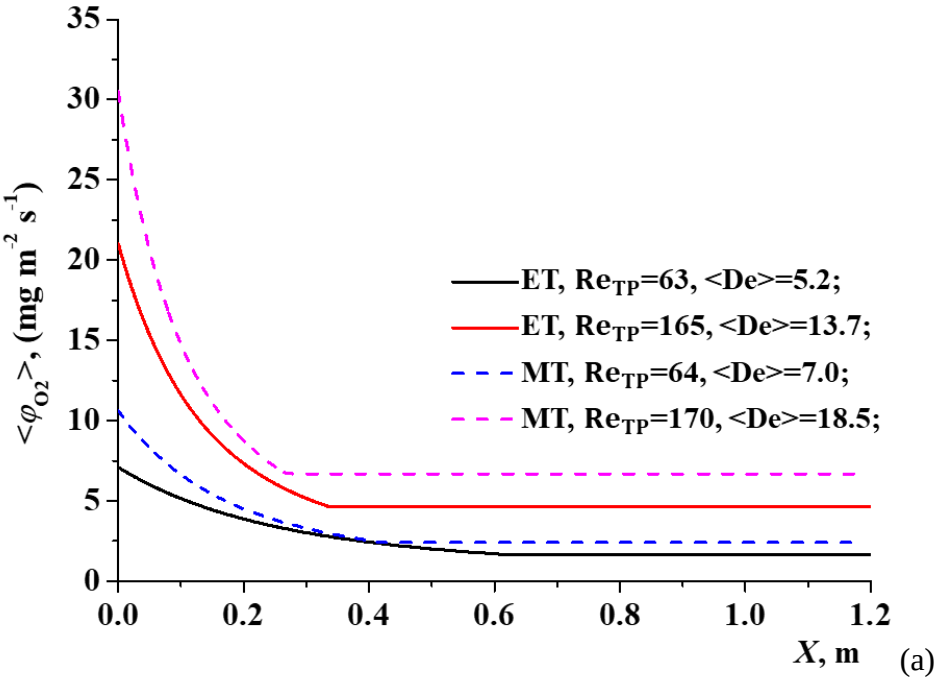

(a)

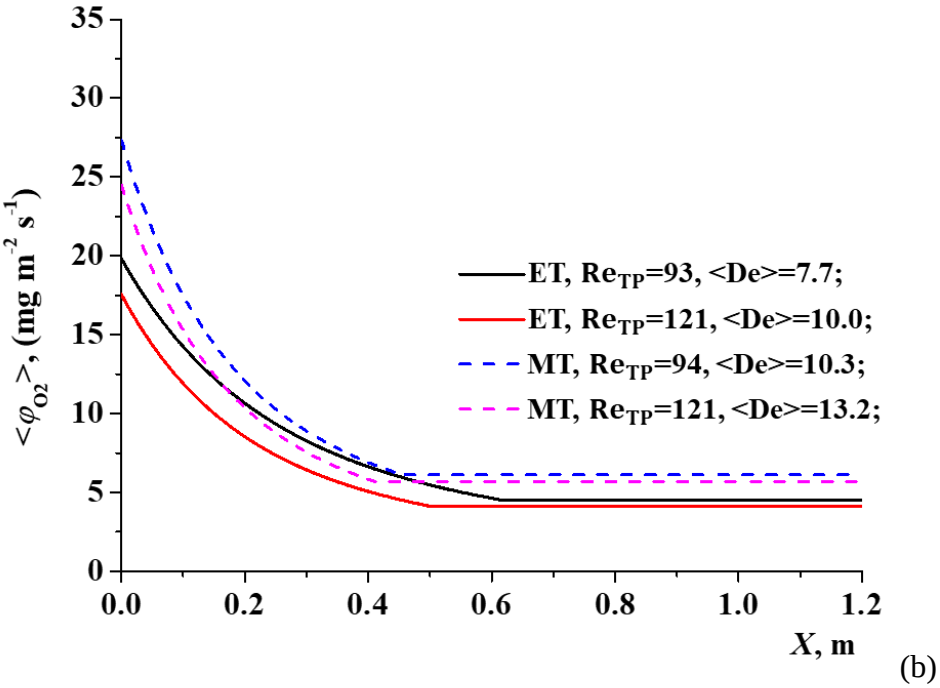

(b)

Fig. 4-8 Gas-liquid mass transfer in the in-plane spiral-shaped milli-reactor: Axial variation of the cumulated mass flux density $\langle \boldsymbol{\varphi_{O_2}}(\boldsymbol{X}) \rangle$ (case S2, without considering LF) for the tubing configurations ET and MT: (a) Re_L = 16.2; (b) Re_L = 64.9.

$\langle \varphi_{O_2}(X) \rangle$ was the mass flux density cumulated in the liquid slugs along the whole length of the tubing, and was intended to take former mass flux into account:

$$\langle \varphi_{O_2}(X_j) \rangle = \frac{\sum_{i=1}^{j} [\varphi_{O_2}(X_i)]}{j} \qquad i=1,2,3\ldots,j; \qquad j=2,3\ldots,n, \tag{4-11}$$

where X_n represented the axial position corresponding to the fully saturated position (i.e., to $X_{coloration}$). From 0 to $X_{coloration}$, the X axis was divided into n sections in total and the difference between adjacent axial positions was 10^{-4}, i.e., $\Delta X = X_{i+1}-X_i = 10^{-4}$ m. The subscript i varied from 1 to j and j varied from 2 to n.

Fig. 4-8 presents the axial variation of the cumulated mass flux density $\langle \varphi_{O_2}(X) \rangle$ at various liquid Reynolds numbers, Re_L, for both ET and MT tubing configurations (the mass flux density here was calculated without considering LF, case S2). It can be observed that, whatever the operating condition, $\langle \varphi_{O_2}(X) \rangle$ gradually decreased along the X and finally tended towards a constant value. A similar trend was also found in case S1 (with considering LF).

At a given Re_L, $\langle \varphi_{O_2}(X) \rangle$ was higher in the MT than in the ET configuration. At Re_L = 16.2 and for the same configuration, $\langle \varphi_{O_2}(X) \rangle$ increased with Re_{TP} (see Fig. 4-8 (a)). Surprisingly, in Fig. 4-8 (b), at Re_L = 64.9, an opposite trend was observed. A reasonable explanation for this discrepancy could be that the decrease of $\langle L_S \rangle$ (e.g., -44% in ET) was more pronounced compared to the increase of $\langle U_B \rangle$ (e.g., 29% in ET).

The "intrinsic" Sherwood number, Sh (i.e., the one corresponding to the physical absorption process) can be estimated from the measured apparent Sherwood number (using the resazurin colorimetric method) if the enhancement factor, E, was known. According to Van Krevelen and Hoftijzer (1948), the

approximate solution (implicit) of E could be estimated by introducing Hatta number for the second-order reaction.

$$E = \frac{\mathrm{Ha}\sqrt{(E_i - E)/(E_i - 1)}}{\tanh\left(\mathrm{Ha}\sqrt{(E_i - E)/(E_i - 1)}\right)} \tag{4-12}$$

where E_i and Ha were the limit enhancement factor and the Hatta number, respectively. The Hatta number represented the ratio between the reaction rate and the diffusion rate in the liquid film. They were further expressed as follows.

$$E_i = 1 + \frac{D_{DH}\, C_{DH,0}}{2 D_{O2}\, C^*_{O2}} \tag{4-13}$$

$$Ha = \frac{\sqrt{k_2\, C_{DH,0}\, D_{O2}}}{k_L} \tag{4-14}$$

where the liquid side mass transfer coefficient, k_L, can be deduced using the measured Sherwood number Sh:

$$k_L = \frac{\mathrm{Sh}\, D_{O2}}{d_B(X)} = \frac{\langle \varphi_{O_2}(\mathrm{X}) \rangle}{E\, C^*_{O_2 L}(X)} \tag{4-15}$$

Therefore, from Eqs. (4-12) to (4-15), Ha and E could be calculated by solving the following two implicit equations:

$$E = \frac{\mathrm{Ha}\sqrt{\left(1 + \frac{D_{DH} C_{DH,0}}{2 D_{O2} C^*_{O2}} - E\right) \Big/ \left(1 + \frac{D_{DH} C_{DH,0}}{2 D_{O2} C^*_{O2}} - 1\right)}}{\tanh\left(\mathrm{Ha}\sqrt{\left(1 + \frac{D_{DH} C_{DH,0}}{2 D_{O2} C^*_{O2}} - E\right) \Big/ \left(1 + \frac{D_{DH} C_{DH,0}}{2 D_{O2} C^*_{O2}} - 1\right)}\right)} \tag{4-16}$$

$$Ha = \frac{E\, C^*_{O_2 L}(X)\sqrt{k_2\, C_{DH,0}\, D_{O2}}}{\langle \varphi_{O_2}(\mathrm{X}) \rangle} \tag{4-17}$$

The reaction rate constant k_2 of 1.28×10^6 L mol^{-1} s^{-1} found by Yang et al. (2016a) was adopted here. Note that some subsequent measurements were later implement by Hoppe (2019) and will be considered in Chapter 5.

- (case S1) The Hatta numbers were found to be greater than 5 for all operating cases, both in ET and MT, and the enhancement factor ranged from 1.07 to 1.08;
- (case S2) When the Hatta numbers ranged between 3 and 17, the enhancement factors were between 1.05 and 1.07 and, when Ha ranged from 0.3 to 3 for other operating conditions, *E* tended towards unity.

Thus, from these calculations, the overestimation of the Sherwood number caused by chemical reaction (oxidation of DH to RF) was below 10% for all conditions and was neglected in the subsequent section.

4.2.5 Scaling laws for the cumulated Sherwood number

The former variation was described using dimensional parameters, namely, $\langle\varphi_{O_2}(X)\rangle$. In a first attempt to group all the experimental data in a single master curve, the Sherwood number and a normalized time *t** defined from the coloration time were introduced:

$$t^* = \frac{t}{t_{\text{coloration}}} = \frac{X}{\langle U_B\rangle\, t_{\text{coloration}}} = \frac{X}{4\, N_{\text{circulation}}\, \langle L_S\rangle} \tag{4-18}$$

where $N_{\text{circulation}}$ was defined as the number of recirculation loops needed to reach the full coloration time:

$$N_{\text{circulation}} = \frac{t_{\text{coloration}}}{t_{\text{circulation}}} = \frac{t_{\text{coloration}}}{4\langle L_S\rangle/\langle U_B\rangle} \tag{4-19}$$

The average numbers $N_{\text{circulation}}$ for ET and MT were found to be 32.7 ± 4.4 and 26.1 ± 3.1, respectively. The cumulated Sherwood number could be

calculated with Eq. (4-10), in which the enhancement factor, *E*, was considered as the unit.

In addition, the Péclet number, Pe, was introduced to evaluate the effect of the ratio between the advective transport and diffusion transport rates:

$$\mathrm{Pe} = \langle \mathrm{Re_B} \rangle \, \mathrm{Sc} \tag{4-20}$$

where Sc was the Schmidt number, defined as $\mathrm{Sc} = \frac{\mu_\mathrm{L}}{\rho_L D_{O2}}$, fixed in the present study at 348. $\mathrm{Re_B}$ was the bubble Reynolds number, defined here as $\langle \mathrm{Re_B} \rangle = \frac{\rho_\mathrm{L} \langle U_\mathrm{B} \rangle \langle d_\mathrm{B} \rangle}{\mu_\mathrm{L}}$. To evaluate the effects of centrifugal force, the average Dean number, defined from $\langle \mathrm{De_B} \rangle = \langle \mathrm{Re_B} \rangle \sqrt{\frac{1}{\langle \lambda \rangle}}$, was also considered.

A scaling-law is thus proposed to separate the developing zone (entrance effect) from the fully developed zone by the normalized time *t**. This function is expressed as

- for $t^* \geq 1$ (fully developed zone):

$$\mathrm{Sh}(t^*) = \mathrm{W_1} \, \mathrm{Pe}^{0.5} \, \langle \mathrm{De_B} \rangle \, \frac{\langle L_\mathrm{S} \rangle}{d_{it}} \tag{4-21}$$

- for $t^* < 1$ (entrance zone):

$$\begin{aligned} \mathrm{Sh}(t^*) = {} & \mathrm{W_2} \, \mathrm{Pe}^{0.5} \, \langle \mathrm{De_B} \rangle \, \frac{\langle L_\mathrm{S} \rangle}{d_{it}} \, e^{-\mathrm{W_3} t^*} (1 - t^*) \\ & + \mathrm{W_1} \, \mathrm{Pe}^{0.5} \, \langle \mathrm{De_B} \rangle \, \frac{\langle L_\mathrm{S} \rangle}{d_{it}} \end{aligned} \tag{4-22}$$

where the exponential coefficient of Pe was fixed at 0.5, as verified by previous researchers (Kastens et al., 2015; Roudet et al., 2017; Yang, 2017).

All the experimental data obtained for ET and MT (25 operating conditions in total) were regressed by the nonlinear model in Matlab and two cases

(cases S1 and S2) were considered. The regressed coefficients are listed in Table 4-2, according to whether the liquid film is considered (case S1) or not (case S2). It can be seen that W_1 and W_2 in case S2 were almost 5 and 4 times higher than those in case S1. Such differences confirmed the importance of the liquid film contribution in the whole mass transfer. It was found that this scaling law enabled all the Sherwood numbers for both tubing configurations to be grouped together.

Table 4-2 Gas-liquid mass transfer in the in-plane spiral-shaped milli-reactor: regressed dimensionless coefficients of scaling laws for ET and MT.

Case	Configuration	$W_1\times10^3$	$W_2\times10^3$	W_3	$N_{circulation}$	MAPER
S1	ET	2.14	6.96	1.90	32.7	23%
(with LF)	MT				26.1	17%
S2	ET	10.78	30.68	2.01	32.7	25%
(without LF)	MT				26.1	20%

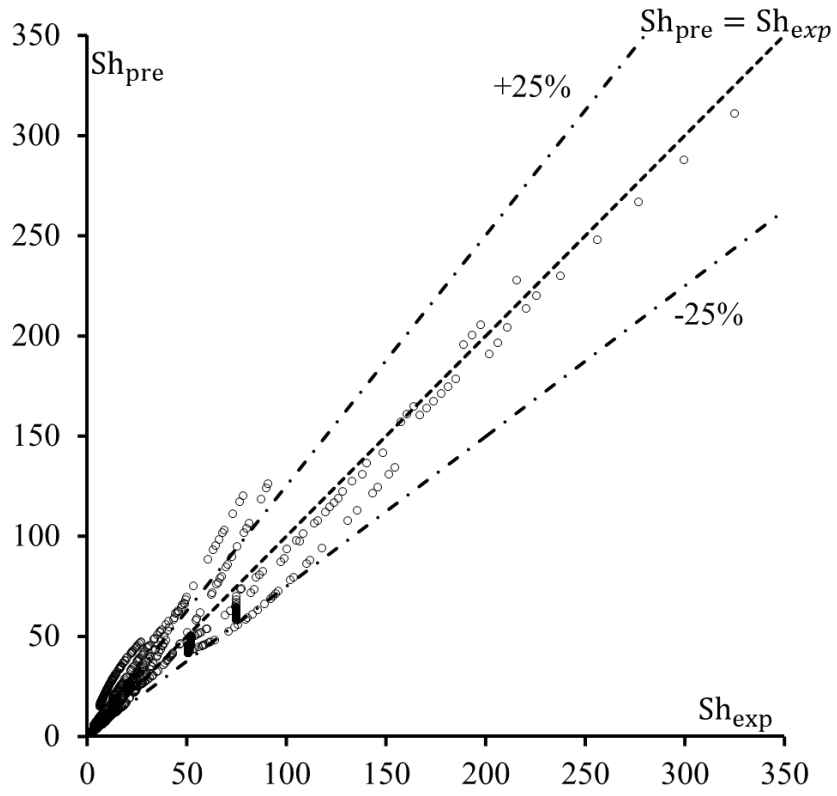

Fig. 4-9 Comparison between the predicted Sh_{Pre} and experimental Sh_{Exp} in case S2 (without LF) for ET configuration.

In Fig. 4-9, the predicted and experimental Sherwood numbers were compared using the worst conditions, i.e., highest deviation (i.e., case S2 in ET). It can be observed that the scaling law performed well for Sh > 100. When Sh < 100, the deviation became larger, which corresponded to some extreme conditions, namely when the liquid slug length L_S was very long and Re_B was very small. Under this condition, the recirculation time was quite long and deviated from the assumption of perfect mixing in the liquid slug. The proposed Sh scaling law thus leaded to an overestimation.

This first attempt of proposing a scaling law had the advantage of revealing and dissociating the entrance effects and steady state during mass transfer process. Eq. (4-21) represented the fully developed mass transfer state, obtained far from the T-junction, where the Sherwood number did not depend on the dimensionless time (i.e., on the axial position). The corresponding fully established Sherwood number, noted Sh_∞, was then proportional to $Pe^{0.5}$, $\langle De_B \rangle$ and $\langle L_S \rangle / d_{it}$. Therefore, Sh_∞ was higher in MT than ET due to a higher $\langle De_B \rangle$.

The entrance effect was represented by the first term in Eq. (4-22), corresponding to the initial time at bubble formation (i.e., $(W_1 + W_2)\, Pe^{0.5}\, \langle De_B \rangle\, \frac{\langle L_S \rangle}{d_{it}}$). It can be deduced that the entrance effect was affected by centrifugal forces for both cases and was proportional to $\langle De_B \rangle$. The time required to reach the fully developed zone was smaller for MT than ET, because a lower number of recirculation loops, $N_{circulation}$, was needed to achieve the fully developed zone in MT. This would suggest that the mass transfer dynamics were closely related to the recirculation intensities and also to the induced Dean flow (Zaloha et al., 2012).

4.3 Conclusion

The aim of this original experimental study was to investigate gas-liquid mass transfer around Taylor bubbles (air) in an in-plane, spiral-shaped milli-reactor. Using the resazurin-based colorimetric technique and advanced image processing, the axial variation of equivalent O_2 concentration in liquid slugs was experimentally characterized over a long distance (~ 3 m) inside the milli-reactor.

The main findings were the following:

1) Average overall volumetric liquid side mass transfer coefficients $\langle k_L \cdot a \rangle$ could be easily and directly acquired from the coloration position. They increased linearly with recirculation frequency f_c, which would suggest that the recirculation loops inside the liquid slugs played an important role in the mass transfer mechanism (i.e., $\langle U_B \rangle$ and $\langle L_S \rangle$). The intensification factor in terms of $\langle k_L \cdot a \rangle$ between the two configurations (ET and MT), was found almost identical to the increase of the average Dean number.
2) Considering the pressure drop, bubble expansion and bubble velocity increase, the axial variation of cumulated mass flux density $\langle \varphi_{O_2}(X) \rangle$ was deduced. It was found that $\langle \varphi_{O_2}(X) \rangle$ gradually decreased with the axial position and finally tended towards a constant value.
3) Finally, the cumulated Sherwood number was correlated with a normalized time (depending on the recirculation time), dimensionless liquid slug length, Péclet number and Dean number. An original scaling law was proposed for both ET and MT configurations, and discussed according to whether the liquid film was considered or not in the modeling. This law offered the advantage to dissociate the contribution of the entrance effects from the overall mass transfer.

All these findings could provide important information for implementing gas-liquid mass transfer in continuous-flow reactors. Future studies will need to

focus on the contribution of the liquid film to the mass transfer and further investigate the entrance effects.

Chapter 5. Bubble hydrodynamics during formation and flowing stages at a cross-junction in a straight milli-channel

Abstract

In this chapter, the investigations of bubble formation patterns and gas-liquid hydrodynamics at a cross-junction in a straight milli-channel were reported. The bubble formation process could be divided into the filling and squeezing stages, and their characteristic frequencies were compared at various conditions. It was found that the filling and squeezing frequencies were controlled mainly by the gas and liquid superficial velocities, respectively. The bubble formation was then characterized by the length of the gas finger (right after pinch-off) and two patterns were identified depending on if the pinch-off occurred inside of the cross-junction or not. Furthermore, the squeezing and dripping schemes of bubble formation were also identified depending on if the gas finger fully blocked the channel or not. The transitions between bubble formation patterns (or schemes) were determined by the gas Weber number and liquid Capillary number. From the analysis of bubble formation characteristic time, the bubble length could be theoretically predicted as $\frac{L_B}{w_{hl}} \propto 1 + \frac{w_{squeezing}}{w_{hl}} \frac{j_G}{j_L}$, which was consistent with the experimental results, indicating that the bubble formation process was composed of filling and squeezing stage. Finally, the wetting and dewetting phenomena were described.

Introduction

As reported in the Chapter 1 (section 1.2.1.2), the bubble formation regimes were identified by many researchers and found affected by various factors (e.g., Capillary and Weber numbers, the gas-liquid superficial velocity ratio, etc.). But the impact of bubble formation on mass transfer still needs further investigation. In Chapter 4, in the in-plane spiral shaped milli-reactor, and in meandering milli-channel as already shown by Yang et al. (2017a), it was observed that the mass transfer flux density, or Sherwood number, progressively decreased along the channel length until reaching a plateau. Such trend pointed out the occurrence of strong entrance effects which were related to the bubble formation step. To get a deeper understanding of the phenomena, this chapter will report the bubble hydrodynamics (such as the bubble formation regimes, bubble lengths, bubble velocities, etc.) at the cross-junction in a straight milli-channel. It will be served as basis for the subsequent Chapter 6, which will be devoted to the study of the mass transfer under the same conditions.

Section 5.1 gives out the experimental setup, image post-treatments and data processing for gas-liquid hydrodynamics. In section 5.2, the bubble formation mechanism will be presented, in terms of the bubble formation characteristic frequencies and bubble formation patterns. Section 5.3 describes the flow regimes and bubble shapes. In the section 5.4, the bubble lengths, liquid slug length and bubble velocities will be associated to the gas-liquid superficial velocity ratio and two-phase superficial velocities. The interfacial area is reported in section 5.5. At last, the wetting and dewetting phenomena of the liquid film are described in Section 5.6.

5.1 Materials and methods

5.1.1 Experimental setup

The experimental setup, flow control equipment and fluid properties were described in Chapter 2 (section 2.2.2).

5.1.2 Gas-liquid hydrodynamics

After the image acquisition step, an original Matlab program (implemented by Matlab® R2017b, see Appendix 4) was dedicated to extract the hydrodynamic characteristics, such as: the bubble length and velocity, and the liquid slug length, which were defined in Fig. 1-3.

5.2 Bubble formation mechanisms

5.2.1 Bubble formation characteristic times and frequencies

As previously introduced in Chapter 1 (section 1.2.1.2), the bubble formation at a cross-junction could be divided into three stages (Abadie, 2013):

- Filling (also called expansion) stage, shown from Fig. 5-1 (c) to (h). The gas finger (defined as the coming gas thread) grew and entered the main channel until it occupied most of the channel. In the meantime, the liquid from two side channels passed around the gas finger.
- Squeezing (also called expansion) stage, shown from Fig. 5-1 (i) to (o). The channel was mainly blocked by the growing gas finger, and then the bubble neck was squeezed until reaching a minimum neck width.

– Fast pinch-off stage, shown from Fig. 5-1 (o) to (p). This stage could be considered as an instantaneous breakup. The characteristic time of this process was far smaller compared to the previous two stages.

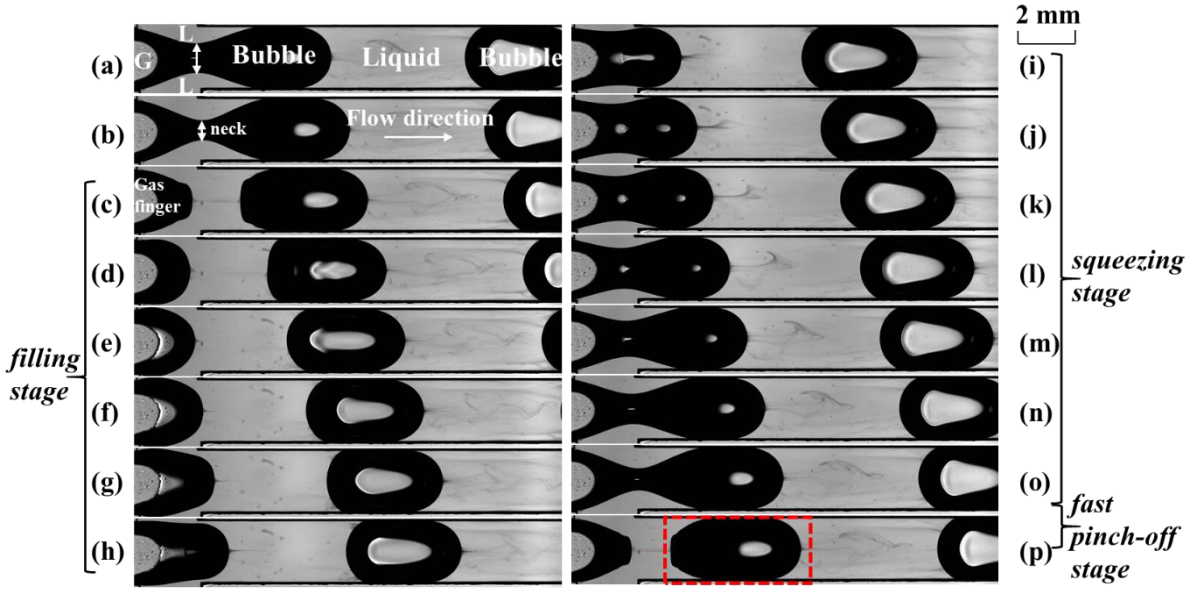

Fig. 5-1 Representative bubble formation process (air and RGN colorimetric solution) at the cross-junction, operating conditions: j_L = 17.9 and j_G = 10.7 cm s^{-1}. The time interval between image sequences is 2.5 ms.

With the present image acquisition frequency (400 fps), the characteristic time of fast pinch-off stage was hard to be separated from the squeezing stage and thus included into the squeezing stage. Therefore, the bubble formation time, t_{BF}, could be considered as below:

$$t_{BF} = t_{filling} + t_{squeezing} \tag{5-1}$$

Considering the frequency of each stage, they could be presented as below:

$$\frac{1}{f_{BF}} = \frac{1}{f_{filling}} + \frac{1}{f_{squeezing}} \tag{5-2}$$

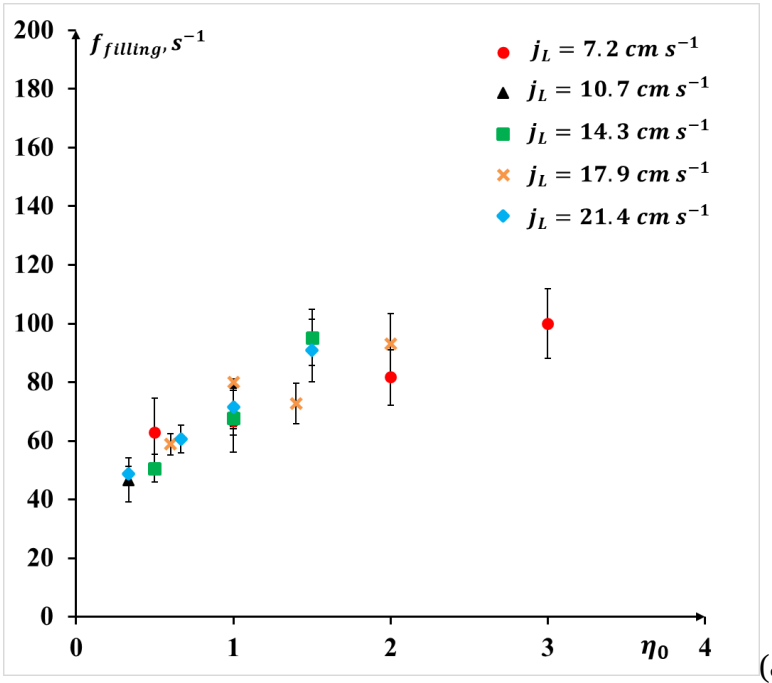

(a)

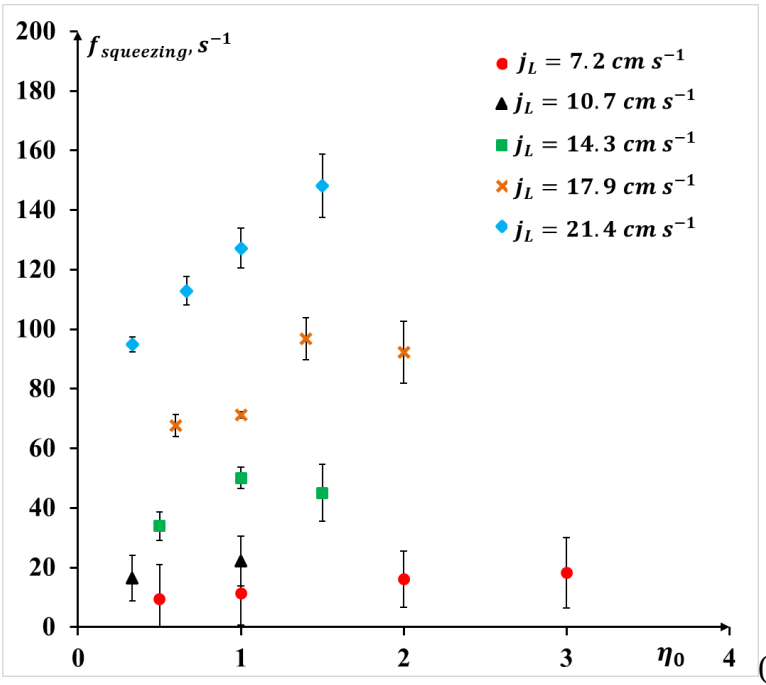

(b)

Fig. 5-2 Bubble formation mechanisms: frequencies of (a) the filling stage, (b) squeezing stage, as a function of the gas-liquid superficial velocity ratio η_0.

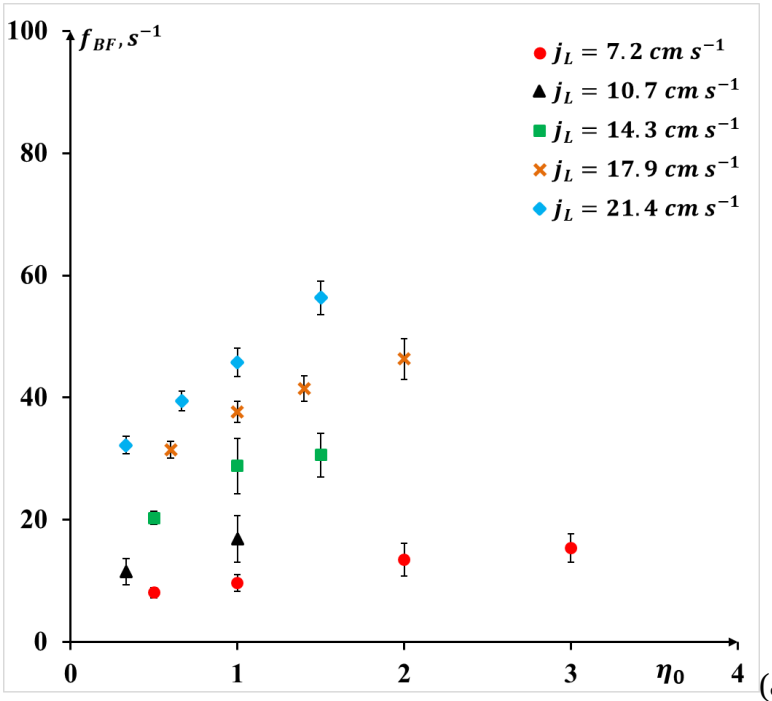

(a)

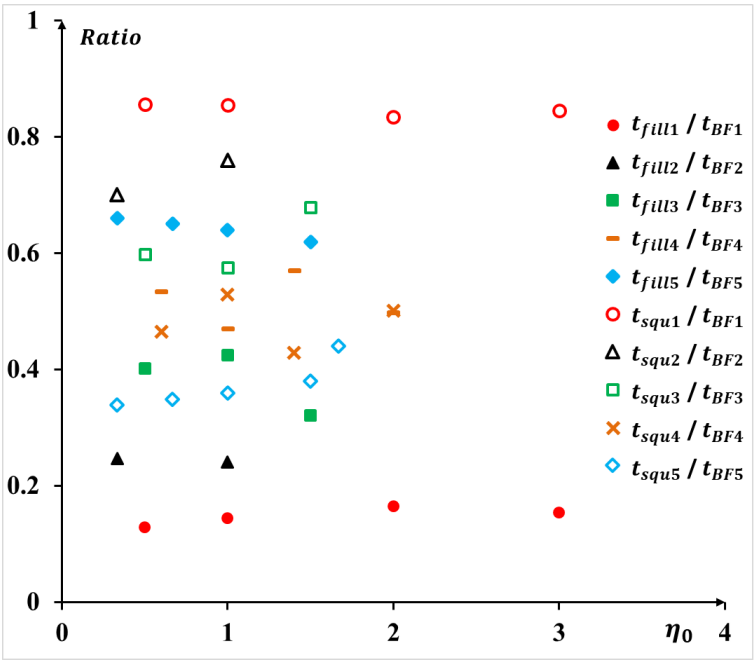

(b)

Fig. 5-3 Bubble formation mechanisms: (a) bubble formation stages as a function of the gas-liquid superficial velocity ratio η_0, (b) the ratio of the filling time and squeezing time compared to the overall bubble formation time. From 1 to 5, the number represents the liquid superficial velocities are at 7.2, 10.7, 14.3, 17.9, and 21.4 cm s^{-1}, respectively.

Fig. 5-2 shows the frequencies corresponding to the overall bubble formation process, the filling stage and the squeezing stage, and their variations with various gas-liquid superficial velocity ratios η_0 (for each operating condition,

500-1000 images were used). It can be observed from Fig. 5-2 (a) and (b) that the filling frequencies were slightly dependent on the superficial liquid velocities, contrary to the squeezing frequencies. At a given j_L, these two frequencies increased with the ratio η_0. Therefore, the bubble formation frequencies, shown in Fig. 5-3 (a), increased with the ratio η_0 at a given j_L, and vice versa.

Fig. 5-3 (b) displays the relative ratio for the filling and squeezing characteristic times compared to the overall bubble formation times. It is observed that, at a given η_0, with the increase of the liquid superficial velocities, the ratio between the filling time and formation time ($t_{filling}$ / t_{BF}) increased, and the ratio between the squeezing time and formation time ($t_{squeezing}$ / t_{BF}) decreased in the meantime. Thus, when the liquid superficial velocity j_L was small, the squeezing stage was the longest ($t_{squeezing}$ / t_{BF} ~ 0.85), whereas, for the highest j_L, the filling stage was the main contribution to the overall process ($t_{filling}$ / t_{BF} ~ 0.60 - 0.70). It is also interesting to note both ratios globally remained less sensitive to the gas-liquid superficial velocity ratio, especially for the lowest j_L.

5.2.2 Bubble formation patterns

As reviewed in the Chapter 1 (section 1.2.1.2), there were mainly three types of bubble formation regime: squeezing, dripping, and jetting.

Fig. 5-4 displays typical instantaneous gas-liquid Taylor flows right after the bubble pinch-off **(**i.e., at the cross- junction position X_1 = 0) for various operating conditions (j_L: 3.6 - 42.9 cm s^{-1}, j_G: 7.2 - 35.7 cm s^{-1}). The generated bubble sizes were bigger than the channel widths under present operating conditions. According to the characteristics and descriptions of bubble formation regimes (i.e., whether the bubble totally blocked the channel), they were mainly located in the squeezing (e.g., the case shown in Fig. 5-1) and dripping regime (e.g., for the case $Ca_{TP} = 8.5\times10^{-3}$, j_L = 42.9 cm s^{-1}, j_L = 14.3 cm s^{-1}) in this study.

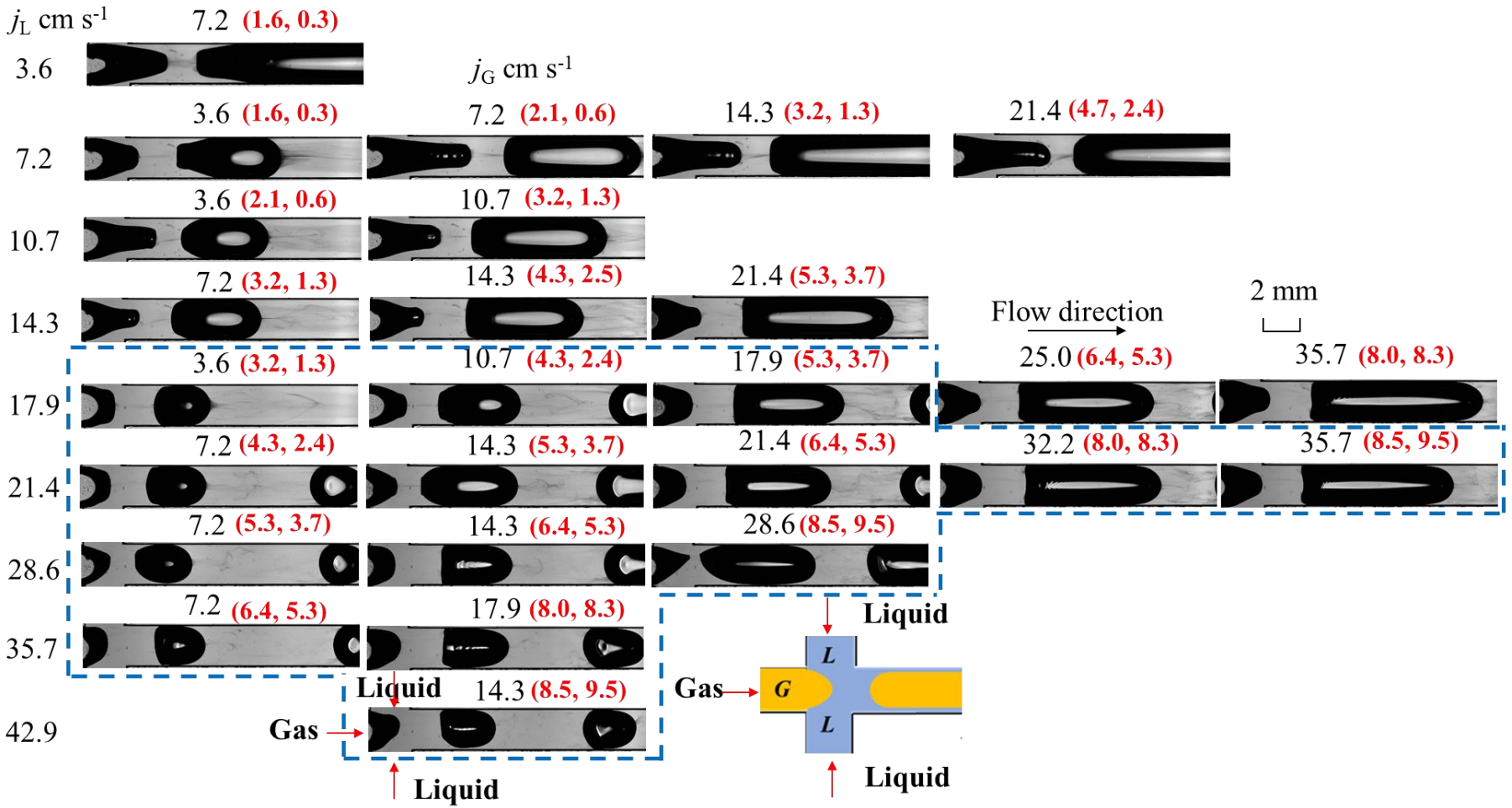

Fig. 5-4 Cartography of the instantaneous gas-liquid Taylor flows (air and RGN colorimetric solution) right after the bubble pinch-off at the cross- junction position $X_1 = 0$, for various operating conditions. The dimensionless numbers in the red brackets correspond to ($Ca_{TP}\times10^{-3}$, We_{TP}). Pinch-off patterns I and II are located inside and outside of the dotted blue box respectively.

Furthermore, it can be observed that the gas finger lengths (i.e., the coming gas thread) right after the bubble pinch-off changed with the gas and liquid superficial velocities.

Depending on the gas finger lengths, two pinch-off patterns could be identified:

- The pinch-off pattern I, where the pinch-off of the bubble was located inside of the cross- junction (i.e., without entering the main channel). This pattern was marked inside the dotted blue box of Fig. 5-4.
- The pinch-off pattern II, where the pinch-off of the bubble was located outside of the cross-junction (namely occurred inside the main channel). This pattern was marked outside the dotted blue box of Fig. 5-4.

At a given liquid superficial velocity, the pinch-off position was likely moving towards the main channel with the increase of gas superficial velocity (i.e., the transition from patterns I to II). Contrarily, at a given gas superficial velocity, the pinch-off position was likely moving towards the cross-junction with the increase of liquid superficial velocity (i.e., the transition from pattern II to I).

To quantitively quantify the bubble formation pattern, the gas finger which was ruptured by the liquid right after the bubble pinch-off was considered. The related length (starting from the cross-junction) could be measured by image processing as shown in Fig. 5-5. For each operating condition, an average gas finger length was obtained using 1000 images, and then normalized by the width of the liquid inlet side channels (w_{side}, see Appendix 3). Therefore, as plotted in Fig. 5-6, two pinch-off patterns could be simply distinguished, depending whether l_{GF}/w_{side} was higher or lower than one unit. It is noted that the standard deviations (STD) for the pinch-off pattern II were significantly higher than those of pattern I.

Fig. 5-5 Typical image processing for extracting gas finger right after the bubble pinch-off (j_L = 17.9 and j_G = 25.0 cm s^{-1}): (a) raw image of gas finger, (b) extracted gas finger and l_{GF} represents the length of the gas finger.

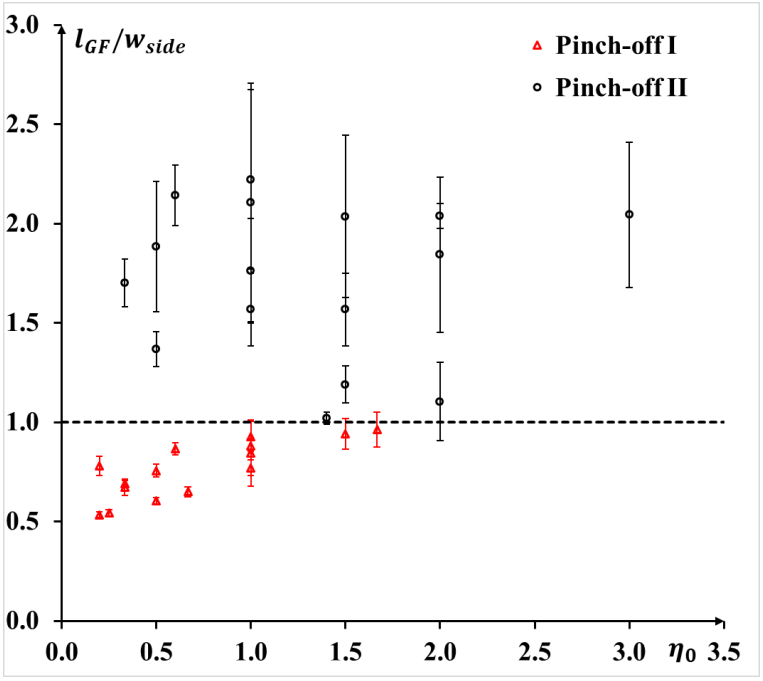

Fig. 5-6 Bubble formation patterns obtained at the cross-junction: normalized gas finger length right after the bubble pinch-off versus the gas-liquid superficial velocity ratio.

To analyze the established balance between the inertial, viscous, and interfacial forces during the bubble pinch-off process, Fig. 5-7 identifies two flow patterns by plotting of the two-phase Capillary number ($\mathrm{Ca}_{TP} = \frac{\mu_L j_{TP}}{\sigma_L}$) versus the

gas-liquid superficial velocity ratio η, and the liquid phase Capillary number ($\mathrm{Ca}_L = \frac{\mu_L j_L}{\sigma_L}$) versus the gas phase Weber number ($\mathrm{We}_G = \frac{\rho_L {j_G}^2 w_{hl}}{\sigma_L}$).

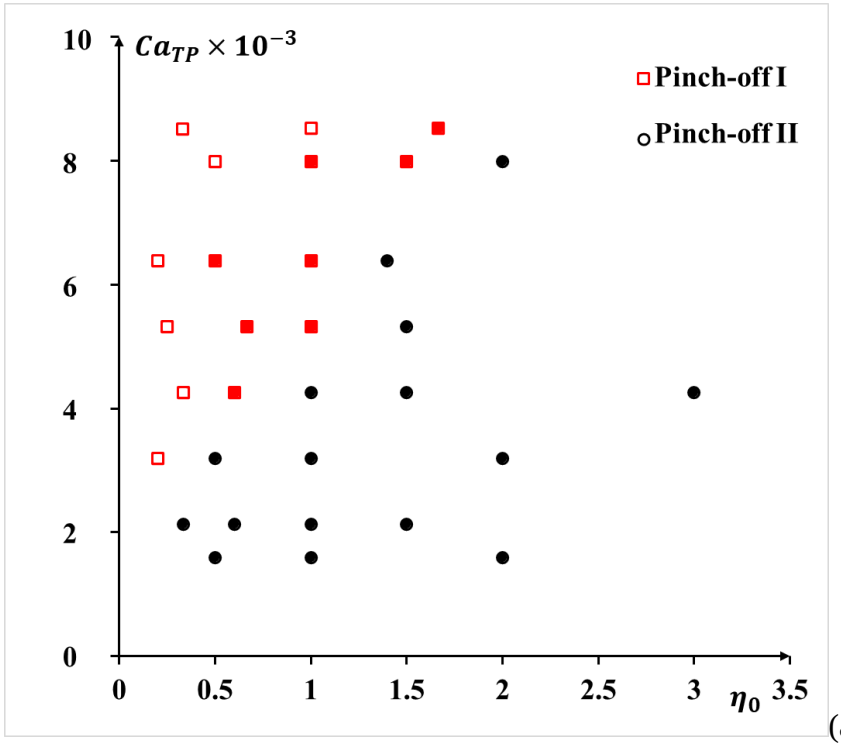

(a)

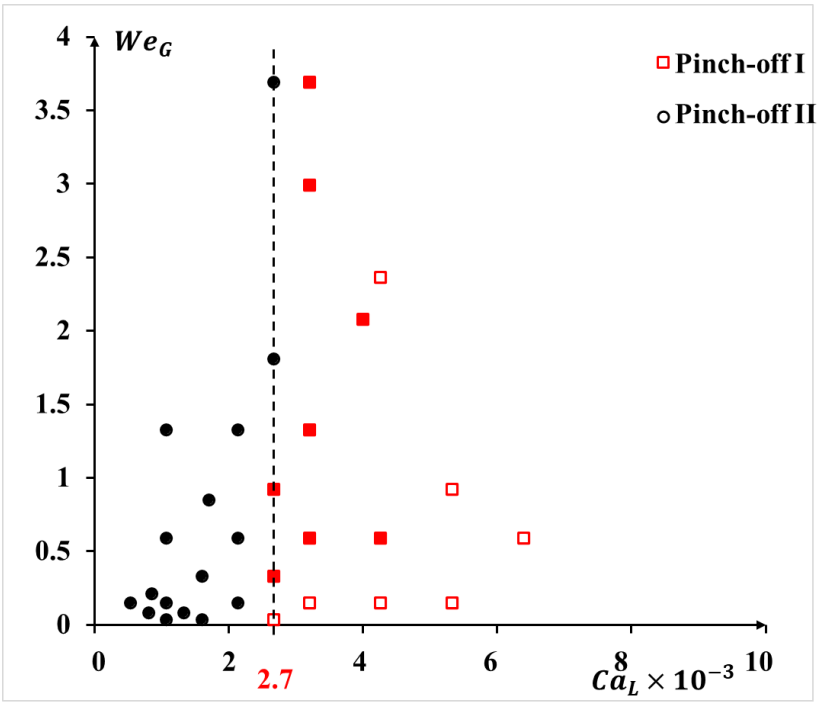

(b)

Fig. 5-7 The plot of identified pinch-off patterns for (a) two-phase Capillary numbers versus the gas-liquid superficial velocity ratios and (b) gas Weber numbers versus the liquid Capillary numbers. Empty and solid symbols represent dripping and squeezing regimes, respectively.

In addition, the squeezing and dripping regimes identified from Fig. 5-4 were also plotted in Fig. 5-7 for comparison.

In Fig. 5-7 (a), it can be observed that at a given two-phase Ca_{TP} number, the pinch-off pattern moved from I to II with creasing η. At a given η, an increase of Ca_{TP} number turned the pinch-off pattern II to I (i.e., the increase of j_{TP}). Furthermore, the dripping regimes were found mainly at low η and high Ca_{TP} number, whereas the squeezing regimes were found mainly at high η. And the transitions between the dripping and squeezing regimes were consistent with the simulation results from Li et al. (2019a), as shown in Fig. 1-7. In addition, the pinch-off pattern II all belonged to the squeezing regimes, while there were hybrid squeezing and dripping regimes for pinch-off pattern I.

Fig. 5-7 (b) further analyzed the transitions between each regime (either dripping or squeezing) and each pinch-off pattern (either I or II) by the gas phase Weber number and liquid phase Capillary number. It can be observed that the liquid phase Capillary number Ca_L had a major impact on transitions between pinch-off patterns, and the critical Ca_L was found around 2.7×10^{-3}. In addition, the dripping regimes were mainly encountered at high Ca_L and low We_G number whereas the squeezing regimes were located at low Ca_L. This was also in accordance with the identified bubble formation regimes reported by Sontti and Atta (2019), as shown in Fig. 1-6.

5.3 Flow regimes and bubble shape

The gas-liquid flow regimes were identified for two fluid systems (air/deionized water; air/RGN colorimetric solution) under various gas and liquid flow rates at the observing position X_2 = 17 mm, as displayed in Fig. 5-8. From Fig. 5-8 (a), for the air-deionized water system, the contact line between gas, liquid and channel wall was formed under small gas and liquid flow rates (see

dotted red box in Fig. 5-8 (a)). The appearance of the contact lines made the bubble rear no more hemispherical. But with increasing two-phase Ca_{TP} or We_{TP} number (i.e., more dominant effects of viscous or inertial forces compared to the interfacial force), the three-phase contact lines disappeared, and tiny liquid film was formed between the bubbles and the channel walls.

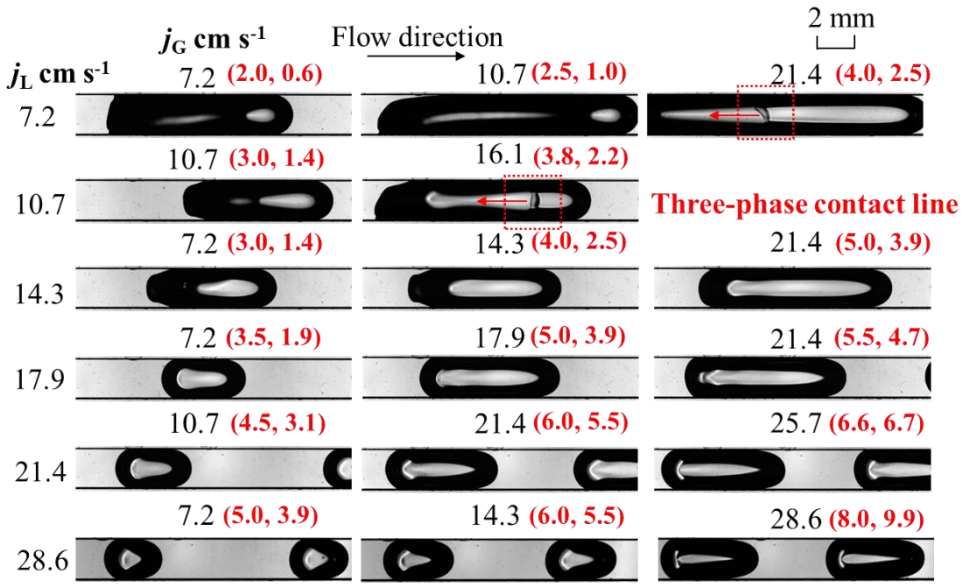

(a)

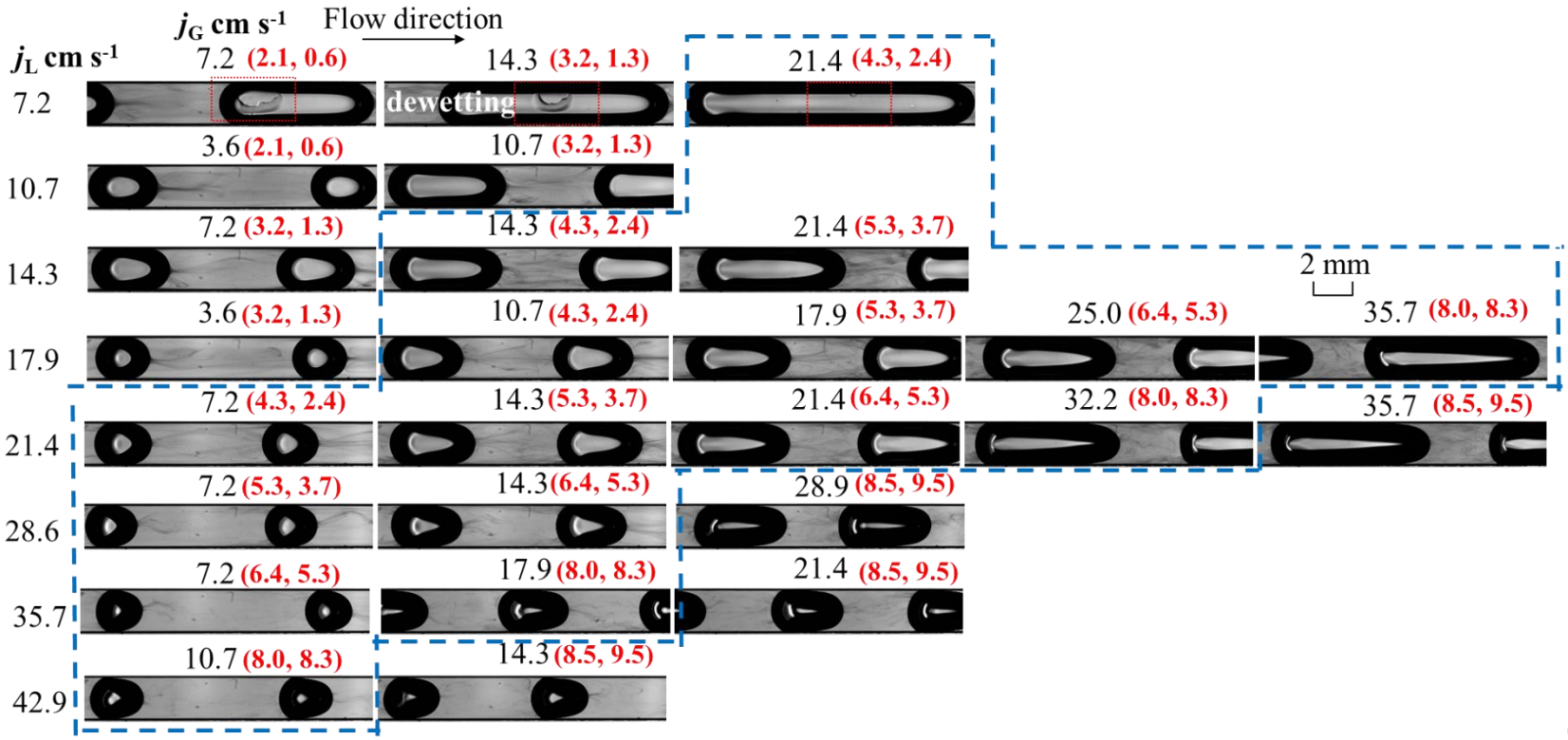

(b)

Fig. 5-8 Cartography of gas-liquid flows obtained for various operating conditions at the observing position X_2 = 17 mm: (a) air and deionized water; (b) air and RGN colorimetric solution. The numbers inside the red brackets correspond to ($Ca_{TP}\times10^{-3}$, We_{TP}). The dotted red boxes point out the location of wetting/dewetting phenomena. The dotted blue box corresponds to the Taylor flow regime.

In addition, Fig. 5-8 (b) shows that the change in liquid properties (from deionized water to RGN colorimetric solution) induced strong differences in terms of wetting and dewetting phenomena, and thus of bubble shapes. One could also observe that:

- When $We_{TP} < 1.3$ ($Ca_{TP} < 3.2\times10^{-3}$), dewetting phenomena occurred for long bubbles.
- When $We_{TP} < 3.7$ ($Ca_{TP} < 5.3\times10^{-3}$), the bubble nose and rear were symmetrical with each other and could be described by hemispherical caps with same curvatures.
- An increase in Ca_{TP} or We_{TP} number induced bubble deformation and made bubble nose slender and bubble rear flatter. When $We_{TP} > 8.3$ ($Ca_{TP} > 8.0\times10^{-3}$), the bubble was significantly deformed and presented like a bullet.
- At the same η, the increase in Ca_{TP} or We_{TP} number decreased the bubble and liquid slug lengths (Korczyk et al., 2019; Schuler et al., 2021).

Therefore, in Fig. 5-8 (b), the Taylor flow regime associated with conditions where hemispherical bubble nose and tail and moderate bubble length was marked by a dotted blue box. It was obtained under moderate Ca_{TP} (4.3×10^{-3} - 8.0×10^{-3}) and We_{TP} (2.4 - 8.3) numbers and will be further discussed in terms of bubble and liquid slug lengths in section 5.4.

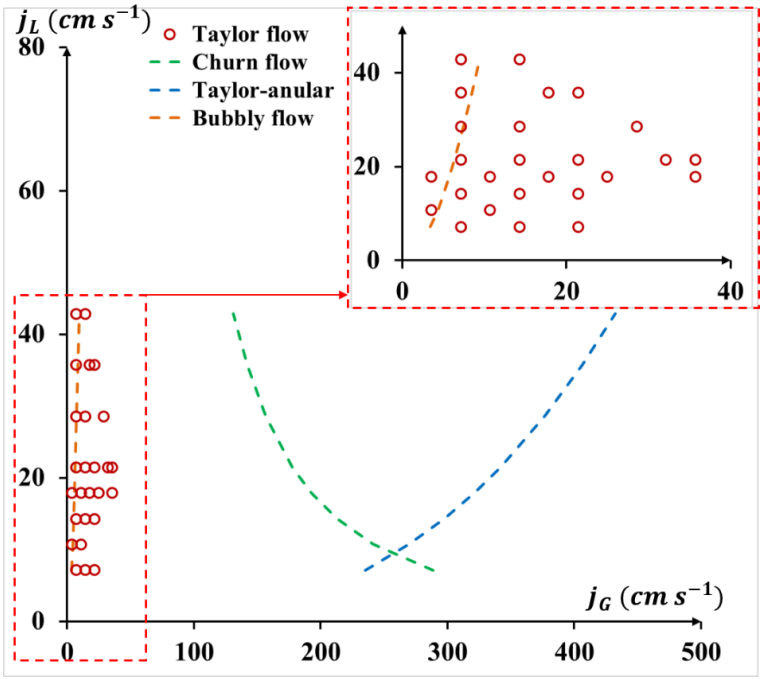

Fig. 5-9 Straight milli-channel with a cross-junction: flow map for air/RF colorimetric solution using the approach from Haase et al. (2020). Green, blue and orange dotted lines represent the transition boundaries between the Taylor flow to the churn flow, Taylor-annular flow, and bubby flow, respectively.

These findings on the various gas-liquid flow regimes, and the associated bubble shapes, are consistent with the ones observed by Yang (2017) in a straight square channel with three turns (2×2mm, length 1 m). Note that the same material (PMMA) for manufacturing the channel was used in this study and in the ones of Yang (2017), but some changes in wettability property of the wall could not be excluded.

In addition, Fig. 5-9 demonstrates the flow map calculated according to the approach proposed by Haase et al. (2020a) using transition boundaries in Table 1-1 (section 1.2.1.1) in the straight milli-channel with a cross-junction. It can be observed that their approach could correctly predict most of the Taylor regimes, whereas there were some slight deviations between the bubbly flow and Taylor flow regimes.

5.4 Normalized bubble length, liquid slug length and bubble velocity

Fig. 5-10 (a) plots the relationships between the normalized bubble lengths with the gas-liquid superficial velocity ratios η_0, only in the case of the Taylor flow regime identified from Fig. 5-8 (b) (i.e., moderate Ca_{TP} and We_{TP} numbers). Four observing positions (i.e., $X_1 / w_{hl} = 0$, $X_6 / w_{hl} = 52$, $X_8 / w_{hl} = 88$, $X_{12} / w_{hl} = 223$) were chosen because they covered from the start to the end of the milli-channel. The bubble lengths were normalized by the hydraulic diameter of the main channel width w_{hl} (see Appendix 3, Eq. (A 3-4)). First, one can observe that the bubble lengths maintained constant whatever the axial positions X, indicating that the pressure drop was small and the expansion effect of gas phase was negligible here. In addition, the normalized bubble length could also be predicted using the scaling law proposed by Garstecki et al. (2006) (initially proposed for T-junction), as follows:

$$\frac{L_B}{w_{hl}} = 1.83\,\eta_0 + 1, \qquad \text{MAPER: } 4.4\% \tag{5-3}$$

One can analyze the bubble length from the characteristic time in section 5.2.1, as below (Abadie, 2013):

$$t_{filling} \propto \frac{w_{hl}}{U_{filling}} \propto \frac{w_{hl}}{j_G} \tag{5-4}$$

$$t_{squeezing} \propto \frac{w_{squeezing}}{U_{squeezing}} \propto \frac{w_{squeezing}}{j_L} \tag{5-5}$$

$$t_{BF} \propto \frac{L_B}{U_{BF}} \propto \frac{L_B}{j_G} \tag{5-6}$$

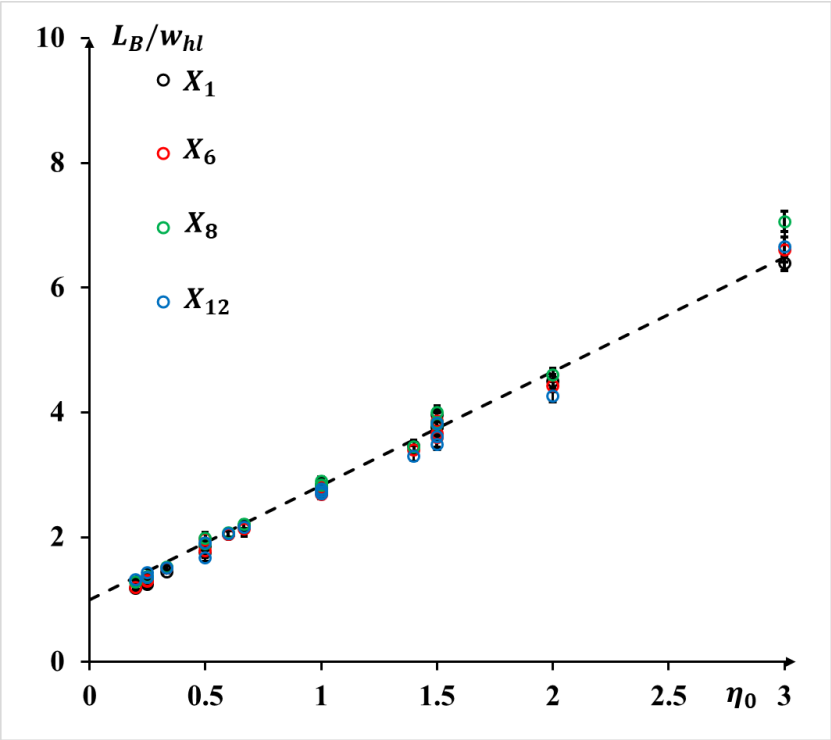

(a)

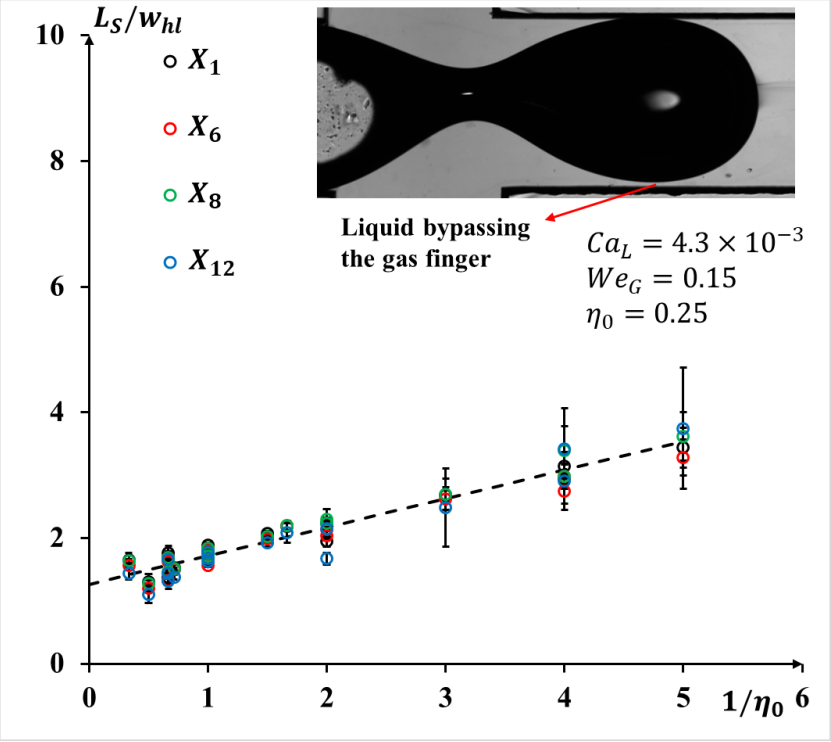

(b)

Fig. 5-10 Hydrodynamics of bubble formation at the cross-junction milli-channel: (a) normalized bubble length versus the gas-liquid ratio η_0. (b) Normalized liquid slug length versus the inverse of η_0. Four observing ROI positions ($X_1/w_{hl} = 0$, $X_6/w_{hl} = 52$, $X_8/w_{hl} = 88$, $X_{12}/w_{hl} = 223$) and four groups of two-phase superficial velocities ($j_{TP} = 28.6$, 35.7, 42.9, 53.6 cm s^{-1}) were considered.

Combining Eqs. (5-4) to (5-6) and replacing them in Eq. (5-1), then the bubble length could be correlated as:

$$\frac{L_B}{w_{hl}} \propto 1 + \frac{w_{squeezing}}{w_{hl}} \frac{j_G}{j_L} \tag{5-7}$$

In Eq. (5-3), deduced from experiments, a value of one as intercept was also obtained, confirming that, in the present case, the bubble formation could be described with both filling and squeezing stages. The coefficient of 1.83 was also in accordance with the one obtained in the straight channel (equal to 1.58) and in the meandering channel (equal to 1.69) by Yang (2017). The theoretical prediction of bubble length by Eq. (5-7) was also in accordance with the experimental results from Chapter 3 in the in-plane spiral-shaped milli-reactor. However, the intercepts were higher than 1 (i.e., 3.46 and 4.13 for MT and ET configurations) in the in-plane spiral-shaped milli-reactor, which was probably due to the effects of wettabilities and centrifugal forces.

Fig. 5-10 (b) plots the relationships between the normalized liquid slug lengths and the inverse of η_0. Unlike the cases of L_B, the standard deviations (STD, see Appendix 5) of normalized liquid slug length were relatively higher when $1/\eta_0$ was higher than 2. As illustrated by the image (right before the bubble pinch-off) inserted in Fig. 5-10 (b), the conditions corresponded to cases (identified as dripping regimes, see Fig. 5-7) where the channel was not fully blocked by the bubble and so, the coming liquid can freely enter into the liquid slug and bypass the gas thread. Under such dripping regimes, the pinch-off became triggered by the viscous force and inertial force, instead of the increased pressure force induced at the upstream of the gas thread. However, for the squeezing regimes (Schuler et al., 2021), the channel was blocked by the bubble and the induced increased pressure force at the upstream of the bubble thread finally triggered the breakup.

The normalized liquid slug length could be at last described by the following scaling law:

$$\frac{L_S}{w_h} = \frac{0.46}{\eta_0} + 1.26, \quad \text{MAPER: } 7.6\% \tag{5-8}$$

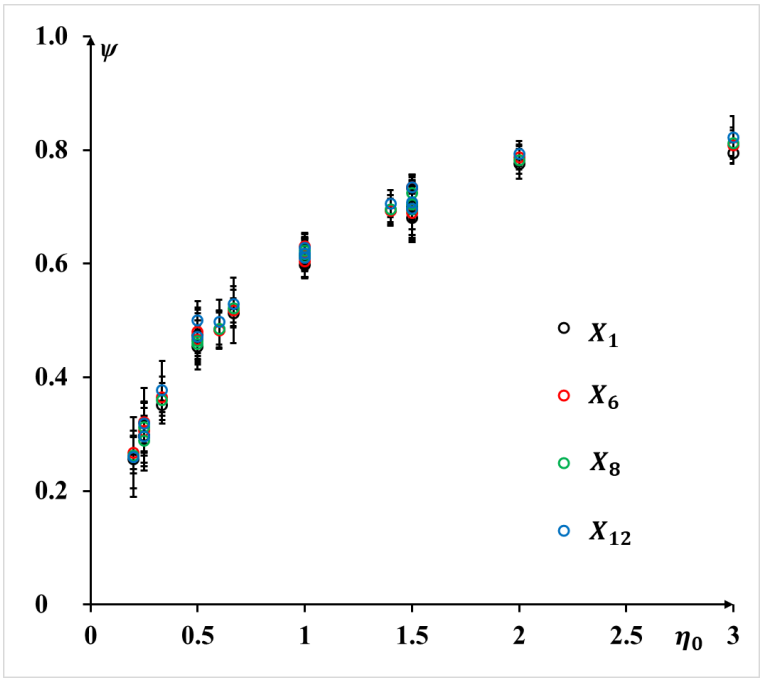

(a)

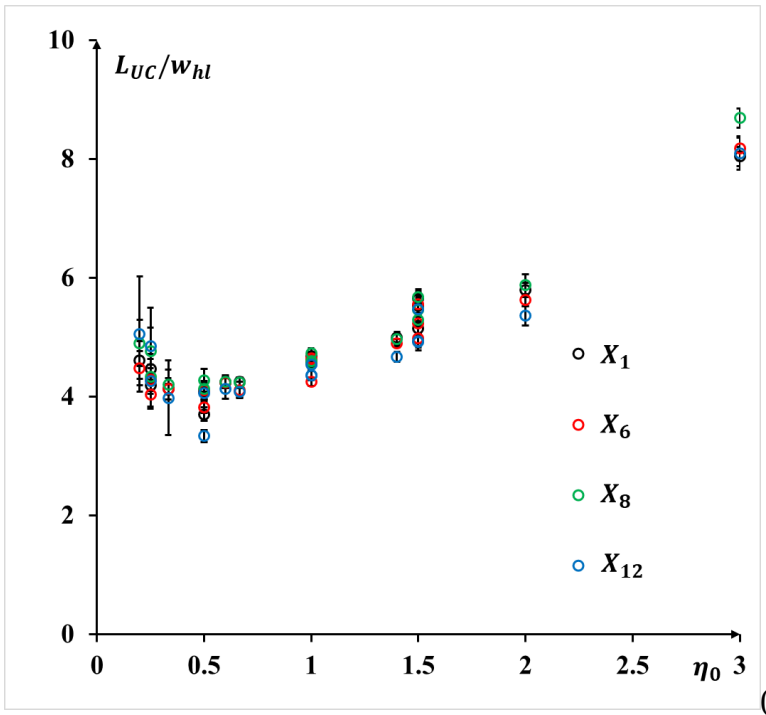

(b)

Fig. 5-11 Hydrodynamics of bubble formation at the cross-junction milli-channel: (a) Normalized unit cell length versus η_0, and (b) Relative length of bubble compared to the unit cell length ψ versus η_0. Four observing ROI positions ($X_1 / w_{hl} = 0$, $X_6 / w_{hl} = 52$, $X_8 / w_{hl} = 88$, $X_{12} / w_{hl} = 223$) and four groups of two-phase superficial velocities ($j_{TP} = 28.6, 35.7, 42.9, 53.6$ cm s^{-1}) were considered.

The relative length of the bubble, ψ, was defined according to Eq. (3-14) and plotted in Fig. 5-11 (a):

$$\psi = L_B / L_{UC} \tag{5-9}$$

The axial positions and the gas and liquid flow rates had no effect on the variations of ψ. With an increase of η_0, ψ increased significantly until reaching a plateau close to 0.8 for $\eta_0 > 2$, presenting identical trend as in Fig. 3-10 (b) for in-plane spiral-shaped milli-reactor.

In addition, Fig. 5-11 (b) plots the relations between the normalized unit cell lengths ($L_{UC} = L_B + L_S$) versus the η_0. When η_0 was higher than 2 or lower than 0.5, the deviations were relatively higher compared to the ones belonged to η between 0.5 and 2. The variations of L_{UC} with η_0 passed through a minimum when η_0 = 0.5, also presenting identical trend as in Fig. 3-10 (a) for in-plane spiral-shaped milli-reactor (minimum L_{UC} was achieved when η = 0.8).

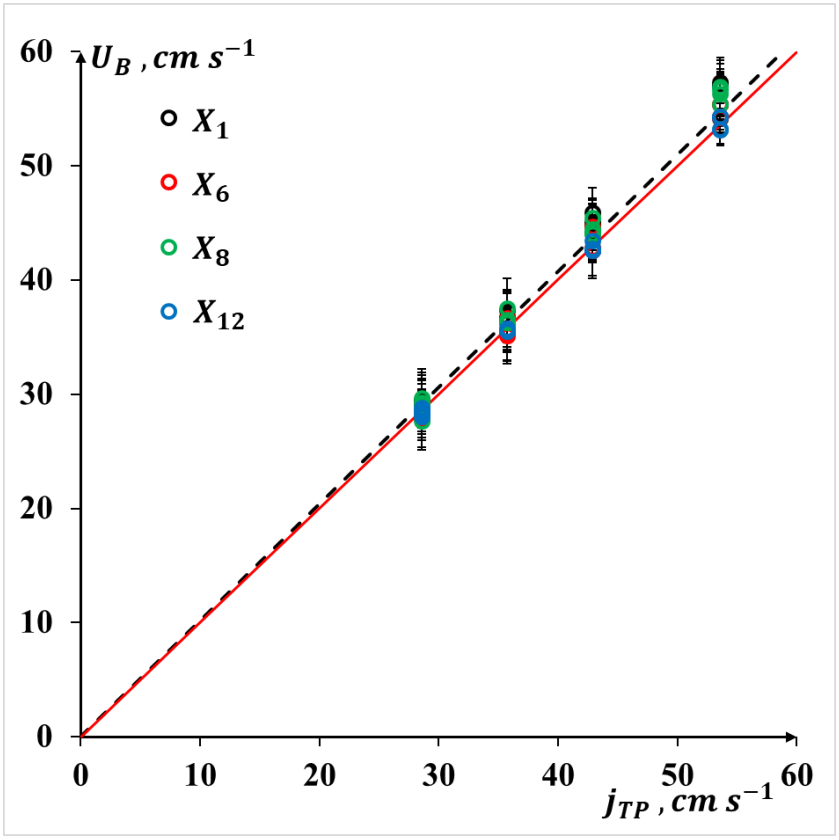

Fig. 5-12 Bubble velocities versus two-phase superficial velocities for four observing positions ($X_1 / w_{hl} = 0$, $X_6 / w_{hl} = 52$, $X_8 / w_{hl} = 88$, $X_{12} / w_{hl} = 223$).

Fig. 5-12 compares the bubble velocities with the two-phase superficial velocities for different observing positions. The bubble velocities could be described by the drift flux model as below:

$$U_B = 1.02\, j_{TP}, \quad \text{MAPER: } 2.04\% \tag{5-10}$$

Eq. (5-10) would suggest that the bubbles traveled at a velocity almost equal to the two-phase superficial velocities. Note that the bubble velocities remained constant whatever the axial positions in the straight milli-channel.

5.5 Interfacial area

In order to estimate the specific interfacial area in one unit cell, hemispherical shapes for bubble nose and rear were assumed. This was true only when $We_{TP} < 8.3$ (see Fig. 5-8. section 5.3). Concerning the bubble body, a cylindrical shape was considered to simplify the calculation.

The critical Capillary number for the transition between a circular cross-sectional shape of the bubble (Fig. 5-13 (a)) and a square one with curved corners (Fig. 5-13 (b)) occurred at 10^{-2} according to Boden et al. (2014) and Fries et al. (2008). As the two-phase Ca number were below 8.5×10^{-3} in this study, the liquid film thickness between bubble and channel side walls, δ_{wall} (i.e., δ_v and δ_h in Fig. 5-13) could be considered as constant according to Fries et al. (2008), and close to 2% of the hydraulic diameter of the channel (i.e., $\delta_{wall} \approx 43\ \mu m$). From Fries et al. (2008), the liquid film thickness between bubble and channel corners, δ_{corner}, was around 10% of the hydraulic diameter of the channel (i.e., $\delta_{corner} \approx 216\ \mu m$). Due to the simplification of cylindrical bubble body shape (Fig. 5-13 (a)), the mean absolute deviation (MAD, defined in Appendix 5) on the interfacial area a was estimated at 5% compared to the cases in Fig. 5-13 (b), which proved that the assumption of cylindrical bubble body was acceptable.

In Appendix 8, an experimental approach was proposed to estimate the liquid film thickness in the vertical direction (i.e., δ_v), and implemented under a single operating condition ($Ca_{TP} = 2.3\times10^{-3}$, $Re_{TP} = 277$) as a first attempt. δ_v was thus found equal at 1% of the channel hydraulic diameter w_{hl} (i.e., 24 μm), which was slightly smaller than the predicted one (2% of w_{hl}) by Fries et al. (2008). In the future, this method should be applied to other operating conditions to be validated.

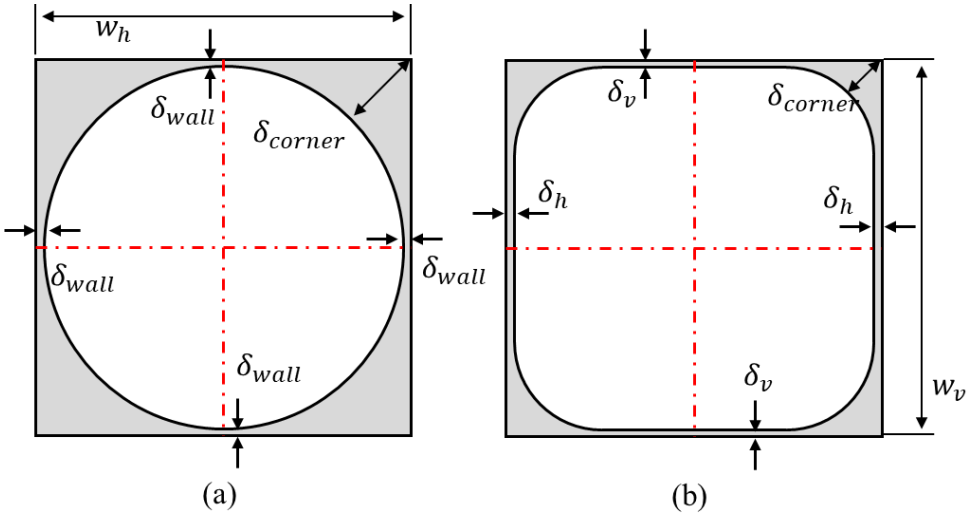

Fig. 5-13 Representation of the cross-sectional shape of Taylor bubble, in a square channel: (a) circular; (b) squared with curved corners.

Thus, considering the assumptions of bubble shape (i.e., cylindrical bubble body shape, hemispherical shapes for bubble nose and rear), the bubble interface area and the specific interfacial area in one unit cell could be calculated as below:

$$S_B = S_{B\_cap} + S_{B\_film} = \pi(w_{hl} - 2\delta_{wall})^2 + \pi(w_{hl} - 2\delta_{wall})(L_B - w_{hl}) \quad (5\text{-}11)$$

$$a = \frac{S_B}{V_{UC}} = \frac{\pi(w_{hl}-2\delta_{wall})^2+\pi(w_{hl}-2\delta_{wall})(L_B-w_{hl})}{(L_B+L_S){w_{hl}}^2} \quad (5\text{-}12)$$

where w_{hl} was the hydraulic diameter of the channel (see Appendix 3). L_B and L_S were the bubble length and liquid slug length obtained in section 5.2.3 and listed in Table A 10-1 (see Appendix 10).

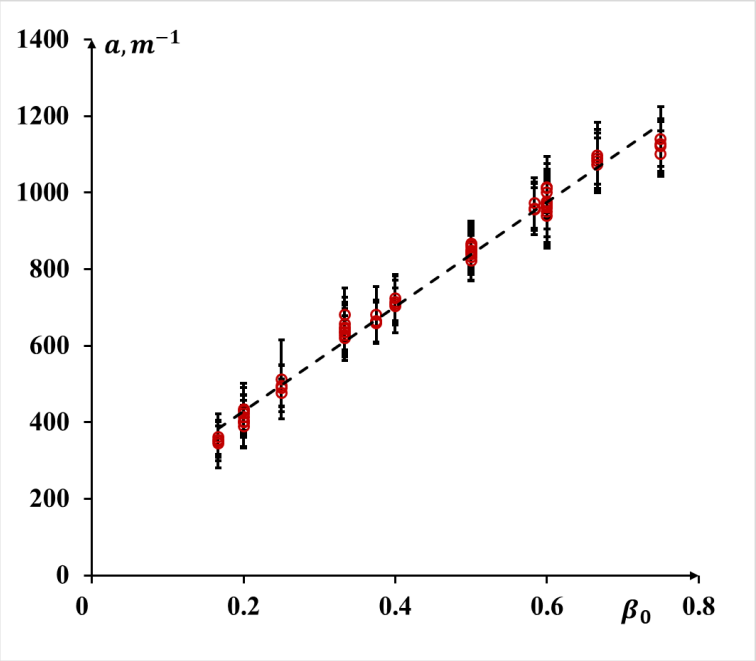

Fig. 5-14 Bubble formation at the cross-junction**:** evolution of the specific interfacial area a versus the dynamic gas hold-up β_0 under four groups of two-phase superficial velocities (j_{TP} = 28.6, 35.7, 42.9, 53.6 cm s^{-1}) at four observing positions: $X_1 / w_{hl} = 0$, $X_6 / w_{hl} = 52$, $X_8 / w_{hl} = 88$, $X_{12} / w_{hl} = 223$.

Fig. 5-14 displays the variation of specific interfacial area a with the dynamic gas hold-up β_0, defined by j_{G0} / j_{TP}. Whatever the observing positions, the specific interfacial area a remained unchanged. It varied linearly with dynamic gas hold-up, as also observed by Yang et al (2017), in a meandering millimetric square channel. This would suggest that no matter how L_B varied, S_B / V_B remained almost constant, ranged between 100 and 1200 m^{-1}.

5.6 Visualization of wetting and dewetting phenomena

From the previous flow regimes, we observed the wetting and dewetting phenomena (Fig. 5-8). In this section, more details will be discussed.

Fig. 5-15 (a) and (b) show the wetting process (development of liquid film) right after the bubble pinch-off (setting as the beginning time point, $t = 0$) for two fluid pairs, air/deionized water and air/RGN colorimetric solution, respectively. From Fig. 5-15 (a), the bubble was moving forwards, and in the meantime, the development of liquid film was moving backwards, from bubble nose to rear, which was opposite to the flow direction. For Fig. 5-15 (b), the liquid film grew faster than the ones for air/deionized water in Fig. 5-15 (a). When the liquid film was fully developed, the bubble rear presented hemispherical shape.

Fig. 5-16 illustrates how the phenomenon of liquid film disappearance occurred for air/RGN colorimetric solution (at the position $X = 17$ mm and under two operating conditions). It can be observed that the dewetting points were almost identical for these two operating conditions, which would indicate the disappearance of liquid film was triggered by the inherent properties of walls (i.e., wettabilities, partially wetting in this case, as the water contact angle was around 64° (Ngai et al., 2017)) and/or the impurities at this point. By analogy to heterogeneous nucleation, the dewetting process was usually considered as a stochastic process and sensitive to impurities. In addition, this phenomenon did not exist anymore with increasing two-phase Capillary numbers (i.e., increasing liquid film thickness). The appearance of the dewetting film would generate some disturbances to the flow field and thus affect the mass transfer, which need to be further investigated.

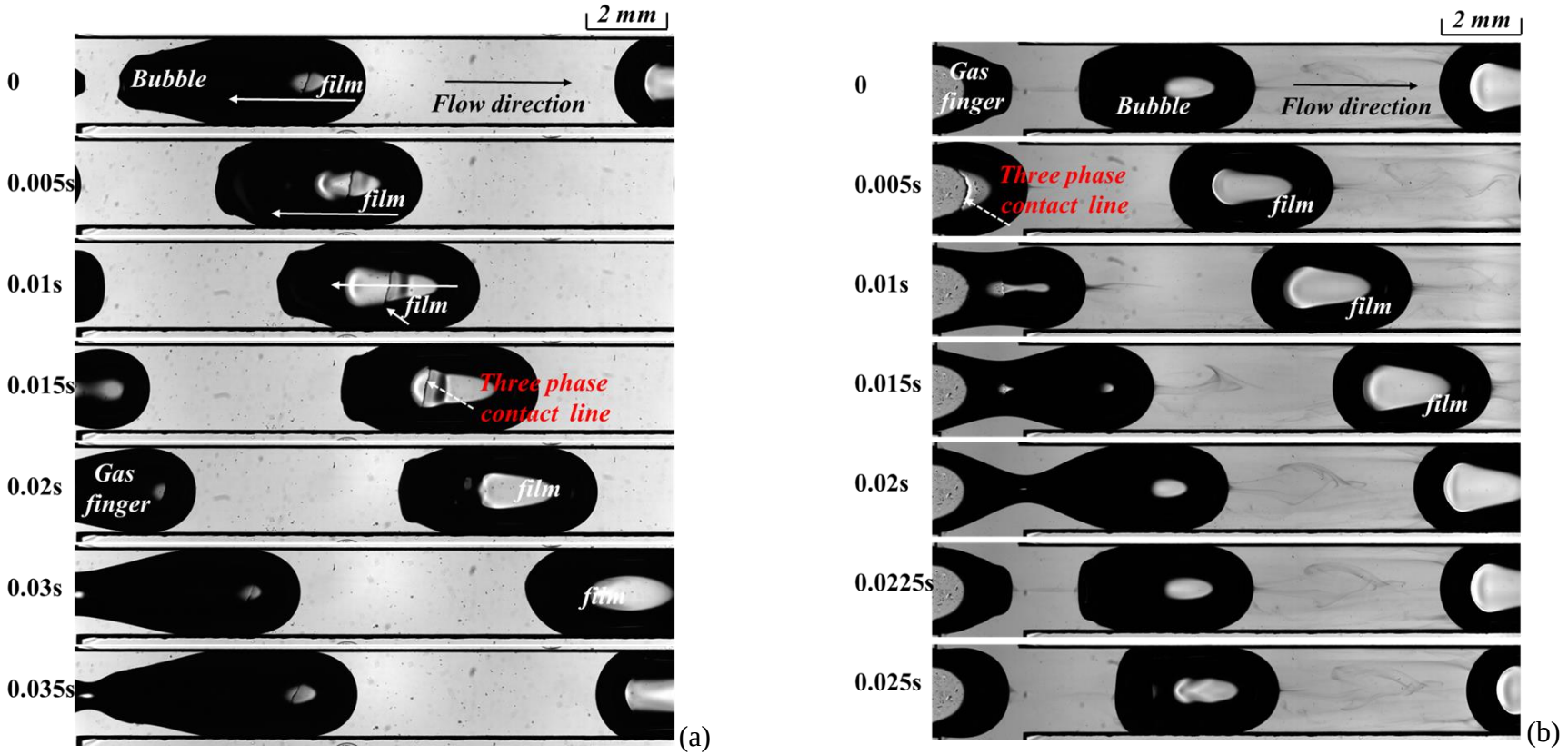

Fig. 5-15 Bubble formation at the cross-junction milli-channel: illustration of wetting (development of liquid film) phenomena at cross-junction (X = 0) for (a) air/deionized water, j_L = 21.4 cm s^{-1} and j_G = 10.7 cm s^{-1}; and (b) air/RGN colorimetric solution j_L = 17.9 cm s^{-1} and j_G = 10.7 cm s^{-1}.

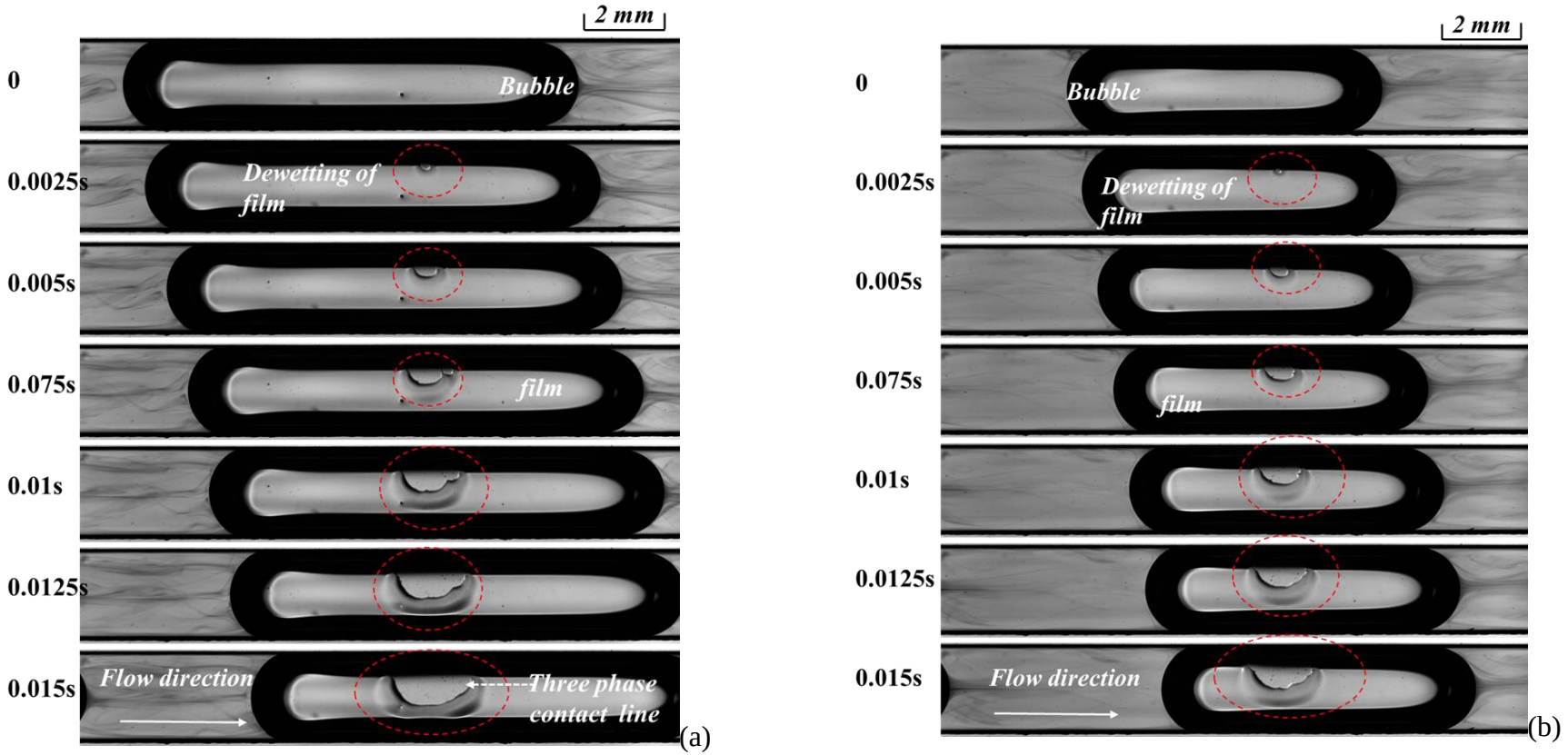

Fig. 5-16 Bubble formation at the cross-junction milli-channel: illustration of dewetting phenomena (disappearance of liquid film) at X = 17 mm for air/RGN colorimetric solution (a) j_L = 7.2 cm s^{-1} and j_G = 14.3 cm s^{-1}; and (b) j_L = 7.2 cm s^{-1} and j_G = 7.2 cm s^{-1}.

5.7 Conclusion

Gas-liquid hydrodynamics around Taylor bubbles have been investigated in a straight milli-channel with a cross-junction during the bubble formation and bubble flowing stage at twelve observing positions. The main findings were as follows:

1) The bubble formation broadly consisted of gas filling and liquid squeezing stages, and the filling and squeezing frequencies were mainly controlled by the gas and liquid superficial velocities, respectively.

2) Based on the gas finger length (normalized by the width of side channel), two patterns of bubble pinch-off were identified. The transition between them could be determined by a critical liquid Capillary number at 2.7×10^{-3}. The squeezing and dripping regimes of bubble formation were also characterized and associated to the gas Weber number and liquid Capillary numbers.

3) Flow regimes of gas-liquid flow were described, and Taylor flow regimes were identified under moderate Ca_{TP} ($4.3 - 8.0\times10^{-3}$) and We_{TP} (2.4 - 8.3) numbers. In addition, dewetting phenomena of lubrication liquid film were observed when $We_{TP} < 1.3$. Bubble shapes were affected by Ca_{TP} or We_{TP}, in particularly, bubble nose and bubble rear presented slender and flatter, respectively, with the increase of Ca_{TP} or We_{TP} number.

4) In the Taylor flow regime, bubble length and liquid slug length could be described by the scaling law based on the gas-liquid superficial velocity ratio and the inverse of it, respectively. This was consistent with the theoretical prediction of bubble length using the filling and squeezing characteristic time.

Chapter 6. Mass transfer during and after the bubble formation stages at a cross-junction in a straight milli-channel

Abstract

Using the resazurin based colorimetric technique and improved image acquisition and magnification, the equivalent oxygen concentration field inside the liquid slugs was visualized during and after the bubble formation stage at a cross-junction in a straight milli-channel. First, two different mechanisms were observed for the development of oxygen concentration fields depending on the two-phase Reynolds numbers (Re_{TP}). Under low Re_{TP}, a jet-like central oxygen concentration 'finger' was formed between the newly formed front bubble and the back gas finger at the bubble pinch-off point. Right after the bubble pinch-off, the dissolved oxygen was transported first by the entering liquid from two side inlets, and later by the developing recirculation loop inside the liquid slug. Under higher Re_{TP}, two highly concentrated oxygen concentration spots were formed near the front bubble rear and the channel wall region, and a much more complex flow structure in the liquid slug appeared. Then, whatever the operating conditions, the variations of the averaged oxygen concentrations followed a nearly linear relation as a function of the axial position, and the mass flux density decreased with increasing axial positions. During the bubble formation process, the cumulated oxygen mass was described by three stages depending on the development of the liquid slug. At last, the overall volumetric liquid side mass transfer coefficients ($k_L a$) obtained in different configurations were compared and found to increase linearly with the recirculation frequencies. A scaling law considering the

curvature ratio and the recirculation frequencies could then be proposed to predict the $k_L a$.

Introduction

In Chapter 5, the gas-liquid hydrodynamics was characterized at the cross-junction in milli-channel. In the continuity, this chapter reports investigations on the gas-liquid mass transfer characteristics around Taylor bubbles during and after the bubble formation process at the same experimental setup.

When scrutinizing the literature, it is surprising to remark that few works are devoted to investigate the role of the bubble formation stage into the overall gas-liquid mass transfer process occurring in Taylor flows. Fries and Rohr (2009) specifically investigated the effects of inlet geometry on mass transfer, and showed that a carefully designed inlet geometry could enhance mass transfer by varying unit cell lengths. Tan et al. (2012a) and Yang et al. (2016b) then quantified a large contribution (45-90%) of the bubble formation stage on mass transfer when compared to the overall bubble flowing stage. Up to now, the detailed mechanisms controlling the amounts of species transferred from the bubble to the liquid phase during the bubble formation stage was not well understood. This Chapter 6 aims at filling this gap by getting deeper understanding on the mass transfer mechanism during the bubble formation process at a cross-junction, thanks to the implementation of the resazurin-based colorimetric method.

For this purpose, this chapter will be organized as follows. Section 6.1 will describe the experimental setup and illustrate the image processing and calibration methods for mass transfer. In section 6.2, the equivalent oxygen concentration fields during the bubble formation and flowing stage will be described. The axial variations of average oxygen concentrations and mass flux density will be presented as a function of the axial position in section 6.3. The enhancement factor induced by the colorimetric chemical reaction will be estimated in section 6.4. Then, the cumulated oxygen mass with the development of liquid slug during the

bubble formation will be demonstrated by three stages in section 6.5. The overall volumetric liquid side mass transfer coefficients $k_L \cdot a$ will be related to the recirculation frequencies in all configurations in this work and the ones from the literature. Finally, a scaling law will be proposed for the overall volumetric liquid side mass transfer coefficient by the curvature ratio and the recirculation frequencies in section 6.6.

6.1 Materials and methods

6.1.1 Experimental setup

The experimental setup, flow control equipment and fluid properties were described in Chapter 2 (section 2.2.2).

6.1.2 Gas-liquid mass transfer

For the calibration process, five aqueous solutions at different RZ concentrations (purity being considered) were prepared: 0, 0.009 and 0.019, 0.037 and 0.074 g L^{-1}. The concentration of glucose and NaOH were kept at 20 g L^{-1}. Once prepared, air was injected to fully convert the DH solution to the RF solution. A portable dissolved oxygen probe (HQ40d, accuracy: ± 0.1 mg L^{-1}) was used to verify that a fully conversion was reached, namely, when the measured oxygen concentration was higher than zero. Then the fully converted solutions (pink) were immediately injected into the millimetric channel. For each RF concentration, 200 frames containing colorless solution (without RF) or fully converted solution were taken, as shown in Fig. 6-1. This process was repeated three times to reduce experimental uncertainties. At last, for each RF concentration, a time-averaged gray value image was obtained to eliminate the slight deviation between instantaneous gray values. Note that this calibration

procedure was made again each time when the ROI positions (i.e., axial positions, X_i) were changed.

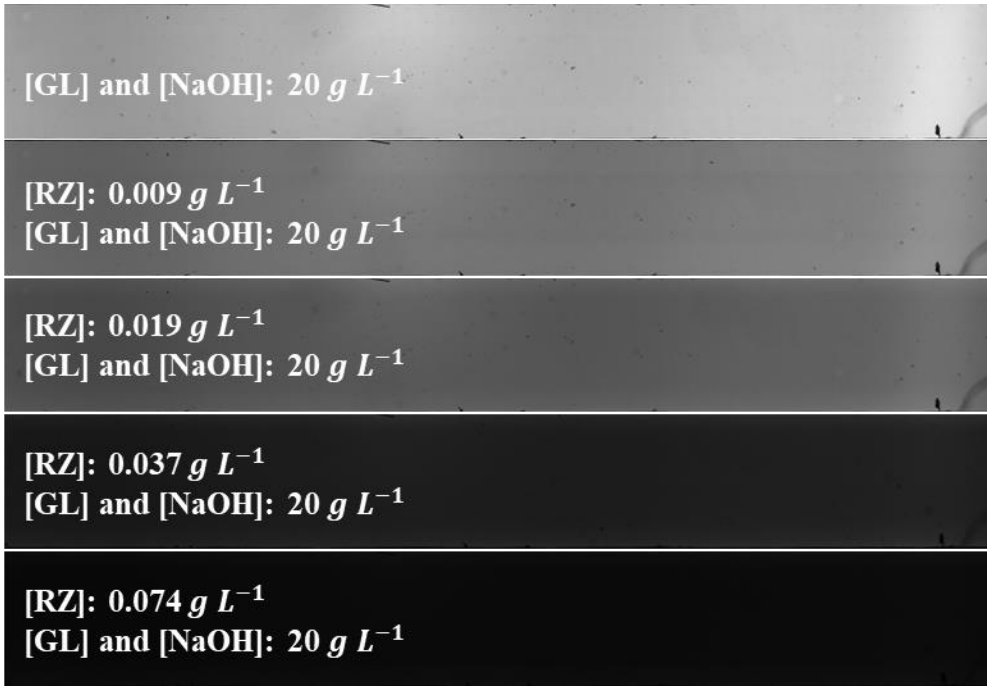

Fig. 6-1 Raw images containing various [RZ] in milli-channel used for the calibration procedure.

Fig. 6-2 (a) shows the calibration relationship between the RF concentration and the absorbance of resorufin, *A*, at different observing positions:

$$A = -\log\left(\frac{\overline{\sum I}}{\overline{\sum I_0}}\right) \tag{6-1}$$

where $\overline{\sum I_0}$ and $\overline{\sum I}$ were the averaged gray intensities at a zero RF concentration and at a given RF concentration, obtained considering all the pixels inside of channels at a given ROI position, respectively.

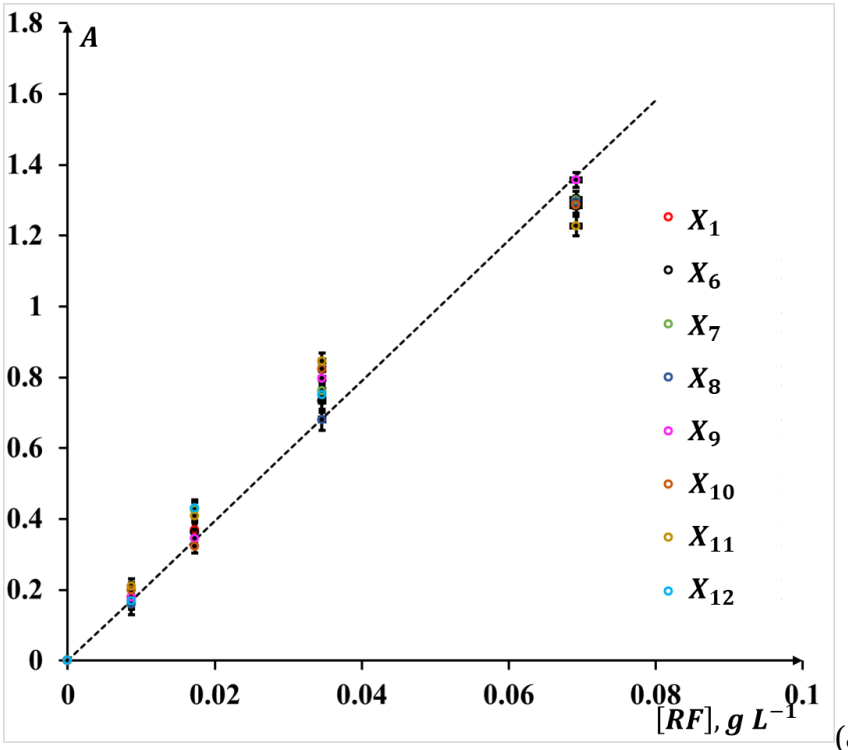

(a)

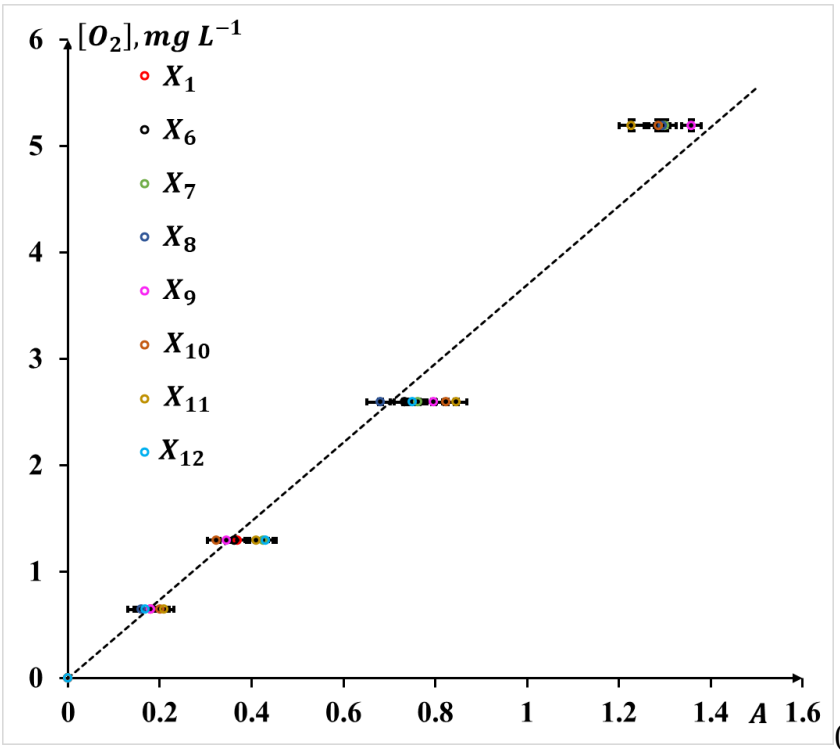

(b)

Fig. 6-2 Calibration relations for mass transfer in the milli-channel with a cross-junction: (a) Calibration relationships between [RF] (considering 93% purity) and the absorbance of resorufin at different ROI positions. (b) Calibration relationships between equivalent O_2 concentration and the absorbance of resorufin at different ROI positions.

Note that, contrary to the study presented in Chapter 4, a global calibration (instead of the pixel-by-pixel calibration) was implemented here, as the set-up involved a square channel and not a tube (no radial change of the light penetration depth). Furthermore, a logarithmic function, linking the absorbance to the gray intensities, was applied to establish the calibration curve for calculating the equivalent oxygen concentrations, instead of the linear relation converting the gray values to the equivalent oxygen concentrations used in Chapter 4 (see Eq. (4-1) and Fig. 4-2 (a)). Indeed, here, the light was monochromatic (see Table 2-6). However, the oxygen concentrations in the depth direction were always assumed as homogeneous.

It is shown that the relationships between A and [RF] were almost linear and followed an identical trend whatever the observing position. From [RF], the equivalent O_2 concentration was deduced considering the stoichiometry of the reaction (i.e., one mole of DH reacts with 0.5 moles of oxygen to form one mole of RF, see Fig. 2-1). Finally, the calibration relationship between the equivalent O_2 concentration and the absorbance of RF was obtained ($[O_2] = 3.70 \cdot A$, MAPER: 11%), as shown in Fig. 6-2 (b). For reminder, the term "equivalent" was used because in reality the oxygen concentration in the liquid phase was null: indeed, oxygen was fully consumed by DH to form RF, according to an instantaneous oxidation reaction (see Yang et al. (2016a)).

The differences (average SD: 0.02) of absorbance A at different ROI positions were probably caused by the uncertainty of each calibration and the variations of light at different positions.

Fig. 6-3 (a) presents the main steps of the image processing, starting from a raw image of gas-liquid flow ($j_L = j_G = 10.72$ cm s^{-1}, $X = 308$ mm). It consisted of four steps for the image processing (see Appendix 4):

(i) Identifying liquid slugs and bubbles from the images and removing bubbles from the images, as shown in Fig. 6-3 (b) and (c).

(ii) Converting gray values in the liquid slugs into the absorbance value of RF using Eq. (6-1).

(iii) Obtaining equivalent O_2 concentrations using the established calibration relation in Fig. 6-2 (b).

(iv) Then plotting the equivalent O_2 concentrations filed shown in Fig. 6-3 (d).

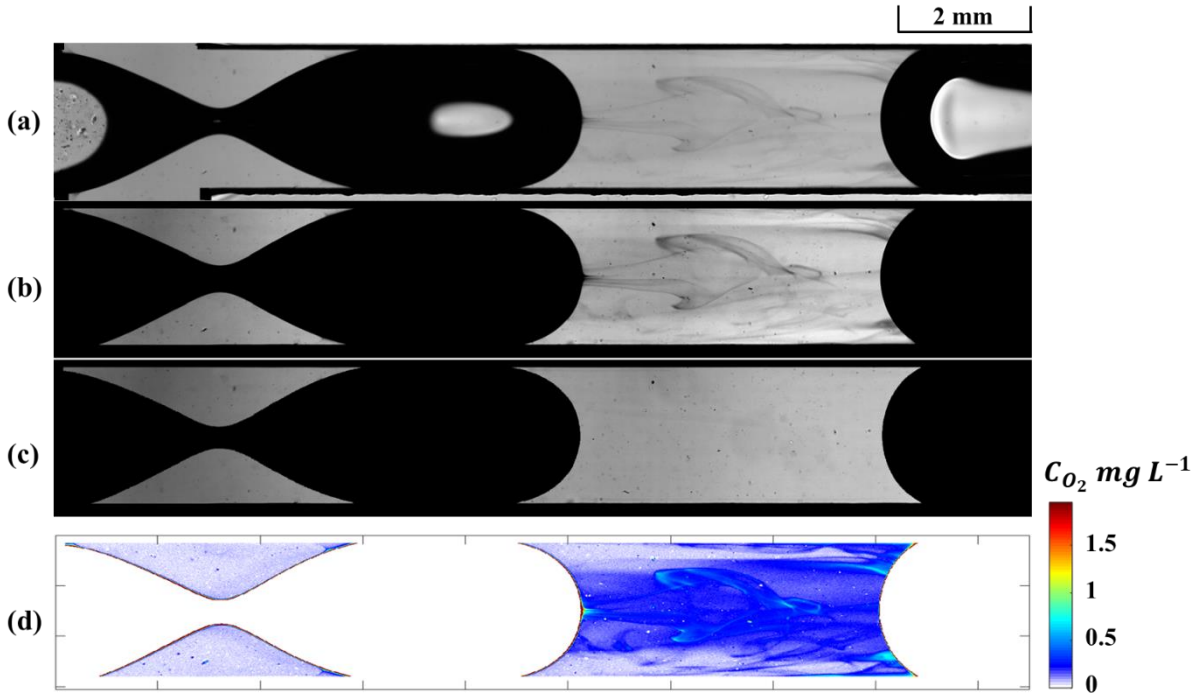

Fig. 6-3 Image processing implemented to study the gas-liquid mass transfer during the bubble formation stage: (a) raw image of gas-liquid flow. (b) Image with remaining liquid of RF signal. (c) Image with remaining liquid of GL and NaOH. (d) Equivalent O_2 concentration. Operating condition: j_L = 17.9 cm s^{-1}, j_G = 10.7 cm s^{-1} at the cross-junction.

As a reminder, the recorded intensity value for each pixel was an overall value for the different planes (i.e., *x-y* plane, see Fig. 2-9 (a)) along the depth direction (i.e., z direction, see Fig. 2-9 (a)). It is noted that, from a theoretical point of view, the intensity values could not be linearly added together for different planes (because of the exponential attenuation of light), whereas the absorbance values could be. Therefore, for each pixel, the calculated absorbance

corresponded to the summation of absorbance values in different planes along the depth direction. It should be kept in mind that the Beer-Lambert law should be applied only if the concentration is homogeneous in the depth direction at given wavelength. In the present experiments, due to the flow structure, some heterogeneities in terms of dissolved species (i.e., gradients of oxygen concentration) existed in the depth direction. This level of heterogeneities could not be accuretaly obtained and varied depending on the operating conditions. However, one could roughly estimate the heterogeneities in the horizontal plane (i.e., *x-y* plane, see Fig. 2-9 (a)) recorded by the camera. The heterogeneity here was defined as a percentage of the standard deviation errors (SD, see Appendix 5) with respect to the averaged equivalent oxygen concentrations inside of the liquid slug. Taking five representative operating conditions of j_{TP} = 28.6 cm s^{-1}, and twelve ROI observing positions, the heterogeneities were estimated between 1% and 20% and decreased with the ROI observing positions, which was acceptable.

6.2 Equivalent O2 concentration fields

By implementing the colorimetric technique and applying the image processing, the equivalent O_2 concentration fields in the liquid slugs could be obtained at the cross-junction and further, at different axial positions in the channel. Note that it was not possible at present to measure them in the liquid film close to the wall.

6.2.1 Bubble formation process

The time-variations of equivalent O_2 concentration fields during bubble formation process are described in Fig. 6-4 and Fig. 6-5 under various operating conditions. Noted that the equivalent O_2 concentration fields inside of the liquid

film was not obtained here. Fig. 6-4 presents a case where the bubble formation process covered an extremely long period of 3975 ms (around half of the complete bubble formation process). Under this condition, the associated Ca_{TP} and Re_{TP} were equal to 5.9×10^{-5} and 8, respectively. The capillary force was thus dominant compared to the viscous force and inertial force. Before the pinch-off point (-112.5 ms < t < -2.5 ms), some layers of dissolved O_2 formed on both sides of the gas finger neck and became gradually thicker. At the bubble pinch-off point, these layers merged, generating a jet-like central oxygen concentration 'finger' between the just-formed bubble and the gas finger. Then the gas finger grew, protruded into the main channel, and finally blocked the main channel (0 < t < 2112.5 ms). During this stage, the dissolved O_2 was carried by the entering liquid from two side inlets. As the Reynolds number was very low, the equivalent O_2 field remained highly symmetric with respect to the centerline of the main channel. Once the main channel was fully blocked by the coming gas finger (2612.5 < t < 3862.5 ms), the liquid from the side inlets hardly entered into the main channel and the recirculation loop started to develop inside the liquid slug. Therefore, as the liquid flow inside the liquid slug presented higher velocities along the centerline and a negative velocity near the channel wall, the dissolved O_2 concentration was transported from the tip of the gas finger to the rear of the formed bubble. In the meantime, the thickness of the dissolved O_2 region near gas finger got thicker, enabling to better disperse oxygen in the radial direction of channel.

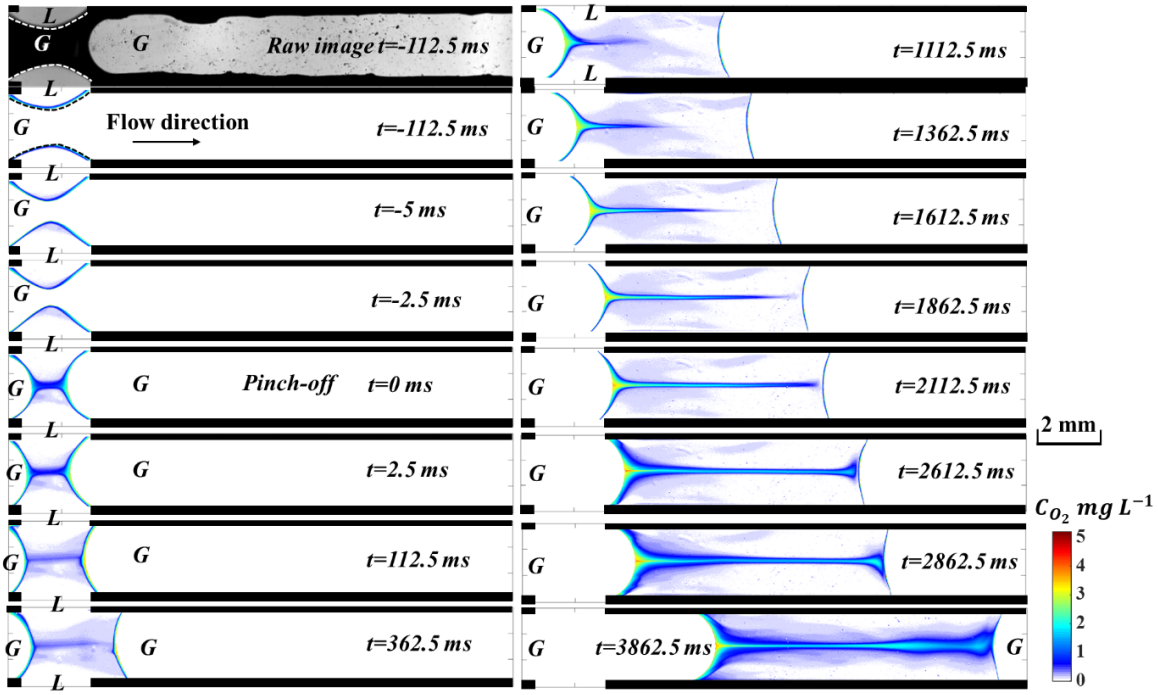

Fig. 6-4 Time-variation of the equivalent O_2 concentration fields during the bubble pinch-off process at X_1 = 0 mm, operating condition: j_L = 0.2 cm s^{-1}, j_G = 0.2 cm s^{-1} and Re_{TP} = 8.

Fig. 6-5 shows the time-variation of the equivalent O_2 concentration fields for three other operating conditions, where the gas-liquid superficial velocity ratio η was equal to 1 and the corresponding Ca_{TP} and We_{TP} to 3.2×10^{-3} and 1.3 (case (b)), 4.3×10^{-3} and 2.7 (case (c)), 6.4×10^{-3} and 5.3 (case (d)). In these cases, the whole bubble formation period was shortened due to higher gas and liquid superficial velocities (55 ms, 32.5 ms and 20 ms respectively, against 8247.5 ms in the case (a)).

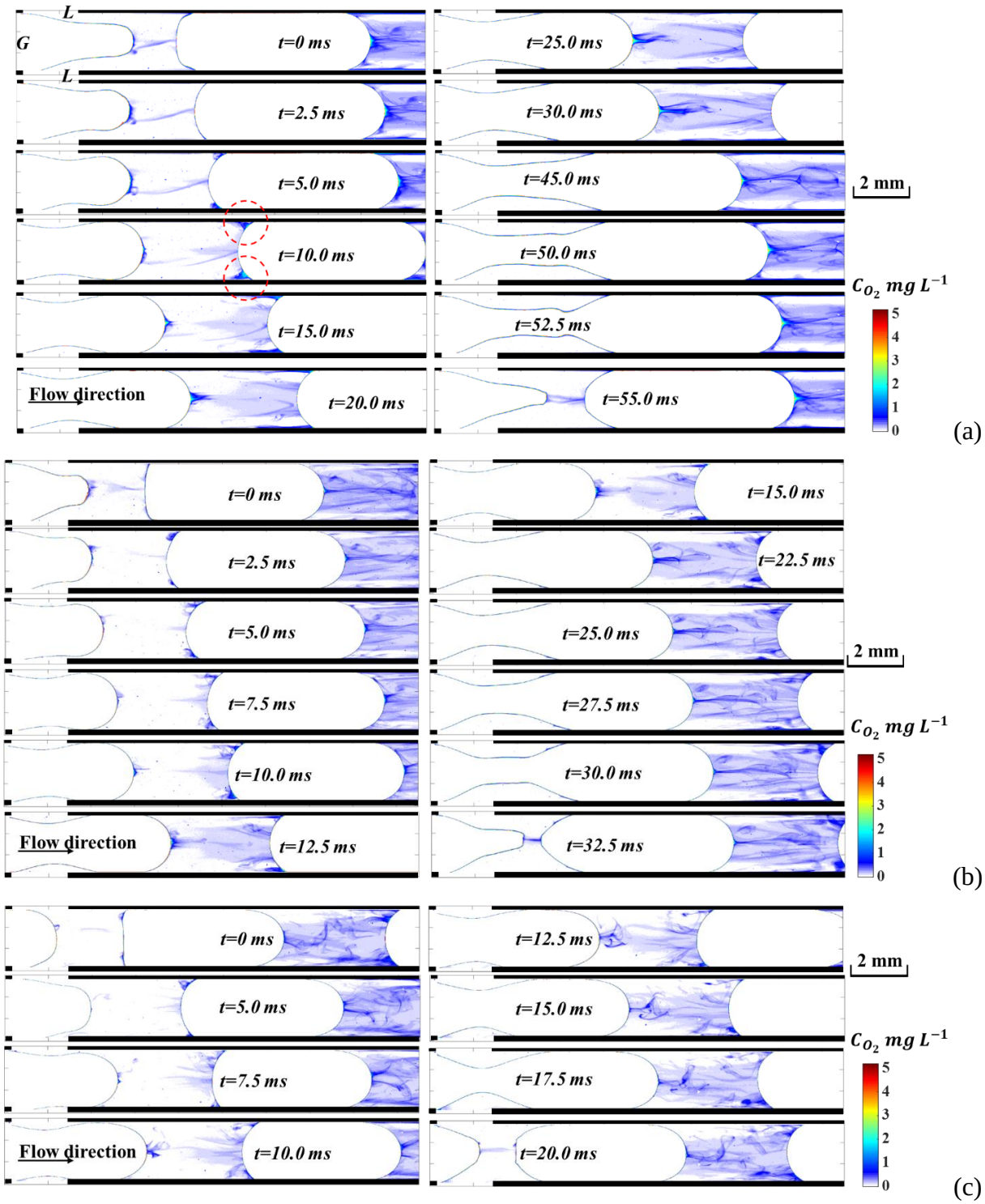

Fig. 6-5 Time-variation of the equivalent O_2 concentration fields during the bubble pinch-off process for various operating conditions at X_1 = 0 mm: (a) j_L = 10.7 cm s^{-1}, j_G = 10.7 cm s^{-1} and Re_{TP} = 416, (b) j_L = 14.3 cm s^{-1}, j_G = 14.3 cm s^{-1} and Re_{TP} = 555, (c) j_L = 21.4 cm s^{-1}, j_G = 21.4 cm s^{-1} and Re_{TP} = 832.

One can observe that the jet-like central oxygen concentration 'finger' at the centerline became no more visible from Fig. 6-5 (a) to (c), as the times to break up the gas finger were short (up to 412 times lower compared to case (a)). Contrary to Fig. 6-4, at the stage where the main channel was fully blocked by the coming gas finger, two spots of high equivalent O_2 concentration can be distinguished near the formed bubble rear and channel wall region, marked by two red circles in Fig. 6-5 (a). This phenomenon could be attributed to the developed recirculating loop inside of liquid slug. Indeed, in the region between the bubble rear and the channel wall, the liquid flow came from the centerline and turned backwards along the channel wall, thus carrying the dissolved oxygen due to the diffusive transfer between the liquid and the bubble rear (see Fig. 1-13 (c), mechanism N° 3). It was also possible that the liquid coming from the channel corner (surrounding the front bubble) could contribute to these two spots of high equivalent O_2 concentration, because of the diffusive transfer between the liquid film in the corner and the bubble lateral body, and the convective transfer within the liquid film, as illustrated in Fig. 1-13 (c) (mechanism N° 5 and N°7). Further investigations need to be implemented by PIV and PLIFI.

6.2.2 Bubble flowing process

Fig. 6-6 presents the instantaneous evolution of the equivalent O_2 concentration fields at a total two-phase superficial velocity j_{TP} of 28.6 cm s^{-1}, for six observing positions (i.e., six flowing times calculated using U_B) and for different gas-liquid superficial velocity ratios η. For these conditions, the Ca_{TP} and We_{TP} numbers were equal to 4.3×10^{-3} and 2.4, respectively. Therefore, the effects of η_0 on the equivalent O_2 concentration fields could be quantified from the comparison between Fig. 6-6 (a), (b) and (c).

One can observe that the dissolved O_2 inside the liquid slug became higher in general as far as the bubbles flowed inside the channel (i.e., with increasing axial positions or flowing times). At X_2 = 17 mm, where the liquid slug was not far from the bubble formation point, the recirculating flow inside of liquid slug was not yet fully established. Along the centerline region and near wall region of the liquid slug, the equivalent O_2 concentration presented higher values than the ones of other regions, due to the convective transfer of oxygen by the recirculation loop and within the liquid film (see Fig. 1-13, mechanism N° 6 and N° 7). However, in some cases, the region near the bubble rear along the centerline also presented a lower equivalent O_2 concentration. As the bubble flowed along the channel, the tip region near the bubble nose always held higher equivalent O_2 concentrations until reaching an almost uniform field, as seen in the last position X_{12} in Fig. 6-6 (a). However, in Fig. 6-6 (b) and (c), even for the last position X_{12}, some gradients of equivalent O_2 concentration still existed inside the liquid slug. Therefore, at an identical two-phase superficial velocity j_{TP} (i.e., at almost same bubble velocity), an increase of gas-liquid superficial velocity ratios η_0 (i.e., shorter liquid slugs) led to improve the mixing inside the liquid slug, to increase the equivalent O_2 concentration and further to enhance the mass transfer from gas phase to liquid phase.

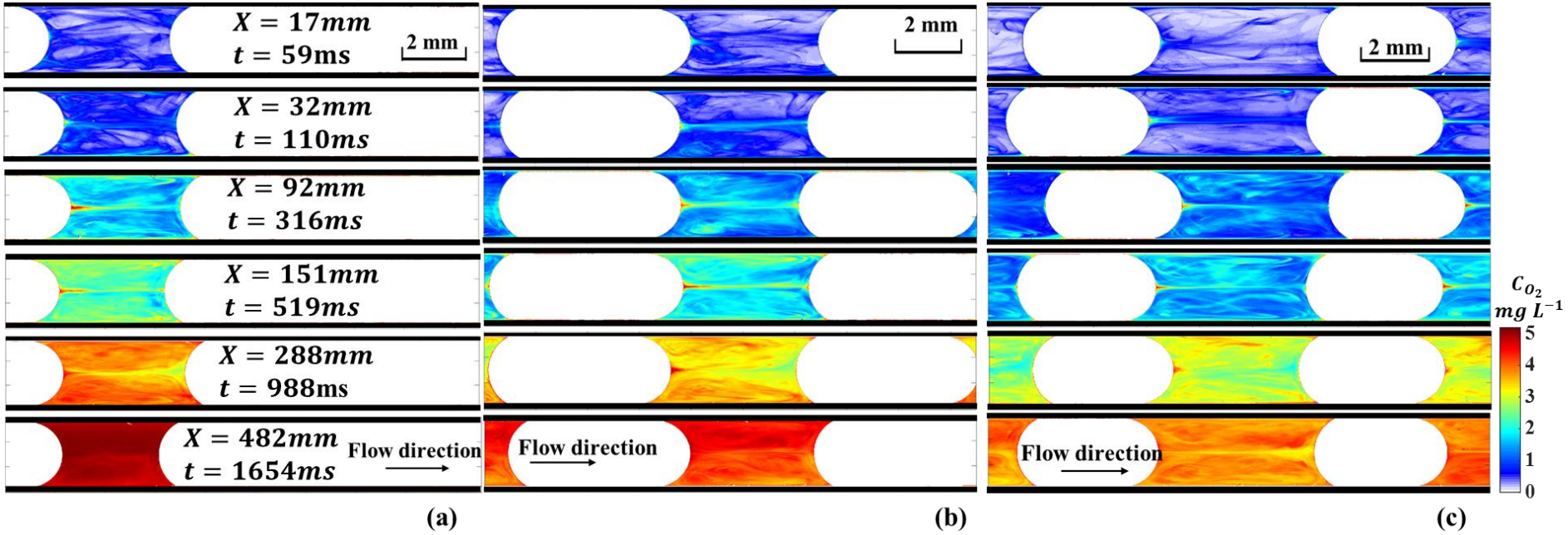

Fig. 6-6 Equivalent O_2 concentration fields during the bubble flowing process at j_{TP} = 28.6 cm s^{-1} under different gas-liquid superficial velocity ratio: (a) η_0 = 3, b) η_0 = 1, (c) η_0 = 0.6. The time indicated in the figure corresponds to the time required for the liquid slug to travel to the X position. Black arrows indicate the flow direction.

6.3 Axial variation of O_2 concentration and mass flux density

The averaged O_2 concentrations could be calculated at different observing positions X, according to Eq. (4-2). Noted that $C(x,y)$ was the local equivalent oxygen concentration depicted in Fig. 6-6 (averaged over the channel depth, w_v) and measured only in the liquid slug. Ω was the cross-sectional area of the channel ($\Omega = {w_{hl}}^2$, see Appendix 3).

Fig. 6-7 plots this averaged concentration $\overline{C_{O_2}}$, normalized by the maximum oxygen concentration C_{max} (i.e., 5.2 mg L^{-1}, see section 2.2.2) as a function of the axial positions, under each two-phase superficial velocity j_{TP}. At a given j_{TP}, an increase of gas-liquid superficial velocity ratio η_0 logically increased the amount of oxygen transferred by unit of liquid slug volume, as observed in Fig. 6-6. When $\overline{C_{O_2}}/C_{max}$ kept below 0.8, the normalized O_2 concentrations increased linearly with axial positions.

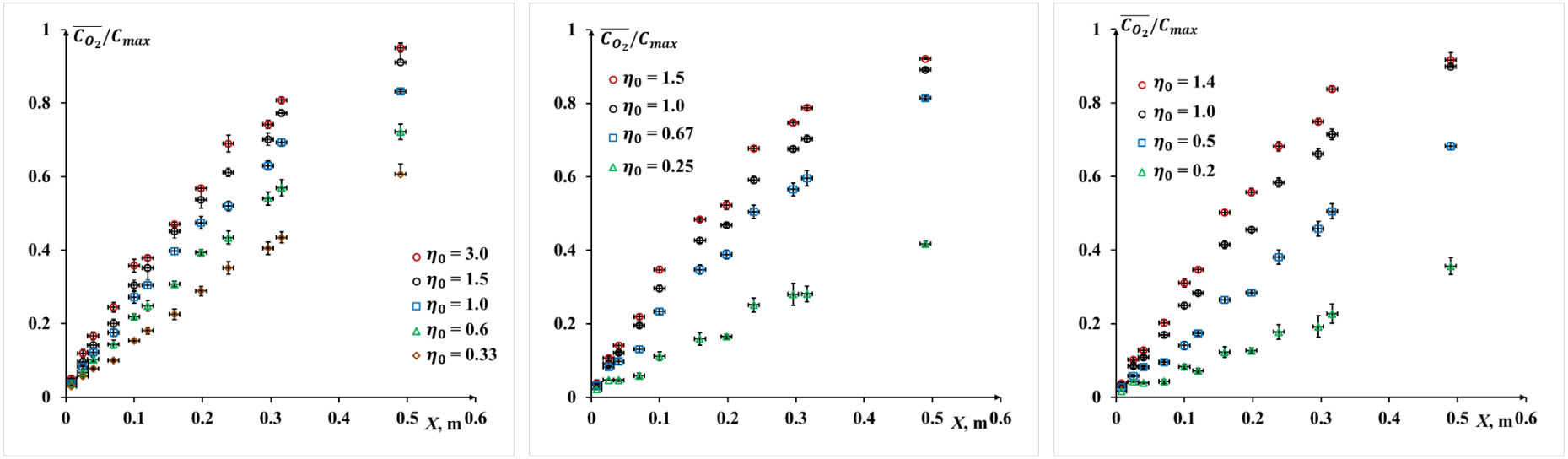

(a) (b) (c)

Fig. 6-7 Comparison of the axial evolution of normalized average equivalent O_2 concentrations in the liquid slug along the channel for different operating conditions: (a) j_{TP} = 28.6 cm s^{-1} and Re_{TP} = 555; (b) j_{TP} = 35.7 cm s^{-1} and Re_{TP} = 693; (c) j_{TP} = 42.9 cm s^{-1} and Re_{TP} = 832.

Fig. 6-8 compared the normalized averaged equivalent O_2 concentration in the liquid slug at a flowing time of 544±1 ms (calculated using the bubble velocity, X/U_B) for three two-phase superficial velocities j_{TP} corresponding to three axial positions X_7, X_8 and X_9, respectively. Generally, the equivalent O_2 concentration in the liquid slugs increased:

- At given j_{TP}, with the increase of η_0.
- At given η_0, with the increase of j_{TP}.

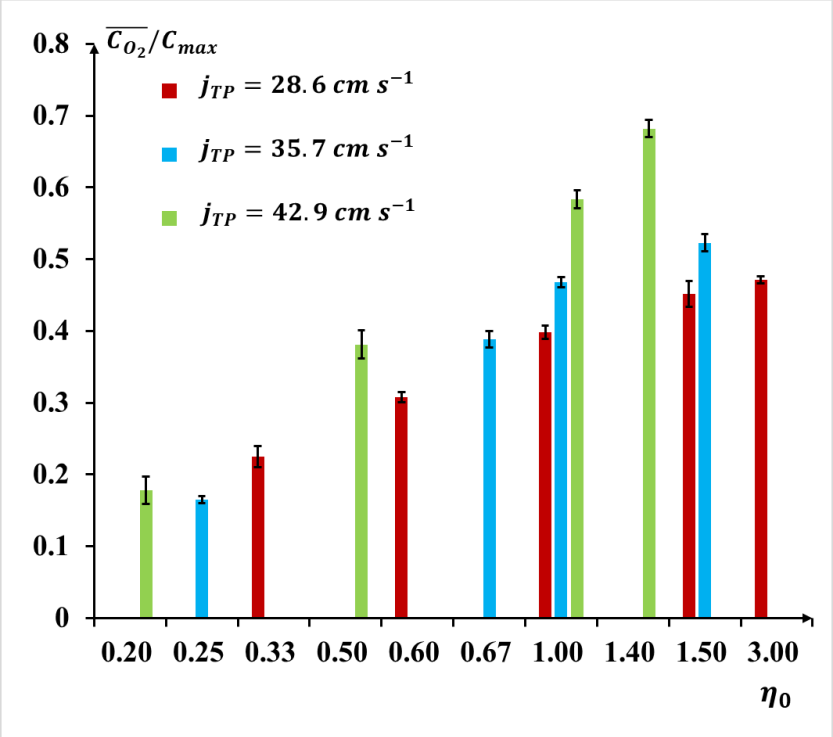

Fig. 6-8 Comparison of normalized average equivalent O_2 concentration in the liquid slug under different operating conditions with same flowing time of liquid slug (at 544 ± 1 ms) at different axial positions (X_7, X_8, and X_9 corresponded to j_{TP} = 28.6, 35.7 and 42.9 cm s^{-1}).

In addition, the mass flux density cumulated in the liquid slugs along the axial positions, noted φ_{O_2} is calculated according to the equation defined in Table 4-1, but the bubble velocity U_B and bubble surface S_B were considered as constant

and obtained from Eq. (5-10) and Eq. (5-11) (bubble nose and rear were assumed as hemispherical shape).

Therefore, the variations of φ_{O_2} in the liquid slugs with the axial positions are plotted for three two-phase superficial velocities j_{TP}, in Fig. 6-10 (a), (b) and (c). For all the operating conditions, whatever j_{TP} and η_0, the mass flux density sharply decreased over the first milli meters after the cross-junction and finally tended towards a constant value. At given axial position X and j_{TP}, an increase of η_0 induced the increase of the mass flux density φ_{O_2}.

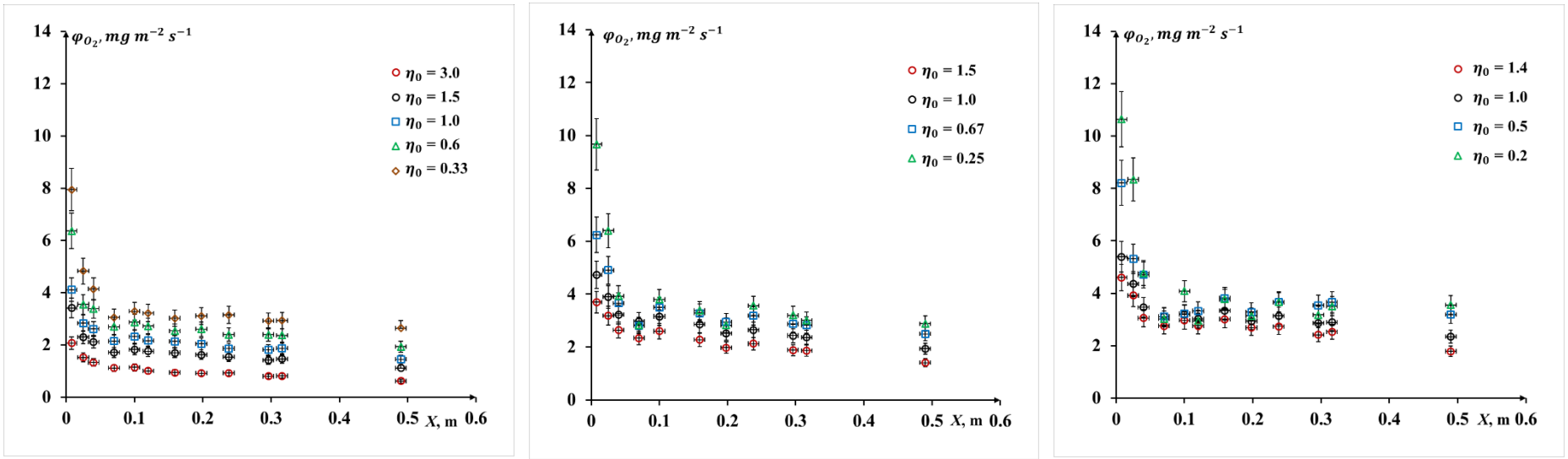

(a) (b) (c)

Fig. 6-9 Evolution of mass flux density versus axial positions X under different operating conditions: (a) j_{TP} = 28.6 cm s^{-1}; (b) j_{TP} = 35.7 cm s^{-1}; (c) j_{TP} = 42.9 cm s^{-1}.

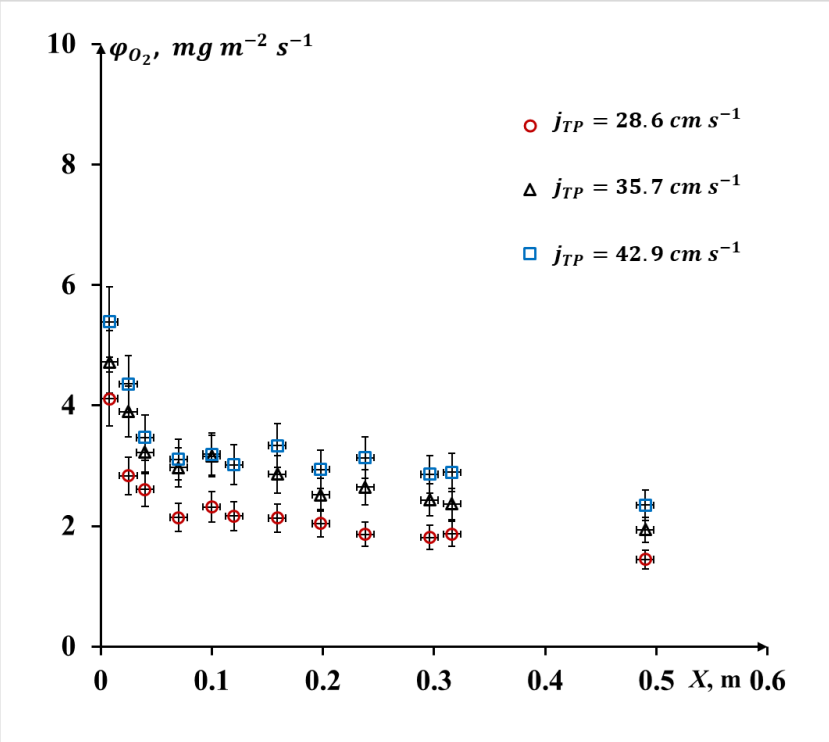

(d)

Fig. 6-10 Evolution of mass flux density versus axial positions X for η_0 = 1 under different two-phase superficial velocities.

In Fig. 6-13, at given axial position X and η_0, an increase of j_{TP} induced the increase of the mass flux density φ_{O_2}. One can note that the final constant value of the mass flux density could be achieved after 0.2 m for all operating conditions, indicating that the entrance effects (bubble formation stage) occurred until X = 0.2 m.

6.4 Estimation of enhancement factor

Due to the presence of colorimetric chemical reaction, the enhancement factor E need to be deduced first. Ha and E can be calculated by solving two implicit equations (4-16) and (4-17) presented in Chapter 4. Here, the saturated oxygen concentration was adopted as 8.15 mg L^{-1} since there was no bubble expansion and the pressure drop was below 7 kPa.

Two reaction rate constants k_2 were considered here, namely the 1.28×10^6 L mol^{-1} s^{-1} as proposed by Yang et al. (2016a), and 0.67×10^6 L mol^{-1} s^{-1} later measured by Hoppe (2019) (this was an averaged value obtained from different concentrations of glucose and NaOH). For all the conditions displayed in Fig. 6-9, for both k_2:

- when the Hatta numbers ranged between 3 and 8.6, the enhancement factors were between 1.02 and 1.04.
- when Ha ranged from 0.65 to 3, E tended towards to unity.

Thus, these calculations would suggest that there was no enhancement caused by the colorimetic chemical reaction on the mass transfer. Thus, E was considered as unity in the following section.

6.5 Cumulated oxygen mass during bubble formation process

The cumulated oxygen mass inside one liquid slug during the formation of the back bubble was considered (i.e., the considered liquid slug was in front of the forming bubble).

As shown in Fig. 6-11, according to the development of the liquid slug, the liquid slug could be divided into three stages:

a. the liquid surrounding the gas finger neck, squeezed the gas finger until the pinch-off of the front bubble;
b. after the pinch-off of the front bubble, the liquid entered the main channel until the back gas finger fully blocked the channel;
c. the liquid slug formed and was separated by the back gas finger and front formed bubble.

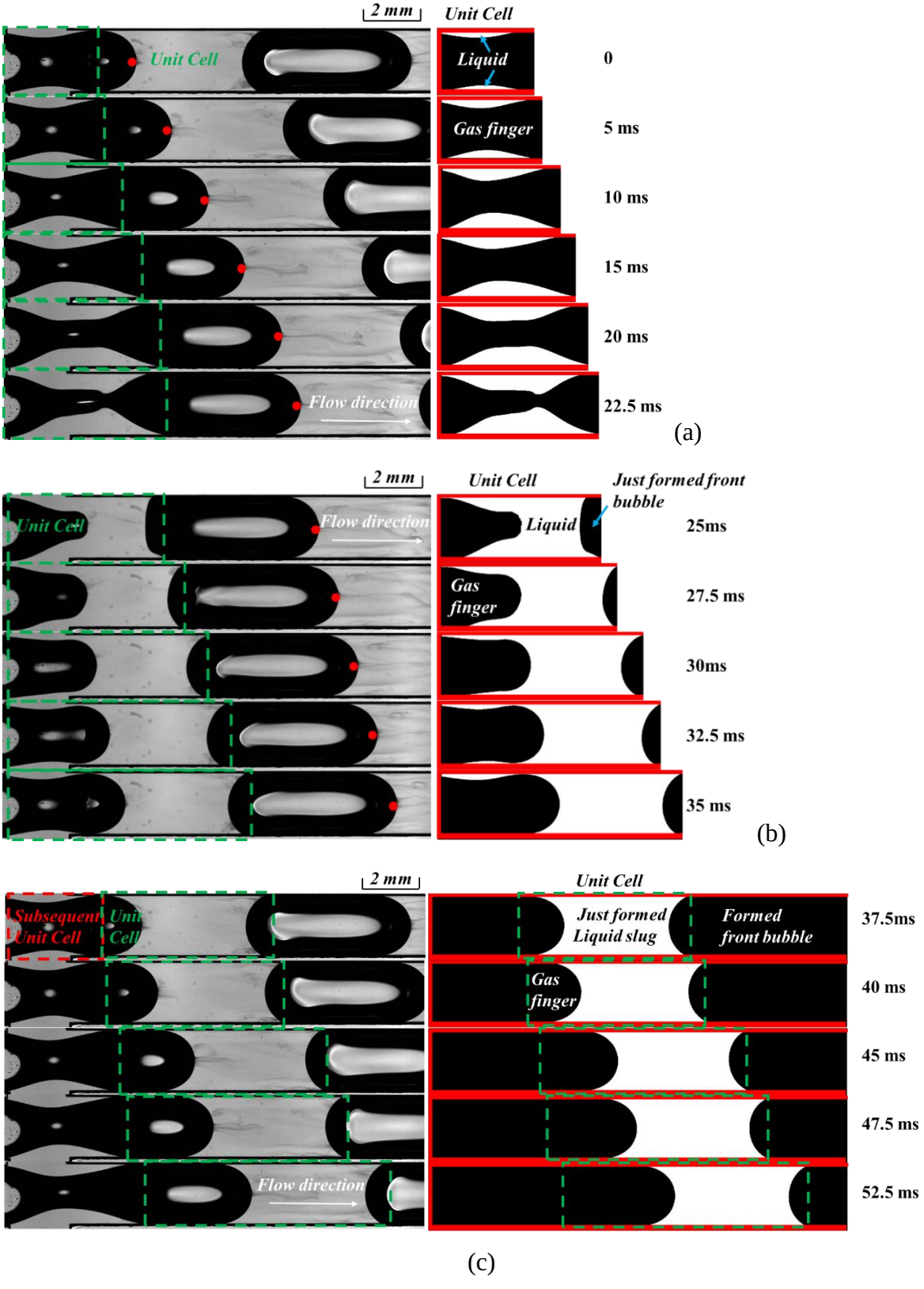

Fig. 6-11 Illustration of the development of unit cell, liquid slug and bubble during the bubble formation process, stage (a) the squeezing liquid surrounding gas finger, stage (b) the entering liquid after the pinch-off of the front bubble but before the block of channel by gas finger, stage (c) the liquid slug separated by gas finger and formed bubble.

The second column in Fig. 6-11 shows the liquid extracted by Matlab, and the unit cell was marked by the green dotted box.

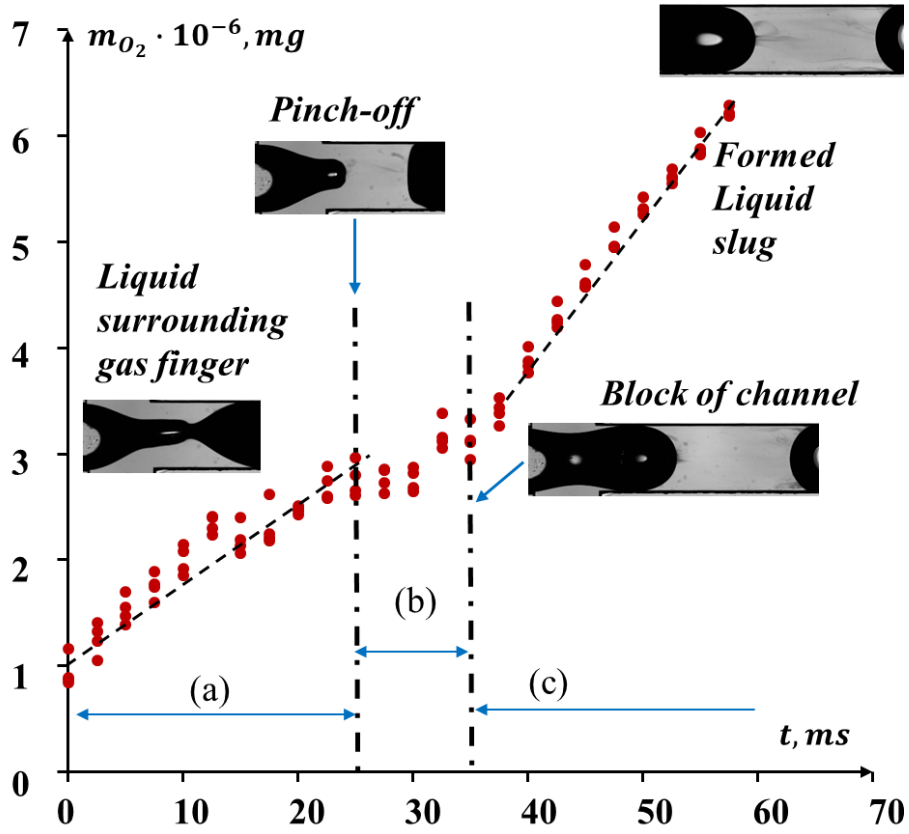

Fig. 6-12 Evolution of cumulated oxygen mass inside liquid during bubble formation pinch-off process. Operating conditions: η_0 = 1, j_{TP} = 28.6 cm s^{-1}.

Fig. 6-12 displays one example of the variation of the cumulated oxygen mass in the liquid during the bubble formation. The variation could be divided into three stages which corresponded to the ones in Fig. 6-11. It is observed that the cumulated oxygen mass in stages (a) and (c) were almost linearly increasing versus time. The gas finger velocity for stage (a) and the formed bubble velocity in stage (b) were estimated according to the displacement of the gas finger nose or bubble nose (see solid red dots in Fig. 6-11). They showed that, during the stage (a), the gas finger was accelerating until the bubble pinch-off and its velocities increased from 24.8 to 28.1 cm s^{-1}, and that, during the stage (b), the formed bubble velocity were almost constant and around 28.6 cm s^{-1}. The fast growth of oxygen mass in stage (c) could be thus to the consequences of the developing

recirculation loop in the formed liquid slug and also of the accelerating movement of subsequent gas finger. The oxygen mass at the stage (b) slightly varied, probably due to a 'dilution effect' induced by the fresh liquid coming from side channels.

Further quantitative calculations of bubble surface and liquid volume are reported in Appendix 9.

In the future, deeper studies relating the local variations of mass transfer rates and the gas finger velocities need to be further implemented to have a better understanding.

6.6 Comparison of the overall mass transfer coefficients obtained in the spiral-shaped milli-reactor, in the straight channel with a cross-junction and in the literature

The overall volumetric liquid side mass transfer coefficient $k_L \cdot a$ can be deduced from the oxygen mass balance in the liquid phase according to Eq. (4-3). As a reminder, t represented the traveling time of the bubble until reaching the axial position X ($t = X/U_B$) and $\overline{C_{O_2}(X)_{rl}}$ was equal to zero because of a full consumption of O_2 by DH in the liquid slug.

From the variations of equivalent O_2 concentration versus X shown in Fig. 6-7, it is seen that $\overline{C_{O_2}(X)}$ could be considered as linearly increasing with X (i.e., time t). Using the least square method, the slope coefficient (noted ζ) between $\overline{C_{O_2}(X)}$ and X could be obtained. Therefore, the overall volumetric liquid side mass transfer coefficient $k_L \cdot a$ could be calculated as follows:

$$k_L\, a = \frac{\zeta \times U_B}{C^*_{O_2}} \tag{6-2}$$

As the mass transfer mechanism was affected by the Taylor vortices inside the liquid slug, it was interesting to consider the frequency of loop recirculation adopted from Abiev et al. (2019) according to Eq. (4-6).

The obtained overall volumetric liquid side mass transfer coefficient $k_L \cdot a$ and recirculation frequencies f_c are listed in Appendix 10 (see Table A 10-1).

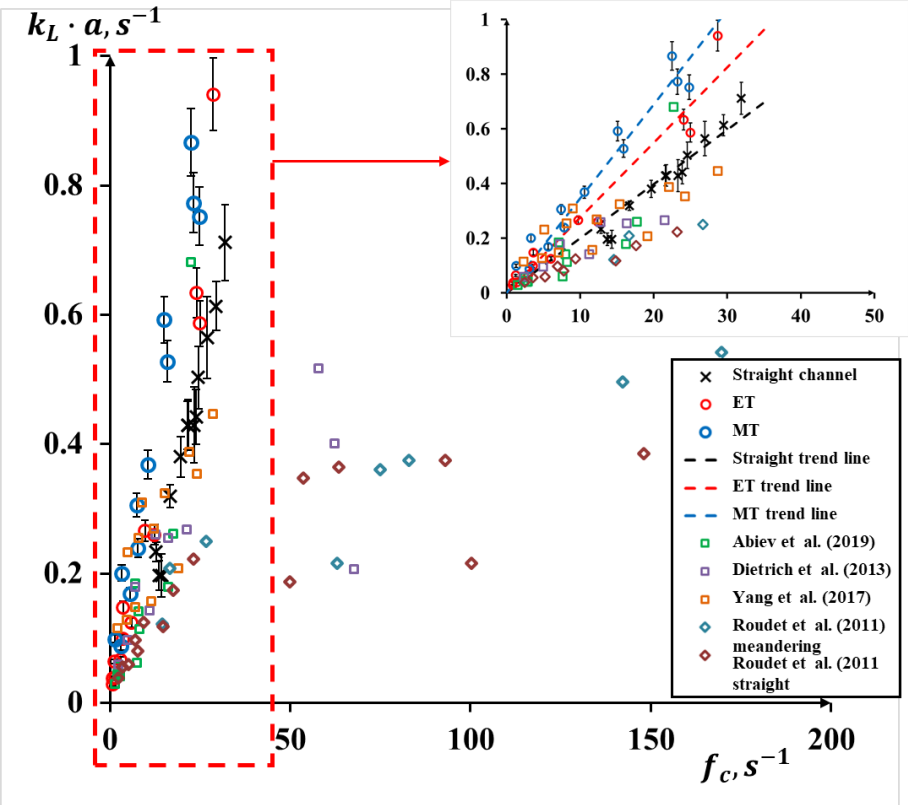

Fig. 6-13 Relationships between the overall volumetric liquid side mass transfer coefficients $k_L a$ and recirculation frequency f_c, for the three different configurations investigated in this work and for the data from the literature.

Fig. 6-13 plots the relationships between the overall volumetric liquid side mass transfer coefficient $k_L \cdot a$ and f_c in this straight milli-channel and compared with the one obtained in ET and MT configurations in Chapter 4 (section 4.2.3). It can be observed that all the $k_L \cdot a$ data followed a linear increase relation with recirculation frequency f_c and can be fitted by Eq. (4-7) using the least square regression. It was found that the linear dimensionless coefficient ω was equal to 1.99×10^{-2} in this straight channel. This coefficient was lower than the ones

obtained in the in-plane spiral-shaped milli-reactor (2.75×10^{-2} and 3.45×10^{-2} for ET and MT configurations), which was possibly due to absence of centrifugal force, different cross-sectional shape (cylindrical tube or squared channel), and channel dimensions. In addition, the minimum Re_{TP} number in straight channel was about 2.4 times of that maximum Re_{TP} number in spiral reactor. This also emphasized the mass transfer intensification caused by the centrifugal force even under lower ranges of Re_{TP} number.

In addition, the data of Roudet et al. (2011) in a straight and meandering channel (2mm, square), Yang et al. (2017a) in a meandering milli-channel (2mm, square), Dietrich et al. (2013a) in a straight milli-channel (2mm, square), and Abiev et al. (2019) in a vertical glass tube (d_{it}, 3mm), were also plotted in Fig. 6-13. They also followed a good linearity with the increase of recirculation frequencies when the recirculation frequencies were lower than 50. Whereas when the recirculation frequencies were higher than 50, it was found that the overall volumetric liquid side mass transfer coefficient $k_L \cdot a$ remained at a plateau and no longer increased linearly with the recirculation frequencies, which was probably due to other factors (e.g., possibilities of bypass flow, shorter flowing time inside of the milli-channels).

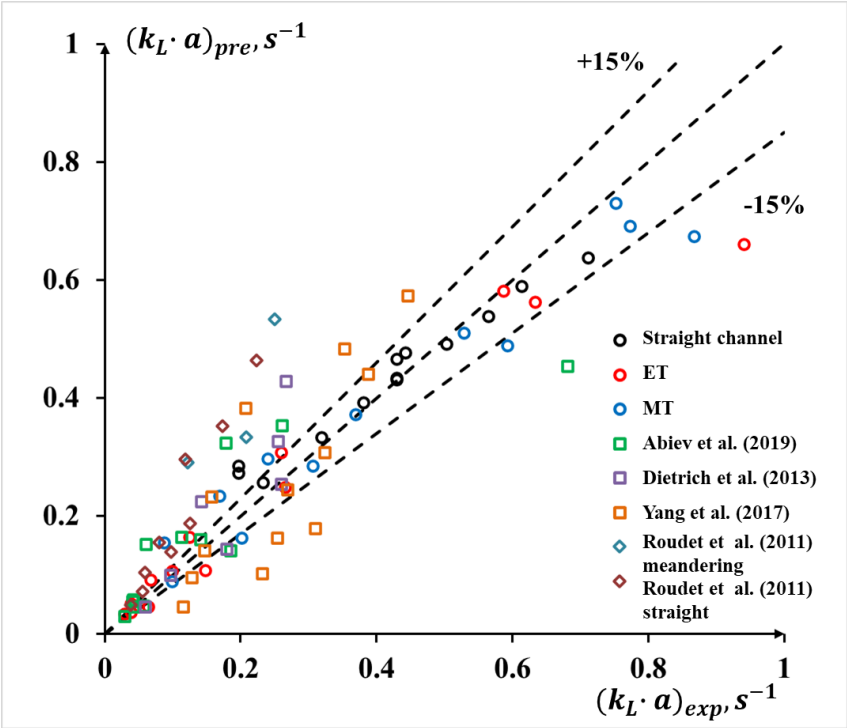

Fig. 6-14 Comparison between the predicted $(k_L\ a)_{pre}$ and experimental $(k_L\ a)_{exp}$ for three different configurations investigated in this work and for the data from the literature.

As mentioned for Fig. 4-6 in section 4.2.3, the intensification factor for $k_L{\cdot}a$ was almost proportional to the increase of $\sqrt{1/\langle\lambda\rangle}$ from ET to MT configurations. For straight channels, the curvature ratio was infinity and $\sqrt{1/\langle\lambda\rangle}$ was thus zero. A scaling law for $k_L{\cdot}a$ and f_c based on $1/\langle\lambda\rangle$ in different configurations were proposed for $f_c < 50$, consisting of two terms as below:

$$k_L\ a = 0.02 f_c + 270.10 \left(\frac{1}{\langle\lambda\rangle}\right)^{1.91} {f_c}^{0.44}, \qquad \text{MAPER: } 15.0\% \tag{6-3}$$

The first term 0.02 represented the coefficient for straight channels. The second term $270.10(1/\langle\lambda\rangle)^{1.91}{f_c}^{0.44}$ represented the effects of centrifugal force caused by curved channel on the mass transfer. Fig. 6-14 compares the predicted $(k_L\ a)_{pre}$ with the experimental $(k_L\ a)_{exp}$ for three configurations used in this work and also the data from Roudet et al. (2011), Dietrich et al. (2013a), Yang et al. (2017a), and Abiev et al. (2019). The proposed scaling law in Eq. (6-3) gave a

good description for all the configurations when recirculation frequencies were under 50, whereas there were some data beyond the ± 15% reliable range of prediction, which could be caused by the variation of inlet geometries or extreme conditions.

6.7 Conclusion

Gas-liquid mass transfer around Taylor bubbles during and after the bubble formation (twelve observing positions) have been investigated in a straight milli-channel with a cross-junction. Using the resazurin-based colorimetric technique and improved image acquisition system (monochromatic light and magnification), the equivalent oxygen concentration fields were visualized and measured. The main findings were the following:

1) It was the first time that the resazurin-based colorimetric method was implemented using a monochromatic light in the image system, thus allowing to apply the Beer-Lambert law to calculate the equivalent oxygen concentrations. The application of the Beer-Lamber law also imposed a homogeneous concentration of dissolved species in the vertical direction. The level of homogeneity (i.e., the percentage of the standard deviation errors (SD) with respect to the averaged equivalent oxygen concentrations inside of the liquid slug) was estimated and found between 1% and 20%.

2) Equivalent oxygen concentration fields were obtained during the bubble formation and flowing stages. At bubble formation stage, for low Re_{TP}, a jet-like central oxygen concentration ‘finger’ formed between the front bubble and back gas finger at the bubble pinch-off point. The dissolved oxygen was carried by the entering liquid from two side channels and later by the developing recirculation loop inside the liquid slug, which propagated forwards and presented symmetrically with respect to the centerline of the main channel. For $Re_{TP} > 416$,

it is noted that two high equivalent oxygen concentration fields near the front bubble rear and channel wall region were formed and equivalent oxygen concentration fields presented more complex structure compared to the one of $Re_{TP} = 8$. At bubble flowing stage, dissolved oxygen inside of the liquid slug was gradually accumulating with the increase of axial positions for all conditions.

3) The average oxygen concentrations increased linearly with the axial position *X*, while the mass flux density decreased with *X*, in accordance with the observations in Chapter 4. Furthermore, at the same flowing time for liquid slugs, it was found that the averaged oxygen concentrations increased with the gas-liquid superficial velocity ratio at given two-phase superficial velocities, and vice versa.

4) During the bubble formation, the cumulated oxygen mass was described by three stages, (a) the variation of cumulated oxygen in liquid surrounding the gas finger neck, (b) cumulated oxygen in liquid after the pinch-off of the front bubble, (c) cumulated oxygen in the liquid slug (separated by the front bubble and back gas finger). The increasing rate of cumulated oxygen mass was found the highest for the third stage in the liquid slug, which was probably due to the combined effect of the developing recirculation loop and of the accelerating gas finger.

5) The overall volumetric liquid side mass transfer coefficients ($k_L\ a$) obtained in the in-plane spiral-shaped milli-reactor, in the straight milli-channel with a cross-junction, and the ones in the literature were compared. They followed a linear increase with the recirculation frequencies for $f_c < 50$. The values of $k_L \cdot a$ in the straight channel were smaller than the ones obtained in ET and MT configurations, verifying the mass transfer intensification induced by the centrifugal force. A scaling law based on recirculation frequency and curvature ratio were at last proposed and applied to all configurations to predict the $k_L \cdot a$.

Chapter 7. Conclusions and perspectives

In this final chapter, the main contributions of this work will be first summarized, and then some scientific perspectives will be presented.

7.1 General conclusions

The chemical industry is one of the largest and most diversified industries, and supplies virtually all sectors of the economy, such as petrochemical, pharmaceutical and fine chemical industries. The growth of the chemical industry during the 21st century has put pressure to achieve sustainable green chemistry and engineering. Continuous-flow technologies, especially micro-structured reactors, are now recognized as relevant alternatives for multiphase batch processing in chemical industry, and become prosperous ways for process intensification. In order to increase the reaction yields and selectivity in continuous flow multiphase reactors, the parameters controlling the mass transfer between phases need to be identified and the related mechanisms well-understood so as to propose relevant scaling laws. In the literature, most of the works are devoted to investigate the hydrodynamics and mass transfer in the case of Taylor flows which involve stable flows of bubbles regularly spaced by liquid slugs, and thus generate high interfacial areas and mass transfer coefficients. In many cases, the performances are quantified using global indicators, and generally in straight and short milli-channels.

The present work aimed at contributing to this scientific field by studying gas-liquid hydrodynamics and mass transfer around Taylor bubbles by means of

a local experimental method. A focus was made on two configurations: bubbles flowing in an in-plane spiral-shaped milli-reactor, and bubbles generated at a cross-junction in a straight milli-channel. The underlying motivations were to better understand first the effect of a continuous change of tubing curvature (i.e., centrifugal force) on the local mass transfer, and secondly the mass transfer mechanism during and just after the bubble formation stage.

The experimental methodology used for visualizing the equivalent oxygen concentration fields and evaluating the mass transfer was the colorimetric technique based on resazurin dye, first proposed by Dietrich et al. (2013a). There were mainly two experimental setups implemented in this work (Chapter 2). The first one, called the in-plane spiral-shaped milli-reactor, was initially designed for flow photochemistry at LGC laboratory (Aillet et al., 2014; Aillet et al., 2016; Loubière et al., 2016). Due to the in-plane Archimedean spiral-shaped design, the tube (FEP, 1mm I.D.) curvature ratios were continuously varying from 52 to 166. Two configurations possessing identical tubing length (~3 m) but covering different curvature ratio domains were investigated, which were denoted by ET and MT (the related average curvature ratios for ET and MT were 145 and 84, respectively). The second experimental setup, located at TBI laboratory, consisted of a straight milli-channel (fabricated using PMMA) with a cross-junction, and was specifically designed for exploring the mass transfer during bubble formation process, so as to get a deeper understanding of the results obtained by Yang et al. (2016b). Some improvements on image acquisition system were also applied, such as the use of monochromatic light (530nm, green light, to apply Beer-Lambert law) and of magnification on Region-of-Interest. For the image and data processing, an original image processing code based on Matlab was dedicated to extract the bubbles and liquid slugs from images captured by Edge or Basler cameras. Then, specific algorithms were compiled to accurately determine the hydrodynamic parameters (e.g., bubble lengths, liquid slug lengths, and bubble

velocities, etc.), and mass transfer characteristics (i.e., the equivalent oxygen concentration fields and their variations with axial positions).

First, the main results of the *hydrodynamic studies in an in-plane spiral-shaped milli-reactor* (Chapter 3) were described as follows. Under a large variation of gas-liquid superficial velocity ratios (0.13 to 9.52), steady Taylor flows were established without coalescence of bubbles and liquid slugs. Very long, stable cylindrical shaped Taylor bubbles (dimensionless bubble length up to 40) and long liquid slugs (dimensionless liquid slug length up to 20) were generated. Under the same gas-liquid superficial velocity ratio, shorter average Taylor bubbles were found in the MT configuration when compared to those in the ET one, while identical average liquid slug lengths were observed in both configurations. With such a long-curved tubing length (3 m), the effect of pressure drops became no more negligible and thus, the bubble lengths and velocities increased linearly with the axial positions in the channel, in both configurations. However, there was no variations of the liquid slug lengths along the axial position. The pressure drops per unit of length measured experimentally were compared with those estimated by Ideal Gas Law and by correlations from the literature. It was found that the capillary pressure drop was dominant when compared to the frictional pressure drop due to the hydrophobicity of FEP tube.

Based on these findings, the *mass transfer characteristics in the in-plane spiral-shaped milli-reactor* were investigated (Chapter 4). The axial variations of the equivalent oxygen concentration inside the liquid slugs were extracted up to 2 meters, but the maximum oxygen concentrations were achieved below 1.2 meters for both configurations. Without considering the hydrodynamic variations with axial positions, the average overall volumetric liquid side mass transfer coefficients ($k_L a$) were acquired from the axial position corresponding to a full coloration. They were found to vary linearly with the recirculation frequency, whatever the configurations. The intensification factor in terms of the $k_L a$ between ET and MT was found almost identical to the increase of the average

Dean number from the ET to MT configurations. Such results would indicate that the mass transfer rates in both configurations were controlled by the centrifugal force induced recirculation loops. Accounting for the flow variations along the channel length (i.e., the changes in pressure drop, bubble length and velocity), the axial variations of cumulated mass flux densities were calculated in both configurations. Generally, they decreased along the axial positions and finally tended towards a constant value. Finally, in the cases where a liquid film around Taylor bubbles existed or not, a unique scaling law was proposed for both configurations, enabling to establish a relationship between the Sherwood number, a normalized coloration time, dimensionless liquid slug length, Péclet number and Dean number.

The decrease of cumulated mass flux densities along the tubing length in Chapter 4 pointed out the necessity to pay a further attention on the mass transfer process during bubble formation stage. A cross-junction geometry was chosen for this purpose. In terms of ***hydrodynamics*** (Chapter 5), it was first observed that the bubble formation was broadly composed of filling and squeezing stages and that the related frequencies were mainly controlled by the gas flow rates and liquid flow rates, respectively. Theoretically, basing on an analysis of the bubble length with respect to the bubble filling and squeezing times, the formed bubble length could be described by a scaling law involving the gas-liquid superficial velocity ratio ($L_B \propto \eta_0$ with an intercept). This theoretical result was verified experimentally in the milli-channel with a cross-junction, but also in the in-plane spiral-shaped milli-reactor with a T-junction. The liquid slug lengths followed the scaling law based on the inverse of gas-liquid superficial velocity ratio ($L_S \propto \frac{1}{\eta_0}$ with an intercept). The scaling laws of bubble and liquid slug lengths were valid for two experimental setups. The bubble velocities were found equal to 1.17 and 1.02 times of the total two-phase superficial velocities in the spiral-shaped milli-reactor and in the straight milli-channel. Based on the positions of gas finger right

after the bubble pinch-off, two pinch-off patterns were identified, depending whether the gas finger was located inside or outside of the cross-junction. The transition boundaries between these two patterns were determined by a critical liquid Capillary number. Unlike the cylindrical Taylor bubble shapes observed in the in-plane spiral-shaped milli-reactor, hemispherical shapes of Taylor bubbles were identified in this straight channel. Furthermore, increasing Ca_{TP} or We_{TP} numbers promoted bubble deformation with slender bubble nose and flatter bubble rear. The wetting and dewetting of liquid film around Taylor bubbles were also illustrated in this partially wetting PMMA channel, indicating the complex structure of liquid film.

The *mass transfer characteristics at the cross-junction in a milli-channel* was investigated in Chapter 6. First, the temporal changes of the equivalent oxygen concentration fields were displayed during the bubble formation process. At a low two-phase Reynolds number (Re_{TP} = 8), a jet-like central oxygen concentration 'finger' between gas finger and formed bubble was illustrated right after the bubble pinch-off, probably due to cumulated oxygen layers near bubble neck during the filling and squeezing stage. With the increase of Re_{TP}, the jet-like central oxygen concentration 'finger' was less obvious to be observed. Two oxygen concentration fields behind the formed bubble and near the channel wall were identified due to the developing recirculation loop or axial dispersion from liquid film surrounding the front bubble in the channel corner. By means of the twelve Region-of-Interest positions implemented, the equivalent oxygen concentrations fields could be followed along the axial positions and the progressive accumulations of oxygen in the liquid slugs were highlighted. The average equivalent oxygen concentrations were found to increase almost linearly with axial positions. In addition, under an identical flowing time for the liquid slug, the average equivalent oxygen concentrations increased with the total two-phase superficial velocities and with the gas-liquid superficial velocity ratios. Finally, it could be possible to gather all the volumetric liquid side mass transfer

coefficients (i.e., the ones obtained in the ET, MT and the straight milli-channel) by relating them with the corresponding recirculation loop frequencies. A scaling law based on recirculation loop frequencies and curvature ratios was proposed and composed of two terms (one for straight channels and the other accounting the effects of centrifugal forces).

All these findings enabled to gain knowledge on gas-liquid hydrodynamics and mass transfer characteristics around Taylor bubbles, especially on the effect on centrifugal forces, during and just after the bubble formation stage. In the future, they could be used to provide guidelines to implement multiphase reactions in continuous flow microstructured reactors.

7.2 Perspectives

This is the end of this thesis but also the start of future works.

1. Even with the results in the present work, more quantitative analyses on mass transfer characteristics during the bubble formation process are still required to fully evaluate the entrance effects and the contribution compared to the overall mass transfer characteristics. They will especially need a more accurate evaluation of the enhancement factor of mass transfer by the reactor. A further estimation and comparison between the mass transfer characteristic time, diffusion time, contacting time, and bubble formation time (i.e., filling and squeezing time) would be also interesting to formalize a principle of entrances effects on mass transfer.

2. One of the big challenges to be solved is to capture the equivalent oxygen concentrations in both the liquid slug and the liquid film by the colorimetric method. Due to the partially wetting channel (PMMA, 64° for

deionized water) and hydrophobic tube (FEP, 98.7° for glucose and NaOH aqueous solutions), we were unfortunately not able to capture the information inside the liquid film in this work. Achieving thicker liquid film could be convenient for measurement purposes, but also beneficial for implying chemical reactions with catalysts embedded on the channel walls. One way is to increase the Capillary numbers ($\delta_{LF} \propto Ca^{\frac{2}{3}} = (\frac{\mu_L j_{TP}}{\sigma_L})^{\frac{2}{3}}$, Bretherton (1961)), for example, by increasing the liquid viscosity and decreasing surface tension.

3. Linked to the second point, investigating the effect of surfactants and/or non-Newtonian fluids on mass transfer draws great scientific perspectives, not only with changing the liquid film but also more relevant to the real complex and different liquid properties which are encountered in chemical systems. It will also allow the scaling laws established in this work to be reinforced or modified. The effect of non-Newtonian fluids (shearing-thinning, shearing-thickening) on mass transfer was investigated in the thesis of Feishi XU (2015-2019) within bubble columns at the TBI laboratory and could be transposed in confined micro/milli-channels. The effect of surfactants is at present studied experimentally in the thesis of Gaëlle LEBRUN (2018-2021) within bubble columns at the TBI laboratory and in the thesis of Kalyani KENTHESWARAN (2018-2021) using numerical simulations at both TBI and LGC laboratories.

4. Apart from experimental techniques, 3D numerical simulations are powerful methods for helping to understand the experimental results obtained by the colorimetric method as they are averaged along the channel depth, and also for investigating some conditions which are hard or impossible to achieve experimentally (e.g., only changing liquid viscosity or surface tension without changing other parameters). Some initial attempts (2D) have been made to explore

the effect of contact angle on the bubble formation in a cross-junction, as shown in Fig. 7-1. They need to be continued in the future.

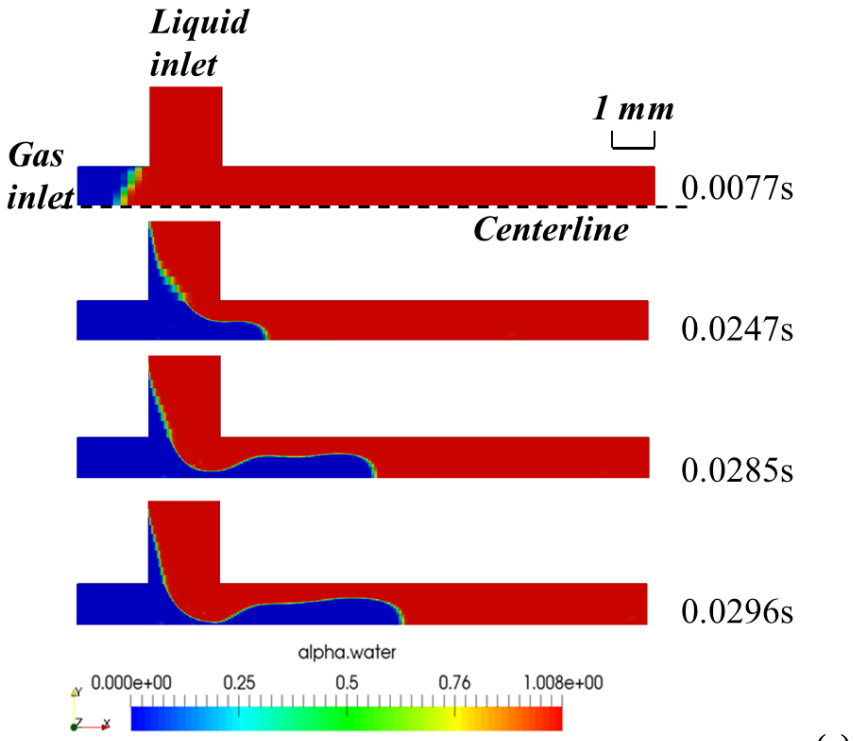

(a)

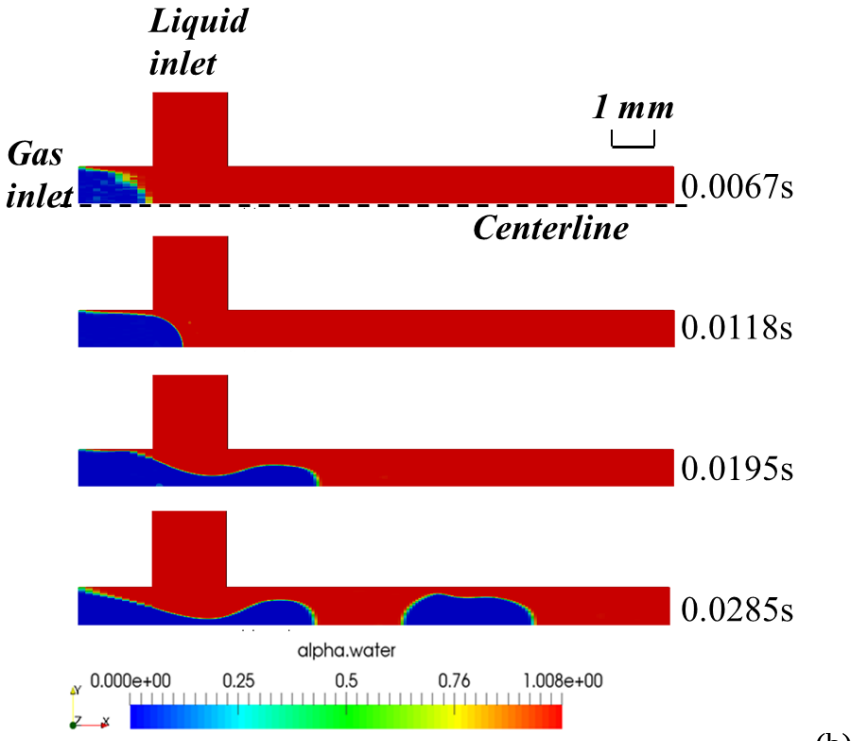

(b)

Fig. 7-1 Two types of bubble formation with different contacting angle at (a) 180°, (b) 0°.

5. The databank for the colorimetric method has to be completed, for example, by acquiring more data about the colorimetric reaction rate constants (i.e., k_2) depending on the glucose and NaOH concentrations, which was partially made by Hoppe (2019). In addition, the reaction rate constant of the back reduction reaction of resorufin also needed to be quantified.

6. Exploring colorimetric techniques with other dyes (e.g., indigo carmine, thionine) and green chemicals (i.e., replacing the glucose and NaOH by vitamin C) could also be promising.

7. Using a laser plane for implementing colorimetric methods to make measurements in a thin layer of the reactor is possible for resorufin dye (highly fluorescent), which could avoid any calibration uncertainties in the depth direction.

8. Developing hybrid tracers (i.e., nano particles with fluorescence) for multi-sensing measurements is promising, which could simultaneously measure the flow fields (acting as PIV) and dissolved concentrations (acting as PLIFI).

9. Analogy with the stirred tank, some further studies associating the recirculation frequencies, the overall volumetric liquid side mass transfer coefficients and specific power consumption (defined as $\iota = \frac{Q_{TP}\,\Delta p_{r0}}{V_{reactor}}$, (Wongwailikhit, 2019)) will be implemented to give a full description for the continuous flow milli-reactors. Some initial attempts have been made in the in-plane spiral-shaped milli-reactor, as shown in Fig. 7-2: it is observed that the overall volumetric liquid side mass transfer coefficients ($k_L\,a$) increased with increasing the specific power consumption. Further investigations will be implemented in the future.

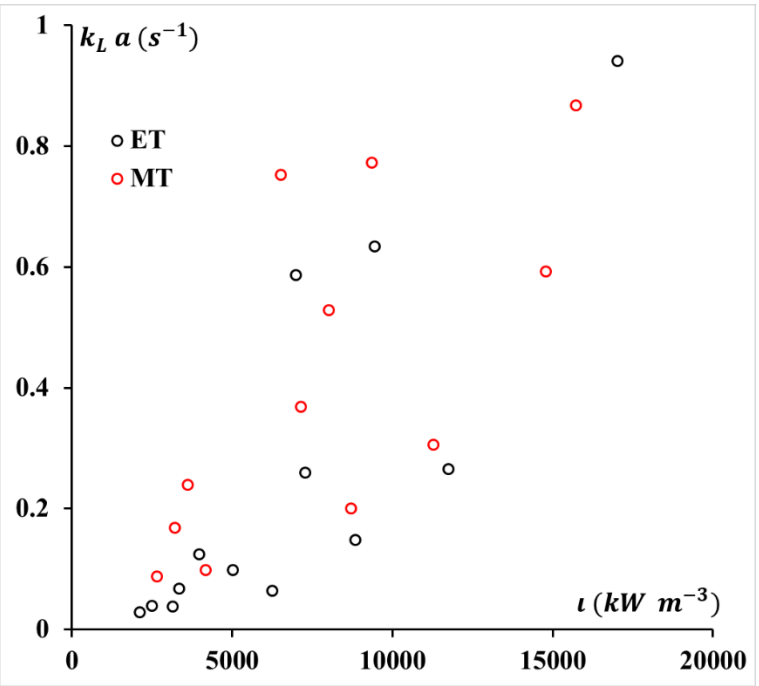

Fig. 7-2 Overall volumetric liquid side mass transfer coefficients as a function of the specific power consumption

Appendices

1. In-plane spiral-shaped milli-reactor: experimental results of gas-liquid hydrodynamics in the ET and MT configurations

Table A 1-1 In-plane spiral-shaped milli-reactor: experimental results of gas-liquid hydrodynamics in the ET configuration.

N	j_L,	j_G,	η_0	Re_L,	Re_G,	Re_{TP},	Ca, $\times10^{-3}$	$\langle De \rangle$,	$\langle U_B \rangle$,	$\langle L_B \rangle$,	$\langle L_S \rangle$,	F_1,	L_{B0},	F_2,$\times10^{-3}$	U_{B0},	F_3,	p_{B0}, $\times10^5$	p_{r0}, $\times10^5$
(-)	cm s^{-1}	cm s^{-1}	(-)	(-)	(-)	(-)	(-)	(-)	cm s^{-1}	mm	mm	(-)	mm	s^{-1}	cm s^{-1}	Pa m^{-1}	Pa	Pa
1	1.8	0.8	0.45	16.2	0.6	24	0.4	2.0	2.7	6.34	8.43	0.61	5.53	0.9	2.6	-0.11	1.34	1.69
2	1.8	1.1	0.6	16.2	0.7	26	0.4	2.2	3.0	7.18	6.58	0.82	6.11	1.5	2.8	-0.13	1.42	1.70
3	1.8	1.4	0.76	16.2	0.9	28	0.5	2.3	3.3	8.14	5.83	1.05	6.74	2.1	3.2	-0.16	1.48	1.68
4	1.8	2.8	1.55	16.2	1.9	41	0.7	3.4	5.3	12.15	4.47	1.11	10.45	3.0	4.6	-0.11	1.33	1.63
5	1.8	5.1	2.85	16.2	3.5	63	1.0	5.2	8.6	18.92	3.58	1.31	16.27	4.1	7.3	-0.08	1.26	1.50
6	1.8	6.9	3.81	16.2	4.6	78	1.3	6.5	10.3	22.83	3.05	1.7	20.51	5.7	9.2	\	1.26	1.44
7	1.8	12.7	7.05	16.2	8.6	130	2.2	10.8	16.9	33.67	2.48	1.82	31.11	7.4	15.2	\	1.19	1.36
8	1.8	16.6	9.22	16.2	11.2	165	2.7	13.7	21.8	40.35	2.18	1.94	37.52	8.6	19.1	-0.05	1.17	1.34
9	3.6	0.9	0.24	32.4	0.6	40	0.7	3.3	4.2	5.04	12.06	0.5	4.34	1.0	4.5	-0.12	1.36	1.61
10	3.6	1.1	0.31	32.4	0.8	43	0.7	3.6	4.5	5.38	10.43	0.59	4.61	1.4	4.7	\	1.40	1.66
11	3.6	3.0	0.84	32.4	2.1	60	1.0	5.0	7.2	8.39	5.01	1.02	7	4.4	6.6	-0.15	1.45	1.65
12	3.6	9.3	2.58	32.4	6.3	116	1.9	9.6	15.1	15.1	3.05	1.18	13.49	8.1	13.3	-0.09	1.28	1.49
13	3.6	16.0	4.44	32.4	10.8	176	2.9	14.6	23.2	21.25	2.41	1.43	19.35	11.8	20.1	-0.07	1.24	1.42
14	7.2	0.9	0.13	64.9	0.6	73	1.2	6.1	7.4	4.19	19.56	0.33	3.75	0.8	8.3	\	1.28	1.57

N	j_L,	j_G,	η_0	Re_L,	Re_G,	Re_{TP},	Ca, $\times10^{-3}$	$\langle De \rangle$,	$\langle U_B \rangle$,	$\langle L_B \rangle$,	$\langle L_S \rangle$,	F_1,	L_{B0},	F_2,$\times10^{-3}$	U_{B0},	F_3,	p_{B0}, $\times10^5$	p_{r0}, $\times10^5$
(-)	cm s^{-1}	cm s^{-1}	(-)	(-)	(-)	(-)	(-)	(-)	cm s^{-1}	mm	mm	(-)	mm	s^{-1}	cm s^{-1}	Pa m^{-1}	Pa	Pa
15	7.2	1.4	0.2	64.9	1.0	78	1.3	6.5	7.8	4.54	15.94	0.37	4.04	1.3	8.6	-0.09	1.29	1.63
16	7.2	3.2	0.44	64.9	2.1	93	1.5	7.7	10.1	5.49	6.95	0.7	4.55	4.9	10.4	-0.15	1.48	1.73
17	7.2	4.9	0.67	64.9	3.3	109	1.8	9.1	12.9	6.41	4.66	0.86	5.24	8.0	12.5	\	1.51	1.77
18	7.2	6.2	0.86	64.9	4.2	121	2.0	10.0	14.9	7.01	3.84	1	5.68	11.0	13.7	-0.18	1.54	1.75
19	7.2	15.5	2.14	64.9	10.5	204	3.4	16.9	26.1	11.22	2.5	1.24	9.58	20.0	23.0	\	1.40	1.60
20	7.2	17.7	2.45	64.9	12.0	224	3.7	18.6	27.3	11.74	2.38	1.22	10.14	21.3	25.2	-0.12	1.37	1.59

Table A 1-2 In-plane spiral-shaped milli-reactor: experimental results of gas-liquid hydrodynamics in the MT configuration

N	j_L,	j_G,	η_0	Re_L,	Re_G,	Re_{TP},	Ca, $\times10^{-3}$	$\langle De \rangle$,	$\langle U_B \rangle$,	$\langle L_B \rangle$,	$\langle L_S \rangle$,	F_1,	L_{B0},	F_2,$\times10^{-3}$	U_{B0},	F_3,	p_{B0}, $\times10^5$	p_{r0}, $\times10^5$
(-)	cm s^{-1}	cm s^{-1}	(-)	(-)	(-)	(-)	(-)	(-)	cm s^{-1}	mm	mm	(-)	mm	(s^{-1})	cm s^{-1}	Pa m^{-1}	Pa	Pa
1	1.8	0.8	0.46	16.2	0.6	24	0.4	2.6	2.5	5.18	7.83	0.71	4.31	1.4	2.3	\	1.50	1.72
2	1.8	1.1	0.61	16.2	0.7	26	0.4	2.8	2.9	5.91	6.4	0.87	4.86	2.0	2.7	-0.18	1.54	1.73
3	1.8	3.2	1.77	16.2	2.2	45	0.7	4.9	5.0	10.1	4.06	0.84	9.07	3.0	4.8	-0.09	1.29	1.47
4	1.8	5.3	2.96	16.2	3.6	64	1.1	7.0	7.9	15.59	3.53	1.21	14.09	4.6	7.6	-0.09	1.27	1.40
5	1.8	7.1	3.97	16.2	4.8	80	1.3	8.7	10.1	19.88	3.23	1.3	18.25	5.1	9.7	-0.07	1.22	1.36
6	1.8	17.1	9.52	16.2	11.6	170	2.8	18.5	22.4	35.12	2.26	1.34	33.26	6.9	21.5	-0.04	1.13	1.31
7	3.6	0.9	0.25	32.4	0.6	40	0.7	4.4	4.1	3.87	12.63	0.39	3.39	1.0	3.9	\	1.35	1.63
8	3.6	1.4	0.38	32.4	0.9	45	0.7	4.9	4.6	4.77	8.94	0.7	3.91	2.5	4.4	-0.18	1.54	1.72
9	3.6	9.3	2.58	32.4	6.3	116	1.9	12.7	14.1	12.95	3.33	1.13	11.56	9.1	13.0	-0.1	1.30	1.48
10	3.6	12.4	3.43	32.4	8.4	144	2.4	15.7	18.2	15.5	2.86	1.18	14.05	10.4	17.0	-0.08	1.26	1.44
11	3.6	16.3	4.51	32.4	11.0	179	3.0	19.5	22.9	18.28	2.47	1.27	16.68	12.4	21.8	-0.08	1.24	1.41
12	7.2	3.3	0.46	64.9	2.2	94	1.6	10.3	10.2	4.91	7.68	0.55	4.24	4.3	9.6	-0.13	1.39	1.71
13	7.2	6.2	0.86	64.9	4.2	121	2.0	13.2	14.0	6.57	4.72	0.99	5.36	11.5	12.7	-0.18	1.56	1.72
14	7.2	11.5	1.6	64.9	7.8	168	2.8	18.3	20.5	8.4	3.39	1.06	7.1	17.2	18.6	-0.15	1.45	1.68
15	7.2	15.4	2.13	64.9	10.4	203	3.4	22.1	25.6	9.58	2.85	1.16	8.14	21.9	22.8	-0.14	1.43	1.60

2. Contact angle measurements for FEP tube in the in-plane spiral-shaped milli-reactor

The contact angle of the prepared solution (GL/NaOH at 20 g L^{-1}) on the FEP tubing material was measured by a Drop shape analyzer-DSA100 (Krüss) at room temperature (293.15 K). A short FEP tube (3 cm length) was used and stretched to make it as straight as possible.

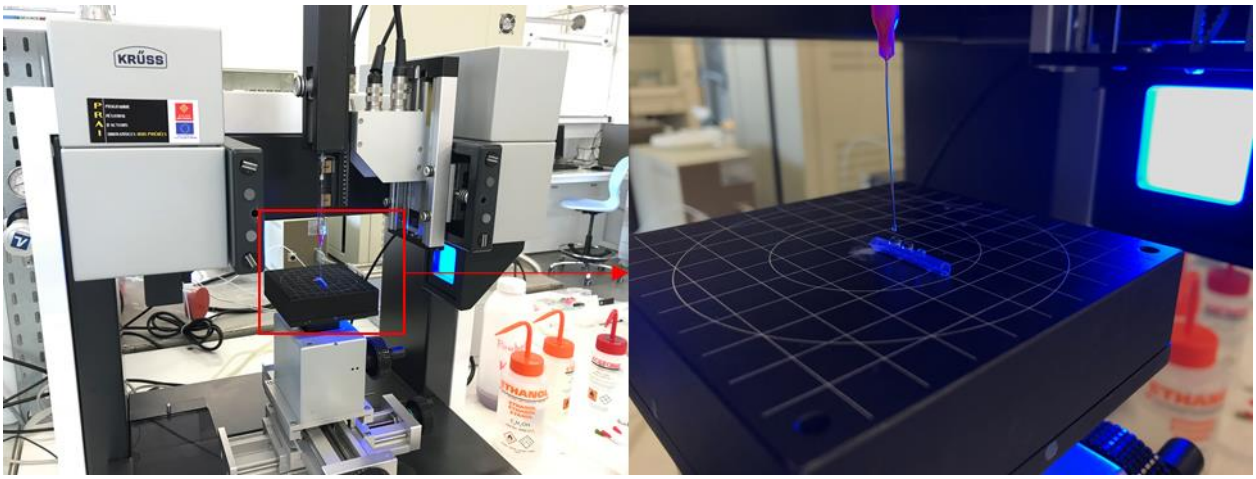

(a)

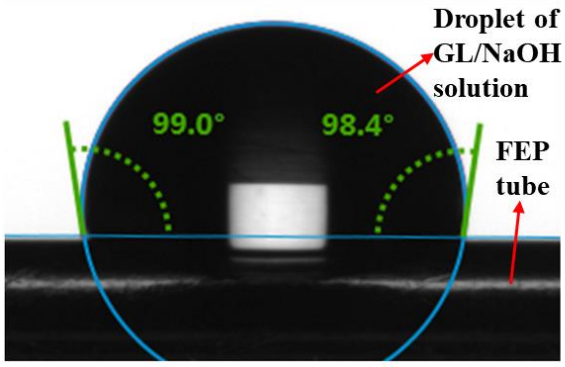

(b)

Fig. A 2-1 (a) Pictures of DSA100 instrument used for contact angle measurements on FEP tube; (b) the measured contact angle (98.7°) of GL/NaOH solution on FEP tube.

3. Calibration of the channel depth at the cross-junction of a straight milli-channel

As shown in Fig. 2-9, all the channels, including the injection inlets of gas and liquid, and the main channel, were designed to have the same square cross section ($w^2 \cong 2\times2$ mm^2). However, it was observed that these dimensions could slightly deviate from 2 mm due to the manufacturing precision and mounting deformation of the channel. As involved in all the calculations for hydrodynamics and mass transfer, it was absolutely required to define a method for determining their exact values.

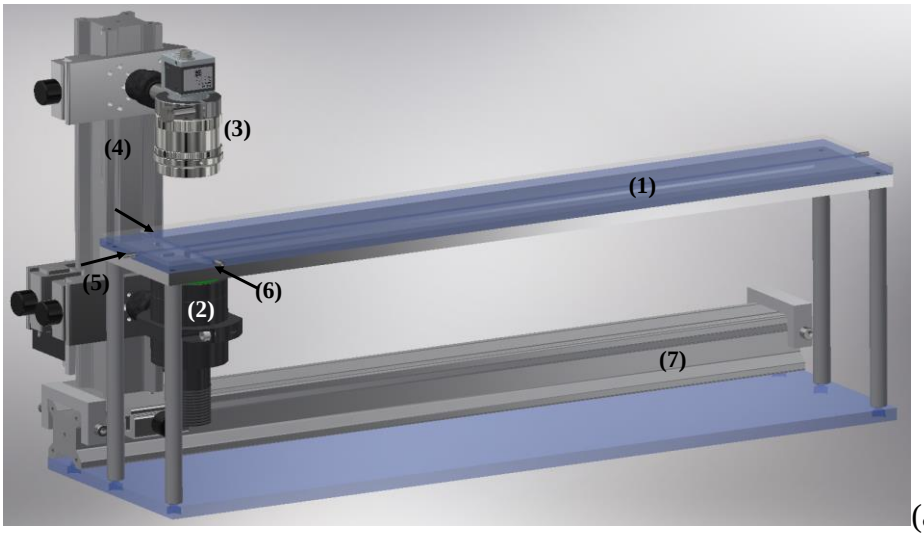

(a)

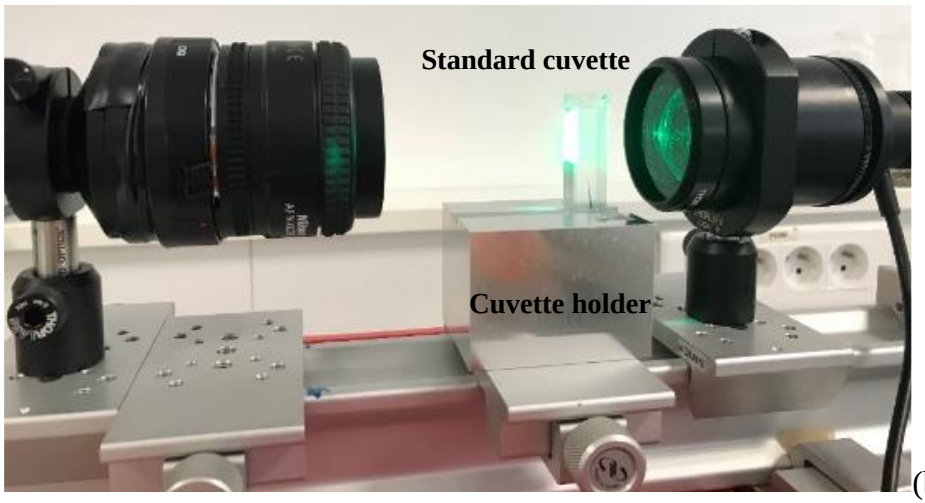

(b)

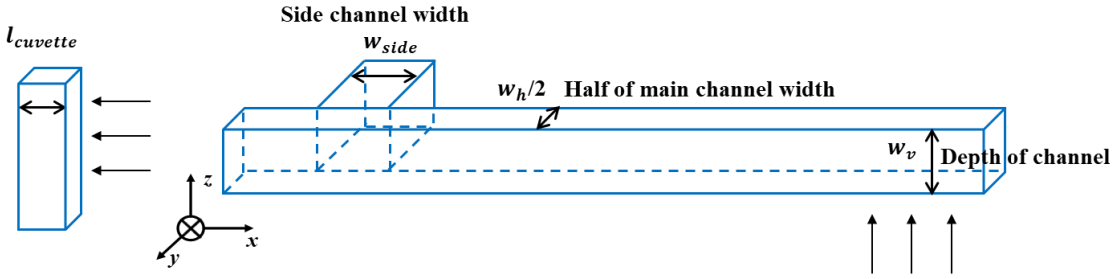

(c)

Fig. A 3-1 (a) Schematic representation of the initial experimental setup (system I): (1) the milli-channel (2) the backlight panel (3) high-speed camera (4) support of camera and backlight (5) gas inlet (6) liquid inlet (7) sliding support; (b) photography of the modified experimental setup (system II) involving the spectrophotometer cuvette; (c) schematic representation of dimensions in cuvette and channel, half of the straight channel with cross-junction is plotted for visualization convenience.

For that, the experimental setup previously presented was modified. As shown in Fig. A 3-1 (a), the camera and backlight with the supporting device (4) were removed together from sliding support (7) and put into horizontal direction. A cell holder with a standard spectrophotometric cuvette (1 cm of optical path length) was fixed in the place of the milli-channel. Fig. A 3-1 (b) shows the picture of this modified experimental setup. For convenience, the milli-channel system shown in Fig. A 3-1 (a) and the cuvette system shown in Fig. A 3-1 (b) were defined as system (I) and system (II).

The channel depth could be calibrated by means of a standard cuvette using the same optical system. According to the Beer-Lambert law applied for the monochromatic light, the absorbance of resorufin A_{RF} could be expressed as below,

$$A_{RF} = \varepsilon\, l\, c \qquad \text{(A 3-1)}$$

where l, was the optical path length, ε (L mol^{-1} cm^{-1}) the molar attenuation coefficient of RF, and c (mol^{-1} L) the molar concentration of the RF (which is the single absorbing species).

Thus, using the same dye and optical system, the optical path length in the milli-channel system (I) could be deduced from the optical path length in the cuvette system (II), according to the following equation:

$$\frac{\ell_{II}}{\ell_I} = \frac{A_{II}}{c_{II}} \times \frac{c_I}{A_I} = \frac{\Upsilon(\mathrm{II})}{\Upsilon(\mathrm{I})} \qquad \text{(A 3-2)}$$

where Υ was a coefficient linked to A and c, defined for each system, and c_I and c_{II} the molar concentrations of RF used in the systems I and II, respectively.

In Fig. A 3-1 (c), the light paths in the two systems were illustrated and as well as the channel widths. The light paths l_{I} and l_{II} for system I and II in Eq. (A 3-2) corresponded to the channel depth w_{v} and the cuvette optical path l_{cuvette}, respectively. Note that the side channel and main channel width w_{side} and w_{h} were calibrated by a micro-ruler (0.1mm), and found at 2.17 and 2.19 mm, respectively.

In addition to the RF dye, another dye, safranin (Sigma Aldrich, CAS 199303, molar mass: 350.84 g mol^{-1}) was used to verify value of the channel depth w_{v} obtained by RF dye, and thus to increase the accuracy of the method. Safranin was chosen because its absorption spectrum presented a peak at the wavelength near 530 nm, as shown in Fig. A 3-2. As a reminder, Fig. 2-5 shows the measured spectra for resorufin dye. From Fig. 2-5 and Fig. A 3-2, it could be observed that resorufin and safranin dyes give out similar absorbance ranges near 530 nm wavelength (the wavelength of the light designed optical system, see section 2.3.2).

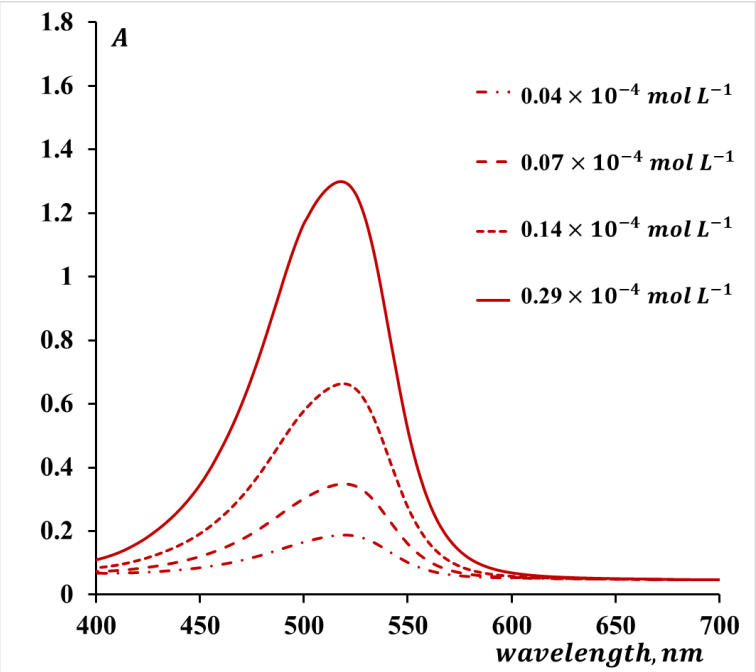

Fig. A 3-2 Absorbance spectra of aqueous solutions of safranin with different molar concentrations, measure with the spectrophotometer Jasco V630.

Table A 3-1 summarized the molar concentrations of safranin and resorufin dyes applied in the cuvette and milli-channel systems, respectively.

Table A 3-1 Calibration of the channel depth in the cross-junction device: concentrations of safranin and resorufin used in the experiments with the cuvette and the millimetric channel systems.

Dye	System	Concentrations×10^{-4} (mol L^{-1})			
Safranin	Cuvette (II)	0.04	0.07	0.14	0.29
Safranin	Milli-channel (I)	0.14	0.29	0.57	1.14
Resorufin	Cuvette (II)	0.10	0.20	0.41	/
Resorufin	Milli-channel (I)	0.41	0.81	1.62	3.25

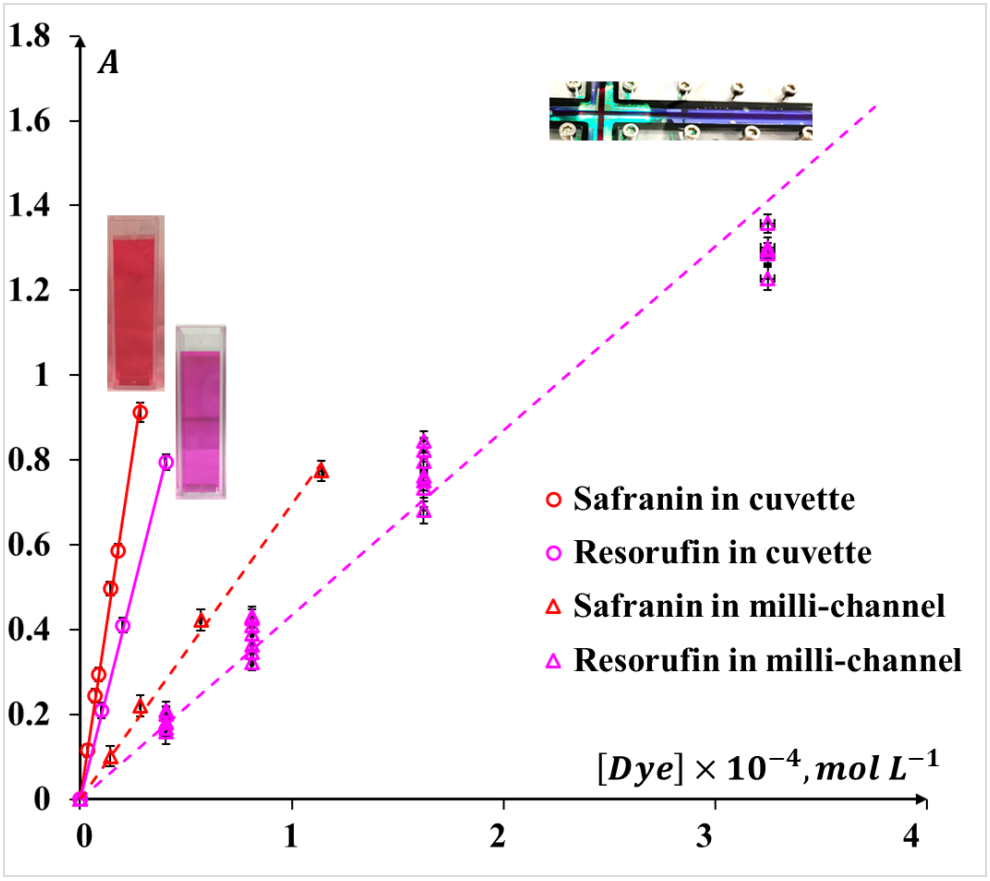

Fig. A 3-3 Calibration of the channel depth in the cross-junction device: relations between absorbance and concentrations of two dyes: resorufin and safranin in the cuvette or milli-channel systems.

Fig. A 3-3 shows the relations between the absorbances and the concentrations of two dyes, respectively, marked by red and pink colors.

- The red and pink circular symbols correspond to the cuvette system (II).
- The red triangular symbols correspond to the millimetric channel system (I) with the safranin dye and considering the first ROI position X_1.
- The pink triangular symbol corresponds to the millimetric channel system (I) with the resorufin dye and considering different ROI positions.

According to the Eq. (A 3-2) and from the relations illustrated in Fig. A 3-3, the channel depth w_v could be calculated as below:

$$w_v = l_{cuvette} \frac{\Upsilon(\mathrm{II})}{\Upsilon(\mathrm{I})} \qquad \text{(A 3-3)}$$

where $l_{cuvette}$ was the thickness of the standard cuvette and equals to 10 mm, ϒ(I) and ϒ(II) were the slopes of the straight lines relating absorbance values to the molar concentrations of the dye ($\Upsilon = \frac{A}{c} = \varepsilon \cdot l$) in the systems (I) and (II), respectively. These slopes were fitted using the least squares method and are listed in Table A 3-2.

Table A 3-2 Calibration of the channel depth in the cross-junction device: the fitted **ϒ** values deduced from **Fig. A 3-3** for safranin and resorufin, in the cuvette and milli-channel systems.

System	Cuvette (I)	Milli-channel (II)	Cuvette (I)	Milli-channel (II)
Dyes	Safranin	Safranin	Resorufin	Resorufin
ϒ (L mol^{-1})	32665	6962	19776	4219
	R^2=0.9972	R^2=0.9959	R^2=0.9993	R^2=0.9696

At last, the channel depths w_v were found at 2.1313 mm and 2.1334 mm by the safranin and resorufin dyes respectively, leading to an average value equaled to 2.13 mm (mean absolute deviation, MAD: 10^{-3}, defined in Appendix 5). This value is slightly higher than the designed 2 mm, which could be caused by the sealing ring added between the top and middle plates and the bottom and middle plates.

Up to now, the horizontal and vertical channel width were obtained and at 2.19 and 2.13mm, respectively. The hydraulic diameter of the channel, noted w_{hl}, is defined as below in Eq. (A 3-4).

$$w_{hl} = 2w_h w_v / (w_h + w_v) \quad \text{(A 3-4)}$$

The calculated hydraulic diameter w_{hl} was then equal to 2.16 mm (MAD: 0.03).

In addition, the molar attenuation coefficient ε could be further deduced through dividing the slope ϒ by l, and were found at 3.3×10^4 and 2.0×10^4 L mol^{-}

^{1} cm^{-1} for safranin and resorufin dyes, which had the same order of magnitude than the values reported in the literature (for safranin 3.4×10^{4} L mol^{-1} cm^{-1} (A Daher, 2012) and for resorufin 2.6×10^{4} L mol^{-1} cm^{-1} (Siu et al., 2014) at 530nm). The relatively big differences of ε for RF may be caused by the presence of glucose and NaOH in the RF solution, and/or of impurities.

4. General Matlab code

General reading code

```
%% clear and close all
close all;
clear;
clc;

%% study cases
file_path='E:\spiralmillreactorexperiments\spiral_sha
pedmillireactor\ET\QL0_85';%file  path  of  all  the
folders
cases(1).name='folder_1'; % folder name
cases(n).name='folder_n'; % folder name

%% Set STANDARD working directories
for jjj=1:length(cases)
    cases(jjj).workdir=fullfile(file_path,cases(jjj).
name); % For MS Windows systems
    cases(jjj).listimages=dir(strcat(cases(jjj).workd
ir,'\*.tif'));
    img_num(jjj)=length(cases(jjj).listimages);
end

%% Clear variables from memory
clearvars jjj
```

General code for extracting inner tube or channel

```
%% dark images
jjj=1; % Case number of background images containing
high concentrations of RF aqueous solution

%% liquid Background image creation
% Average from N background frames
    I1Org=imreadPGM12(fullfile(file_path,cases(jjj).n
ame,cases(jjj).listimages(1).name));
    I1_back=double(I10rg-65536);%create zero

%% average
```

```
    n=length(cases(jjj).listimages); % image numbers
for i=1:n
    I1Org=imreadPGM12(fullfile(file_path,cases(jjj).n
ame,cases(jjj).listimages(i).name));
    I1_back=I1_back+double(I1Org);
end
    I1_back=uint16(I1_back/n);
%%
    imshow(imadjust(I1_back));

%% colorless images
jjj=2; %Case number of background images containing
aqueous solution of GL and NaOH (without RF)
%% liquid Background image creation
% Average from N background frames
    I2Org=imreadPGM12(fullfile(file_path,cases(jjj).n
ame,cases(jjj).listimages(1).name));
    I2_back=double(I14Org-65536
%% average
for ii=1:length(cases(jjj).listimages)
    I2Org=imreadPGM12(fullfile(file_path,cases(jjj).n
ame,cases(jjj).listimages(ii).name));
    12_back=I2_back+double(I2Org);
end
    I2_back=uint16(I2_back/length(cases(jjj).listimag
es));
%%
    figure;
    imshow(imadjust(I2_back));

%% only contain the inner channel and using as mask
I_inner=imabsdiff(I2_back,I1_back);%absolute
difference of two pictures
    [m,n]=size(I_inner);
for i_m=1:m
for j_n=1:n
    if I_inner (i_m,j_n)<=100 % threshold
    I_inner (i_m,j_n)=65536;
    else
    I_inner (i_m,j_n)=0;
    end
end
end
%%
```

```
save('I_inner'); %inner tube or channel mask
```

In-plane spiral-shaped milli-reactor

Hydrodynamics Part

```
jjj=5;% case number
pixel_ruler=0.077; % actual dimention
X_0=1320; % spiral center
Y_0=1085; % spiral center
X_initial=1120; % staring position
Y_initial=2140; % staring position

%%
for t_b=1:100%length(cases(jjj).listimages)
    I1org=imread(fullfile(file_path,cases(jjj).name,c
ases(jjj).listimages(t_b).name));
% end
I1GL=imsubtract(I1org,I_inner);

%% bubble inner
level=multithresh(I1GL,4);
I1_bw=imquantize(I1GL,level);
I1_BW_RGB=label2rgb(I1_bw);
%% bubble inner is 5
    [m,n]=size(I1_bw);
    for i_m=1:m
        for j_n=1:n
            ifI1_bw(i_m,j_n)~=5 %
                I1_bw(i_m,j_n)=0;
            end
        end
    end
%% REMOVE SMALL AREA
I1_bw2=bwareaopen(I1_bw,100);
%imshow(I1_bw2);
%% CHECK PROPOTIES
[I1_bwlabel,n]=bwlabel(I1_bw2,4);
STAT_bubble1=regionprops(I1_bwlabel,'Area','Centroid'
,'Perimeter','EquivDiameter','MajorAxisLength','Minor
AxisLength','Image','Orientation','Extrema');
STATsize_bubble1=numel(STAT_bubble1);
%% calculate the radius
    Radius_B=zeros();
```

```
    theta=zeros();
for i=1:STATsize_bubble1
    x_center=round(STAT_bubble1(i).Centroid(1,1));
    y_center=round(STAT_bubble1(i).Centroid(1,2));
    Radius_B(i,1)=sqrt((X_0-x_center)^2+(Y_0-
y_center)^2)*pixel_ruler;
    STAT_bubble1(i).Radius= Radius_B(i,1);
end
%% check
Major_lenth=100;
radius_B2=85;
noise_num=0;
for i_b=1:STATsize_bubble1
ifSTAT_bubble1(i_b).MajorAxisLength<=Major_lenth||STA
T_bubble1(i_b).Radius>=radius_B2
noise_num=noise_num+1;
    [x_m,y_n]=find(I1_bwlabel(:,:)==i_b);
    xy_num=size(x_m);
    for xy_mn=1:xy_num(1,1)
        I1_bwlabel(x_m(xy_mn,1),y_n(xy_mn,1))=0;
    end
end
end
%% get bubble
sedisk = strel('disk', 6);
I1_bw1_mask = imdilate(I1_bwlabel, sedisk);
I1_bwlabelmask=~I1_bw1_mask;
I1_bwlabelmask=im2double(I1_bwlabelmask);
[m,n]=size(I1_bwlabelmask);
for i_m=1:m
for j_n=1:n
if   I1_bwlabelmask(i_m,j_n)~=0
I1_bwlabelmask(i_m,j_n)=65536;
end
end
end
I1_bwlabelmask=im2uint16(I1_bwlabelmask);
I1_bw2n=imsubtract(I1_lap,I1_bwlabelmask);
BWs=edge(I1_bw2n, 'canny');
sedisk = strel('disk', 6);
BWsdil = imdilate(BWs, sedisk);
BWdfill = imfill(BWsdil, 'holes');
seD = strel('disk',6);
BWfinal = imerode(BWdfill,seD);
```

```
I1_bubbleFV = bwareaopen(BWfinal,100);% bubble mask

%% properties
STAT_bubble=regionprops(I1_bubbleFV,'Area','Centroid'
,'Perimeter','EquivDiameter','MajorAxisLength','Minor
AxisLength','Image','Orientation','Extrema');
STATsize_bubble=numel(STAT_bubble);

%% the distance to centroid and rank them
Radius_initial=sqrt((X_initial-X_0)^2+(Y_initial-
Y_0)^2)*pixel_ruler;
theta_initial=(Radius_initial-5)*(pi/2);
Radius_B=zeros();
theta=zeros();
Axial=zeros();
for i=1:bubble_num
x_center=round(STAT_bubble2(i).Centroid(1,1));
y_center=round(STAT_bubble2(i).Centroid(1,2));
Radius_B(i,1)=sqrt((X_0-x_center)^2+(Y_0-
y_center)^2)*pixel_ruler;
STAT_bubble2(i).Radius= Radius_B(i,1);
fun=@(x)sqrt((5+2.*x./pi).^2+(2./pi).^2);
theta(i,1)=(Radius_B(i,1)-5)*(pi/2);
Axial(i,1)=integral(fun,theta(i,1),
theta_initial)/1000;
STAT_bubble2(i).Axial=Axial(i,1);
end
%% ranking according to radius
[~,ind]=sort([STAT_bubble2.Axial],'ascend');
ranking_bubble=STAT_bubble2(ind);
%% bubble length
for i=1:bubble_num
Radius_BF(i,ii)=ranking_bubble(i).Radius;
bubbleallrotate=imrotate(ranking_bubble(i).Image,270-
ranking_bubble(i).Orientation);
bubble_com=regionprops(bubbleallrotate,'Area','Centro
id','Perimeter','EquivDiameter','MajorAxisLength','Mi
norAxisLength','Image','Orientation','Extrema');
b_rotate_number=numel(bubble_com);
Majorlengh_BF(i,ii)=ranking_bubble(i).MajorAxisLength;
if b_rotate_number>=2
for L_n=1:b_rotate_number
area_L=bubble_com(L_n).Area;
if area_L>100
```

```
bubblerotatesingle=bubble_com(L_n).Image;
end
end
else
bubblerotatesingle=bubble_com.Image;
end
bubbleFS=regionprops(bubblerotatesingle,'Area','Centr
oid','Perimeter','EquivDiameter','MajorAxisLength','M
inorAxisLength','Image','Orientation','Extrema');
x_center=round(bubbleFS.Centroid(1,1));
y_center=round(bubbleFS.Centroid(1,2));
[m,n]=size(bubbleFS.Image);
LB_num=0;
for i_single=1:m
for j=1:n
if bubbleFS.Image(i_single,j)~=0 && j==x_center
LB_num=LB_num+1;
end
end
end
bubble_length(i,ii)=LB_num*pixel_ruler; % axial bubble
length
end
%%
for b_n_t=1:STATsize_bubble
x_t_b(b_n_t,t_b)=STAT_bubble(b_n_t).Centroid(1,1);y_t
_b(b_n_t,t_b)=STAT_bubble(b_n_t).Centroid(1,2);
end

[b,t]=size(x_t_b);
for i_t=1:(t-1)
for i_b=1:b
for j_b=1:b
d(j_b,i_t)=sqrt((x_t_b(j_b,i_t+1)-
x_t_b(i_b,i_t)).^2+(y_t_b(j_b,i_t+1)-
y_t_b(i_b,i_t)).^2);
d_min=min(d(:,i_t));
bubble_distance(i_b,i_t)=d_min;
end
end
end
%% bubble velocity average
bubble_distance2=bubble_distance.*pixel_ruler; %mm
b_distance=bubble_distance2./1000;
```

```
deta_t=0.02;%
velocity_bubble=b_distance./deta_t;
velocity_bubble(velocity_bubble==0)=[];
average_v_c=mean(velocity_bubble);
str_v=std(velocity_bubble);
%% bubble velocity axial
bubble_ranking_initial_x=x_t_b(:,1);
bubble_ranking_initial_y=y_t_b(:,1);
Nzero=nnz(bubble_ranking_initial_x);
bubble_x=[];
bubble_y=[];
%%
for bubble_i=1:Nzero
bubble_x(1,bubble_i)=bubble_ranking_initial_x(bubble_
i,1);
bubble_y(1,bubble_i)=bubble_ranking_initial_y(bubble_
i,1);
[b,t]=size(x_t_b);
for i_t=1:(t-1)
for j_b=1:b
d_single(j_b,i_t)=sqrt((x_t_b(j_b,i_t+1)-
bubble_x(i_t,bubble_i)).^2+(y_t_b(j_b,i_t+1)-
bubble_y(i_t,bubble_i)).^2);
end
Matrixtemporal=d_single(:,i_t);
d_min=min(Matrixtemporal(Matrixtemporal>0));
bubble_single_distance(i_t,bubble_i)=d_min;
for jjjjj=1:b
if d_single(jjjjj,i_t)==d_min
bubble_x(i_t+1,bubble_i)=x_t_b(jjjjj,i_t+1);
bubble_y(i_t+1,bubble_i)=y_t_b(jjjjj,i_t+1);
end
end
end
end
singlebubble_v=bubble_single_distance.*pixel_ruler./d
eta_t./1000;
singlebubble_v(singlebubble_v==0)=[];
%% the position of bubble
Radius_initial=sqrt((X_initial-X_0)^2+(Y_initial-
Y_0)^2)*pixel_ruler;
theta_initial=(Radius_initial-5)*(pi/2);
for i_t=1:t
for i=1:Nzero
```

```
x_center=bubble_x(i_t,i);
y_center=bubble_y(i_t,i);
Radius_B(i_t,i)=sqrt((X_0-x_center)^2+(Y_0-
y_center)^2)*pixel_ruler;
fun=@(x)sqrt((5+2.*x./pi).^2+(2./pi).^2);
theta(i_t,i)=(Radius_B(i_t,i)-5)*(pi/2);
Axial_single(i_t,i)=integral(fun,theta(i_t,i),
theta_initial)/1000;
end
end
```

Mass transfer Part

```
%%Calibration relation

%% Load average background images
load('I0_sub'); % background of colorless image
load('I1_sub'); % background of 0.021
load('I2_sub'); % background of 0.042
load('I3_sub'); % background of 0.076
load('I4_sub'); % background of 0.084
load('I5_sub'); % background of 0.105

FVlinearcoff=zeros(2160,2560);
[x_m,y_n]=find(I_inner(:,:)==0);
xy_num=size(x_m); %
loop_n=xy_num(1,1);
y=[0 1.75 3.50 5.24 6.99 8.73]*0.84;% oxygen
concentration
for loop_i=1:loop_n
    i=x_m(loop_i,1);
    j=y_n(loop_i,1);
    I0_ave=double(I0_sub(i,j));
    I1_ave=double(I1_sub(i,j));
    I2_ave=double(I2_sub(i,j));
    I3_ave=double(I3_sub(i,j));
    I4_ave=double(I4_sub(i,j));
    I5_ave=double(I5_sub(i,j));
    I0=(I0_ave-I0_ave)/65535;
    I1=-(I1_ave-I0_ave)/65535;
    I2=-(I2_ave-I0_ave)/65535;
    I3=-(I3_ave-I0_ave)/65535;
    I4=-(I4_ave-I0_ave)/65535;
    I5=-(I5_ave-I0_ave)/65535;
```

```
x_Grey=[I0 I1 I2 I3 I4 I5];

% Set up fittype and options. linear
    ft=fittype('a*x','independent','x','dependent','y
');
    opts=fitoptions('Method','NonlinearLeastSquares')
;
    opts.Display='Off';
    opts.Lower =[0];
    opts.StartPoint =[0.00002];
    [fitresult, gof] = fit(x_Grey, y, ft, opts );
    FVlinearcoff(i,j) = fitresult.a;
end

save('FVlinearcoff');% linear calibration matrix

% after getting liquid slug mask
I1_liquidslugFV=imsubtract(I1_liquidslug,I1_liquidmas
k);
oxygen_grayimage=double(I1_liquidslugFV);
I1_initialGV=imsubtract(I1_sub,I1_liquidmask); %
for loop_i=1:loop_n
i=x_m(loop_i,1);
j=y_n(loop_i,1);
    I0_ave(i,j)=double(I1_initialGV(i,j));
    greydeta(i,j)=(I0_ave(i,j)-
oxygen_grayimage(i,j))/65535;
    FVlinear=FVlinearcoff(i,j);
    C_oxy=FVlinear*greydeta(i,j));
oxygen_grayimage(i,j)= C_oxy;
end
%% plot
    imagesc(oxygen_grayimage);
    colormap('jet');
    axis image;
    olorbar;
    caxis([0,1]);
    pbaspect([1 1 1]); %set x and y axis same
    xlabel('pixel');
    ylabel('pixel');
    saveas(gcf,'concentration.jpg');
```

Straight milli-channel with a cross-junction

Mass transfer Part

```
% after getting liquid slug mask
I1_liquidslugFV=imsubtract(I1_liquidslug,I1_liquidmas
k);
oxygen_grayimage=double(I1_liquidslugFV);
I1_initialGV=imsubtract(I1_sub,I1_liquidmask);%
k=3.7 %coefficients for absorbance and concentration
for loop_i=1:loop_n
    i=x_m(loop_i,1);
    j=y_n(loop_i,1);
    I(loop_i,1)=double(I1_liquidslugFV(i,j));
    I0(loop_i,1)=double(I1_initialGV (i,j));
    A(loop_i,1)=-log10(I(loop_i,1)/I0(loop_i,1));
    oxygen_grayimage(i,j)=k*A(loop_i,1);
end
```

5. Error analysis

The standard deviation (STD) is calculating as below:

$$STD = \sqrt{\frac{\sum_{i=1}^{n}(\varsigma_i - \bar{\varsigma})^2}{n-1}} \quad \text{(A 5-1)}$$

where ς represents the sample data, $\bar{\varsigma}$ the mean of the sample data, and n the sample size number.

The standard deviation error (SD) is thus given below:

$$SD = \frac{STD}{\sqrt{n}} \quad \text{(A 5-2)}$$

The mean absolute deviation (MAD) is defined by:

$$MAD = \frac{\sum_{i=1}^{n}|\varsigma_i - \bar{\varsigma}|}{n\bar{\varsigma}} \quad \text{(A 5-3)}$$

The mean absolute percentage error (MAPE) is expressed by the formula:

$$MAPE = \frac{1}{n}\sum_{i=1}^{n}\left|\frac{\varsigma_i - \bar{\varsigma}}{\bar{\varsigma}}\right| \times 100\% \quad \text{(A 5-4)}$$

The mean absolute percentage error of regression (MAPER) is expressed by the formula:

$$MAPER = \frac{1}{n}\sum_{i=1}^{n}\left|\frac{\varsigma_{actual} - \varsigma_{pre}}{\varsigma_{actual}}\right| \times 100\% \quad \text{(A 5-5)}$$

where ς_{actual} and ς_{pre} represent the actual and predicted data, respectively, n is the sample size number.

6. Comparison of global and pixel-by-pixel calibration for the in-plane spiral-shaped milli-reactor

In Fig. A 6-1, the profiles of equivalent O_2 concentration along the Γ_Y line (see Fig. 4-1) are compared, depending whether a pixel-by-pixel method or a global method was used for calibration.

For the pixel-by-pixel calibration, the linear regressions of equivalent O_2 concentration and ΔG were implemented for each pixel inside the tube on the image, meaning that the ΔG was calculated for each pixel.

For the global calibration, the linear regression of equivalent O_2 concentration and ΔG was only applied once for all the pixels inside the tube on the image, so ΔG is an average value for all the pixels on the image.

The spiral turn numbers along the Γ_Y line were labeled as 1 to 11 from top to bottom as shown in Fig. 4-1. The slight variations in gray values observed at different tubing positions could be caused by the inhomogeneous light distribution and the complex tubing conditions.

One can see that the equivalent O_2 concentrations obtained by global calibration at a given RZ concentration were scattered (the maximum relative error was 15%) and varied for different spiral numbers. However, the ones using pixel-by-pixel calibration at a given RZ concentration remained uniform (the maximum relative error was 6%) whatever the tubing position. For each spiral turn, the error bar represents the standard deviation (STD, see Appendix 5) for all pixels along the Γ_Y direction belonging to this spiral tube turn. In addition, the obtained maximum equivalent O_2 concentration C_{max} (named “concentration 5” on Fig. A 6-1) was found close to 6.5 mg L^{-1}, instead of the expected 7.3 mg L^{-1} (calculated by Eq. (2-4)). This underestimated equilibrium saturated concentration was caused by the chosen linear regression, in which, for the largest ΔG, the fitted equivalent O_2 concentrations using the linear calibration method

were lower than the real equivalent O_2 concentrations (see Fig. 4-2 (a)).

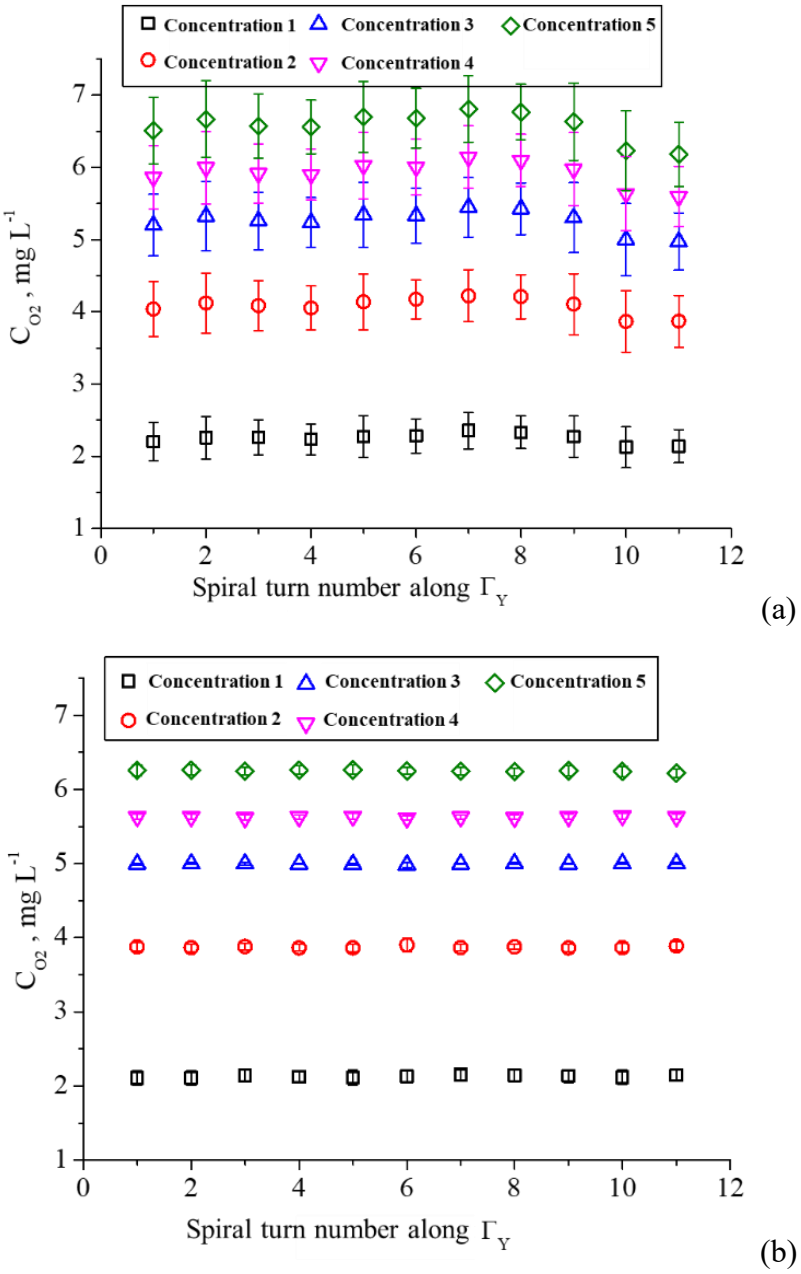

Fig. A 6-1 Profiles of equivalent O_2 concentration along the Γ_Y line at 5 groups of RZ concentrations (numbered from 1 to 5, corresponding to 1.47, 2.93, 4.40, 5.86 and 7.33 mg L^{-1} of O_2) obtained using (a) the global calibration method and (b) the pixel-by-pixel calibration method.

7. Saturated oxygen concentration in the in-plane spiral-shaped milli-reactor

Along the axial location *X*, the O_2 concentration at saturation, $C^*_{O_{2_L}}$(kg m^{-3}), will decrease due to the pressure drop and the decrease of O_2 mole fraction in the bubble. Therefore, the driving force ($C^*_{O_{2_L}} - \overline{C_{O_{2_L}}(X)}_{rl}$) controlling the mass flux inside one unit cell will also change.

The variation of $C^*_{O_{2_L}}(X)$ (kg.m^{-3}) can be described as below:

$$C^*_{O_{2_L}}(X) = H^{cp}_{O_2} * p_{O_2} * M_{O_2} \quad \text{(A 7-1)}$$

where $H^{cp}_{O_2}$ (mol m^{-3} Pa^{-1}), p_{O_2} (Pa) and M_{O_2} (kg mol^{-1}) were Henry's solubility constant, partial pressure of O_2 in the gas phase and O_2 molar mass, respectively.

The dependence of $H^{cp}_{O_2}$ on the temperature could be neglected because all the experiments were implemented under room temperature, $H^{cp}_{O_2}$ thus was equal to 1.21 mol m^{-3} Pa^{-1} (Sander, 2015). The partial pressure of O_2 was not only dependent on the bubble pressure, p_B, but also on the O_2 mole fraction, α_{O2}. One could write the mass flux density first from the Taylor bubble gas side (Eq. (A 7-2)) and from the liquid bulk side (Eq. (A 7-3)), as follows:

$$\varphi_{O_2}(X) = \frac{1}{S_B(X)} \frac{-\mathrm{d}m_{O_{2_G}}(X)}{\mathrm{d}t} = \frac{1}{S_B(X)} \frac{-\mathrm{d}(C_{O_{2_G}}(X) * V_B(X))}{\mathrm{d}t} \quad \text{(A 7-2)}$$

where $V_B(X)$ (m^3) and $S_B(X)$ (m^2) were the bubble volume and bubble interface area, respectively, and $m_{O_{2_G}}(X)$ (kg) and $C_{O_{2_G}}(X)$ (kg m^{-3}) were mass amount and mass concentration of O_2 in the gas phase.

$$\varphi_{O_2}(X) = \frac{V_S}{S_B(X)} \frac{\mathrm{d}\overline{C_{O_{2_L}}(X)}}{\mathrm{d}t} \quad \text{(A 7-3)}$$

where V_S (m^3) was the liquid slug volume.

By combining Eq. (A 7-2) and Eq. (A 7-3), the O_2 concentration in the gas phase could be represented as follows:

$$C_{O_{2_G}}(X) = \frac{1}{V_B(X)}\left(V_B^0 C_{O_{2_G}}^0 - V_S\overline{C_{O_{2_L}}(X)}\right) \quad \text{(A 7-4)}$$

where the first term on the right was the initial O_2 concentration in the bubble and the second term was the decreasing O_2 amount. The initial O_2 amount can be deduced from the initial bubble pressure, according to:

$$V_B^0 C_{O_{2_G}}^0 = n_{O2_G}^0 * M_{O2} = \frac{\alpha_{O2}^0 * p_B^0 * V_B^0 * M_{O_2}}{\mathrm{RT}} \quad \text{(A 7-5)}$$

where $\alpha_{O_2}^0$ was the initial O_2 mole fraction and equal to 0.21 and p_B^0 was the initial bubble pressure, which could be obtained by ideal gas law (see Appendix 1). For the decreasing O_2 amount, namely, $V_S\overline{C_{O_{2_L}}(X)}$, the maximum value was achieved when the equivalent O_2 concentration in liquid slug got saturated, which was equal to $V_S C_{O_{2_L}}^*$.

To conclude, the maximum ratio between the consumed mass amount of O_2 and the initial O_2 mole mass was calculated as follows:

$$\psi = \frac{V_S C_{O_{2_{L_{max}}}}^*}{V_B^0 C_{O2_G}^0} \quad \text{(A 7-6)}$$

where the maximum saturated O_2 concentration was assumed to be proportional to bubble pressure, hence $C_{O2_{L_{max}}}^* = \frac{P_B^0}{P_{atm}} C_{O2_{L_{atm}}}^*$, and the O_2 concentration at saturation (at the atmospheric pressure and 293.15K), $C_{O2_{L_{atm}}}^*$, was found at 8.15 mg/L (Dietrich et al., 2013a). By Eq. (A 7-6), the maximum ratio could be calculated for all the operating conditions, and were found smaller than 10%. These findings showed that, in this study, the decrease of O_2 molar fraction α_{O2} can be neglected, and thus the saturated O_2 concentration was only proportional

to the bubble pressure $p_B(X)$:

$$C^*_{O_{2_L}} = H^{cp}_{O_2} * \alpha^0_{O_2} * M_{O_2} * p_B(X) \quad \text{(A 7-7)}$$

Because the evolution of $p_B(X)$ was assumed to follow a linear decreasing relation, as follows:

$$p_B(X) = F_3 X + p_{B0} \quad \text{(A 7-8)}$$

where F_3 referred to the slopes of the straight lines related to bubble pressure with axial location X; p_{B0} the initial pressure, namely the ones immediately after the bubble forms.

Therefore, $C^*_{O_{2_L}}$ decreased linearly along the axial position.

8. Estimation of the liquid film thickness at the cross-junction of a straight milli-channel

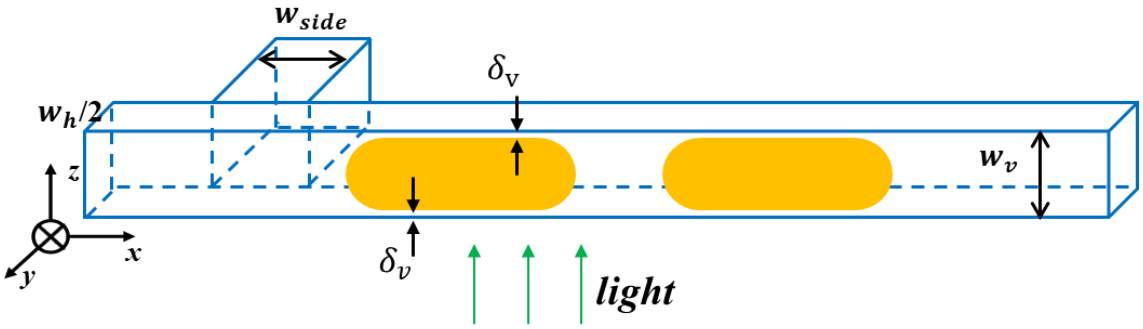

Fig. A 8-1 Schematic representation of the liquid film thickness in the top and bottom.

Based on the same principles than the one used for the estimation of the channel depth (see Appendix 3), the liquid film thickness around bubbles could be obtained considering two groups of fluid system in the milli-channel. Fig. A 8-1 shows the schematic representation of the vertical liquid film, noted δ_v (including top and bottom ones) around the body of a Taylor bubble flowing inside the milli-channel. Under the present capillary numbers (below 8.5×10^{-3}), the cross-sectional Taylor bubble presents more likely the squared shape with curved corners, as shown in Fig. 5-13 (b). As shown in Fig. A 8-1, the top and bottom liquid film thickness will contribute to the absorbance of the liquid phase which could be calculated by the gray level intensities appearing inside of the bubble. There are two groups of fluid pairs:

- One-phase flow (RZ solutions), the aqueous solutions of RZ dye with various concentrations were injected into the milli-channel at the cross-junction.
- Two-phase flow (air/RZ solutions), air and aqueous solutions of RZ dye with various concentrations were injected into the milli-channel at the cross-junction to generate Taylor flow.

The corresponding prepared RZ concentrations for these two fluid pairs were listed in Table A 8-1.

Table A 8-1 Bubble formation at the cross-junction in milli-channel: RZ concentrations used for estimating liquid film thickness.

Fluid pairs	Concentrations×10^{-4} (mol L^{-1})					ϒ ($L\ mol^{-1}$)
Air/RZ;	(a)	(b)	(c)	(d)	(e)	42
RZ	10.9	5.5	4.4	2.2	1.1	1887

For the two-phase Taylor flow, Fig. A 8-2 (a) to (e) shows the image sequences at one operating conditions with the RZ aqueous solutions at different concentrations. It can be observed that the bubble conserved almost identical shape and length whatever RZ concentrations. Fig. A 8-2 (g) shows the bubble inner zone (affected by top and bottom liquid films) extracted by Matlab from the image of Fig. A 8-2 (f) (air and deionized water). In addition, only the bubbles and liquid films between X=8mm and 10 mm were considered, since the liquid film was fully developed in this range and no dewetting phenomena was observed. Then, the averaged intensities for bubble inner zone (i.e., $\overline{\sum I}$) could be calculated, and then, according to Eq. (6-1), the absorbance of RZ, A, could be calculated and presented in Fig. A 8-3.

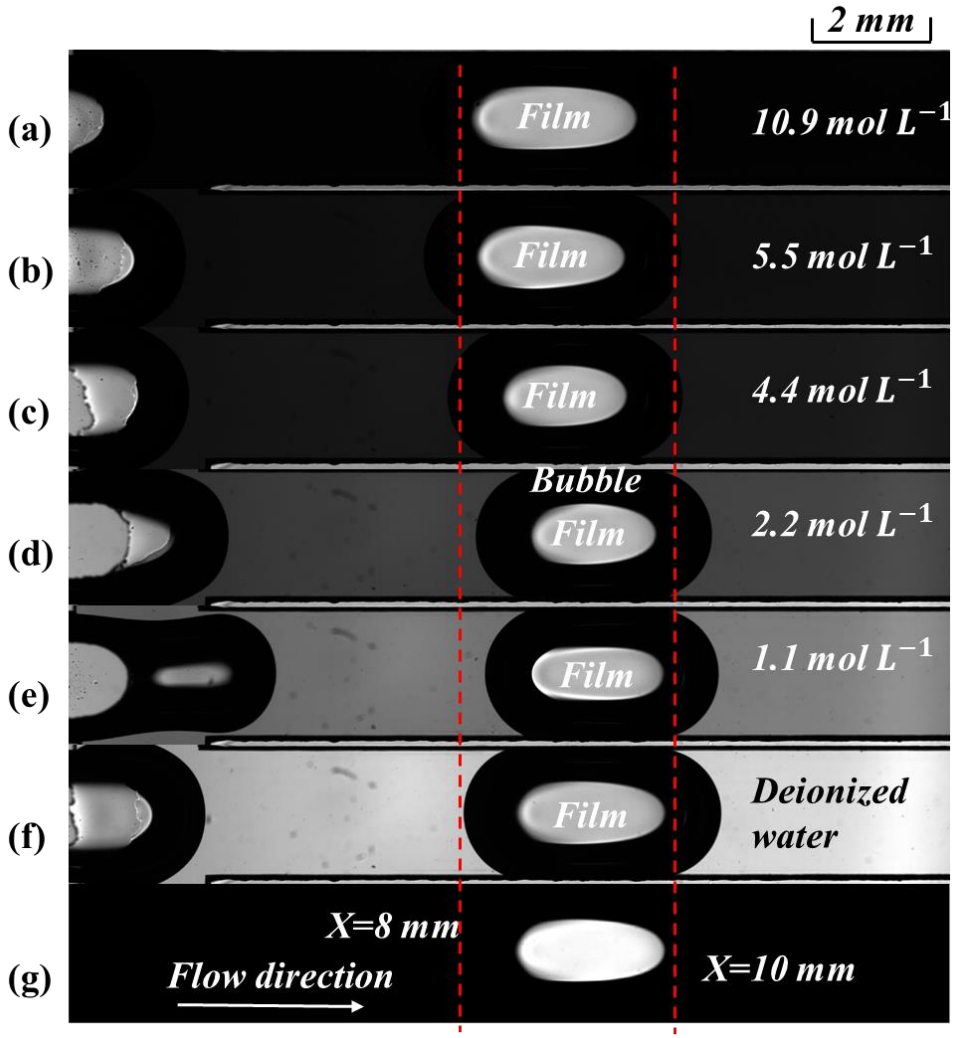

Fig. A 8-2 Bubble formation at the cross-junction in milli-channel: image sequences of developed liquid film for air and various concentrations of RZ dye, (a) to (e): [RZ] = 10.9, 5.5, 4.4, 2.2, 1.1 mol $L^{-1}$and deionized water; (g) extracted liquid film by Matlab for image (f). Operating condition: j_L = 10.7 and j_G = 3.6 cm s^{-1}, Ca = 2.3×10^{-3}, Re_{TP} = 277.

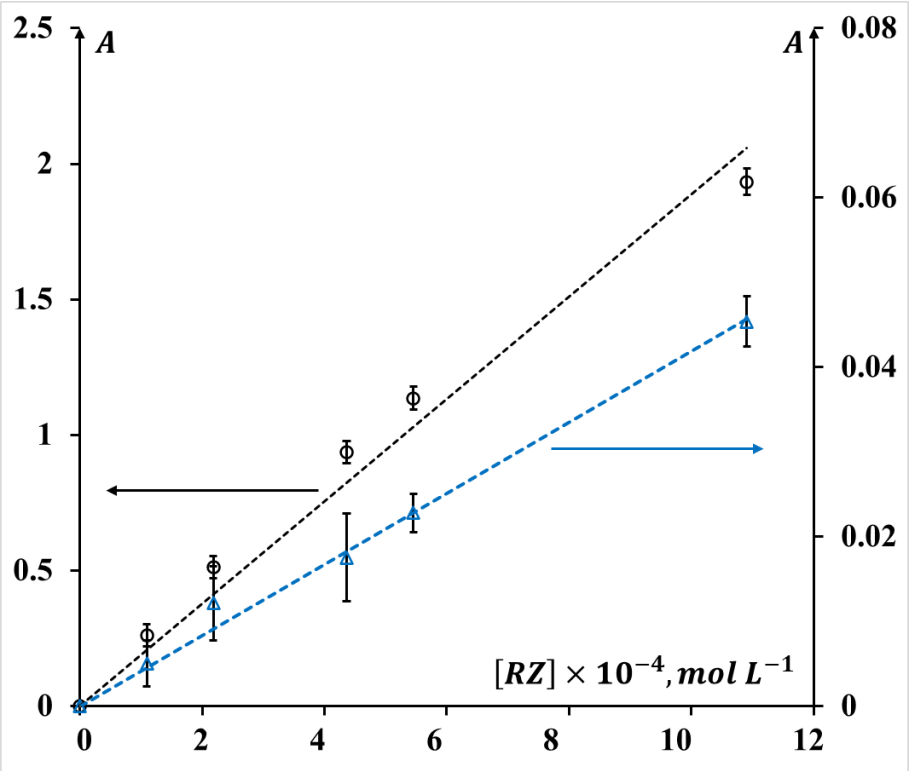

Fig. A 8-3 Bubble formation at the cross-junction in milli-channel: Estimation of the liquid film thickness considering the relations between the absorbance in the bubble inner zone and the concentrations of RZ dye, black and blue points represent RZ solution and air/RZ solution systems.

Combining Eqs. (A 3-2) and (A 3-3) based on Beer-Lambert law, the liquid film in the vertical direction (i.e., at the top and bottom of the bubble body) was calculated as below:

$$\delta_v = \frac{w_v}{2}\frac{\Upsilon_{Air/RZ}}{\Upsilon_{RZ}} \qquad \text{(A 8-1)}$$

where the $\Upsilon_{Air/RZ}$ and Υ_{RZ} were the slopes (fitted using the least squares method) relating the absorbance A and molar concentrations of RZ (shown in Fig. A 8-3) for air/RZ Taylor flows and one-phase flows (RZ solution without air), respectively. The values are reported in Table A 8-1 .

Therefore, in this case (when $Ca_{TP} = 2.3\times10^{-3}$, $Re_{TP} = 277$) the liquid film thickness, δ_v, was found at 1% of the channel depth w_v (i.e., 24 μm), which was slightly smaller than the adopted one (2%w) from Fries et al. (2008). Even if the

accuracy should be improved in the future, and validated for other operating conditions, this method provides new possibilities of fast and simple measurements on liquid film thickness without using complex optical system, like microtomography.

9. Bubble formation process at the cross-junction in a straight milli-channel

The bubble and liquid slug have complex and changing shapes during formation process. As a consequence, the usual parameters characterizing bubbles and liquid slug needed to be calculated differently.

The gas finger was assumed to be axisymmetric according to the *X* axis (i.e., the one related to the axial positions in the channel). The bubbles could be divided into *n* pieces of conical frustum, as shown in Fig. A 9-1. Therefore, the bubbles surface and volume were calculated as follows:

$$S_B = \sum_{i=1}^{n} \pi (r_i + r_{i+1}) \sqrt{(r_i - r_{i+1})^2 + h^2} \quad \text{(A 9-1)}$$

$$V_B = \sum_{i=1}^{n} \frac{\pi h}{3} ({r_i}^2 + {r_{i+1}}^2 + r_i r_{i+1}) \quad \text{(A 9-2)}$$

where h was the height of the conical frustum, r_i and r_{i+1} the radius of the conical frustum.

The liquid volume was calculated as follows

$$V_L = {w_{hl}}^2 \cdot L_{UC} - \sum_{i=1}^{n} \frac{\pi h}{3} ({r_i}^2 + {r_{i+1}}^2 + r_i r_{i+1}) \quad \text{(A 9-3)}$$

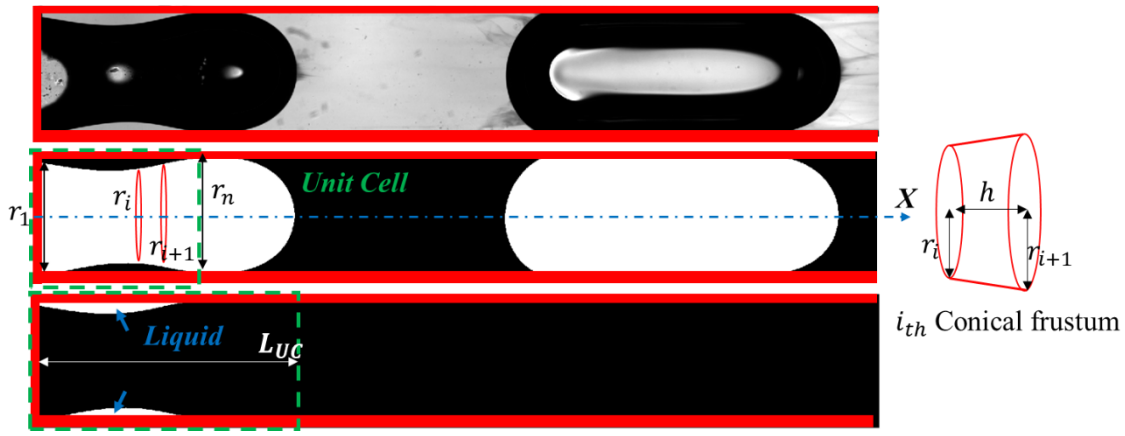

Fig. A 9-1 Schematic representation of the calculation of bubble and liquid slug volume and bubble surface area.

10. Bubble formation at the cross-junction in a straight milli-channel: experimental results of hydrodynamics and mass transfer characteristics

Table A 10-1 Experimental data on gas-liquid hydrodynamics and mass transfer in the straight milli-channel with a cross-junction

N.	j_L	j_G	η_0	Re_L,	Re_G,	Re_{TP}	Ca_{TP}, $\times10^{-3}$	U_B	L_B / w_h	L_S / w_h	a_B	f_c	$(k_L \cdot a)$overall
(-)	cm s^{-1}	cm s^{-1}	(-)	(-)	(-)	(-)	(-)	cm s^{-1}	(-)	(-)	m^{-1}	s^{-1}	s^{-1}
1	7.2	21.4	3	140	31	555	4.3	29.2	6.37	1.39	1138	23.9	0.44
2	11.4	17.2	1.5	221	25	555	4.3	29.2	3.69	1.54	973	21.6	0.43
3	14.3	14.3	1	278	21	555	4.3	29.2	2.79	1.69	856	19.7	0.38
4	17.9	10.7	0.6	347	16	555	4.3	29.2	2.07	1.99	698	16.7	0.32
5	21.4	7.2	0.3	415	11	555	4.3	29.2	1.6	2.59	519	12.8	0.23
6	14.3	21.4	1.5	278	31	693	5.3	36.4	3.69	1.54	973	27.0	0.56
7	17.9	17.9	1	347	26	693	5.3	36.4	2.79	1.69	856	24.6	0.5
8	21.4	14.3	0.7	415	21	693	5.3	36.4	2.19	1.92	731	21.7	0.43
9	28.6	7.2	0.3	555	11	693	5.3	36.4	1.45	3.04	438	13.7	0.2
10	17.9	25.0	1.4	347	37	832	6.4	43.7	3.51	1.56	954	31.9	0.71
11	21.4	21.4	1	415	31	832	6.4	43.7	2.79	1.69	856	29.5	0.61
12	28.6	14.3	0.5	555	21	832	6.4	43.7	1.9	2.14	641	23.3	0.43
13	35.7	7.2	0.2	693	11	832	6.4	43.7	1.36	3.49	380	14.3	0.2

References

A Daher, S., 2012. Determining values of some optical constants for some colorants. Journal of Education and Science 25, 79-86.

Abadie, T., 2013. Hydrodynamics of gas-liquid Taylor flow in microchannels. École Doctorale Mécanique, Énergétique, Génie civil et Procédés, Toulouse, INP.

Abadie, T., Aubin, J., Legendre, D., Xuereb, C., 2012. Hydrodynamics of gas-liquid Taylor flow in rectangular microchannels. Microfluidics and Nanofluidics 12, 355-369.

Abdelwahed, M.A.B., Wielhorski, Y., Bizet, L., Bréard, J., 2012. Characterisation of bubbles formed in a cylindrical T-shaped junction device. Chemical Engineering Science 76, 206-215.

Abiev, , R.S., Butler, C., Cid, E., Lalanne, B., Billet, A.M., 2019. Mass transfer characteristics and concentration field evolution for gas-liquid Taylor flow in milli channels. Chemical Engineering Science 207, 1331-1340.

Abiev, R., Svetlov, S., Haase, S., 2017. Hydrodynamics and Mass Transfer of Gas-Liquid and Liquid-Liquid Taylor Flow in Microchannels. Chemical Engineering & Technology 40, 1985-1998.

Abiev, R.S., 2011. Modeling of pressure losses for the slug flow of a gas-liquid mixture in mini- and microchannels. Theoretical Foundations of Chemical Engineering 45, 156-163.

Abiev, R.S., 2013. Bubbles velocity, Taylor circulation rate and mass transfer model for slug flow in milli-and microchannels. Chemical Engineering Journal 227, 66-79.

Abiev, R.S., 2020. Gas-Liquid and Gas-Liquid-Solid mass transfer model for Taylor flow in micro (milli) channels: a theoretical approach and experimental proof. Chemical Engineering Journal Advances, 100065.

Abolhasani, M., Singh, M., Kumacheva, E., Günther, A., 2012. Automated microfluidic platform for studies of carbon dioxide dissolution and solubility in physical solvents. Lab on a Chip 12, 1611-1618.

Aillet, T., Loubiere, K., Dechy-Cabaret, O., Prat, L., 2014. Accurate measurement of the photon flux received inside two continuous flow microphotoreactors by actinometry. International Journal of Chemical Reactor Engineering 12.

Aillet, T., Loubière, K., Dechy-Cabaret, O., Prat, L., 2016. Microreactors as a Tool for Acquiring Kinetic Data on Photochemical Reactions. Chemical Engineering and Technology 39, 115-122.

Al-Aufi, Y.A., Hewakandamby, B.N., Dimitrakis, G., Holmes, M., Hasan, A., Watson, N.J., 2019. Thin film thickness measurements in two phase annular flows using ultrasonic pulse echo techniques. Flow Measurement and Instrumentation 66, 67-78.

Anderson, L., Wittkopp, S.M., Painter, C.J., Liegel, J.J., Schreiner, R., Bell, J.A., Shakhashiri, B.Z., 2012. What is happening when the blue bottle bleaches: An investigation of the methylene blue-catalyzed air oxidation of glucose. Journal of Chemical Education 89, 1425-1431.

Atasi, O., Haut, B., Dehaeck, S., Dewandre, A., Legendre, D., Scheid, B., 2018. How to measure the thickness of a lubrication film in a pancake bubble with a single snapshot? Applied Physics Letters 113, 173701.

Aussillous, P., Quéré, D., 2000. Quick deposition of a fluid on the wall of a tube. Physics of Fluids 12, 2367-2371.

Badreddine, H., Sato, Y., Niceno, B., Prasser, H.-M., 2015. Finite size Lagrangian particle tracking approach to simulate dispersed bubbly flows. Chemical Engineering Science 122, 321-335.

Barajas, A., Panton, R., 1993. The effects of contact angle on two-phase flow in capillary tubes. International Journal of Multiphase Flow 19, 337-346.

Benizri, D., Dietrich, N., Labeyrie, P., Hébrard, G., 2019. A compact, economic scrubber to improve farm biogas upgrading systems. Separation and Purification Technology 219, 169-179.

Bercic, G., Pintar, A., 1997. The role of gas bubbles and liquid slug lengths on mass transport in the Taylor flow through capillaries. Chemical Engineering Science 52, 3709-3719.

Boden, S., Rolo, T.D.S., Baumbach, T., Hampel, U., 2014. Synchrotron radiation microtomography of Taylor bubbles in capillary two-phase flow. Experiments in Fluids 55, 1-14.

Bretherton, F., 1961. The motion of long bubbles in tubes. Journal of Fluid Mechanics 10, 166-188.

Burns, J.R., Ramshaw, C., 2001. The intensification of rapid reactions in multiphase systems using slug flow in capillaries. Lab on a Chip 1, 10.

Butler, C., Cid, E., Billet, A.-M., 2016. Modelling of mass transfer in Taylor flow: Investigation with the PLIF-I technique. Chemical Engineering Research and Design 115, 292-302.

Butler, C., Lalanne, B., Sandmann, K., Cid, E., Billet, A.M., 2018. Mass transfer in Taylor flow: transfer rate modelling from measurements at the slug and film scale. International Journal of Multiphase Flow 105, 185-201.

Castro-Hernández, E., Van Hoeve, W., Lohse, D., Gordillo, J.M., 2011. Microbubble generation in a co-flow device operated in a new regime. Lab on a Chip - Miniaturisation for Chemistry and Biology 11, 2023-2029.

Chen, H., Meng, Q., Li, J., 2015. Thin lubrication film around moving bubbles measured in square microchannels. Applied Physics Letters 107, 141608.

Chisholm, D., 1967. A theoretical basis for the Lockhart-Martinelli correlation for two-phase flow. International Journal of Heat and Mass Transfer 10, 1767-1778.

Choi, C., Yu, D.I., Kim, M., 2011. Surface wettability effect on flow pattern and pressure drop in adiabatic two-phase flows in rectangular microchannels with T-junction mixer. Experimental Thermal and Fluid Science 35, 1086-1096.

Cook, A.G., Tolliver, R.M., Williams, J.E., 1994. The blue bottle experiment revisited: how blue? how sweet? Journal of Chemical Education 71, 160.

Cubaud, T., Ulmanella, U., Ho, C.-M., 2006. Two-phase flow in microchannels with surface modifications. Fluid Dynamics Research 38, 772.

Dang, M., Yue, J., Chen, G., Yuan, Q., 2013. Formation characteristics of Taylor bubbles in a microchannel with a converging shape mixing junction. Chemical Engineering Journal 223, 99-109.

Dani, A., Guiraud, P., Cockx, A., 2007. Local measurement of oxygen transfer around a single bubble by planar laser-induced fluorescence. Chemical Engineering Science 62, 7245-7252.

De Menech, M., Garstecki, P., Jousse, F., Stone, H.A., 2008. Transition from squeezing to dripping in a microfluidic T-shaped junction. Journal of Fluid Mechanics 595, 141-161.

Deleau, T., Fechter, M.H.H., Letourneau, J.J., Camy, S., Aubin, J., Braeuer, A.S., Espitalier, F., 2020. Determination of mass transfer coefficients in high-pressure two-phase flows in capillaries using Raman spectroscopy. Chemical Engineering Science 228, 115960.

Dessimoz, A.L., Cavin, L., Renken, A., Kiwi-Minsker, L., 2008. Liquid–liquid two-phase flow patterns and mass transfer characteristics in rectangular glass microreactors. Chemical Engineering Science 63, 4035-4044.

Dietrich, N., Hebrard, G., 2018. Visualisation of gas-liquid mass transfer around a rising bubble in a quiescent liquid using an oxygen sensitive dye. heat and mass transfer, 1-9.

Dietrich, N., Loubière, K., Jimenez, M., Hébrard, G., Gourdon, C., 2013a. A new direct technique for visualizing and measuring gas–liquid mass transfer around bubbles moving in a straight millimetric square channel. Chemical Engineering Science 100, 172-182.

Dietrich, N., Mayoufi, N., Poncin, S., Midoux, N., Li, H.Z., 2013b. Bubble formation at an orifice: A multiscale investigation. Chemical Engineering Science 92, 118-125.

Dietrich, N., Poncin, S., Midoux, N., Li, H.Z., 2008. Bubble formation dynamics in various flow-focusing microdevices. Langmuir 24, 13904-13911.

Dietrich, N., Wongwailikhit, K., Mei, M., Xu, F., Felis, F., Kherbeche, A., Hébrard, G., Loubière, K., 2019. Using the "Red Bottle" Experiment for the Visualization and the Fast Characterization of Gas–Liquid Mass Transfer. Journal of Chemical Education 96, 979-984.

Dollet, B., Van Hoeve, W., Raven, J.-P., Marmottant, P., Versluis, M., 2008. Role of the channel geometry on the bubble pinch-off in flow-focusing devices. Physical Review Letters 100, 034504.

Doneux, T., Bouffier, L., Goudeau, B., Arbault, S.p., 2016. Coupling electrochemistry with fluorescence confocal microscopy to investigate electrochemical reactivity: a case study with the resazurin-resorufin fluorogenic couple. Analytical Chemistry 88, 6292-6300.

Duxenneuner, M.R., Fischer, P., Windhab, E.J., Cooper-White, J.J., 2014. Simultaneous visualization of the flow inside and around droplets generated in microchannels. Microfluidics and Nanofluidics 16, 743-755.

Eain, M.M.G., Egan, V., Howard, J., Walsh, P., Walsh, E., Punch, J., 2015. Review and extension of pressure drop models applied to Taylor flow regimes. International Journal of Multiphase Flow 68, 1-9.

Eskin, D., Mostowfi, F., 2012. A model of a bubble train flow accompanied with mass transfer through a long microchannel. International Journal of Heat and Fluid Flow 33, 147-155.

Felis, F., Dietrich, N., Billet, A.-M., Herres-Pawlis, S., Strassl, F., Roig, V., Loubière, K., 2018. Experiments on reactive mass transfer around an oxygen bubble rising freely in a conned cell using a colorimetric method. 19th International Symposium on Applications of Laser and Imaging Techniques to Fluid Mechanics 16-19 July 2018, Lisbon, Portugal. Proceeding.

Felis, F., Strassl, F., Laurini, L., Dietrich, N., Billet, A.-M., Roig, V., Herres-Pawlis, S., Loubière, K., 2019. Using a bio-inspired copper complex to investigate reactive mass transfer around an oxygen bubble rising freely in a thin-gap cell. Chemical Engineering Science.

Fellouah, H., Castelain, C., Ould El Moctar, A., Peerhossaini, H., 2006. A criterion for detection of the onset of Dean instability in Newtonian fluids. European Journal of Mechanics - B/Fluids 25, 505-531.

Fries, D.M., Rohr, P.R.V., 2009. Impact of inlet design on mass transfer in gas–liquid rectangular microchannels. Microfluidics and Nanofluidics 6, 27-35.

Fries, D.M., Trachsel, F., von Rohr, P.R., 2008. Segmented gas–liquid flow characterization in rectangular microchannels. International Journal of Multiphase Flow 34, 1108-1118.

Fries, D.M., von Rohr, P.R., 2009. Liquid mixing in gas–liquid two-phase flow by meandering microchannels. Chemical Engineering Science 64, 1326-1335.

Fu, T., Funfschilling, D., Ma, Y., Li, H.Z., 2010a. Scaling the formation of slug bubbles in microfluidic flow-focusing devices. Microfluidics and Nanofluidics 8, 467-475.

Fu, T., Ma, Y., 2015. Bubble formation and breakup dynamics in microfluidic devices: A review. Chemical Engineering Science 135, 343-372.

Fu, T., Ma, Y., Funfschilling, D., Li, H.Z., 2009. Bubble formation and breakup mechanism in a microfluidic flow-focusing device. Chemical Engineering Science 64, 2392-2400.

Fu, T., Ma, Y., Funfschilling, D., Li, H.Z., 2011a. Bubble formation in non-Newtonian fluids in a microfluidic T-junction. Chemical Engineering and Processing 50, 438-442.

Fu, T., Ma, Y., Funfschilling, D., Li, H.Z., 2011b. Dynamics of bubble breakup in a microfluidic T-junction divergence. Chemical Engineering Science 66, 4184-4195.

Fu, T., Ma, Y., Funfschilling, D., Li, H.Z., 2011c. Gas-liquid flow stability and bubble formation in non-Newtonian fluids in microfluidic flow-focusing devices. Microfluidics and Nanofluidics 10, 1135-1140.

Fu, T., Ma, Y., Funfschilling, D., Zhu, C., Li, H.Z., 2010b. Squeezing-to-dripping transition for bubble formation in a microfluidic T-junction. Chemical Engineering Science 65, 3739-3748.

Fu, T., Ma, Y., Funfschilling, D., Zhu, C., Li, H.Z., 2012. Breakup dynamics of slender bubbles in non-newtonian fluids in microfluidic flow-focusing devices. AIChE Journal 58, 3560-3567.

Gao, Y., Pinho, B., Torrente-Murciano, L., 2020. Recent progress on the manufacturing of nanoparticles in multi-phase and single-phase flow reactors. Current Opinion in Chemical Engineering 29, 26-33.

Garcia-Ochoa, F., Gomez, E., Santos, V.E., Merchuk, J.C., 2010. Oxygen uptake rate in microbial processes: An overview. Biochemical Engineering Journal 49, 289-307.

Garstecki, P., Fuerstman, M.J., Stone, H.A., Whitesides, G.M., 2006. Formation of droplets and bubbles in a microfluidic T-junction - scaling and mechanism of break-up. Lab on a Chip 6, 437-446.

Garstecki, P., Stone, H.A., Whitesides, G.M., 2005. Mechanism for flow-rate controlled breakup in confined geometries: A route to monodisperse emulsions. Physical Review Letters 94, 164501.

Gemoets, H.P., Su, Y., Shang, M., Hessel, V., Luque, R., Noel, T., 2016. Liquid phase oxidation chemistry in continuous-flow microreactors. Chemical Society Reviews 45, 83-117.

Geng, Y., Ling, S., Huang, J., Xu, J., 2020. Multiphase Microfluidics: Fundamentals, Fabrication, and Functions. Small 16, e1906357.

Ghobadi, M., Muzychka, Y.S., 2013. Effect of entrance region and curvature on heat transfer in mini scale curved tubing at constant wall temperature. International Journal of Heat and Mass Transfer 65, 357-365.

Giavedoni, M.D., Saita, F.A., 1999. The rear meniscus of a long bubble steadily displacing a Newtonian liquid in a capillary tube. Physics of Fluids 11, 786-794.

Gourdon, C., Elgue, S., Prat, L., 2015. What are the needs for Process Intensification? Oil & Gas Science and Technology–Revue d'IFP Energies nouvelles 70, 463-473.

Guo, Lin, Liu, W., Tang, X., Wang, H., Liu, Q., Zhu, Y., 2017. Reaction kinetics of non-catalyzed jet aeration oxidation of magnesium sulfite. Chemical Engineering Journal 330, 870-879.

Haase, S., Bauer, T., 2011. New method for simultaneous measurement of hydrodynamics and reaction rates in a mini-channel with Taylor flow. Chemical Engineering Journal 176-177, 65-74.

Haase, S., Bauer, T., Graf, E., 2020a. Gas–Liquid Flow Regime Prediction in Minichannels: A Dimensionless, Universally Applicable Approach. Industrial & Engineering Chemistry Research 59, 3820–3838.

Haase, S., Bauer, T., Hilpmann, G., Lange, M., Ayubi, M.M., Abiev, R., 2020b. Simultaneous Detection of Hydrodynamics, Mass Transfer and Reaction Rates in a Three-Phase Microreactor. Theoretical Foundations of Chemical Engineering 54, 48-63.

Haase, S., Murzin, D.Y., Salmi, T., 2016. Review on hydrodynamics and mass transfer in minichannel wall reactors with gas–liquid Taylor flow. Chemical Engineering Research and Design 113, 304-329.

Han, Y., Shikazono, N., 2009. Measurement of the liquid film thickness in micro tube slug flow. International Journal of Heat and Fluid Flow 30, 842-853.

Hazel, A.L., Heil, M., 2002. The steady propagation of a semi-infinite bubble into a tube of elliptical or rectangular cross-section. Journal of Fluid Mechanics 470, 91-114.

Heil, M., 2001. Finite Reynolds number effects in the Bretherton problem. Physics of Fluids 13, 2517-2521.

Henry Lane, J., 1924. Estimation of sugar in urine by means of Fehling's solution with methylene blue as internal indicator. Analyst 49, 366-371.

Herres-Pawlis, S., Flörke, U., Henkel, G., 2005. Tuning of Copper(I)–Dioxygen Reactivity by Bis(guanidine) Ligands. European Journal of Inorganic Chemistry 2005, 3815-3824.

Hipolito, A., Rolland, M., Boyer, C., De Bellefon, C., 2010. Single pellet string reactor for intensification of catalyst testing in gas/liquid/solid configuration. Oil & Gas Science and Technology–Revue d'IFP Energies nouvelles 65, 689-701.

Hoppe, C., 2019. Determination of the reaction constant of resorufin for the examination of oxygen gas-liquid mass transfer, Master-Thesis, Otto-von-Guericke-Universität Magdeburg, , Master-Thesis, Otto-von-Guericke-Universität Magdeburg.

Hosoda, S., Abe, S., Hosokawa, S., Tomiyama, A., 2014. Mass transfer from a bubble in a vertical pipe. International Journal of Heat and Mass Transfer 69, 215-222.

Howard, J.A., Walsh, P.A., 2013. Review and extensions to film thickness and relative bubble drift velocity prediction methods in laminar Taylor or slug flows. International Journal of Multiphase Flow 55, 32-42.

Huang, H., Dhir, V.K., Pan, L.-m., 2017. Liquid film thickness measurement underneath a gas slug with miniaturized sensor matrix in a microchannel. Microfluidics and Nanofluidics 21, 159.

Ide, H., Kimura, R., Inoue, K., Kawaji, M., 2008. Effect of wetting on adiabatic gas-liquid two-phase flow in a microchannel, ASME 2008 6th International Conference on Nanochannels, Microchannels, and Minichannels. American Society of Mechanical Engineers, pp. 337-342.

Irandoust, S., Andersson, B., 1989. Liquid film in Taylor flow through a capillary. Ind.eng.chem.res, 1684-1688.

Jensen, K.F., 2001. Microreaction engineering—is small better? Chemical Engineering Science 56, 293-303.

Jimenez, M., Miller, B., Bridle, H.L., 2017. Efficient separation of small microparticles at high flowrates using spiral channels: Application to waterborne pathogens. Chemical Engineering Science 157, 247-254.

Kashid, M.N., 2007. Experimental and modelling studies on liquid-liquid slug flow capillary microreactors, Department of Biochemical and Chemical Engineering. University of Dortmund.

Kastens, S., Hosoda, S., Schlueter, M., Tomiyama, A., 2015. Mass Transfer from Single Taylor Bubbles in Minichannels. Chemical Engineering & Technology 38, 1925-1932.

Kastens, S., Meyer, C., Hoffmann, M., Schlüter, M., 2017a. Experimental Investigation and Modelling of Local Mass Transfer Rates in Pure and Contaminated Taylor Flows.

Kastens, S., Timmermann, J., Strassl, F., Rampmaier, R.F., Hoffmann, A., Herres-Pawlis, S., Schlüter, M., 2017b. Test System for the Investigation of Reactive Taylor Bubbles. Chemical Engineering & Technology 40, 8.

Kawahara, A., Sadatomi, M., Matsuo, H., Shimokawa, S., 2011. Investigation of Characteristics of Gas-Liquid Two-Phase Flows in a Rectangular Microchannel with Return Bends, ASME-JSME-KSME 2011 Joint Fluids Engineering Conference. American Society of Mechanical Engineers, pp. 2461-2471.

Kherbeche, A., Mei, M., Thoraval, M.-J., Hébrard, G., Dietrich, N., 2019. Hydrodynamics and gas-liquid mass transfer around a confined sliding bubble. Chemical Engineering Journal 386, 121461.

Kherbeche, A., Milnes, J., Jimenez, M., Dietrich, N., Hébrard, G., Lekhlif, B., 2013. Multi-scale analysis of the influence of physicochemical parameters on the hydrodynamic and gas-liquid mass transfer in gas/liquid/solid reactors. Chemical Engineering Science 100, 515-528.

Khodaparast, S., Atasi, O., Deblais, A., Scheid, B., Stone, H., 2017. Dewetting of thin liquid films surrounding air bubbles in microchannels. Langmuir 34, 1363-1370.

Kolb, W.B., Cerro, R.L., 1991. Coating the inside of a capillary of square cross section. Chemical Engineering Science 46, 2181-2195.

Korczyk, P.M., van Steijn, V., Blonski, S., Zaremba, D., Beattie, D.A., Garstecki, P., 2019. Accounting for corner flow unifies the understanding of droplet formation in microfluidic channels. Nature Communications 10, 2528.

Kováts, P., Martins, F.J., Mansour, M., Thévenin, D., Zähringer, K., 2020. Tomographic PIV measurements and RANS simulations of secondary flows inside a horizontally positioned helically coiled tube. Experiments in Fluids 61, 1-15.

Kováts, P., Pohl, D., Thévenin, D., Zähringer, K., 2018. Optical determination of oxygen mass transfer in a helically-coiled pipe compared to a straight horizontal tube. Chemical Engineering Science 190, 273-285.

Kreutzer, M.T., Kapteijn, F., Moulijn, J.A., Heiszwolf, J.J., 2005a. Multiphase monolith reactors: chemical reaction engineering of segmented flow in microchannels. Chemical Engineering Science 60, 5895-5916.

Kreutzer, M.T., Kapteijn, F., Moulijn, J.A., Kleijn, C.R., Heiszwolf, J.J., 2005b. Inertial and interfacial effects on pressure drop of Taylor flow in capillaries. AIChE Journal 51, 2428-2440.

Kreutzer, M.T., Shah, M.S., Parthiban, P., Khan, S.A., 2018. Evolution of nonconformal Landau-Levich-Bretherton films of partially wetting liquids. Physical Review Fluids 3, 014203.

Krieger, W., Bayraktar, E., Mierka, O., Kaiser, L., Dinter, R., Hennekes, J., Turek, S., Kockmann, N., 2020. Arduino-based slider setup for gas-liquid mass transfer investigations: Experiments and CFD simulations. AIChE Journal 66, e16953.

Krieger, W., Hörbelt, M., Schuster, S., Hennekes, J., Kockmann, N., 2019. Kinetic study of leuco-indigo carmine oxidation and investigation of Taylor and Dean flow superposition in a coiled flow inverter. Chemical Engineering & Technology 42, 2052-2060.

Krieger, W., Lamsfuß, J., Zhang, W., Kockmann, N., 2017. Local Mass Transfer Phenomena and Chemical Selectivity of Gas-Liquid Reactions in Capillaries. Chemical Engineering & Technology 40, 2134-2143.

Kuhn, S., Jensen, K.F., 2012. A pH-sensitive laser-induced fluorescence technique to monitor mass transfer in multiphase flows in microfluidic devices. Industrial & Engineering Chemistry Research 51, 8999-9006.

Kumar, V., Vashisth, S., Hoarau, Y., Nigam, K., 2007. Slug flow in curved microreactors: hydrodynamic study. Chemical Engineering Science 62, 7494-7504.

Kurt, S.K., Warnebold, F., Nigam, K.D.P., Kockmann, N., 2017. Gas-liquid reaction and mass transfer in microstructured coiled flow inverter. Chemical Engineering Science 169, 164-178.

Laborie, S., Cabassud, C., Durand-Bourlier, L., Laine, J., 1999. Characterisation of gas–liquid two-phase flow inside capillaries. Chemical Engineering Science 54, 5723-5735.

Lee, C.Y., Lee, S.Y., 2008. Pressure drop of two-phase plug flow in round mini-channels: influence of surface wettability. Experimental Thermal and Fluid Science 32, 1716-1722.

Lee, C.Y., Lee, S.Y., 2010. Pressure drop of two-phase dry-plug flow in round mini-channels: Effect of moving contact line. Experimental Thermal and Fluid Science 34, 1-9.

Lefortier, S.G., Hamersma, P.J., Bardow, A., Kreutzer, M.T., 2012. Rapid microfluidic screening of CO 2 solubility and diffusion in pure and mixed solvents. Lab on a Chip 12, 3387-3391.

Lewis, J.M., Wang, Y., 2018. Two-phase frictional pressure drop and water film thickness in a thin hydrophilic microchannel. International Journal of Heat and Mass Transfer 127, 813-828.

Lewis, J.M., Wang, Y., 2019. Two-phase frictional pressure drop in a thin mixed-wettability microchannel. International Journal of Heat and Mass Transfer 128, 649-667.

Li, X., He, L., He, Y., Gu, H., Liu, M., 2019a. Numerical study of droplet formation in the ordinary and modified T-junctions. Physics of Fluids 31, 082101.

Li, X., Huang, Y., Chen, X., Sunden, B., Wu, Z., 2020a. Breakup dynamics of gas-liquid interface during Taylor bubble formation in a microchannel flow-focusing device. Experimental Thermal and Fluid Science 113, 110043.

Li, X., Huang, Y., Chen, X., Wu, Z., 2020b. Breakup dynamics of low-density gas and liquid interface during Taylor bubble formation in a microchannel flow-focusing device. Chemical Engineering Science 215, 115473.

Li, Z., Wang, L., Li, J., Chen, H., 2019b. Drainage of lubrication film around stuck bubbles in vertical capillaries. Applied Physics Letters 115.

Liu, H., Zhang, Y., 2011. Droplet formation in microfluidic cross-junctions. Physics of Fluids 23, 082101.

Liu, Y., Yue, J., Xu, C., Zhao, S., Yao, C., Chen, G., 2020. Hydrodynamics and local mass transfer characterization under gas–liquid–liquid slug flow in a rectangular microchannel. AIChE Journal 66, e16805.

Lockhart, R., Martinelli, R., 1949. Proposed correlation of data for isothermal two-phase, two-component flow in pipes. Chem. Eng. Prog 45, 39-48.

Loubière, K., G.F., Radjagobalou R., P.A.B.J.-F., Elgue S., Prat L. Dechy-Cabaret O., , 2017. LED-driven spiral-shaped microreactor as a tool to investigate sensitized photooxygenations. European Photochemistry Association (EPA) Newsletters Special Issue “Synthetic Organic Photochemistry" 93, 42-46.

Loubière, K., Oelgemöller, M., Aillet, T., Dechy-Cabaret, O., Prat, L., 2016. Continuous-flow photochemistry: A need for chemical engineering. Chemical Engineering and Processing: Process Intensification 104, 120-132.

Lu, Y., Fu, T., Zhu, C., Ma, Y., Li, H.Z., 2014a. Pinch-off mechanism for Taylor bubble formation in a microfluidic flow-focusing device. Microfluidics and Nanofluidics 16, 1047-1055.

Lu, Y., Fu, T., Zhu, C., Ma, Y., Li, H.Z., 2014b. Scaling of the bubble formation in a flow-focusing device: Role of the liquid viscosity. Chemical Engineering Science 105, 213-219.

Madana, V.S.T., Ali, B.A., 2020. Numerical investigation of engulfment flow at low Reynolds numbers in a T-shaped microchannel. Physics of Fluids 32, 072005.

Martínez, F.L.D., Julcour, C., Billet, A.-M., Larachi, F., 2016. Modelling and simulations of a monolith reactor for three-phase hydrogenation reactions—Rules and recommendations for mass transfer analysis. Catalysis Today 273, 121-130.

Méhault, C., Vanoye, L., Philippe, R., de Bellefon, C., 2021. Multiphase alternated slug flows: conditions to avoid coalescence and characterization of mass transfer between droplets. Chemical Engineering Journal 407, 127215.

Mei, M., Felis, F., Dietrich, N., Hébrard, G., Loubière, L., 2020a. Hydrodynamics of gas-liquid slug flows in a long in-plane spiral-shaped milli-reactor. Theoretical Foundations of Chemical Engineering 54, 25-47.

Mei, M., Hébrard, G., Dietrich, N., Loubière, K., 2020b. Gas-liquid mass transfer around Taylor bubbles flowing in a long, in-plane, spiral-shaped milli-reactor. Chemical Engineering Science 222, 115717.

Molla, S., Eskin, D., Mostowfi, F., 2011. Pressure drop of slug flow in microchannels with increasing void fraction: experiment and modeling. Lab on a Chip 11, 1968-1978.

Muradoglu, M., Stone, H.A., 2007. Motion of large bubbles in curved channels. Journal of Fluid Mechanics 570, 455-466.

Ngai, J.H., Ho, J.K., Chan, R.K., Cheung, S., Leung, L.M., So, S., 2017. Growth, characterization, and thin film transistor application of CH 3 NH 3 PbI 3 perovskite on polymeric gate dielectric layers. Rsc Advances 7, 49353-49360.

Nirmal, G.M., Leary, T.F., Ramachandran, A., 2019. Mass transfer dynamics in the dissolution of Taylor bubbles. Soft Matter 15, 2746-2756.

Otsu, N., 1979. A threshold selection method from gray-level histograms. IEEE transactions on systems, man, and cybernetics 9, 62-66.

Pan, Z., Zhang, X., Xie, Y., Cai, W., 2014. Instantaneous Mass Transfer under Gas-Liquid Taylor Flow in Circular Capillaries. Chemical Engineering & Technology 37, 495-504.

Patel, R.S., Weibel, J.A., Garimella, S.V., 2017. Characterization of liquid film thickness in slug-regime microchannel flows. International Journal of Heat and Mass Transfer 115, 1137-1143.

Paul, M., Strassl, F., Hoffmann, A., Hoffmann, M., Schlüter, M., Herres-Pawlis, S., 2018. Reaction systems for bubbly flows. European Journal of Inorganic Chemistry 2018, 2101-2124.

Perrot, S., Dutertre-Catella, H., Martin, C., Warnet, J.M., Rat, P., 2003. A new nondestructive cytometric assay based on resazurin metabolism and an organ culture model for the assessment of corneal viability. Cytometry Part A: The Journal of the International Society for Analytical Cytology 55, 7-14.

Piccione, P.M., Rasheed, A.A., Quarmby, A., Dionisi, D., 2017. Direct Visualization of Scale-Up Effects on the Mass Transfer Coefficient through the "Blue Bottle" Reaction. Journal of Chemical Education 94.

Plunkett, R.J., Evans, W.L., 1938. The Mechanism of Carbohydrate Oxidation. XXIV. 1 The Action of aldehydo-d-Glucose and of aldehydo-d-Galactose in Alkaline Solutions2. Journal of the American Chemical Society 60, 2847-2852.

Pollington, S.D., Enache, D.I., Landon, P., Meenakshisundaram, S., Dimitratos, N., Wagland, A., Hutchings, G.J., Stitt, E.H., 2009. Enhanced selective glycerol oxidation in multiphase structured reactors. Catalysis Today 145, 169-175.

Pons, A., Sagués, F., Bees, M., 2004. Chemoconvection patterns in the methylene-blue–glucose system: Weakly nonlinear analysis. Physical Review E 70, 066304.

Pons, A., Sagués, F., Bees, M., Sørensen, P.G., 2002. Quantitative analysis of chemoconvection patterns in the methylene-blue− glucose system. The Journal of Physical Chemistry B 106, 7252-7259.

Pons, A.J., Sagués, F., Bees, M.A., Sørensen, P.G., 2000. Pattern Formation in the Methylene-Blue−Glucose System. The Journal of Physical Chemistry B 104, 2251-2259.

Qu, J., Wang, Q., Li, C., Han, X., He, Z., 2014. A simple model for Taylor flow induced contact angle hysteresis and capillary pressure inside mini/micro-scale capillary tubes. International Journal of Heat and Mass Transfer 78, 1004-1007.

Radjagobalou, R., Blanco, J.-F., Dechy-Cabaret, O., Oelgemöller, M., Loubière, K., 2018. Photooxygenation in an advanced led-driven flow reactor module: Experimental investigations and modelling. Chemical Engineering and Processing - Process Intensification 130, 214-228.

Radjagobalou, R., Blanco, J.-F., Petrizza, L., Le Bechec, M., Dechy-Cabaret, O., Lacombe, S., Save, M., Loubiere, K., 2020. Efficient Photooxygenation Process of Biosourced α-Terpinene by Combining Controlled LED-Driven Flow Photochemistry and Rose Bengal-Anchored Polymer Colloids. ACS Sustainable Chemistry & Engineering 8, 18568-18576.

Roudet, M., Billet, A.M., Cazin, S., Risso, F., Roig, V., 2017. Experimental investigation of interfacial mass transfer mechanisms for a confined high-reynolds-number bubble rising in a thin gap. AIChE Journal 63, 2394-2408.

Roudet, M., Loubiere, K., Gourdon, C., Cabassud, M., 2011. Hydrodynamic and mass transfer in inertial gas-liquid flow regimes through straight and meandering millimetric square channels. Chemical Engineering Science 66, 2974-2990.

Rüttinger, S., Spille, C., Hoffmann, M., Schlüter, M., 2018. Laser-Induced Fluorescence in Multiphase Systems. ChemBioEng Reviews 5, 253-269.

Sander, R., 2015. Compilation of Henry's law constants (version 4.0) for water as solvent. Atmos. Chem. Phys 15, 4399-4981.

Sattari-Najafabadi, M., Nasr Esfahany, M., Wu, Z., Sunden, B., 2018. Mass transfer between phases in microchannels: A review. Chemical Engineering and Processing - Process Intensification 127, 213-237.

Schuler, J., Neuendorf, L.M., Petersen, K., Kockmann, N., 2021. Micro-computed tomography for the 3D time-resolved investigation of monodisperse droplet generation in a co-flow setup. AIChE Journal 67.

Shaffer, P.A., Friedemann, T.E., 1930. Sugar activation by alkali I. Formation of lactic and saccharinic acids. Journal of Biological Chemistry 86, 345-374.

Siu, V.S., Feng, J., Flanigan, P.W., Palmore, G.T.R., Pacifici, D., 2014. A "plasmonic cuvette": dye chemistry coupled to plasmonic interferometry for glucose sensing. Nanophotonics 3, 125-140.

Sobieszuk, P., Aubin, J., Pohorecki, R., 2012. Hydrodynamics and Mass Transfer in Gas-Liquid Flows in Microreactors. Chemical Engineering & Technology 35, 1346–1358.

Sontti, S.G., Atta, A., 2019. Numerical insights on controlled droplet formation in a microfluidic flow-focusing device. Industrial & Engineering Chemistry Research 59, 3702–3716.

Stankiewicz, A., Van Gerven, T., & Stefanidis, G., 2019. The Fundamentals of Process Intensification. John Wiley & Sons.

Sun, R., Cubaud, T., 2011. Dissolution of carbon dioxide bubbles and microfluidic multiphase flows. Lab on a Chip 11, 2924.

Tan, J., Lu, Y.C., Xu, J.H., Luo, G.S., 2012a. Mass transfer characteristic in the formation stage of gas-liquid segmented flow in microchannel. Chemical Engineering Journal 185, 314-320.

Tan, J., Lu, Y.C., Xu, J.H., Luo, G.S., 2012b. Mass transfer performance of gas-liquid segmented flow in microchannels. Chemical Engineering Journal 181, 229-235.

Taylor, G., 1961. Deposition of a viscous fluid on the wall of a tube. Journal of Fluid Mechanics 10, 161-165.

Thulasidas, T., Abraham, M., Cerro, R., 1995. Bubble-train flow in capillaries of circular and square cross section. Chemical Engineering Science 50, 183-199.

Thulasidas, T.C., Abraham, M.A., Cerro, R.L., 1997. Flow patterns in liquid slugs during bubble-train flow inside capillaries. Chemical Engineering Science 52, 2947-2962.

Tibiriçá, C.B., do Nascimento, F.J., Ribatski, G., 2010. Film thickness measurement techniques applied to micro-scale two-phase flow systems. Experimental Thermal and Fluid Science 34, 463-473.

Tice, J.D., Song, H., Lyon, A.D., Ismagilov, R.F., 2003. Formation of droplets and mixing in multiphase microfluidics at low values of the Reynolds and the capillary numbers. Langmuir 19, 9127-9133.

Tsoligkas, A.N., Simmons, M.J.H., Wood, J., 2007. Influence of orientation upon the hydrodynamics of gas–liquid flow for square channels in monolith supports. Chemical Engineering Science 62, 4365-4378.

Van Baten, J., Krishna, R., 2004. CFD simulations of mass transfer from Taylor bubbles rising in circular capillaries. Chemical Engineering Science 59, 2535-2545.

Van Hecke, W., Bockrath, R., De Wever, H., 2019. Effects of moderately elevated pressure on gas fermentation processes. Bioresource Technology 293, 122129.

Van Hoeve, W., Dollet, B., Versluis, M., Lohse, D., 2011. Microbubble formation and pinch-off scaling exponent in flow-focusing devices. Physics of Fluids 23, 092001.

Van Krevelen, D., Hoftijzer, P., 1948. Kinetics of gas-liquid reactions part I. General theory. Recueil des Travaux Chimiques des Pays-Bas 67, 563-586.

van Steijn, V., Kleijn, C.R., Kreutzer, M.T., 2009. Flows around Confined Bubbles and Their Importance in Triggering Pinch-Off. Physical Review Letters 103.

van Steijn, V., Kreutzer, M.T., Kleijn, C.R., 2007. μ-PIV study of the formation of segmented flow in microfluidic T-junctions. Chemical Engineering Science 62, 7505-7514.

Vandu, C.O., Liu, H., Krishna, R., 2005. Mass transfer from Taylor bubbles rising in single capillaries. Chemical Engineering Science 60, 6430-6437.

Vashisth, S., Kumar, V., Nigam, K.D., 2008. A review on the potential applications of curved geometries in process industry. Industrial & Engineering Chemistry Research 47, 3291-3337.

Vashisth, S., Nigam, K., 2007. Experimental investigation of pressure drop during two-phase flow in a coiled flow inverter. Industrial & Engineering Chemistry Research 46, 5043-5050.

Verma, R.K., Ghosh, S., 2019. Two-Phase Flow in Miniature Geometries: Comparison of Gas-Liquid and Liquid-Liquid Flows. ChemBioEng Reviews 6, 5-16.

Wongwailikhit, K., 2019. Etude du transfert de masse gaz-liquide dans une colonne à bulles et à pulvériser avec ajout de milieu solide. Toulouse, INSA.

Xu, F., Hébrard, G., Dietrich, N., 2020. Comparison of three different techniques for gas-liquid mass transfer visualization. International Journal of Heat and Mass Transfer 150, 119261.

Xu, J.H., Li, S., Tan, J., Luo, G., 2008. Correlations of droplet formation in T-junction microfluidic devices: from squeezing to dripping. Microfluidics and Nanofluidics 5, 711-717.

Xu, K., Tostado, C.P., Xu, J.H., Lu, Y.C., Luo, G.S., 2014. Direct measurement of the differential pressure during drop formation in a co-flow microfluidic device. Lab on a Chip 14, 1357.

Yang, L., 2017. Local investigations of gas-liquid mass transfer around Taylor bubbles flowing in straight and meandering millimetric channels using a colorimetric method. Toulouse, INSA.

Yang, L., Dietrich, N., Loubière, K., Gourdon, C., Hébrard, G., 2016a. Optical methods to investigate the enhancement factor of an oxygen-sensitive colorimetric reaction using microreactors. AIChE Journal.

Yang, L., Dietrich, N., Loubière, K., Gourdon, C., Hébrard, G., 2016b. Visualization and characterization of gas-liquid mass transfer around a Taylor bubble right after the formation stage in microreactors. Chemical Engineering Science 143, 364-368.

Yang, L., Loubière, K., Dietrich, N., Men, C.L., Gourdon, C., Hébrard, G., 2017a. Local investigations on the gas-liquid mass transfer around Taylor bubbles flowing in a meandering millimetric square channel. Chemical Engineering Science 165, 192-203.

Yang, L., Nieves-Remacha, M.J., Jensen, K.F., 2017b. Simulations and analysis of multiphase transport and reaction in segmented flow microreactors. Chemical Engineering Science 169, 106-116.

Yang, L., Xu, F., Zhang, Q., Liu, Z., Chen, G., 2020. Gas-liquid hydrodynamics and mass transfer in microreactors under ultrasonic oscillation. Chemical Engineering Journal, 125411.

Yao, C., Dong, Z., Zhang, Y., Mi, Y., Zhao, Y., Chen, G.W., 2015. On the leakage flow around gas bubbles in slug flow in a microchannel. AIChE Journal 61, 3964-3972.

Yao, C., Dong, Z., Zhao, Y., Chen, G., 2014. An online method to measure mass transfer of slug flow in a microchannel. Chemical Engineering Science 112, 15-24.

Yao, C., Zhao, Y., Chen, G., 2018. Multiphase processes with ionic liquids in microreactors: hydrodynamics, mass transfer and applications. Chemical Engineering Science 189, 340-359.

Yao, C., Zhao, Y., Ma, H., Liu, Y., Zhao, Q., Chen, G., 2021. Two-phase flow and mass transfer in microchannels: A review from local mechanism to global models. Chemical Engineering Science 229, 116017.

Yao, C., Zhao, Y., Zheng, J., Zhang, Q., Chen, G., 2020. The effect of liquid viscosity and modeling of mass transfer in gas–liquid slug flow in a rectangular microchannel. AIChE Journal 66, e16934.

Yao, C., Zheng, J., Zhao, Y., Zhang, Q., Chen, G., 2019. Characteristics of gas-liquid Taylor flow with different liquid viscosities in a rectangular microchannel. Chemical Engineering Journal 373, 437-445.

Ye, X., Hao, T., Chen, Y., Ma, X., Jiang, R., 2020. Liquid film transport around Taylor bubble in a microchannel with gas cavities. Chemical Engineering and Processing - Process Intensification 148, 107828.

Yin, Y., Fu, T., Zhu, C., Guo, R., Ma, Y., Li, H., 2018. Dynamics and mass transfer characteristics of CO2 absorption into MEA/[Bmim][BF4] aqueous solutions in a microchannel. Separation and Purification Technology 210, 541-552.

Yue, J., 2017. Multiphase flow processing in microreactors combined with heterogeneous catalysis for efficient and sustainable chemical synthesis. Catalysis Today 308, 3-19.

Yue, J., Chen, G., Yuan, Q., Luo, L., Gonthier, Y., 2007. Hydrodynamics and mass transfer characteristics in gas–liquid flow through a rectangular microchannel. Chemical Engineering Science 62, 2096-2108.

Zaloha, P., Kristal, J., Jiricny, V., Völkel, N., Xuereb, C., Aubin, J., 2012. Characteristics of liquid slugs in gas–liquid Taylor flow in microchannels. Chemical Engineering Science 68, 640-649.

Zhang, Peng, Yao, C., Ma, H., Jin, N., Zhang, X., Lü, H., Zhao, Y., 2018. Dynamic changes in gas-liquid mass transfer during Taylor flow in long serpentine square microchannels. Chemical Engineering Science 182, 17-27.

Zhang, Weipeng, Wang, X., Feng, X., Yang, C., Mao, Z.-S., 2016. Investigation of Mixing Performance in Passive Micromixers. Industrial & Engineering Chemistry Research 55, 10036-10043.

Zhang, C., Fu, T., Zhu, C., Jiang, S., Ma, Y., Li, H.Z., 2017. Dynamics of bubble formation in highly viscous liquids in a flow-focusing device. Chemical Engineering Science 172, 278-285.

Zrimšek, P., Kunc, J., Kosec, M., Mrkun, J., 2004. Spectrophotometric application of resazurin reduction assay to evaluate boar semen quality. International journal of andrology 27, 57-62.